INFORMATION TO USERS

This manuscript has been reproduced from the microfilm master. UMI films the text directly from the original or copy submitted. Thus, some thesis and dissertation copies are in typewriter face, while others may be from any type of computer printer.

The quality of this reproduction is dependent upon the quality of the copy submitted. Broken or indistinct print, colored or poor quality illustrations and photographs, print bleedthrough, substandard margins, and improper alignment can adversely affect reproduction.

In the unlikely event that the author did not send UMI a complete manuscript and there are missing pages, these will be noted. Also, if unauthorized copyright material had to be removed, a note will indicate the deletion.

Oversize materials (e.g., maps, drawings, charts) are reproduced by sectioning the original, beginning at the upper left-hand corner and continuing from left to right in equal sections with small overlaps. Each original is also photographed in one exposure and is included in reduced form at the back of the book.

Photographs included in the original manuscript have been reproduced xerographically in this copy. Higher quality 6" x 9" black and white photographic prints are available for any photographs or illustrations appearing in this copy for an additional charge. Contact UMI directly to order.

UMI

A Bell & Howell Information Company
300 North Zeeb Road, Ann Arbor MI 48106-1346 USA
313/761-4700 800/521-0600

Reproduced with permission of the copyright owner. Further reproduction prohibited without permission.

MEASUREMENT OF GLOBAL VARIABLES AND CORRELATIONS OF POSITIVE AND NEGATIVE TRACKS PRODUCED IN SILICON ON LEAD INTERACTIONS AT 14.6 GeV/c PER INCIDENT NUCLEON AT THE AGS

by

EFSTRATIOS EFSTATHIADIS

A dissertation submitted to the Graduate Faculty in Physics in partial fulfillment of the requirements for the degree of Doctor of Philosophy, The City University of New York

1996

UMI Number: 9707085

UMI Microform 9707085

UMI
300 North Zeeb Road
Ann Arbor, MI 48103

This manuscript has been read and accepted for the Graduate Faculty in Physics in satisfaction of the dissertation requirement for the degree of Doctor of Philosophy.

5/23/96
Date

Prof. Martin A. Kramer Martin A. Kramer
Chair of Examining Committee

7/11/96
Date

Prof. Joseph B. Krieger Joseph B. Krieger
Executive Officer

Dr. Martin Den Boer

Dr. Wlodek Guryn Wlodek Guryn

Dr. Ronald S. Longacre Ronald S. Longacre

Dr. Leonard O. Roellig Leonard O. Roellig

Supervisory Committee

THE CITY UNIVERSITY OF NEW YORK

ABSTRACT

MEASUREMENT OF GLOBAL VARIABLES AND CORRELATIONS OF POSITIVE AND NEGATIVE TRACKS PRODUCED IN SILICON ON LEAD INTERACTIONS AT 14.6 GeV/c PER INCIDENT NUCLEON AT THE AGS

by

Efstratios Efstathiadis

Adviser: Professor Martin A. Kramer

Relativistic heavy ion collisions provide a unique experimental tool to study strongly interacting matter at extreme conditions of density and temperature. It is predicted that under such extreme conditions the basic structure of hadronic matter should undergo a fundamental change (a phase transition) from a system of nucleons and mesons to a phase of deconfined quarks and gluons, a phase known as quark-gluon plasma (QGP). The goal of relativistic heavy ion collisions is to determine the thermodynamic properties of the state produced in energetic nuclear collisions and understand the phase structure as these states evolve from the initial collision to the burst of particles that reach the detectors.

This thesis provides important information on the production of positive and negative particles in relativistic Si on Pb collisions (experiment E810) at the AGS. We present the results of the analysis of 12051 central events. Rapidity, transverse mass distributions and inverse exponential and Boltzmann slopes for negative pions and protons are presented. A low transverse mass enhancement in the production of negative pions was observed, which can give an estimate of the number of excited nucleons in our data.

We estimated an average of 1.8 pions per participating nucleon are produced. Rapidity and transverse energy distributions play an important role in the discussions of nuclear stopping, a paramount element in estimates of the temperature and densities of the large volume of hot compressed, nuclear matter after a central nuclear collision. Positive-negative track correlations were observed in our data and were used to get an estimate of the population of excited nucleons, and thus the temperature of the system (≈ 81MeV in the forward rapidity region).

The RANDOM event generator is introduced and used to study strangeness production in heavy ion collisions at the AGS.

A thorough understanding of the reaction mechanisms in relativistic heavy ion collisions is an important prerequisite in any search for quark-gluon plasma production. Global quantities have proven to be valuable tools for understanding the reaction mechanisms.

ACKNOWLEDGMENTS

My association with this experiment has been rewarding. In addition to the scientific competence demonstrated by the members of our collaboration, there has been evident an outstanding spirit of cooperation and comradeship. I would like to take this opportunity to thank the many people who have contributed directly and indirectly, to the work described in this thesis.

It is impossible to adequately thank Prof. Seymour J. Lindenbaum who introduced me to the physics of relativistic heavy ion collisions a few years ago. His four decades outstanding career in physics has benefited me with his tremendous experience and wisdom. Unfortunately, because of his illness, we were not able to finish my thesis work. I send to him my best wishes for a quick recovery.

I would like to express my heartfelt thanks to Prof. Martin A. Kramer. When Prof. Lindenbaum become unavailable, Prof. Kramer agreed to take over supervising my thesis research and to continue working with me on the same subject. He became my official advisor and he guided me to the end of my thesis with his constant advice, support, and patience. He provided me with lot of encouragement and he was always ready to help with bureaucratic difficulties.

This thesis wouldn't be possible without the contribution of Dr. Ronald S. Longacre. I thank him for his continuous assistance, encouragement, inspiration and guidance. I am grateful to him for his valuable contributions to all phases of the experiment and the analysis. The advice and guidance he has provided in writing this thesis is very much appreciated.

I have had many useful discussions with Dr. Alfred C. Saulys. He helped me with his suggestions and guidance in the analysis stage.

I am fortunate to have had the opportunity to work with many physicists, engineers, and technicians of E810/E891, E881 and STAR at BNL.

I would like to thank the members of the committee: Prof. Marten Den Boer, Dr. Wlodek Guryn and Prof. Leonard Roellig. I thank them for serving on my committee and making the time to listen to my work and read my thesis.

I thank my fellow students Kaihui Zhao, Yujie Zhu and Visiting Prof. Chang S. Chan for many enlightening conversations.

I acknowledge the invaluable Liz Mogavero and Sharon Smith who have helped on a large amount of paper work for an off campus foreign student to survive. Whatever the task, they have always tried to do even more than called for.

I offer my sincere gratitude to my parents and my family for their patience, support and understanding during all the time it took me to get here. Last but not least, I thank my wife, Eleni. Her understanding, motivation, support and love were essential in the completion of this thesis. She enriched my life by bringing in the world our daughter a few months ago.

This work was completed with the support of the US Department of Energy under contract numbers DE-FG02-91ER40645, DE-AC02-83ER40107 and The City University of New York PSC-BHE Research Award Program.

CONTENTS

LIST OF TABLES

LIST OF FIGURES

When you start on your journey to Ithaca,
then pray that the road is long,
full of adventure, full of knowledge.
Konstantinos Kavafis ("ITHACA")

1. INTRODUCTION

1.1 The fundamental forces

It is an impressive demonstration of the unifying power of physics to realize that all the phenomena observed in the natural world can be attributed to the effects of just four fundamental forces [1, 2, 3, 4]. These are the familiar forces of gravity and electromagnetism, and the not-so-familiar weak and strong forces. Only two of these forces, gravity and electromagnetism, have significant effects at observable ranges. The effects of the weak and strong nuclear forces are confined to within, at most, 10^{-15} m of their sources. It is worthwhile summarizing a few key facts about each of the four forces.

1.1.1 Gravity

Gravity is the far most familiar of the forces in human experience. The source of the force is the mass and is always attractive between two masses (m_1, m_2) and is always directed along a line joining the two (r). The gravitational force is described classically by Newton's law:

$$F = G\frac{m_1 m_2}{r^2} \tag{1.1}$$

The strength of the force is governed by constant G (table 1). We notice the effects of gravity because it is the only long-range force acting between electrically neutral particles. In the microworld the effects of gravity are mainly negligible.

The relativistic theory of gravitation (general relativity theory) was developed by Einstein on the basis of the idea that the theory must be uniquely determined by the requirement of invariance under local transformations. General relativity has predicted and quantitatively described a number of new effects as the deflection of light rays and radio waves by a gravitational field (that of the sun), gravitational waves and black holes. Unfortunately, attempts to construct a quantum theory of gravitation have so far been unsuccessful. This is mostly due to two factors. The first is that gravitational interactions between individual elementary particles is very weak and thus lies beyond the capabilities of experimental study in the laboratory. The second is that it must be the most complex of all known theories. The complexities in a quantum relativistic theory increase sharply as the value of the spin of the particle increases (the graviton, which is responsible for gravity, has spin 2 in these theories).

	Gravity	**Electromagnetic**	**Weak**	**Strong**
Field quantum	Graviton	Photon	Intermediate bosons $W^{\pm}$, Z^0	Gluons (8)
Dimensionless coupling constant	$G_N m_p^2 \approx 10^{-38}$	$\alpha = 1/137$	$G_N m_p^2 \approx 10^{-5}$	$\alpha_S \approx 1$
Source	Mass	Electric charge	"Weak" charge	Strong charge
Range (m)	∞	∞	10^{-18}	10^{-15}
Typical cross sectionat 1GeV (mb)	10^{-77} $g + p \rightarrow g + p$	10^{-1} $\gamma + p \rightarrow \gamma + p$	10^{-11} $\nu + p \rightarrow \nu + p$	10^{1} $n + p \rightarrow n + p$
Typical lifetime of particle states (sec)		10^{-21} $\Sigma^0 \rightarrow \Lambda^0 + \gamma$	10^{-6} Beta decay	10^{-23} $\Delta^+ \rightarrow p + \pi^0$

Table 1: The four basic forces [2]. Cross sections are expressed in mb (where 1 barn = 10^{-24} m^2). The stronger the force the larger is the effective scattering area (cross section), and the shorter the lifetime of the particle state.

1.1.2 Electromagnetism

Electromagnetic forces have infinite range allowing macroscopic phenomena to guide our understanding of classical electromagnetism, and it is a reasonably strong force, allowing its microscopic phenomena to be observed and to guide our formulation of *Quantum Electrodynamics* (QED). The source of this force is the electric charge which can be either positive or negative. The force is attractive between unlike charges and repulsive between like charges. For two charges at rest the electrostatic force between them is given by Coulomb's law:

$$F = K\frac{N_1eN_2e}{r^2} \tag{1.2}$$

K is a constant depending on electric permittivity of free space, N_1e and N_2e are the two charges and r their distance. A moving charge has associated with it not only an electric field, but also a magnetic field. When a charge is subject to an acceleration, then a variation in electric and magnetic fields is propagated out through space to signal the event. Electromagnetic phenomena are all described in the classical regime by Maxwell's equations [5]. One interesting feature of these equations is that they are asymmetric owing to the absence of a fundamental quantum of magnetic charge. In an atom, electrons are bound to the nucleus by the Coulomb force to occupy a region of about 10^{-8} cm in extent.

The theory of Quantum Electrodynamics extends Maxwell's theory to atomic scale and it was developed in the 1930s and 1940s [6]. In QED interactions take place via the exchange of photons. The exchanged photons are "alive" only for a period concomitant with the constraints of the uncertainty principle and are known *as virtual photons*. QED is the most accurate of all physical theories. The accuracy of calculations in QED is based on the techniques of perturbation theory, using the small dimensionless parameter $\alpha = e^2/4\pi\hbar c \approx 1/137$. We can control the level of accuracy of the calculations by including higher and higher order virtual processes. In fact, QED calculations of certain atomic and electronic properties agree with experiment to within one part in a billion ([4, 6]).

1.1.3 The weak force

Many nuclei are known to be unstable and to emit several kinds of particles when they decay; historically these particles are called alpha particles, beta rays and gamma rays. A beta ray is an electron emitted when a neutron in a nucleus decays into a proton, an electron and an electron antineutrino:

$$n \to p + e^- + \bar{\nu}_e \tag{1.3}$$

The proton remains in the nucleus; the electron and its antineutrino escape. This decay has a half-life of about 18 minutes. This period is much longer than any of the phenomena associated with the strong force, and there is no reason to expect the influence of the electromagnetic force to affect the decay of the uncharged neutron. So, it is clear that neutron decay is due to some qualitatively new force of nature. Beta decay is just one of many manifestations of the weak interaction. The weak interactions take place between all the quarks and lepton constituents. It is so weak, however, that it is usually swamped by the much stronger electromagnetic and strong interactions, unless these are forbidden by conservation rules. By the 1950s it was known that all weak processes could be described in terms of current-current interactions as proposed by Fermi in 1934. In weak processes the charge-changing currents appear to interact locally (at a single point) without the help of an intermediary (as the photon in QED). The coupling constant for this local interaction (denoted by G_F and called Fermi constant) is not dimensionless as α in QED. In units of energy, the measured value of G_F^{-1} equals 293 GeV. This lead to the idea that the interaction between the weak currents is mediated by a "heavy photon", called the *W* boson; its existence explains the short range of the weak interactions.

Since both the weak and the electromagnetic interactions involve electric charges, these two might be manifestations of the same basic force. This argument not only predicts the existence of a *W* boson, but also yields a rough estimate of its mass: 25 GeV/c^2.

Several attempts were made in 1950s and 1960s (Schwinger, Glashow, Ward, Salam) to construct an "electroweak theory" in terms of a local gauge (Yang-Mills) theory that generalizes QED. Weinberg calculated the masses of weak bosons in 1967. The success of the electroweak theory culminated in 1982 with the discovery at CERN of the W boson at almost exactly the predicted mass [7, 8, 9]. The foundation of the Electroweak theory is the gauge symmetry SU(2) × U(1). Here SU(2) is the group of weak isospin and U(1) is the group of weak hypercharge. The electroweak theory differs from pure electrodynamics and from chromodynamics (next section) in two features. First the gauge symmetry is spontaneously broken and consequently the weak gauge bosons, the so-called intermediate bosons $W^{\pm}$ and Z^0, are massive. Second, the theory is mirror-asymmetric.

1.1.4 The strong force

When the neutron was discovered by J. Chadwick in 1932, it became obvious that a new force of nature must exist to bind together the neutrons and the protons (referred to generically as nucleons) within the nucleus. The strong force must be very strongly attractive to overcome the mutual repulsions felt by the protons and to hold the nucleons together inside a nucleus, in a region of about 10^{-12} cm. The strong force is of extremely short range (1 fm, 1fm = 10^{-15} m); in fact, the force may be thought as of acting between two protons only when they are actually touching. Strong forces do not distinguish between protons and neutrons, a property known as *charge independence* (in a more technical language, the proton and the neutron transform into each other under isospin rotations and the Lagrangian of the strong interaction is invariant under these rotations). The particles that participate in strong interactions are called *hadrons*. Leptons do not feel the strong force.

In the early 1960s, with the advent of accelerators, many so-called elementary particles had been discovered, each with well-defined values of the various quantum numbers. In 1961 both Gell-Mann and Neeman proposed that all hadrons could be classified in multiplets of the symmetry group called SU(3) [10, 11], figure 1.1. The great triumph of this proposal was the prediction and subsequent discovery of the omega minus (Ω^-). The Ω^- was discovered at the AGS at Brookhaven National Laboratory by Nicholas Samios in 1964 [12], and it filled a vacant space in one of the SU(3) multiplets.

At that time the problem was whether or not such a plethora of different particles could be regarded as truly elementary. Just as the periodic table was eventually explained in terms of a few basic building blocks, so the hadronic zoo was arranged by postulating the existence of a small number of "truly elementary point-like particles" called *quarks*. In 1963 Gell-Mann and, independently, Zweig realized that all hadrons could be constructed from three spin-1/2 fermions, designated *u*, *d*, and *s* (up, down, and strange). The SU(3) symmetry that manifested itself in the table of "elementary particles" arose from an invariance in the Lagrangian of the strong interaction to rotations among these three objects (quarks). This global symmetry is exact only if the u, d, and s quarks have identical masses. Since this is certainly not the case, SU(3) is a broken global symmetry. It is established, however, that SU(3) symmetry among the u, d, and s quarks is preserved by

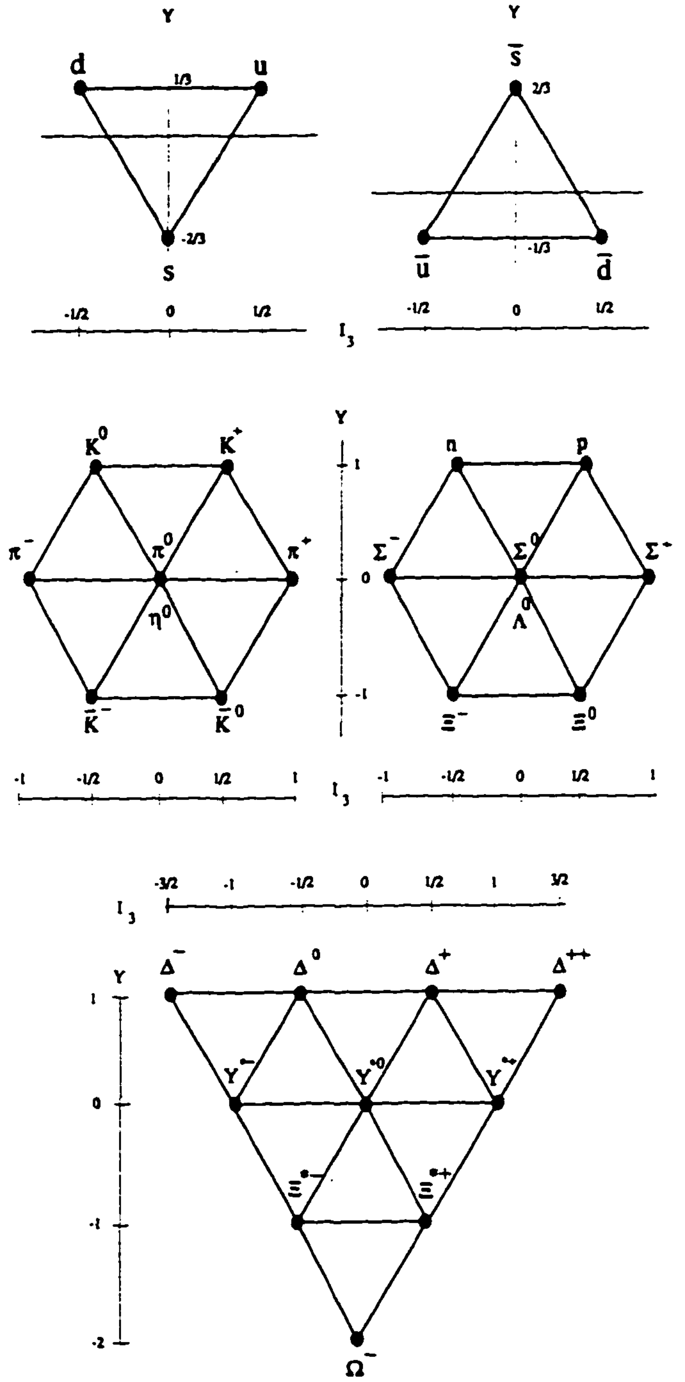

Figure 1.1: The eightfold way classified the hadrons into multiplets of the symmetry group SU(3) [11]. Each particle is plotted according to the quantum numbers I_3 (the third component of strong isospin) and strong hypercharge Y (Y = S + B, where S is strangeness and B is baryon number).

the strong interaction. Nowadays, one refers to this SU(3) symmetry as a *flavor* symmetry, with u, d, and s representing quark flavors. This nomenclature is to distinguish it from another and quite different SU(3) symmetry possessed by quarks, a local symmetry that is associated directly with the strong force and has become known as the SU(3) of color. The theory resulting from this symmetry is called *Quantum Chromodynamics* (QCD) (from the Greek Χρωμα (chroma) = color).

1.1.5 Towards unification

There has always being a suspicion, and hope, that all four forces were manifestations of one source and could therefore be described by a single unified field theory. Down to distances of 10^{-12} cm electromagnetism is the dominant force among the elementary particles. However, at this distance, the strong force, heretofore absent, suddenly comes into play and completely dominates the interparticle dynamics. The weak force is present at all scales but only as a small effect. At the shorter distances being probed by present-day accelerators, the weak and electromagnetic forces become comparable in strength but remain several orders of magnitude weaker than the strong force. It is at this scale that the fundamental similarity of all three forces begins to emerge. Thus as the scale changes, not only does each force itself change, but its relationship to the other forces undergoes a remarkable evolution. The theoretical description of the strong, weak and electromagnetic interactions is now considered well established and the theory shows these forces to be quite similar despite their experimental differences. The formulation has been so successful that it has been coined *the standard model* and serves as a starting point for discussing a grand unification of all forces, including that of gravitation. The formalism of the standard model enables us to describe the strong, weak, and electromagnetic interactions as different manifestations of a single symmetry principle, the principle of local symmetry. The standard model has many arbitrary parameters and leaves unanswered a number of important questions, but one has to keep in mind that it embodies a single unifying principle and therefore seems to point the way toward a grander unification.

1.2 Quantum chromodynamics(QCD) and Quark-Gluon Plasma (QGP)

1.2.1 Quarks and Gluons

QCD is the fundamental theory for understanding strong interaction physics. The field theory for quarks and gluons belongs to a special class of theories known as gauge field theories. The interaction in a field theory can be represented as arising from the requirement that the Lagrangian is invariant under a local gauge transformation. This invariance is called a local gauge invariance. Each quark comes in three varieties (for convenience referred to as *color*: red (r), blue (b), and yellow (y)). A local gauge transformation (color transformation) changes the color of the quark and thus changes the particle, while in QED the local transformation simply changes the phase of an electron. In QED the freedom to change the phase of the electron introduces the photon field (gauge field). A similar procedure in QCD introduces the gluon field. Since there are eight independent symmetry transformations that change the color of a quark, there are eight spin-1 (boson) gluons analogous to the one photon field in QED. The extension of the U(1) local gauge invariance of QED to more complicated symmetries such as SU(2) and SU(3) was first done by Yang and Mills in 1954. These larger symmetry groups involve the so called non-abelian algebras, so they are called non-abelian theories or Yang-Mills theories. The theory of strong interactions (QCD) is based on an SU(3) non-abelian gauge field theory instead of an abelian U(1) theory, like QED.

Quarks	Q	I_z	C	S	T	B	Mass (MeV)
u	2/3	1/2	0	0	0	0	5.6±1.1
d	-1/3	-1/2	0	0	0	0	9.9±1.1
c	2/3	0	1	0	0	0	1350±50
s	-1/3	0	0	-1	0	0	199±33
t	2/3	0	0	0	1	0	180000±15000
b	-1/3	0	0	0	0	-1	≈5000

Table 2 : Properties of quarks. Q is the electric charge, I_z is the z-component of the isospin, C is the charm quantum number, S is the strangeness, T is the topness, and B the bottomness. Quarks: *u*: up, *d*: down, *c*: charm, *s*: strange, *t*: top, and *b*: bottom.

1.2.2 Asymptotic freedom and confinement

Although the gluons are the counterpart of photons in that they have spin one and are massless, they possess one crucial property not shared by photons: they themselves carry color; it is as if photons were charged. This difference has many profound physical consequences. For example, gluons can interact with themselves, and in effect weaken the force at short distances. The opposite effect occurs in QED: screening effects weaken the effective electric charge at large distances. The weakening of color charge at short distances in known as *asymptotic freedom*. This phenomenon was observed in deep inelastic scattering experiments of leptons from nucleons in which the three quarks behave essentially as free particles and explains why hadrons at high energies behave as if they were made of almost free quarks, even though quarks have never been observed free experimentally. In QED the smallness of the coupling constant (α) implies that perturbation theory is applicable. In fact QED calculations of certain atomic and electronic properties agree with experiment to within one part in a billion. In QCD the coupling constant [13] depends on the circumstances and is related to the scale of the momentum transfer(q) by:

$$\alpha_S = \frac{4\pi}{(\frac{11}{3}N_C - 2\frac{N_F}{3})\ln(-\frac{q^2}{\Lambda})} \tag{1.4}$$

N_C is the number of colors ($N_C = 3$) anf N_F the number of flavors ($N_F = 6$).

For large momentum transfers or small distances the coupling strength between color charges decreases (the interaction becomes weaker). Thus, due to the smallness of the coupling constant at small distances or large momentum transfers, perturbative calculations can be used and they provide reliable results that are verified experimentally. The "short distance" is defined by Λ in (1.4) and can be determined only by experiments. It is estimated around 100 - 200 MeV. Thus, the weakening of the force at large energies and at short distances means that we can use perturbation theory to calculate hadronic processes.

The self-interaction of gluons also explains the apparently permanent *confinement* of quarks. No free quarks have ever been observed. They remain confined within hadrons. The confinement property implies that the interaction between quarks, due to exchange of gluons, is increasingly attractive with increasing distance. Even though color is confined, residual strong color forces can leak out in the form of colorless pions or other hadrons and be responsible for the binding of protons and neutrons in nuclei. If one attempts to separate two color sources, a quark and an antiquark, say, the color field between the two sources is limited to a thin filament about 1 fm across, with a resulting effective potential increasing linearly with r. It costs about 1GeV/fm to pull the quark and anti-quark apart. This is the string tension in QCD. If case of bigger kicks, nothing prevents the energy stored in the flux tube from materializing into mesons, in particular pions, which have a mass of only 0.14 GeV and no color. These mesons can escape into the vacuum taking a fraction of the momentum of the system. Instead of seeing a quark escaping, one sees a string of pions with small transverse momenta with respect to the axis of the flux tube. This is a *hadronic jet*. The large momentum transfers that are involved in the production of jets justifies the use of perturbative QCD. Using perturbative QCD calculations [14, 15] we can obtain cross sections and angular distributions of jets. Two-jet and three-jet systems were observed at proton-antiproton collisions at CERN and in electron-positron annihilation. Perturbative QCD also provides rather precise calculations for energy levels of the "quarkonium" (bound systems of heavy quark-antiquark pairs, like charmonium).

Although techniques have been developed and perturbative QCD has many successes, at large distances (10^{-13} cm) and small momentun transfers the "strong" nature of the force becomes dominant and perturbation theory is not valid. In the non-perturbative case the problems are rather difficult. Lattice gauge theory and phenomenological models [16] are being used in the non-perturbative region to provide a qualitative guide to understand some aspects of strong interaction phenomena. Lattice calculations provide the most efficient approach but progress is slow because of the tremendous computer power which is needed in order to provide precise results. One of the results obtained so far, following this approach, is the existence of two phases, a hadronic phase at low energy density and a Quark-Gluon Plasma (QGP) at high energy density. Obtaining evidence for a phase transition is therefore an important new test of QCD.

1.2.3 Deconfinement and Quark-Gluon Plasma

An important consequence of QCD under extreme conditions of density and temperature is the existence of QGP (Quark Gluon Plasma) [17, 18]. QCD predicts that the nuclear matter at densities a few times the nuclear density or at high temperatures ($K_BT \approx 200$ MeV) will not continue to be in hadronic form but become a "soup" of quarks and gluons. The quarks and gluons are now not confined in hadrons but are free to move in much larger (macroscopic) volumes. Again, the issue of deconfinement falls into the non-perturbative region of QCD. Using lattice QCD in the pure SU(3) gauge theory (no quarks in the system) predict a first order transition. The critical temperature is predicted to be around 200 MeV at low density. Lattice QCD calculations including quarks are not completely clear regarding the question of a phase transition.

Figure 1.2 shows a phase transition in lattice gauge calculation [19]. The generic behavior predicted by these calculations is shown in early QCD lattice results, in which the energy density is shown as a function of the temperature. Monte Carlo techniques are used to evaluate the partition function on a finite space-time lattice hence the calculation appears as discrete points with statistical errors. The the energy density ε is normalized to the ideal Stephan-Boltzmann gas form ε_{SB}. At a critical temperature T_C, an abrupt change occurs corresponding to a first-order phase transition from an ideal gas of hadrons to an ideal Quark-Gluon Plasma. Present lattice QCD calculations are probing the details of particle structure and thermodynamic properties near the phase transition and attempting to extend the results to the case of non-zero baryon density. While the order of the physical phase transition is still uncertain, depending delicately on the effective mass of quarks, the critical energy density for plasma formation is clearly predicted to be in the range 1-3 GeV/fm^3. This is to be compared with an energy density of 0.15 GeV/fm^3 for normal nuclear matter, and a density of 0.5 GeV/fm^3 inside a nucleon.

Figure 1.3 shows the phase diagram of nuclear matter [19]. Temperature is plotted vs. net baryon density for an extended volume of nuclear matter in thermal equilibrium. Normal nuclear matter appears at the point shown on the density axis, at zero temperature: this is the neighborhood explored by traditional nuclear physics experiments. The region of the phase transitions corresponding to quark deconfinement (at temperature T_C) is indicated. Above T_C, hadrons dissolve into quarks and gluons. The indicated trajectories show two avenues for probing the quark-gluon plasma with high energy nucleus-nucleus collisions: by reaching high baryon densities among the hot, compressed fragments of the colliding nuclei, and at very high temperatures in the central rapidity region among thermally produced particles where conditions may approximate those of the early universe.

Simple thermodynamic and phenomenological arguments may provide some understanding of the phase change. A useful phenomenological description of quarks in hadrons is provided by the MIT bag model [20]. In the MIT bag model quarks are treated as massless particles inside a bag of finite dimension and are infinitely massive outside the bag. Confinement in the model is a result of the balance of the bag pressure B, which is directed inward. The bag pressure is the phenomenological quantity introduced to take into account the nonperturbative effects of QCD. The value of the "bag pressure" B is in the range:

$$145 \text{ MeV} < B^{1/4} < 235 \text{ MeV (natural units)} \qquad (1.5)$$

We can interpret the bag model as indicating that the essential effect of non-perturbative QCD is to give rise to an inward bag pressure of magnitude B. This inward pressure is balanced by the quantum stress arising from the wave functions of the quarks. It is clear that if the pressure of the quark matter is increased, there will be a point when the outward pressure is greater than the inward pressure. When that happens the bag no longer confine the quark matter. Thus a new phase of matter containing the quarks and gluons in an unconfined state is possible. A larger pressure of quark matter arises when: 1) the temperature of the matter is high and/or when 2) the baryon density is large.

To get an idea of the critical energy density (ε_c) and the critical baryon density (b_c) let's consider a quark-gluon system in thermal equilibrium at a high temperature T, within a volume V. For simplicity, let us first consider the number of quarks to be equal to the number of antiquarks (baryon chemical potential equal to 0). The light quarks (up and down) are assumed to be massless (from table 2, their masses are much smaller than 200 MeV) and we can ignore all interactions among the constituents of the plasma (except

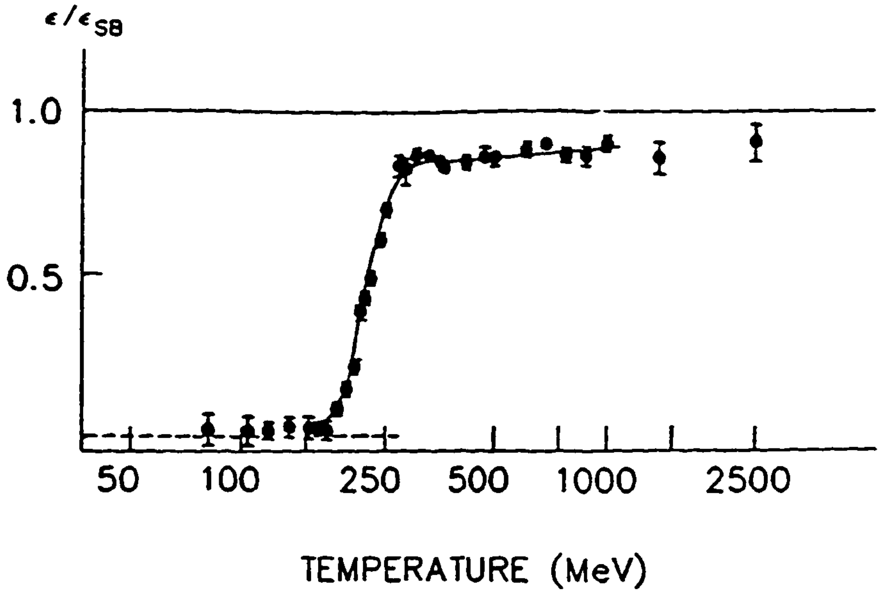

Figure 1.2: Phase transition in lattice gauge calculation.

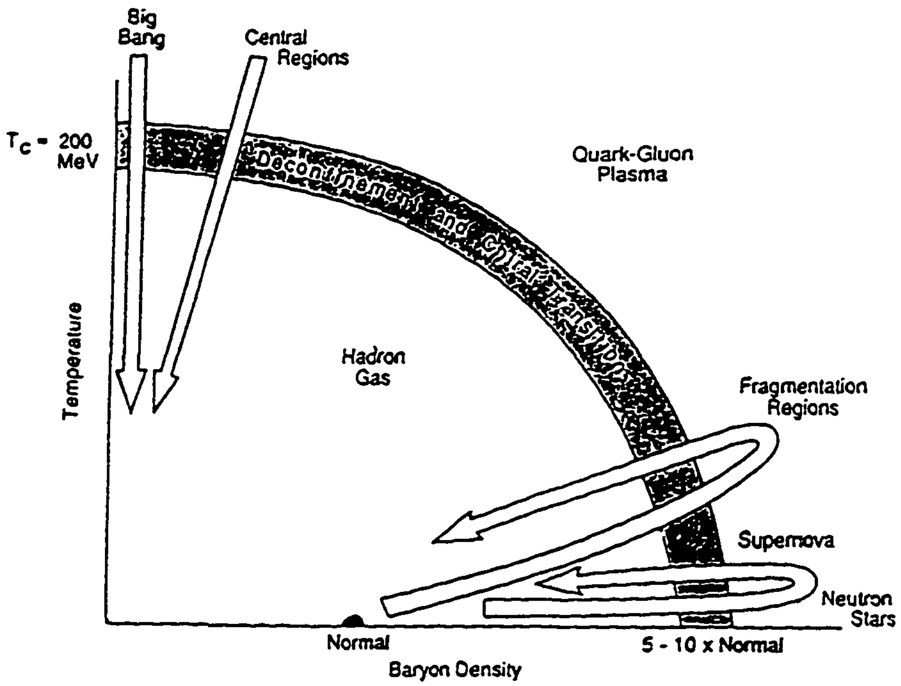

Figure 1.3: Phase diagram of nuclear matter.

for the assumption of thermalization) [18, 21]. The energy density per degree of freedom is :

$$\varepsilon = 37\frac{\pi^2}{30}T^4 \tag{1.6}$$

and the pressure:

$$P = 37\frac{\pi^2}{90}T^4 \tag{1.7}$$

From (1.6) and for T=200 MeV we get ε = 2.54 GeV/fm^3. By setting the pressure from (1.7) equal to the bag constant we get:

$$T_c = (\frac{90}{37\pi^2})^{\frac{1}{4}}B^{\frac{1}{4}} \tag{1.8}$$

At the other extreme of zero temperature (T=0) and non-zero baryon number ($\mu_q \neq 0$, μ_q is the baryon-chemical potential), the pressure is :

$$P = \frac{\mu_q^4}{2\pi^2} = B \Rightarrow \mu_q = (2\pi^2 B)^{\frac{1}{4}} \tag{1.9}$$

and the number density of baryons:

$$n_B = \frac{4}{3}(\frac{1}{2\pi^2})^{\frac{1}{4}}B^{\frac{3}{4}} \tag{1.10}$$

from which we get: n_B = 0.72/fm^3. This value of QGP should be compared with the nucleon baryon density n_B = 0.14/fm^3. Thus the critical baryon density is about 5 times the normal nuclear matter density. When the baryon density exceeds this density, the baryon bag pressure is not strong enough to withstand the pressure due to the degeneracy of quarks, and the confinement of quarks within individual baryon bags will not be possible, leading to formation of a state of deconfined quarks.

1.2.4 Why look for Quark-Gluon Plasma ?

Searches for Quark-Gluon Plasma are not only a big issue in QCD, but also in Astrophysics and Cosmology, although their arguments will not be presented here. To summarize [22, 23]:

1. It is a big issue in QCD. While one is confident that color is no longer confined at high enough density and /or temperature, our approach to QCD at large distances, where color confinement takes place is not precise enough yet. Insight from experiment is very much needed.
2. It is a big issue in astrophysics. The very high pressure at the core of neutron stars could lead to the formation of a QGP. This would affect the dynamics of the star and in particular its cooling rate.
3. It is a big issue in cosmology. The temperature of the universe varies as $t^{-1/2}$ as one approaches the Big-Bang. One eventually reaches a temperature where a QGP should be formed. This happens at about 10^{-5} sec after the Big-Bang, when the temperature of the universe is 200 MeV.

> *Then pray that the road is long.*
> *That the summer mornings are many,*
> *that you will enter ports for the first time*
> *with such pleasure, with such joy!*
> Konstantinos Kavafis ("ITHACA")

2. THE EXPERIMENT

2.1 The Si beam

The acceleration of heavy ion beams at Brookhaven National Laboratory (BNL) starts with the Tandem Van de Graaff accelerator. The Tandem Van de Graaff accelerator injects heavy ions into a synchrotron. Figure 2.1 shows the functional diagram of the Tandem area [24, 25]. The negative ions, with charge -e, are accelerated from ground to +15 MV potential. They pass through the stripping foil in the high voltage terminal, leaving with a most probable charge $+Q_T$, which is a function of the element being accelerated. The electrons are removed by successive collisions with the atoms in the target. The partially stripped ions are accelerated back to ground potential, increasing their energy by 15 Q_T MeV. Exiting from the Van de Graaff, they pass through a second stripping foil (for Gold ions the second stripping foil is a 20 $\mu g/cm^2$ thick Carbon). The second stripping foil follows the first 90^0 analyzing magnet and a second 90^0 magnet selects the charge state Q_F to be transported to the synchrotron. Table 3 shows the Tandem operation parameters for a high voltage terminal of 15MV. S_T and Q_T are the stripping efficiency and most probable charge state after the negative ions have been accelerated to the high voltage terminal and stripped in a thin carbon foil, S_F and Q_F are the same parameters for the final stripping target. The heavy ions are then injected to the Alternating Gradient Synchrotron (AGS), after following a 2000 ft. long tunnel with eight quadrupole doublets to keep the beam focused. The tunnel is of modest size (≈ 10 feet wide) with sufficient space for servicing the various magnets and vacum systems.

For beams of ions with high A (such as Au, A=197) higher energies are required to produce sufficiently intense beams of fully stripped ions. Such ions are first injected into the booster (circ. = 201.75 m) and then into the AGS (circ.= 807.11 m). After extraction from the Booster, the ions pass through one more stripping target, become completely stripped and then are injected into the AGS, figure 2.2. Particle bunches at the AGS are accelerated to the top AGS energy (11.6 GeV/amu for Au, 14.6 GeV/amu for Si, 28 GeV/amu for protons). At the AGS a series of alternately converging and diverging magnetic lenses of equal strength, properly spaced around the orbit, provide strong restoring forces for displacements in position or angle within the orbit[1]. The strong focusing leads to free oscillations of higher frequency, shorter wavelength, and smaller amplitude than for a synchrotron with uniform field gradient. The vacuum at the AGS is of

---

[1] The alternating gradient focusing idea was proposed in 1952 by Livingston, Courant and Snyder.

the order of 10^{-7} Torr in order to limit the beam losses. The main source of beam losses is electron capture (less than 3%)[2]. The beam is extracted from the AGS in rather small spills (1 sec).

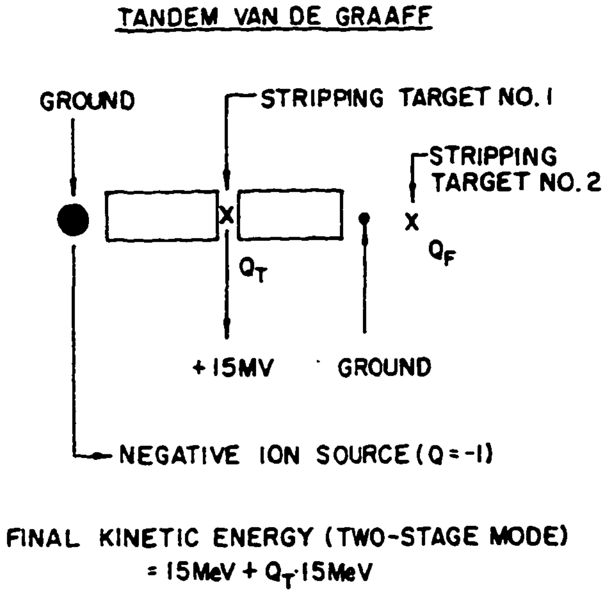

Figure 2.1: Tandem Van de Graaf with stripping targets.

	Q_T	S_T %	Kinetic Energy MeV/amu	β_F	Q_F	S_F %	Current* part-μ-amp
Deuterium	+1	70	15.0	.1768	+1	100	525.**
Carbon	+5	39	7.5	.1262	+6	90	82.
Sulfur	+9	36	4.7	.1002	+14	40	20.
Copper	+11	27	2.9	.0782	+21	27	11.
Iodine	+13	20	1.65	.0595	+29	20	6.
Gold	+13	19	1.0	.0463	+33	17	5.

*75% transmission efficiency.
**Requires source development.

Table 3: Tandem operation parameters

---

[2] Energy loss due to synchrotron radiation is negligible for heavy ions and protons due to their large mass.

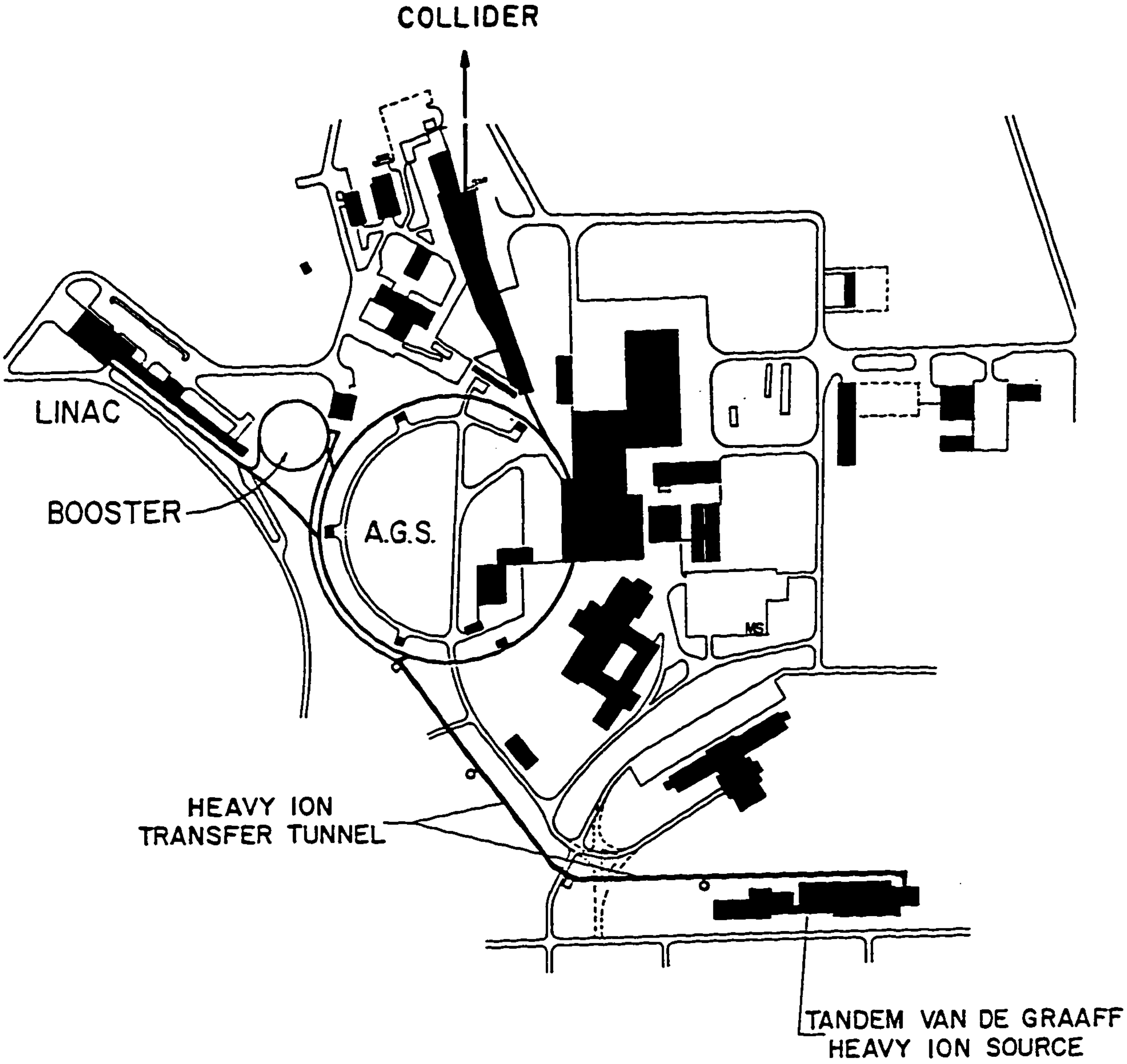

Figure 2.2: The AGS complex.

2.2 The experimental setup

Figure 2.3 shows a general view of the E810 experimental setup. After extraction from the AGS the Si ion beam bends using dipole magnets and gets focused using two quadrupole magnets. One quadrupole magnet focuses in X and the other one in Y. These magnets are further upstream and not shown in the diagram. One of the first things we need to do is to check that we really get Si ions and not something lighter that could have been created in interactions of the ions with the beam pipe. This check is done using a threshold in the pulse height from the Cherenkov counter C. Since all the incident ions have the same momentum, the lighter incident ions (less mass) have a higher velocity than Si ions and this causes the emission of Cherenkov light. (We need to check that because some of the accelerated Si ions interact with the beam pipe and also among themselves, creating e^+e^- pairs that are easily absorbed and thus change the incident ion mass and charge). To define the beam we use plastic scintillator counters S1, S2, and S3 and Cherenkov counter C. When an energetic charged particle goes through a scintillator counter it losses a small fraction of its energy by exciting the atoms or molecules of the scintillating medium. The deexitation of the molecules or atoms will cause the emission of light that can be amplified and converted into electric pulses. So, we require that the beam particles go through S1 and S3 but not through the Halo veto counter S2. This ensures that the particles that hit the target are from accelerated Si ions and not from particles from other sources. We also use Proportional Wire Chambers (PWC's) to define the direction of the beam. The beam PWC's have two X planes and one Y plane since Y is of secondary importance. (Wire spacing is 0.0625" and wire diameter 0.0007" gold plated

Tungsten, number of wire planes: 128, gas: 0.3 % Freon 113B, 14 % isobutane, 5 % dimethoxy methane and Argon). Thus the BEAM trigger was defined as: BEAM = S3 * C * (NOT S2) * S1.

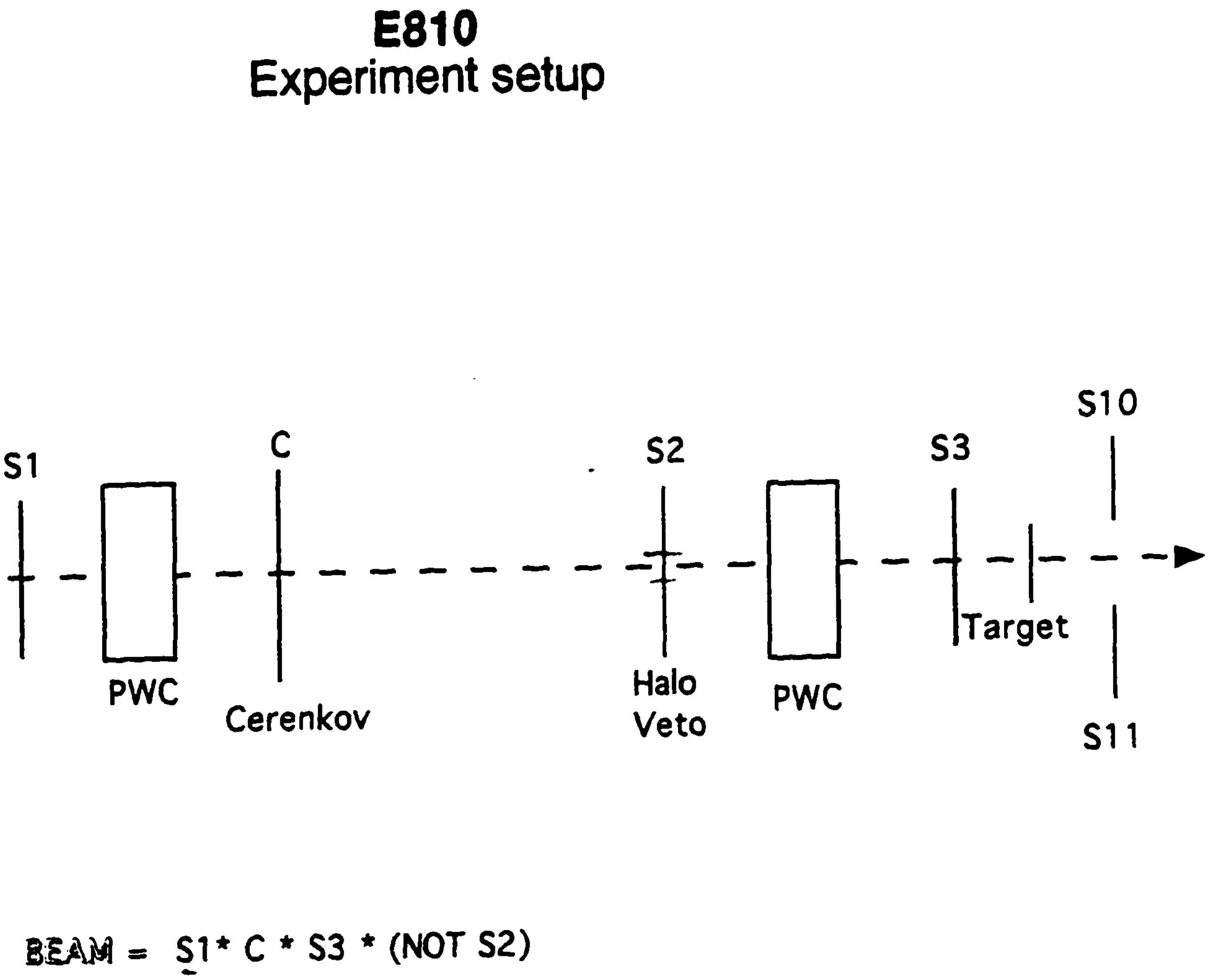

Figure 2.3: General view of E810 experimental setup.

2.3 Targets

Experiment E810 used the 14.6xA GeV/c Si beam provided by the AGS to bombard various targets. Target thickness was selected to reduce gamma ray conversion which would give incorrect hadron multiplicities. Gamma rays (from π^0 decays) could convert to electrons and thus contaminate the tracks assigned to the primary vertex. This is the main source of electron contamination in our data. In order to reduce this type of contamination we used thin targets. Tables 4 and 5 below list various targets used by E810 and the radiation lengths (L_{rad}) for various materials.

Target	*Thickness [mm]*	*% of Lrad*
Al	0.8	0.9
Si	1.22	1.3
Cu	0.125	1.0
Au	0.025	0.8
Pb	0.2	3.5

Table 4: List of targets used by E810.

Material	*[gr/cm^2]*	*[cm]*
Air	36.20	300050
Al	24.01	8.9
Si	21.82	9.36
Cu	12.86	1.43
Pb	6.37	0.56

Table 5: Radiation lengths for various materials.

2.4 The MPS magnet

The MPS magnet [26] is one of the world's largest magnets for use in elementary particle experiments. The field volume between the poles is 4.60m long x 1.80m wide x 1.20m high, figure 2.4. The magnetic field has been mapped for central field corresponding to 5, 7.5 or 10 KGauss (.5, .75, or 1 Tesla), and weights 700 tons. The magnet rests on hydraulic pads which allow a 30^0 rotation ($\pm 15^0$) about a pivot point 45 cm inside the magnet from its upstream end. The large field volume permits experiments to place detectors in the field and near the target, thereby enchancing the probability that the products of an interaction will be measured (some neutrals like Λ^0 and K_S are measured via their charged decay products). In general, the choice of the magnet for a TPC (Time Projection Chamber) has to be tailored to the particular experiment. However, all TPC magnets have the requirement of high uniformity. The limit on the integrated nonuniformity in the magnetic field over the full drift length of a track segment is $\cong 1$ part in 10^4. The value of the magnetic field is chosen as to provide enough bending. Table 6 gives the value of the Magnetic field with the approximate operating current. The current was used for guidance only during turning the magnet on. To set the operating field we used the calibration curves to determine the Hall voltage corresponding to the required field, figure 2.5.

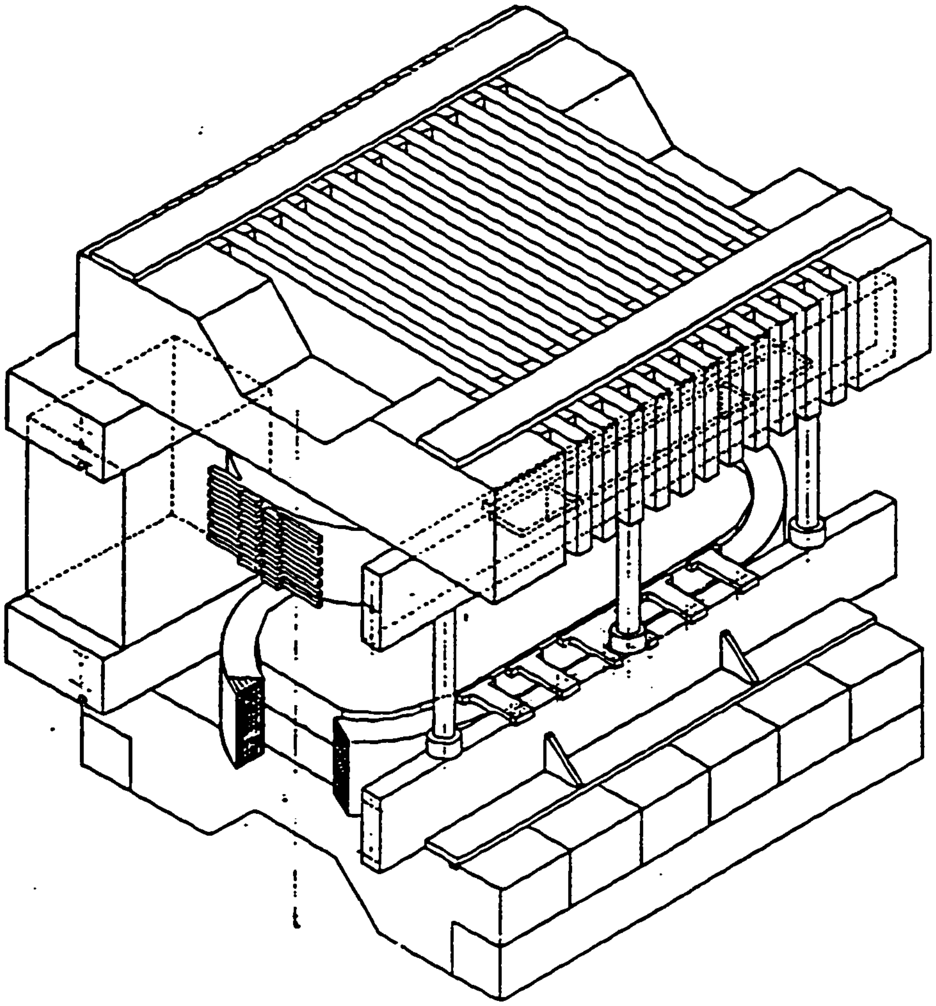

Figure 2.4: The MPS magnet.

Magnetic Field (Tesla)	Approximate current (A)
0.50	3460
0.75	6060
1.0	9800

Table 6: Magnetic field and the corresponding operating current.

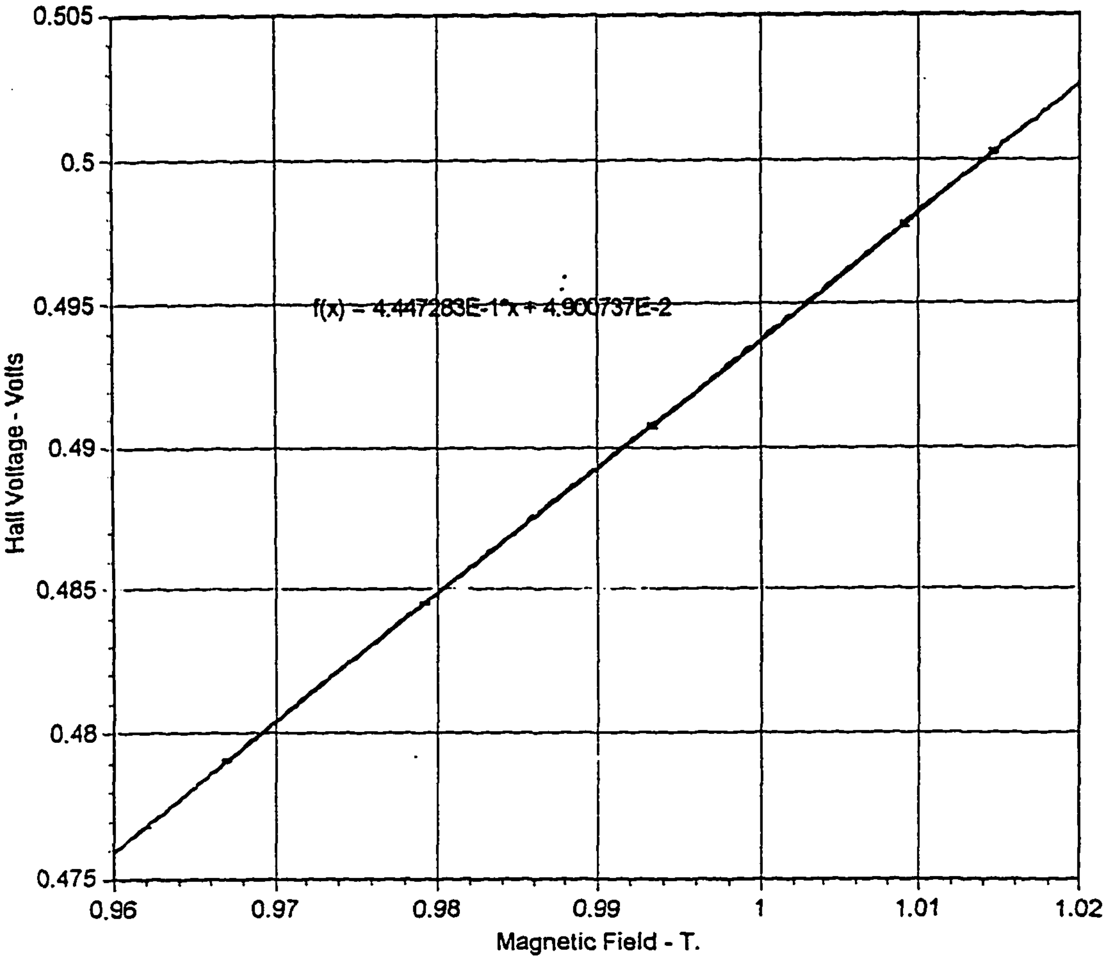

Figure 2.5: Calibration curves used to determine the magnetic field.

2.5 The Time Projection Chamber (TPC) modules

The tracking detector of Experiment E810 consists of three Time Projection Chamber (TPC) modules [27, 28, 29, 30, 31]. The TPC is a general purpose tracking device which can provide good spatial resolution by giving for each space point on a track a unique measurement of the space coordinates x, y, z. This eliminates the difficulty of most previous devices which gave only two coordinates and for which multiple tracks required costly and time-consuming analysis to untangle the correct combination of coordinate measurements. Some TPCs can measure dE/dx for particle identification. TPCs can make measurements over a large solid angle and can operate in very crowded environments, where many tracks are created at the same time. In our case the detector covers the forward hemisphere in the Nucleon - Nucleon Center of Mass (CM) frame, which is 20^0 in the Laboratory frame. The three TPC modules used by E810 were placed in the uniform magnetic field produced by the MPS magnet, Figure 2.6. The magnetic field has two purposes: First, it bends the tracks allowing measurement of their momentum. Second, it reduces transverse diffusion of electrons during their drift, giving increased precision to spatial measurements.

2.5.1 Electric field - Gating grid

Figure 2.7 is the front view of a TPC module used by E810, showing principal components (60 cm high, 65 cm wide, 47 cm long). As the beam[3] passes through the center of the TPC ionization electrons produced by charged tracks will drift along the

---

[3] A typical beam is 1.5 cm wide and 0.6 cm high.

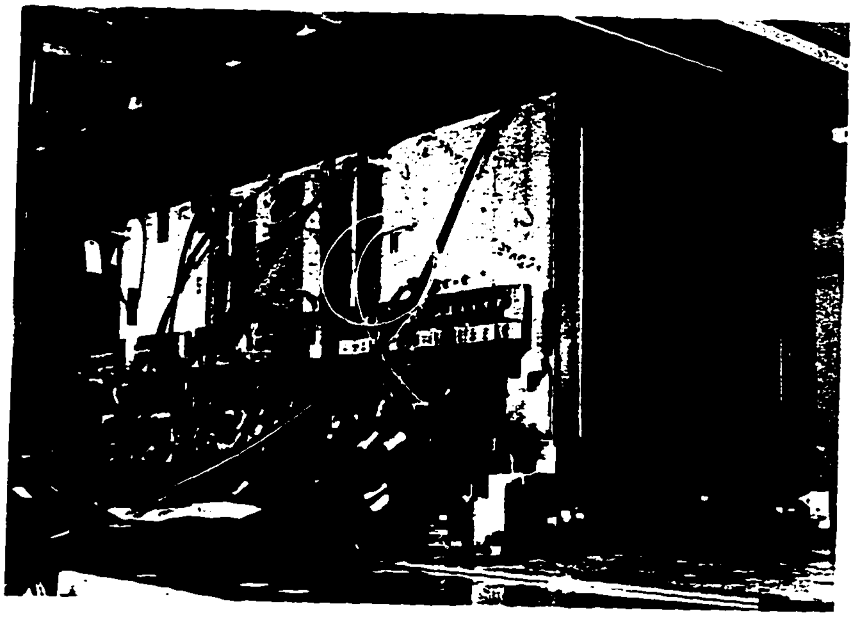

Figure 2.6: Picture of the three TPC modules sitting in the MPS magnet.

electric field lines to the amplification region. The electric field in each module (330 V/cm) is produced by a field cage with double sided printed circuit boards on the sides and a double row of wire electrodes at each end serve to shape the electric drift field. The uniformity of the electric field has to match that of the magnetic field, otherwise $\vec{E}X\vec{B}$ forces will distort the trajectories of the drifting electrons. The main source of distortions of the electric field is positive ions moving through the good field region during the process of collection. The major source of positive ions are ions produced in the gas amplification process at the readout anodes that leak into the drift volume. Because of the low mobility of ions (thousands of times slower than electrons at equal fields) a positive space charge is created, with as a consequence a local distortion of the electric field (this will also limit the maximum beam rate). This is particularly disturbing in the drift space, an extended region of moderate electric field. In a typical TPC geometry, ions will take around one third of a second to cross a 1m long drift space (the drift velocity of electrons was $2.7\text{x}10^6$ cm/sec). The positive space charge in the drift region modifies the field strength and therefore the drift velocity; for spatially non-uniform ion production rates (such is always the case in a practical detector), transverse components of field are generated and result in distortions in the trajectories of drifting electrons, even more so in the presence of a magnetic field.

A solution to the problem of positive space charge in the drift volume has been found by introducing *a gating grid* before the amplification region, made transparent to electrons on selected events, figure 2.8. The gating grid consists of a mesh of close, parallel wires *alternatively* polarized to opposite potentials so as to block all drifting charges (electrons drifting from the drift region to the detector region, and positive ions in the reverse direction). In coincidence with events recognized of interest by an external trigger, the gating wires are pulsed at a potential restoring transparency for 30 μs, a little longer than the maximum drift time, allowing ionization from the tracks to reach the amplification region. Because of their slower drift velocity, positive ions from amplification at the anode do not reach the gating grid before the gate is closed, further improving the gating of the TPC. Gain changes and distortions of the electric field due to positive ions, as well as two vertex resolution and track reconstruction efficiency, were studied by exposing the TPCs to high fluxes equivalent to more than 10^7 minimum ionizing particles per second, [32].

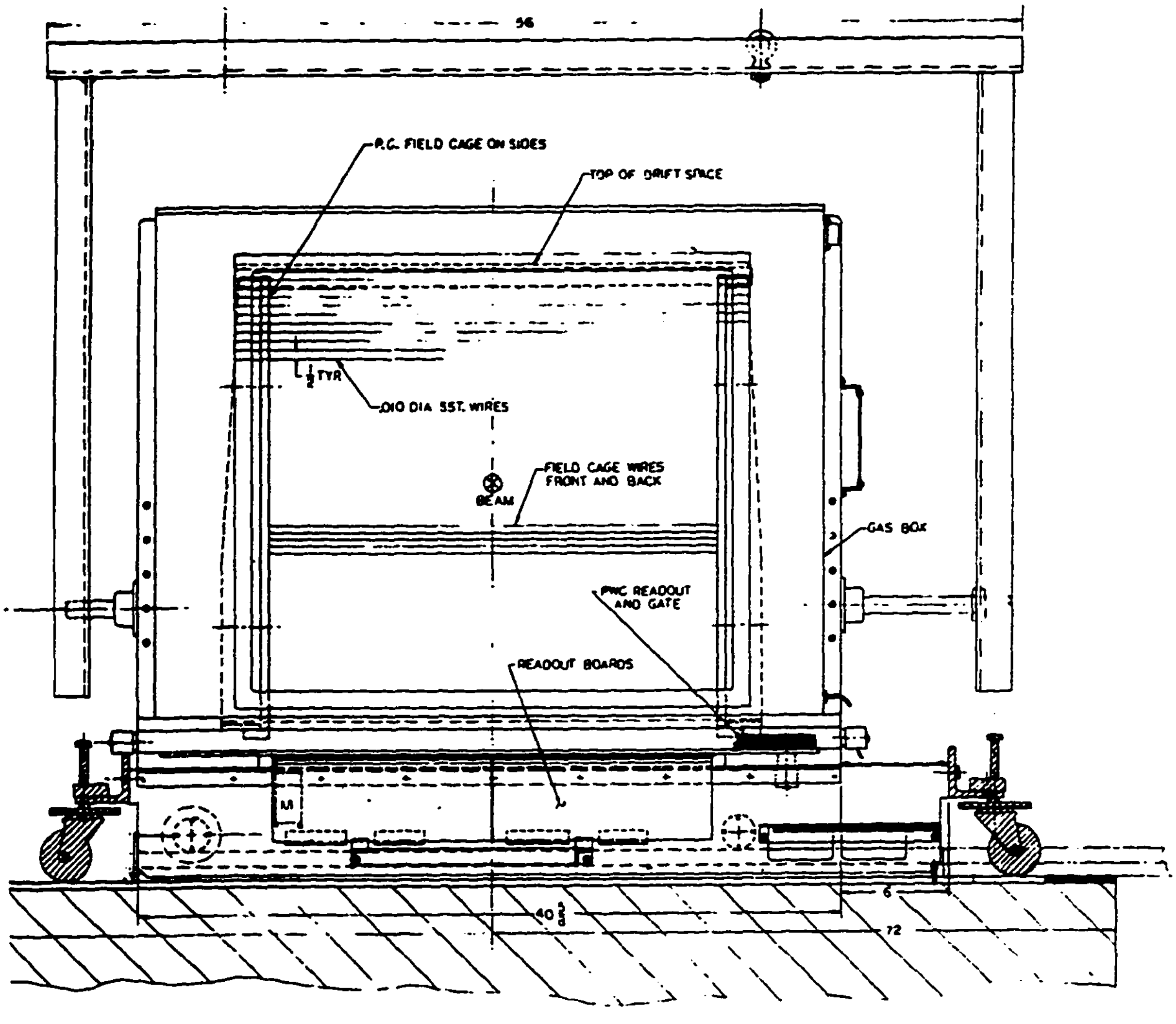

Figure 2.7: Front view of a TPC module showing principal components.

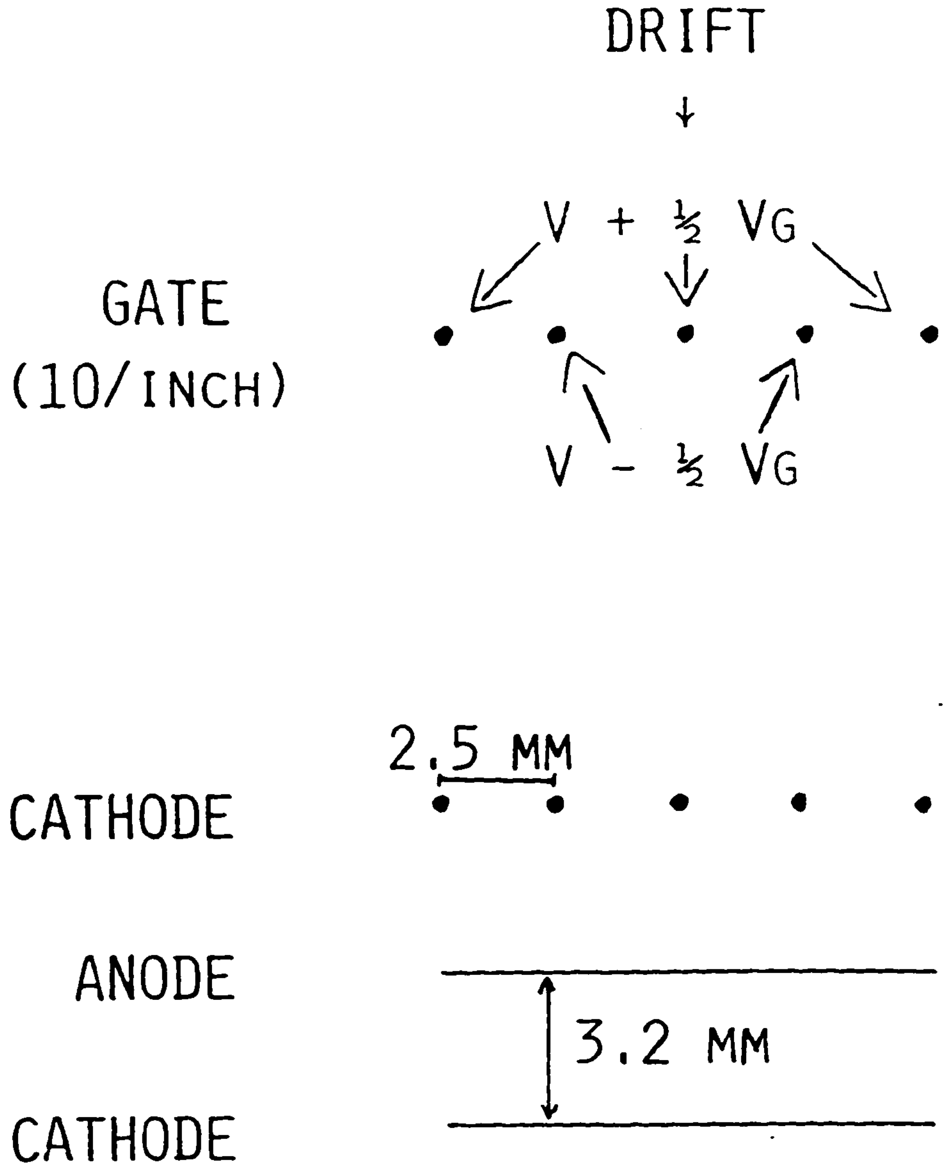

Figure 2.8: Schematic of the arrangement of the electrodes in the detector endcap.

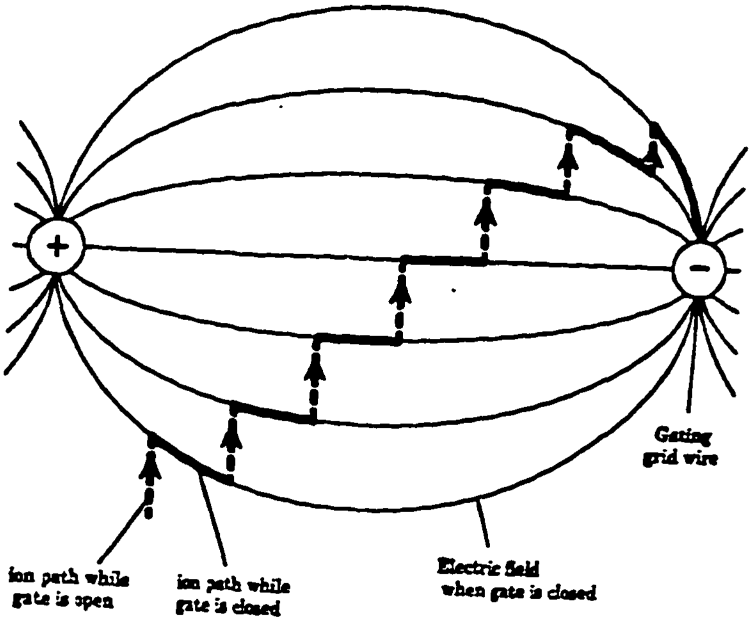

Figure 2.9: Path of the ions and electric field lines near the gating grid.

2.5.2 Proportional wire system

The proportional wire system is where charge multiplication and detection is performed in such a way as to be able to determine their point of origin in the gas volume. Electrons produced by charged particles in the drift region must pass through the gating grid and a wire cathode in order to reach the anodes, where they are multiplied by the avalanche process. A second solid copper (CuC) cathode, placed 3.2 mm below the anode plane, helps to achieve high gain (it minimizes space charge effects). The readout is achieved by 36 rows (12 per module), spaced 3.8 cm apart, of 256 short anode wires (1 cm long, 2.54 mm apart). The wire number gives the (x, z) coordinate and the drift time the y coordinate, for unambiguous 3D points along the tracks. In addition, a set of *field wires* alternating the sense wires in every row are used to focus the avalanche towards the anodes. Only the anodes are read out. This has the noticeable advantage, as compared to a pad readout, of providing larger signals for the same gain. On the negative side, the device is not suitable for measurements of energy loss, dE/dx, since the gain profile along the segments of wire is certainly far from uniform (owing to the influence of the insulators at the edges).

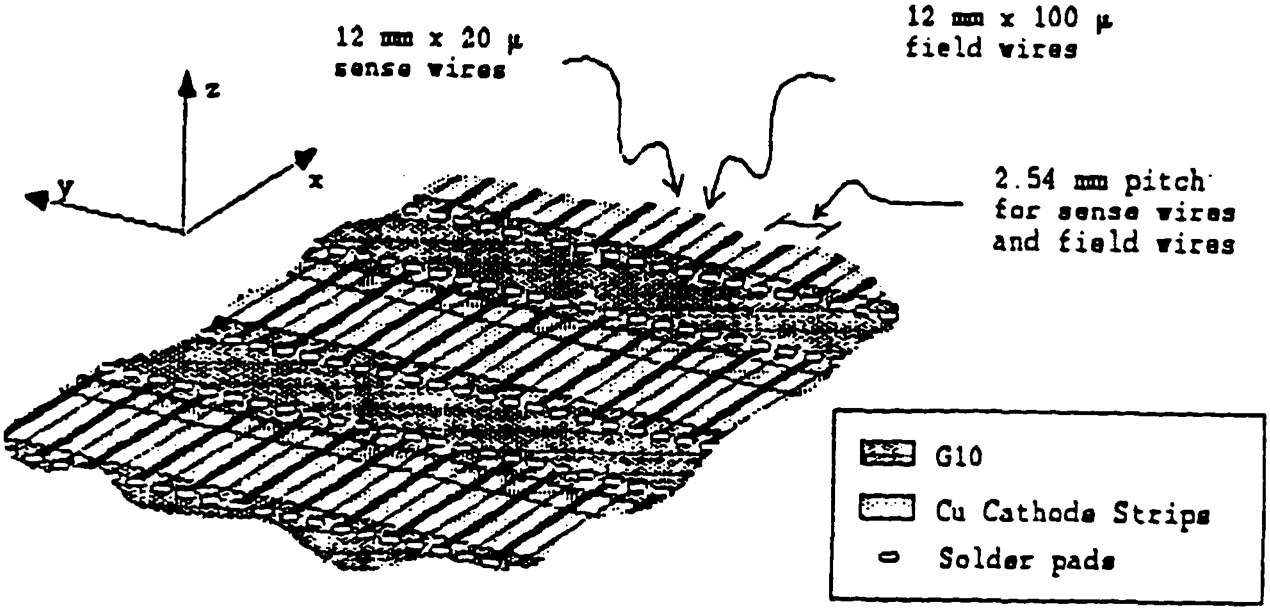

Figure 2.10: End-cap of the MWPC used in the NA36 TPC, similar to the one used by E810 [28].

2.5.3 Choice of drift gas

Several factors govern the choice of a filling gas [33, 34]. Most important are: good proportionality, low working voltage, high gain, high rate capability, and cost. In general these conditions are met by using a gas mixture rather than a pure one. The main gas is monatomic because polyatomic molecules have many non-ionizing energy dissipation modes available. The choice between monatomic gases is dictated by a high specific ionization. Noble gases meet the above requirements and disregarding for economic reasons Xenon and Krypton, the choice falls naturally to Argon. But Argon has the disadvantage of a high excitation potential (11.6eV) . Excited Argon atoms can deexcite giving rise to high energy photons with energies of the order of 11.6 eV which is well above the ionizing potential of any metal constituting the Cathode and causing further avalanches. Also Argon ions can neutralize in the Cathode extracting electrons. Both problems can be solved by the addition of polyatomic gases, such as methane or alcohol. These molecules act as *quenchers*, by absorbing the radiated photons and then dissipating this energy through dissociation or elastic collisions. Methane, for example, can absorb photons in the range 7.9 to 14.5 eV, which covers the range of energy of photons emitted by Argon. When a polyatomic molecule neutralizes in the Cathode secondary emission is very unlikely.

The problem of using organic quenchers is the recombination of dissociated organic molecules which results in the formation of solid and liquid polymers which accumulate on the anode and cathode of the detector (aging effect). Positive ions reaching the cathode must then diffuse to be neutralized. When high flux of radiation is present this might be a problem. Only a complete cleaning can regenerate the counter. Another way around is the use of non-polymerizing quenchers like alcohols. Finally, for sealed gas counters an additional problem is the consumption of quencher. Assuming a gain of 10^6 and 100 electron - ion pairs per event, about 10^8 molecules must dissociate per event. This, of course, is not a problem when a continuous flow is used.

Addition of small quantities of electronegative gases, like freons, can help us get the highest possible gains. Electronegative gases can capture electrons forming negative ions that cannot induce avalanches. If the mean free path for electron capture is shorter than the Anode to Cathode distance, electrons liberated at the Cathode will have little probability of reaching the Anode. To preserve detection efficiency, however, only limited amounts of electronegative gases can be used.

Another important factor is the variation of τ (mean collision time between drifting electrons and the gas molecules) with E/P, where E is the drift electric field and P the pressure. Electrons have an energy at which their collision cross section with Argon atoms goes through a minimum (Ramsauer - Townsend effect). Since the electron energy is a function of E/P, at the correct value of E/P the cross section becomes a minimum, and τ becomes a maximum. Thus the choice of gas in a TPC is coupled to the electric field, the pressure and the magnetic field (through diffusion coefficients).

In E-810 and generally in heavy-ion experiments where high multiplicities are expected, two track resolution is more important than spatial resolution, so a low diffusion gas is required. Considering the above and looking for a low diffusion gas, the gas we used in our TPC modules was 79% Argon, 16% isobutane, and 5% dimethoxymethane (diffusion was about 1 mm per 50 cm of drift distance)

2.5.4 The electronics

Since dE/dx is not measured in this system, the electronics is only required to give time information. In order to read out the many closely spaced short anodes at minimum cost, a circuit was designed that allows each individual channel to be mounted directly on the chamber and to occupy only the anode wire spacing. The circuit for each channel is shown in figure 2.11 [27]. Sixteen channels are assembled in a hybrid package (LeCroy HTD 161S,M) with inputs spaced 2.54 mm apart. Shaping-time constants were selected to match the anode waveform. An integration time constant of 50 ns and a differentiation time constant of 200 ns were chosen to minimize noise and maximize two-track separation. Time information is recorded with a memory driven by a counter to serve the function of a shift register. Each hybrid contains memory capable of recording 1024 time samples from each channel. To reduce possible local noise pickup, all logical levels are ECL -the clock and address lines are terminated differential ECL.

To minimize the control circuitry two kinds of hybrids are used. One type is called a master and in addition to the amplifier-shaper-comparator and memory for 16 channels has the counter used to address the memory plus the control logic used necessary to read out itself plus seven slave hybrids. The slave hybrids contain only the amplifier-shaper-comparator and memory required for 16 channels. The printed circuit boards are assembled with one master and seven slaves, Figure 2.12, which is sufficient for 128 anode readouts and is externally accessed by one clock line, one data line and 14 control lines. The data line is common to the two hybrid cards in a row and the other lines are common to the whole TPC, thus only 27 lines are used to connect over 3000 channels per module to the external electronics. The time samples are obtained at 50 MHz and the data are sequentially read from each channel's memory at 25 MHz. This serial string of data bits is encoded into wire number, drift time and cluster size by FASTBUS modules in which all rows are encoded simultaneously. Consequently the entire readout is completed in 10 ms. This amount of dead time is acceptable because of other limitations on trigger rate. The on-chamber performance of the hybrid allows input sensitivity of less than 1 μA. Thus the chamber gas gain is as little as a few times 10^4.

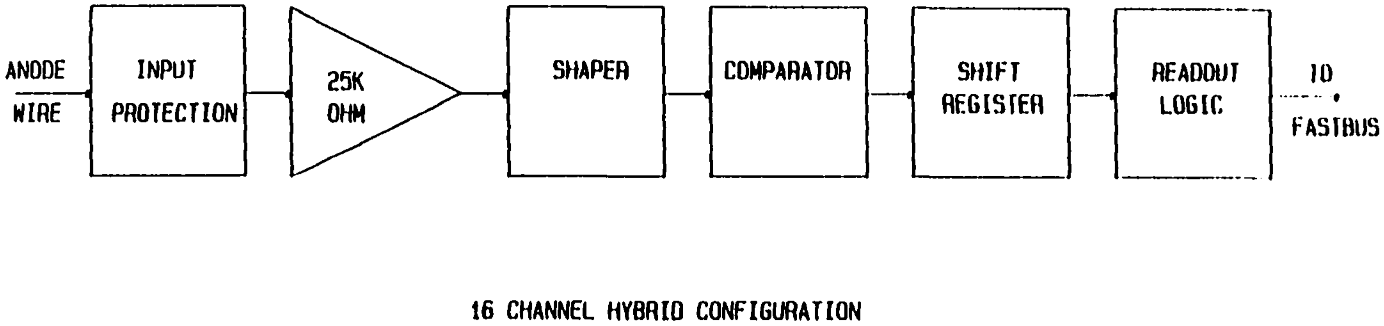

Figure 2.11: Schematic of individual channel electronics.

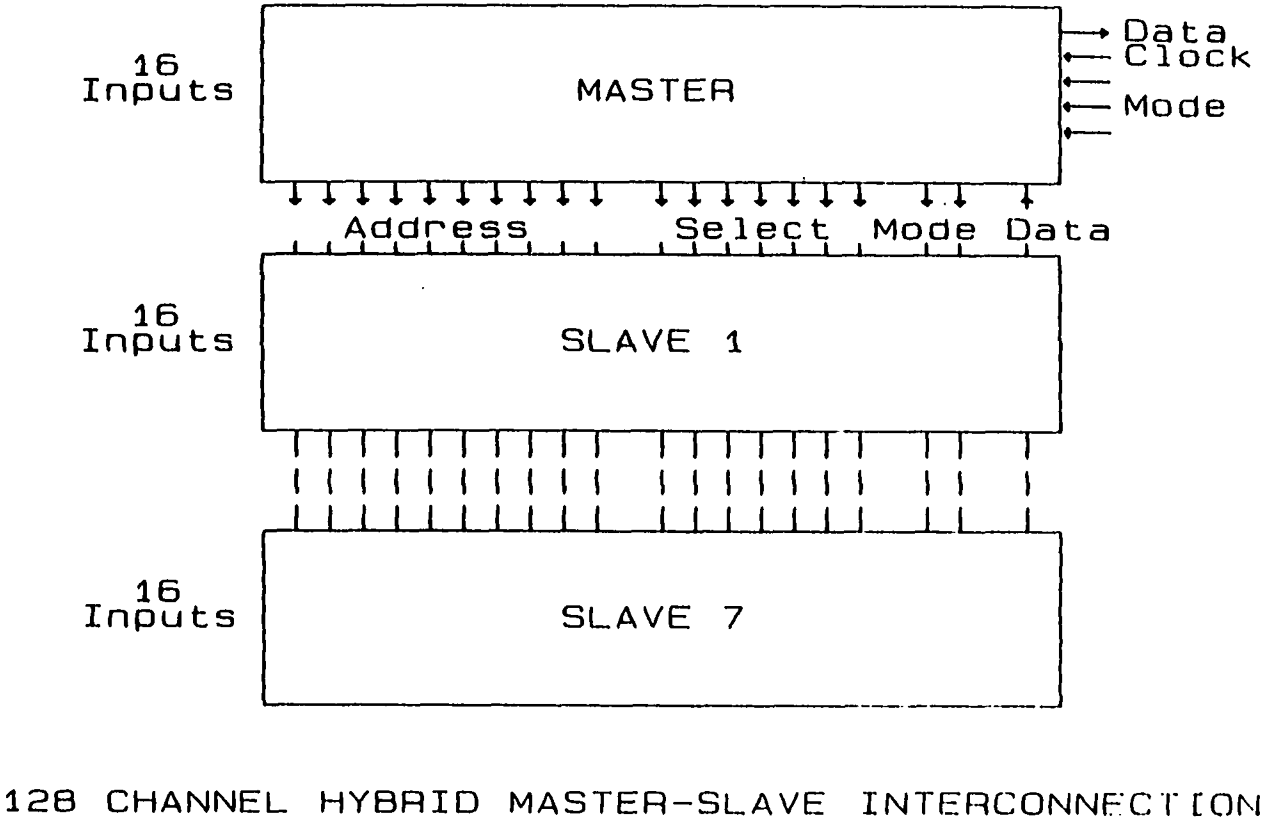

Figure 2.12: Layout of a 128-channel hybrid printed-circuit board.

2.5.5 Summary of E810 TPC characteristics

Table 7 summarizes the characteristics of the TPC modules used by E810.

parameters		units
B	.5 or 1.0	Tesla
Gas	Argon(79%)- Isobutane(16%)- Dimethoxymethane(5%)	
E	330	V/cm
P	1	Atm (760 Torr)
E/P	0.43	V/(cm Torr)
Drift velocity[4]	2.3	cm/μs
Drift distance	0.6	m
End cap area	0.3	m^2
Volume	0.18	m^3

Table 7: Characteristics of TPC modules used by E810.

---

[4] The drift velocity was measured in calibration runs with the magnet on and off (alignment runs). The error was less than 1%.

2.6 The Trigger

Figure 2.13 shows the E810 experimental setup [35] . The beam passed through the center of the TPCs and was limited to 5000 ions per spill to minimize the amount of ionization deposited in the TPC's. The incident Si ions were identified by a thin plastic Cherenkov counter (22" x 4"x 1/4" thickness). Two beam PWC's were used to determine the size of the beam. We required that the beam go through the Halo veto counter (S2). Scintillator counter S1 was located in front of the first beam PWC and S3 was in front of the target.

Two scintillator counters S10 and S11 (4" x 4" x 1/4" thick) located 20 cm behind the target and 2.5 cm above and below the beam line were used to select interactions from the target. A veto counter (S9) (9" x 9" x .5" thick), located 8 m downstream, was used to veto on high Z fragments. The pulse height of this counter was recorded for possible further software cuts. The interaction trigger was defined as:

INTERACTION = BEAM * S10 * S11* (NOT S9)

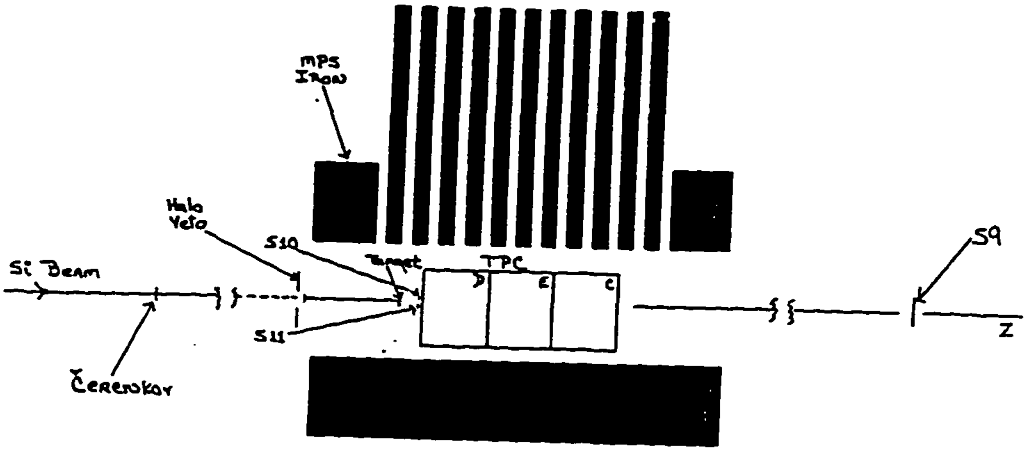

Figure 2.13: The E810 experimental set up.

2.7 The data acquisition system (DAQ)

The data-acquisition system used in the MPS (Multi-Particle Spectometer) is a FASTBUS based system which reads out CAMAC based devices as well by the use of a FASTBUS branch driver (STRUCK 320 module) [27]. The host computer is a VAX-750 and it is interfaced to the FASTBUS by means of a computer interface module (STRUCK 300 module, CFI) to VAX UNIBUS. As shown in figure 2.14, data reading and formatting is done by the SLAC scanner processors (SSP's) resident in the FASTBUS system. A multiprocessor software system on VAX computers is used to communicate with the SSP's, record the data and monitor on-line the progress of high energy and heavy ion experiments. Each spill of data is stored by SSP0 to the FASTBUS memory which is a LeCroy 1892 with 4 Mega Bytes capability before being written to magnetic tape by the host VAX. The magnetic tape drives recorded the data on 6250 bpi tapes and were capable of writing 125 inches/second. The system has been timed to record $\cong$ 450 KiloBytes/second within 2 seconds between spills (beam spill time is 1 sec, AGS cycle time is 3 seconds).

As shown in figure 2.14 the system operates as follows:

1. When an interesting event is detected by fast trigger logic, a trigger pulse is sent to the main SSP (SSP0)
2. SSP0 disables any further triggers and reads a module in a CAMAC crate to obtain a trigger classification.

3. SSP0 passes trigger class information to other SSP's and issues commands to start up the other SSP's on the cable segment.
4. Each SSP reads out the module specified in its own DEVICE LIST loaded in at the beginning of the run for various trigger classes, data from each module is organized by the SSP's into a buffer with a header.
5. When all SSP's on the cable segment have completed their device readouts, SSP0 reads their formatted data and appends this to its own buffer with an additional header. Several events are formatted into a bigger buffer and written to the FASTBUS memory, and when it is the end of the spill, SSP0 sets up a flag to let the host VAX read it. When the host VAX reads the whole spill, it checks with the online computer to see if it wants a data sample. If yes, it will send a few events to the online computer through DECNET. In any case, data is written to tape.
6. End of Event, SSP0 re-enables triggers from fast trigger logic, and the sequence repeats from step 1.

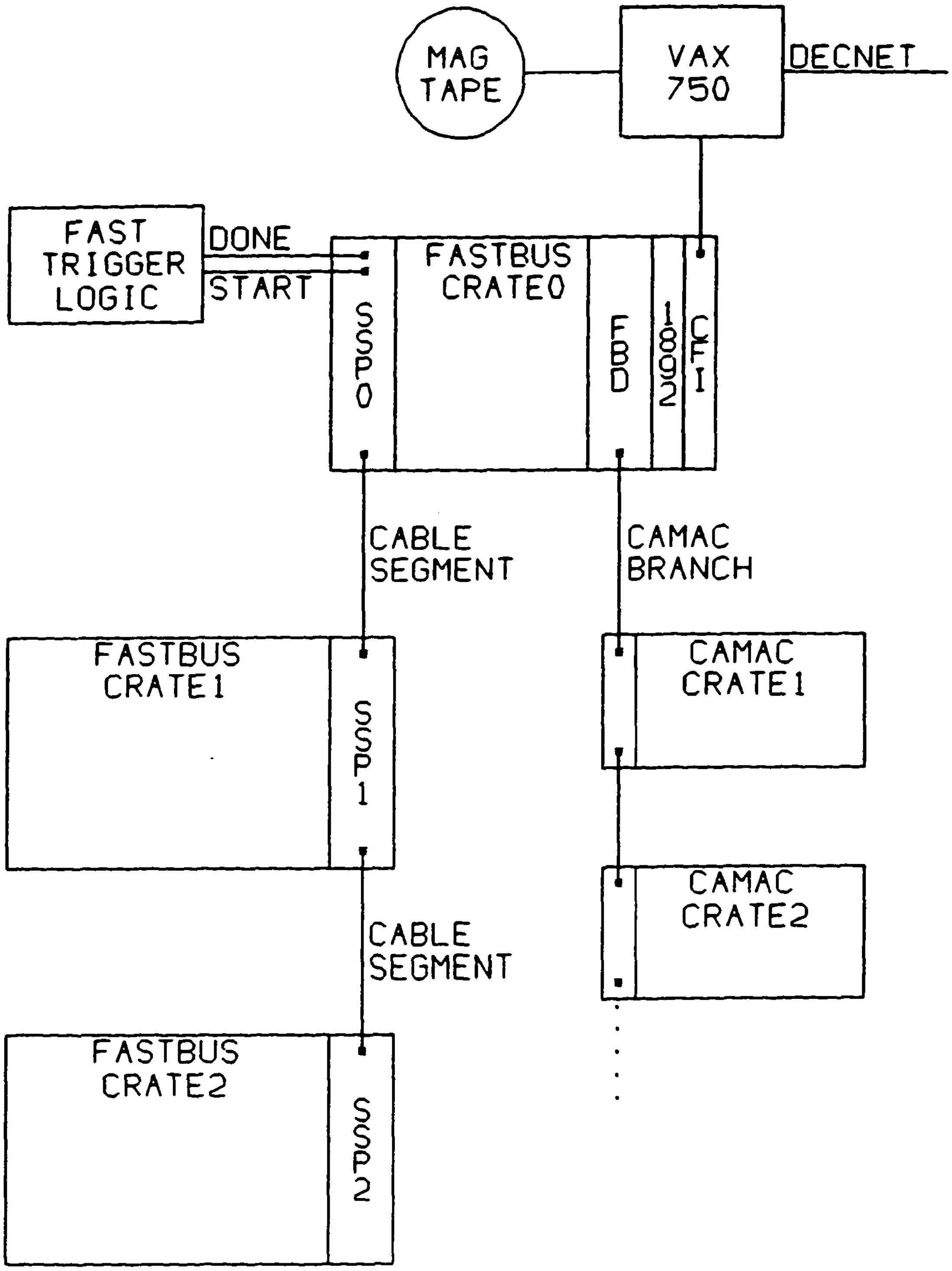

Figure 2.14: The MPS data-acquisition (DAQ) system hardware block diagram.

2.8 The reconstruction program

The track reconstruction program consists of three parts: a local pattern recognition which associates contiguous readouts wires to form a single hit, a subroutine which partitions the hits into slices in the yz-view (the vertical plane containing the beam and the vertical magnetic field) and the track reconstruction section [36, 37].

The TPC is partitioned into slices in the yz projection. The slices we are using are approximately 1 cm high near y=0 (the beam region) and approximately 5 cm high at the top and bottom. The hits in the readout wires are indexed by slice number in each wire row, and the track recognition program normally searches hits only within a single slice, thereby greatly speeding up the track finding. The program will follow a track across slice boundaries when necessary.

The track recognition starts at the downstream end of the TPC and works upstream. Only those hits within the working slice are searched; however if the track approaches a slice boundary, the hits in the adjacent slice are added to the search list. A track in the process of reconstruction is called a chain. There are 36 rows of readout along the beam. When three hits on adjacent can be spatially associated in three dimensions, a chain is initialized. The chain is developed upstream by local association from row to row in three dimensions. Absence of hits in two consecutive rows or two or more hit candidates in the same row terminates the stage of chain development. In the next stage (linear) least square fits are performed in the (x,z), (y,z) views. If the fits are successful, the fitted orbit is extended over missing wire rows and consistent hits are added to the chain. If the fitting fails there is provision for seeking out and discarding bad hits.

In the case of Si on Pb events we were able to reconstruct more than 100 tracks per event. In the case on Au on Au events we had to deal with the “merging effect”. The density of tracks in the first TPC module was so high that the track reconstruction program would actually “cut” tracks. We did Monte Carlo simulations of Au on Au events and we estimated a “merging effect“ of 30% when we used the same experimental setup as in Si on Pb collisions (target was located at z = 45 cm, 35 cm away from the first TPC module). We decided to move the target to z = 0 cm (80 cm away from the target) in order to reduce the track density at the first TPC module, and thus reduce the “merging effect”. Figure 2.15 shows different views of reconstructed tracks for Si on Pb events.

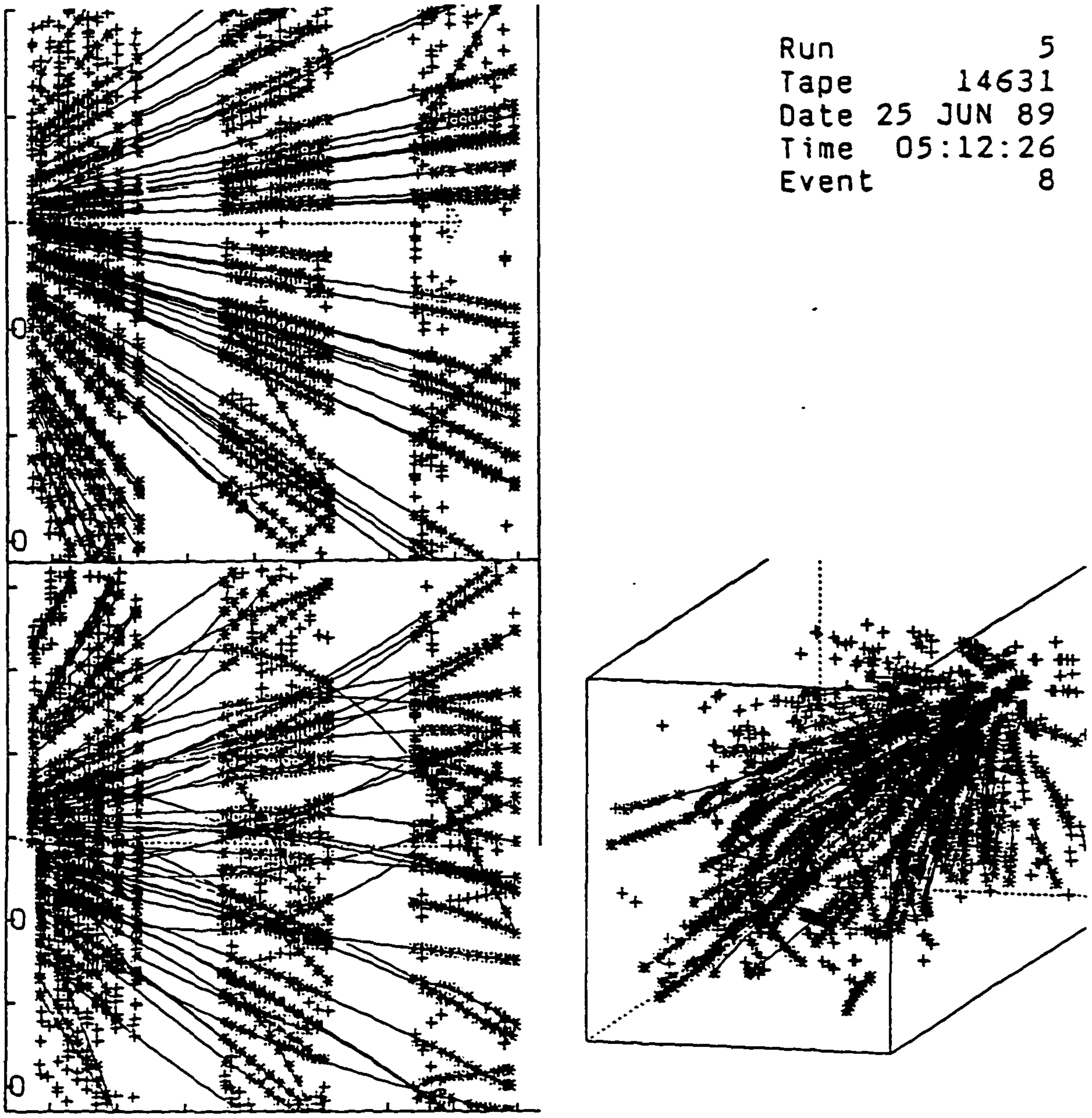

Figure 2.15: Different views of reconstructed tracks in a Si on Pb event. The top left figure is the yz view, the bottom left is the zx view and the right is a 3D view of the event.

3. THE RANDOM EVENT GENERATOR

3.1 Motivation - Strangeness at the AGS - The HIJET model

One of the most important goals of (ultra-)relativistic heavy ion collisions is the investigation of the phase transition from the hadronic matter to the Quark Gluon plasma (QGP). It is predicted that abundant strangeness production should accompany the formation of QGP [18, 38, 39, 40]. The greatly increased abundance of gluons in the plasma phase would lead to large scale production of quark-antiquark pairs. At temperatures comparable to the mass of the s quark or higher, production of $s\bar{s}$ pairs is not greatly suppressed relative to $u\bar{u}$ and $d\bar{d}$ pairs. If we assume that a blob of plasma is formed and that we define a temperature T, the gluon density is directly related to the temperature (Appendix 2):

$$\varepsilon_g = \frac{8}{15}\pi^2 T^4 \tag{3.1}$$

There is therefore a rather large gluon density ($\cong$ 5 fm^3 at T$\cong$ 250 MeV) and these gluons have enough energy to create $s\bar{s}$ pairs, since the critical temperature is much larger than the strange quark mass. The gluon-gluon cross section is large and one therefore expects a rapid formation of $s\bar{s}$ pairs which quickly yield a reasonable statistical equilibrium.

An additional enhancement for new production of $s\bar{s}$ pairs relative to $u\bar{u}$ and $d\bar{d}$ pairs is expected in a baryon rich environment through *Pauli blocking* [41]: In the baryon rich environment of an ion collision, the exclusion principle pushes $u\bar{u}$ and $d\bar{d}$ to higher energy, where they are no longer strongly favored over $s\bar{s}$ pairs. For a baryon rich QGP the Fermi energy is nearly equal to Fermi momentum, because the masses of u and d quarks are almost zero. At $\rho \cong 10\rho_0$, the Fermi energy is $\cong$ 450 MeV (Appendix 3) which is larger or comparable to the mass of $s\bar{s}$ (which is equal to $2m_sc^2 \cong$ 300-400 MeV). In the QGP phase, when the Fermi sea of light quarks reaches a certain level, creating a pair of light quarks takes as much energy as creating a pair of strange quarks. When the temperature drops, as the plasma explodes, most of the strange quarks are frozen out of equilibrium, rather than annihilating into lighter quarks. They eventually appear as many strange particles.

In the Hadronic phase, softer gluon-induced processes have a low cross section for producing $s\bar{s}$ pairs. It should be pointed out, however, that strangeness enhancement can also be expected in high-density hadronic matter, even in the absence of a QGP, provided that at least a partial equilibration (detailed balance) between strange and non strange degrees of freedom could take place via associate production reactions, such as

$\pi+n \rightarrow K+\Lambda$, or $\pi+\pi \rightarrow K\bar{K}$. The question is, of course, how rapidly this kind of equilibrium can be reached. Since the time scale in a typical nuclear collision is very short, we cannot assume the strangeness content of a Hadronic Gas to be saturated (in "absolute chemical equilibrium"). The chemical relaxation time constant (the time required to produce strange quark flavor in the abundance corresponding to fully saturated phase space) is strongly phase dependent, as quite different processes are contributing in the QGP or HG states of hadronic matter.

The first observation of enhanced strangeness at the Alternating Gradient Synchrotron (AGS) at 14.5 GeV per nucleon came from E802 [42]. They reported an enhancement of the K^+/π^+ ratio as compared to pp data[1] and FRITIOF calculations[2] at similar energies. They reported a ratio of K^+/π^+ approximately (24±5)% and a K^-/π^- ratio of 4% within the angular range of 14^0 - 28^0 for central Si on Pb collisions. This enhancement can be easily explained using the QGP scenario: an $\bar{s}$ quark could easily find an u quark to form a K^+, but it is not easy for an s quark to find a $\bar{u}$ to form a K^- since light quarks (u and d) are more abundant than light anti-quarks ($\bar{u}$ and $\bar{d}$) and also since s $=\bar{s}$. Similarly, $\Lambda(uds)$ and $K^0(d\bar{s})$ should be distilled, K_s should be half distilled, since $K_s=(1/\sqrt{2})(\bar{d}s+d\bar{s})$.

---

[1] In pp collisions the ratio K^+/π^+ is 5±4% [43] and K^-/π^- is 3-6%

[2] FRITIOF: The independent fragmentation scheme FRITIOF assumes that the projectile nucleons move on straight lines through the target and hit only those target nucleons which are within a tube of a cross section given by the inelastic nucleon - nucleon cross section, 33mb (the spectator nucleons are always neglected). The excited (with increased masses but decreased momenta) projectile and target nucleons decay independently after the actual collision has ceased. Therefore the produced hadrons do not interact (no secondary interactions), they have an infinite mean free path. Thus within the framework of FRITIOF model, one obtains the same K^+/π^+ and K^-/π^- ratios as in elementary nucleon - nucleon collisions at the same COM energy.

The first attempt to reach the observed ratios without requiring the formation of QGP was to include secondary interactions in Monte Carlo event generators. The inclusion of secondary interactions failed to reach the observed ratio [44]. The main reason is that associated production of strangeness by πN collisions should be heavily suppressed in the AGS experiments, because most of these collisions occur below the production threshold $m_\Lambda + m_K$. It was only after the inclusion of exited hadronic states (resonances), such as ρ, K^*, a_1, Δ, N^*, that we got close to the observed K/π ratios. The motivation for including resonances in event generators came from the fact that proton - proton collisions at 12 and 24 GeV/c showed that a majority of inelastic collisions yield final states containing one or more of the low-lying resonances (such as Δ, ρ, e.t.a.). Basically, what resonances do is that they provide a mechanism for pion absorption. The retention of π-mesons within the resonance results in an overall increase in the average baryon - baryon collision energy. Experiments E810 [35, 45, 46, 47] and E802 [48, 42, 49, 50, 51, 52] at the AGS have measurements of single-strange particle production. Both experiments report an enhancement of strange particle production over pp collisions at the same energies (Table 8). Up to this point many of the characteristics of the experimental results regarding strangeness at the AGS, such as particle yields, rapidity distributions, inverse slopes e.t.a., have been explained by conventional cascade models [53, 54, 55, 56].

	Factor of enhancement
K^+	2.1
K^-	2.8
ϕ	2.3
Λ	2.9

Table 8: Enhancement of strange particle production in Si on Pb collisions over pp collisions at similar energies.

The HIJET model [57], modified for AGS energies, is known as AGSHIJET. The only input parameter of this model controls the formation time and in turn the strength of secondary interactions. AGSHIJET uses geometry and cross sections to determine whether two particles collide. Later, N*'s were added through purely empirical observation to make AGSHIJET+N* [58]. The addition of N*'s created more energetic collisions and thus increased the number of ΛK and $K\overline{K}$ pairs produced[3]. Figures 3.1 to 3.4 show the predictions of AGSHIJET (with and without N*), for the rapidity distribution of K_s and Λ, from the Si and Pb target respectively, with zero formation time. Although this is not a physically justifiable result, it was used to indicate that even in this extreme best attempt case the model could not get enough K_s and Λ^0. AGSHIJET+N* underestimates the production of single strange particles by a factor of 2 and double strange particles by a factor of 8. In figures 3.5 to 3.8 we show the exponential inverse slopes as a function of rapidity for K_s and Λ from the Si and Pb target respectively. AGSHIJET+N* clearly underestimates them especially at midrapidities. By looking at the inverse slopes of Λ's we suspected that if we leave the processes that create strange particles unchanged but somehow increase the number of collisions per event we could get closer to the experimentally observed inverse slopes. So we developed a new model that uses the same scattering routines and cross sections as AGSHIJET+N*, but the number of collisions per event would be an input parameter. Figure 3.9 shows the inverse slopes of Λ^0 as a function of rapidity for Si on Si collisions with different number of collisions per

---

[3] The production of Kaons increases sharply with the collision energy and it is only a minor source of K_s in pp collision at the energy level of interest.

event. As we increase the number of collisions per event we warm up the Λ^0's and they get more thermal in nature. After 50 collisions per event the Λ^0's are "fresh" and the inverse slopes are the same as AGSHIJET+N*, which means that in the AGSHIJET+N* model the Λ^0's are formed from initial collisions and have limited p_T. As the number of collisions is increased the Λ^0's are heated up by collisions with nucleons and become more thermal in nature. This motivated us to develop a model in which the number of collisions per event would be an input parameter.

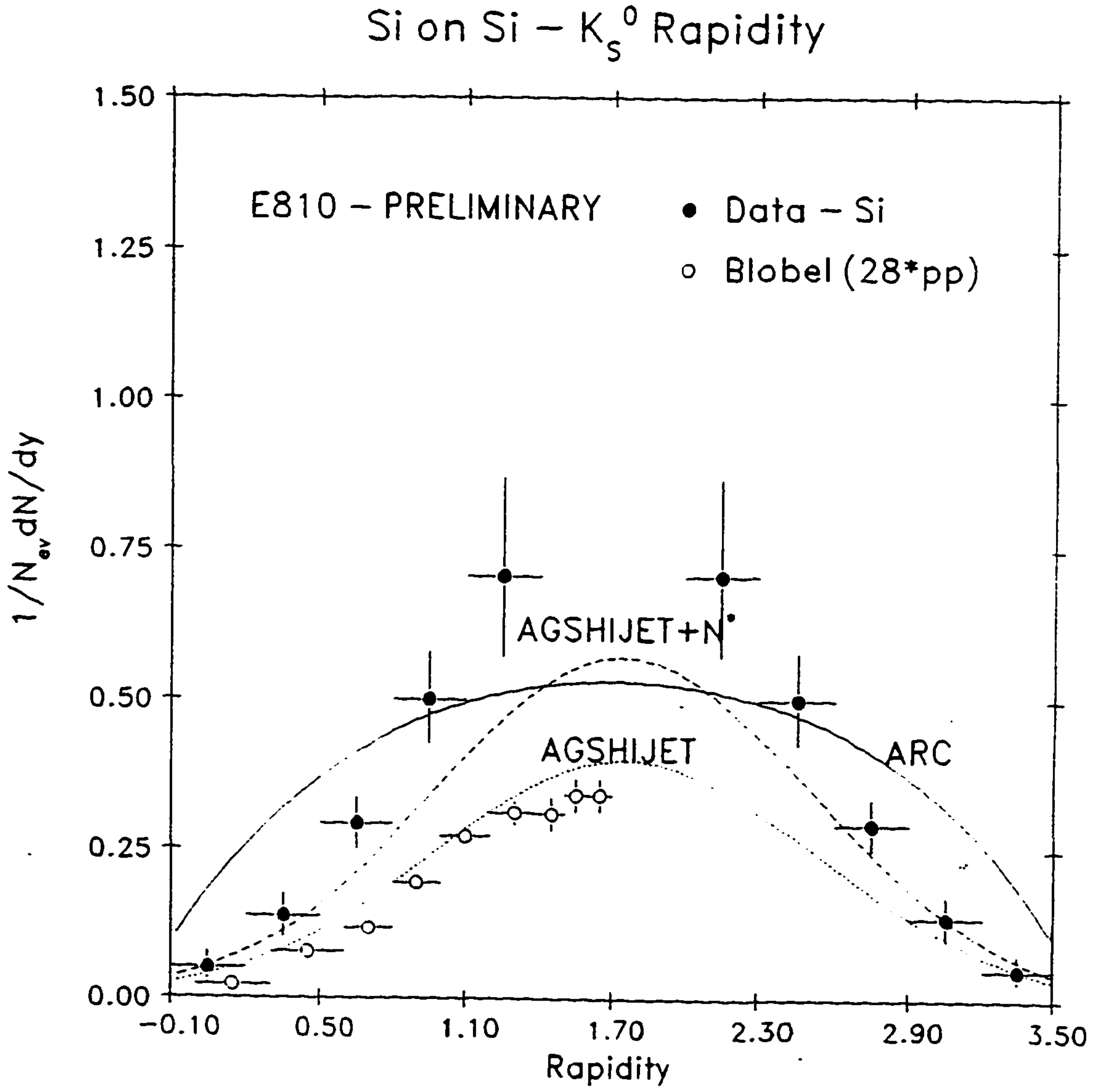

Figure 3.1: Rapidity distribution for K_s for Si on Si collisions. The solid points above a rapidity of 1.7 are the E810 measurements (below 1.7 are symmetric projections). The open circles are pp data at similar energies scaled by 28 from [59]. The dotted line is the prediction of AGSHIJET, the dashed line is the prediction of AGSHIJET+N* and the solid line is the prediction of another cascade model, ARC [55, 56].

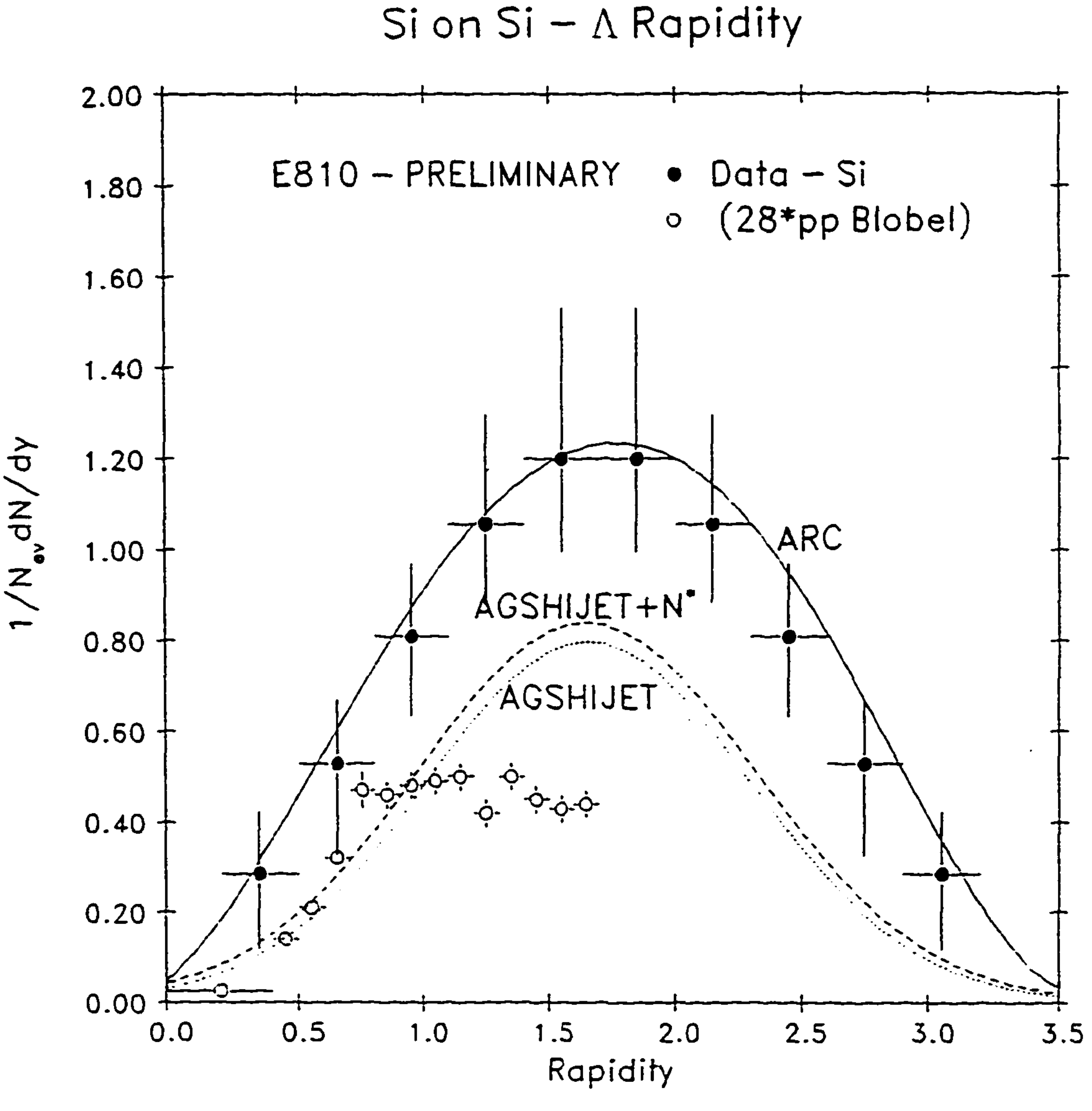

Figure 3.2: Rapidity distribution for Λ for Si on Si collisions. The various lines are explained in figure 3.1.

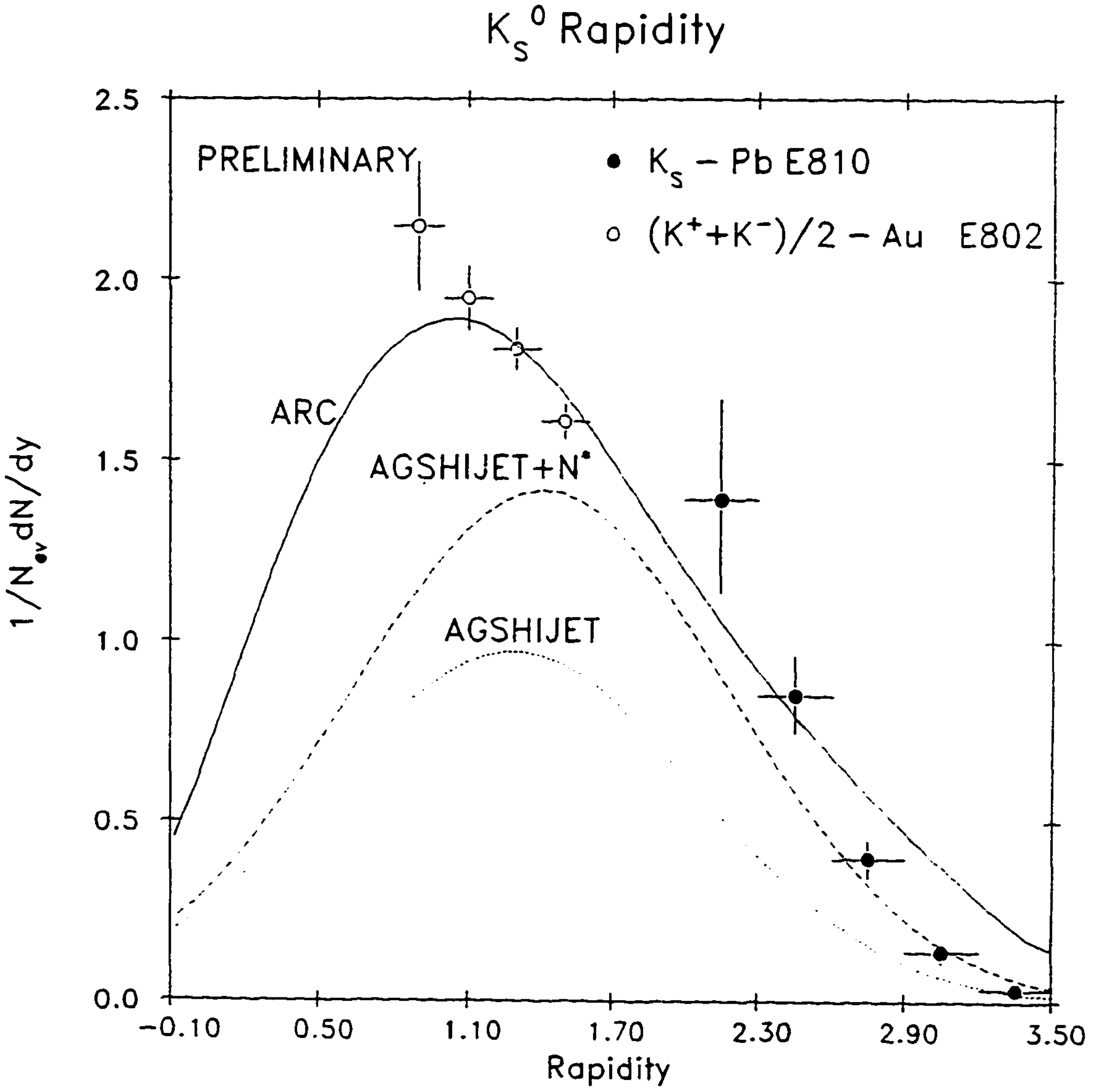

Figure 3.3: Rapidity distribution for K_s for Si on Pb collisions. The various lines are explained in figure 3.1.

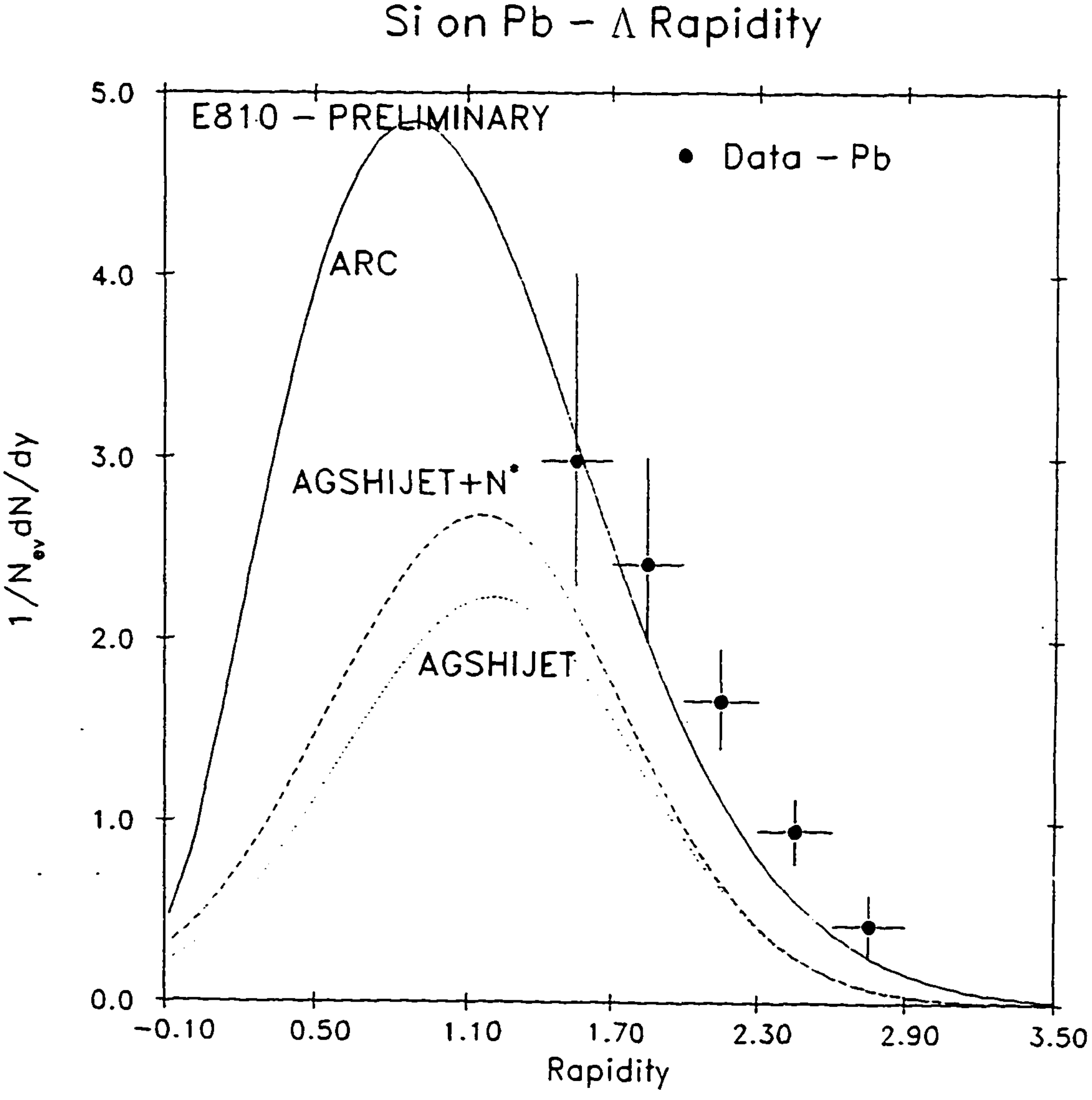

Figure 3.4: Rapidity distribution for Λ for Si on Pb collisions. The various lines are explained in figure 3.1.

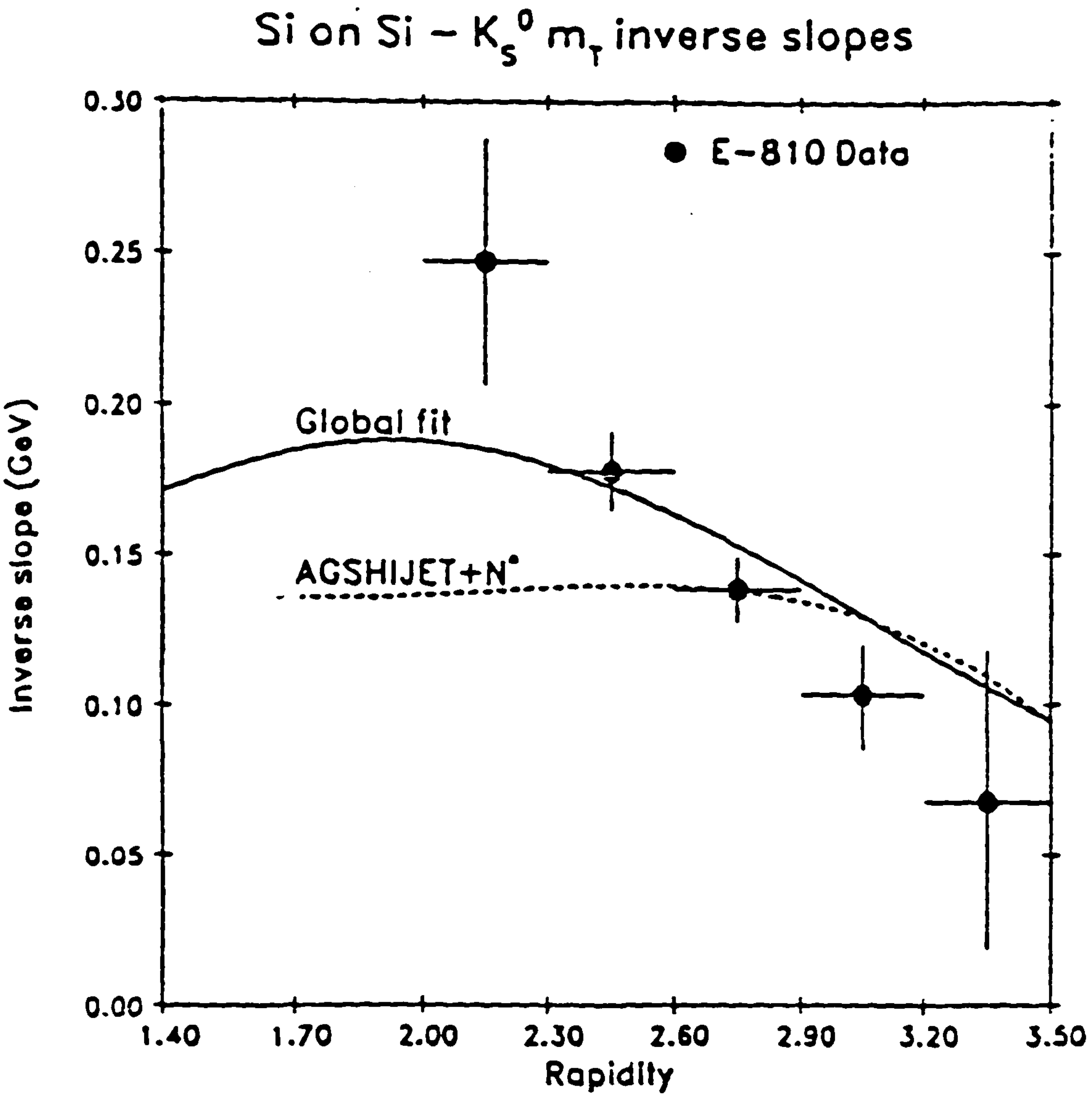

Figure 3.5: Inverse exponential slopes for K_s from the Si target. The solid curve is the global fit of the form: Aexp(Bm_T) with A constant and B = a + b • cosh(y-y_0).

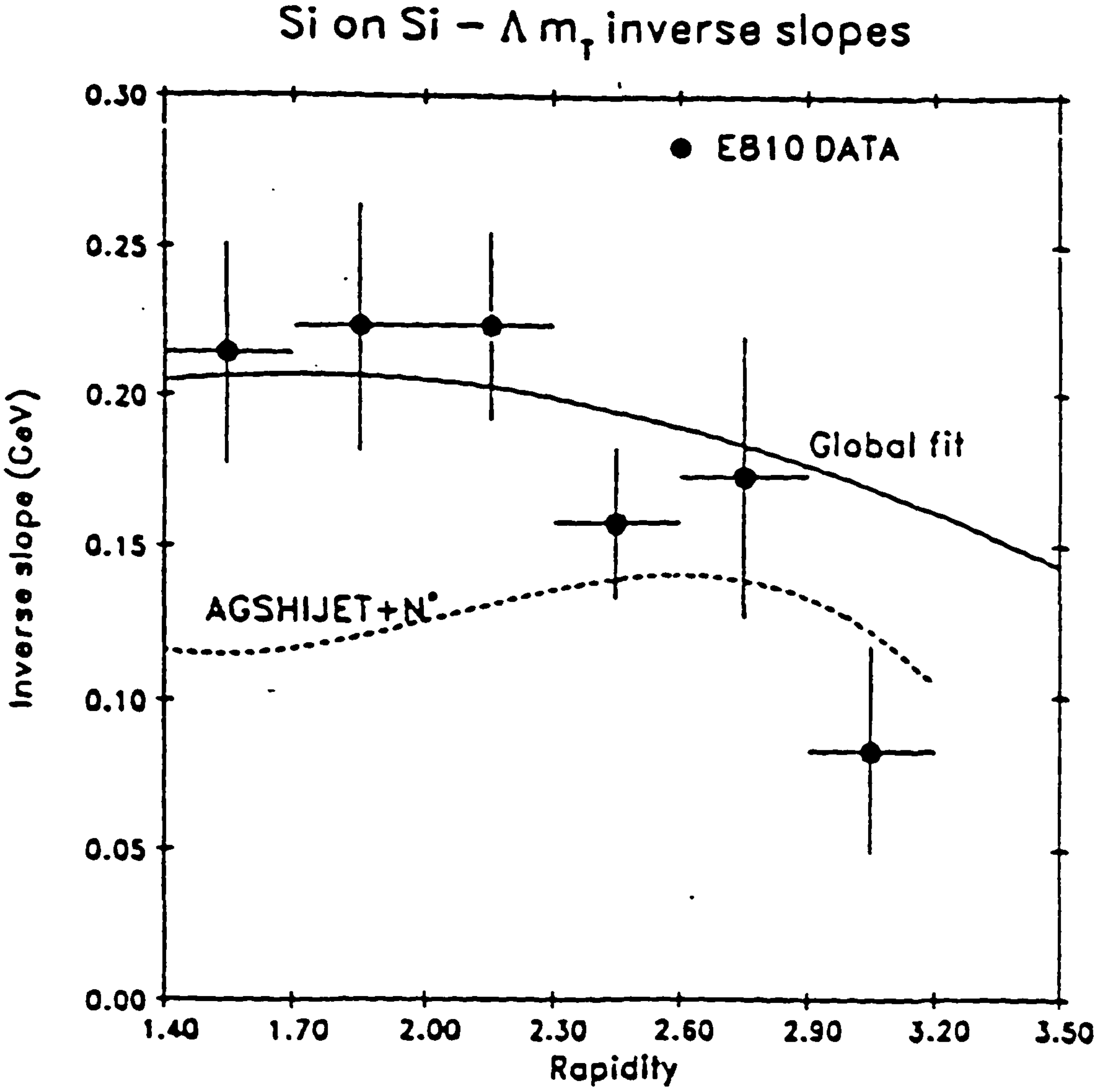

Figure 3.6: Inverse exponential slopes for Λ from the Si target. The solid curve is the global fit of the form: $A\exp(Bm_T)$ with A constant and $B = a + b \cdot \cosh(y - y_0)$.

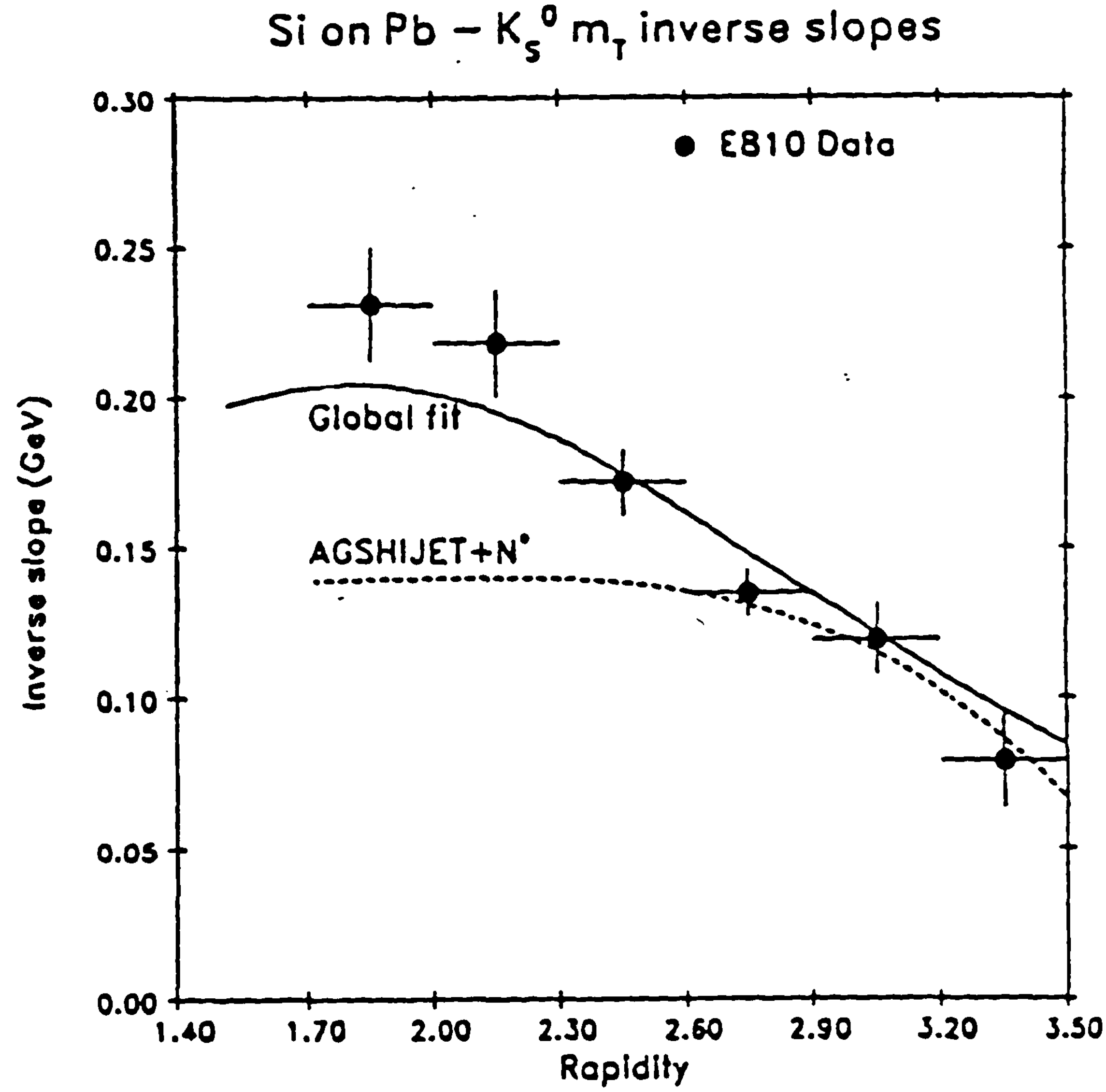

Figure 3.7: Inverse exponential slopes for K_s from the Pb target. The solid curve is the global fit of the form: $A\exp(Bm_T)$ with A constant and $B = a + b \cdot \cosh(y-y_0)$.

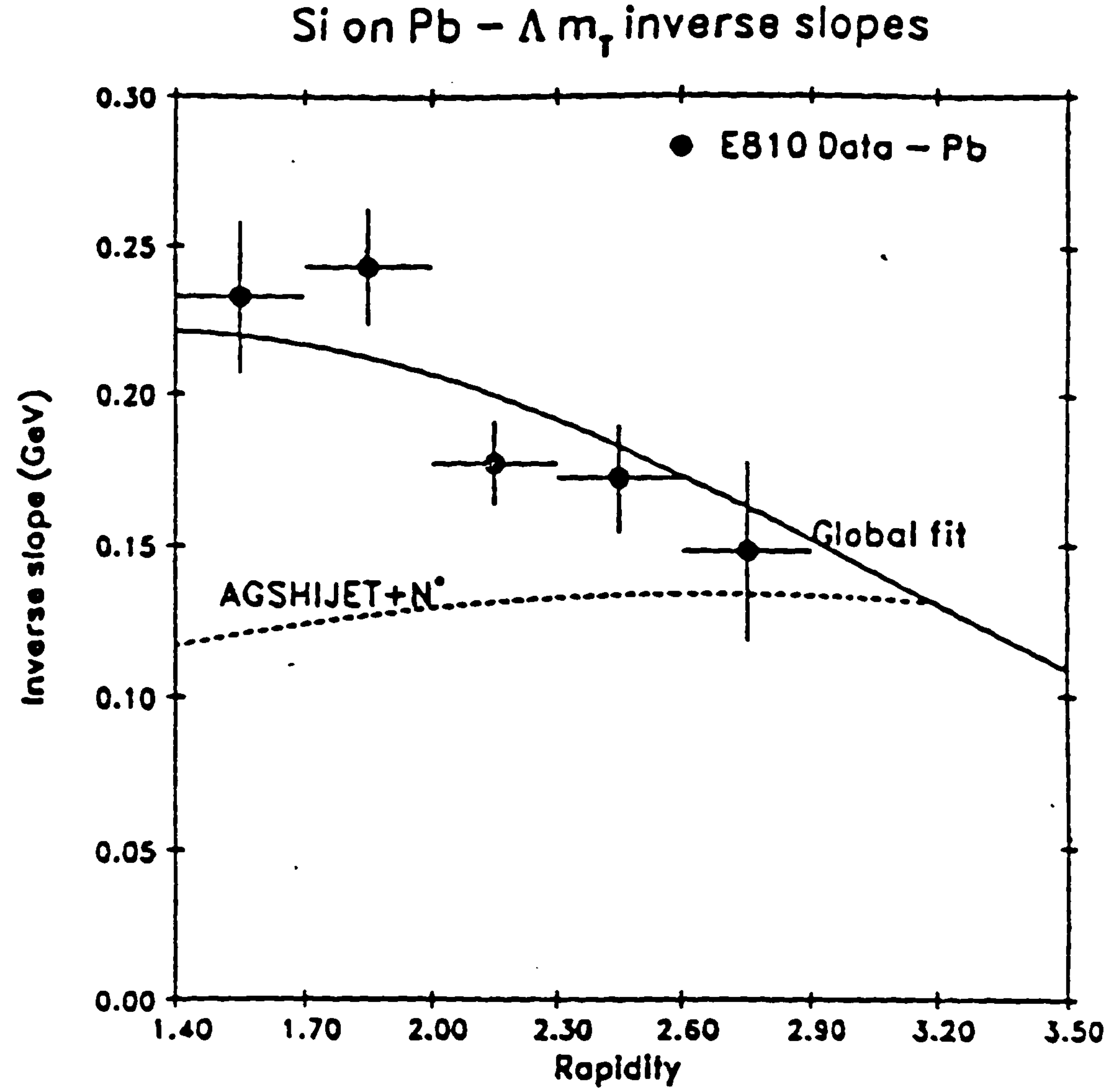

Figure 3.8: Inverse exponential slopes for Λ from the Pb target. The solid curve is the global fit of the form: Aexp(Bm_T) with A constant and B = a + b • cosh($y-y_0$).

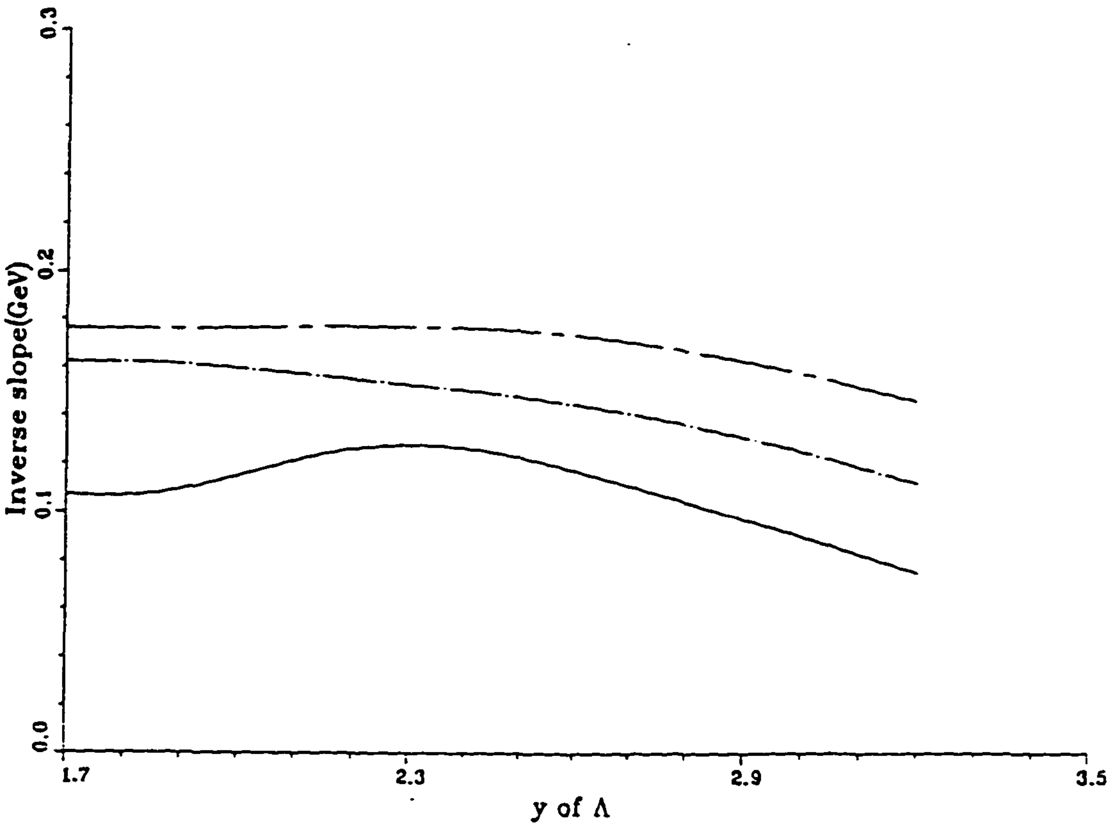

Figure 3.9: Inverse exponential slopes of Λ's for Si on Si collisions as predicted by a preliminary version of the RANDOM model. The solid line is for 50col/event, the dotted for 150 col/event and the dashed for 250 col/event.

3.2 Description of the RANDOM model

In order to simulate and try to understand the physics involved in Si on Si and Si on Pb interactions we developed an event generator called RANDOM [60]. RANDOM is a simple collision model that scatters particles randomly with probabilities proportional to their cross sections, without using any space-time information. RANDOM uses the scattering routines and cross sections of HIJET[4]. In RANDOM the nuclei are treated as clusters of nucleons; we assume that the two colliding nuclei stick together and the nucleons start to collide randomly. Fermi motion and nuclear forces are not taken into account, so all binary collisions are between free particles. The cross sections and the scattering dynamics do not depend on whether the particles have previously participated in an interaction. The number of collisions per event is an input parameter. We determine the optimum value for the number of collisions per event by comparing the predictions of the model for proton and pion rapidity distributions with experimental data.

Figure 3.10 shows the main characteristics of RANDOM. All the particles are stored in the particle list. For each entry in the particle list we keep the particle id and its four-vector (p_x, p_y, p_z, E). Initially the particle list contains the target and projectile nucleons with $p_x=p_y=0$, E=5.388/2GeV (in the nucleon-nucleon center of mass) and $p_z=2.53$ GeV/c for projectile nucleons (target nucleons have $p_z=-2.53$ GeV/c). We randomly choose to scatter two particles from the particle list. If one of the particles is a resonance (Δ, ρ, N*, K*, e.t.a.) that decayed, we scatter one of the products of the decay with the other particle from the particle list. The probability of decay of resonances

---

[4] We added meson-meson interaction in the HIJET routines but this has a minor effect in the strangeness production.

depends on the resonance width. We then calculate the cross section of the two colliding particles (by calling subroutine RSIGMA). The cross sections[5]will determine if collisions take place. The cross sections we use in our code are parametrizations of measured cross sections, otherwise we use the Additive Quark Model for unknown cross sections. If the collision passes the RSIGMA test, we call subroutine SECINT that computes the energy loss of the colliding particles and production of particles. SECINT forms multi - pomeron chains, with each chain fragmenting according to the Field - Feymann algorithm. SECINT combines a low energy parametrization of baryon-baryon baryon-meson and meson-meson which smoothly interfaces with a high energy modified version of MINBIAS. The products of the interaction are added at the end of the particle list. At the end of the event we decay all remaining resonances. We check that the model conserves energy, momentum, charge, baryon number etc. Some of the processes we have in our model are listed in figure 3.11.

---

[5] Cascade codes like HIJET, ARC use cross sections to define the region of interaction. ($< \sqrt{\sigma / \pi}$)

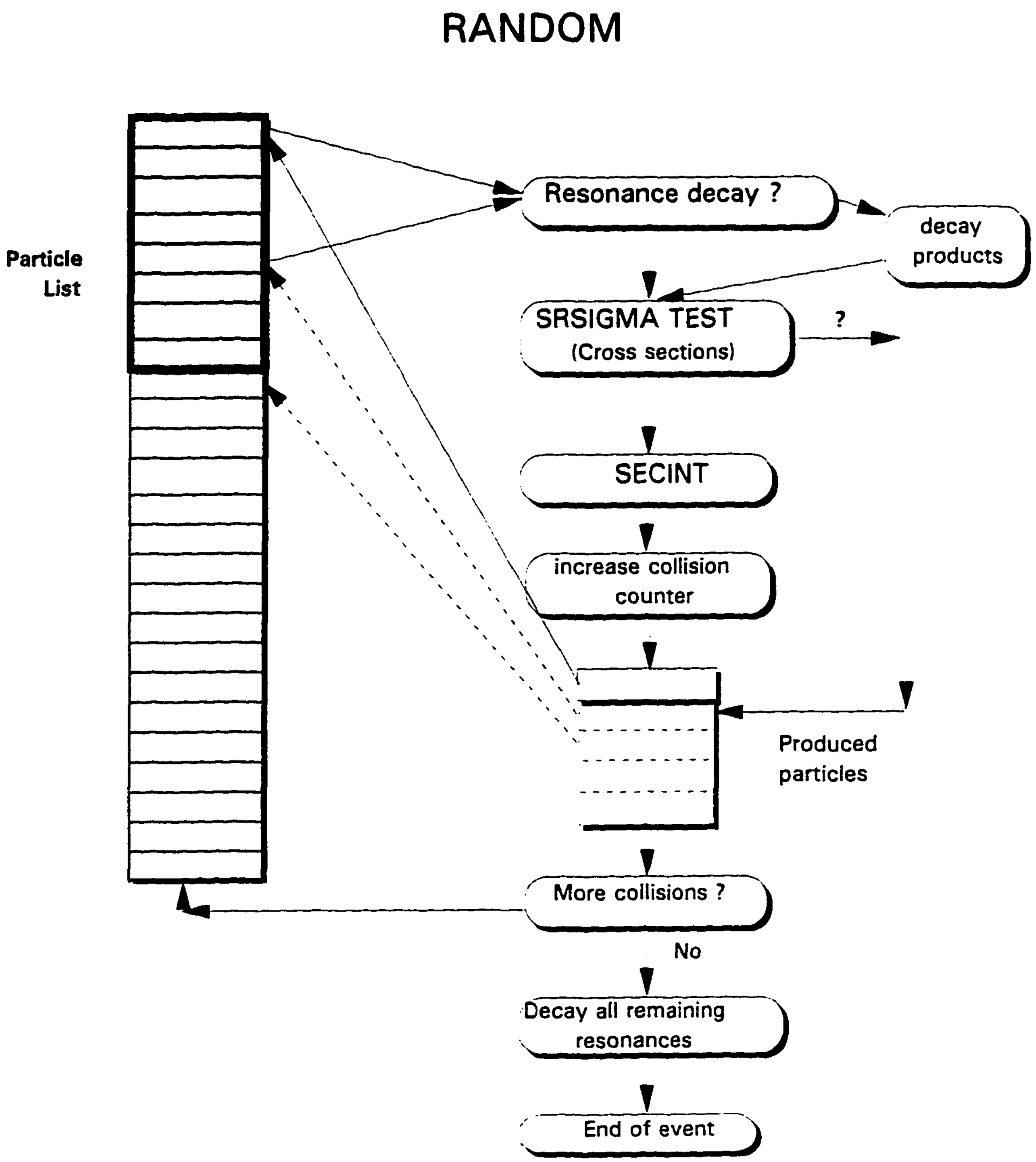

Figure 3.10: General diagram of RANDOM

$NN \rightarrow NN$

$NN \rightarrow N\Delta$

$NN \rightarrow \Delta\Delta$

⋮

$\Delta N \rightarrow \Delta N$

$\Delta N \rightarrow NN$

$\Delta N \rightarrow \Delta\Delta$

⋮

$\Lambda N \rightarrow \Lambda N$

$\Lambda N \rightarrow \Sigma N$

$\Lambda N \rightarrow \Xi K N$

$\Sigma N \rightarrow \Xi K N$

⋮

Isobars

$\pi N \rightarrow N^*$

$\Delta\pi \rightarrow N^*$

$\rho N \rightarrow N^*$

$KN \rightarrow Y^*$

$\Lambda\pi \rightarrow Y^*$

$\Sigma\pi \rightarrow Y^*$

$K\Delta \rightarrow Y^*$

$\Lambda\rho \rightarrow Y^*$

$\Sigma\rho \rightarrow Y^*$

$\rho\pi \rightarrow a_1$

$N^*N \rightarrow NN$

$N^*N \rightarrow \Delta N$

$Y^*N \rightarrow \Lambda N$

$Y^*N \rightarrow \Sigma N$

$NN \rightarrow N^*N$

$\Delta N \rightarrow N^*N$

$\Lambda N \rightarrow Y^*N$

$\Sigma N \rightarrow Y^*N$

$\pi\pi \rightarrow a_1\pi$

$a_1\pi \rightarrow \pi\pi$

Figure 3.11 : Processes we consider in RANDOM

$N\pi \rightarrow N\pi$
$N\pi \rightarrow \Delta$
$N\pi \rightarrow \Delta\pi$
$N\pi \rightarrow N\rho$
$N\pi \rightarrow N\eta$
$N\pi \rightarrow \Lambda K$
$N\pi \rightarrow \Sigma K$

$\Delta\pi \rightarrow N\pi$
$\Delta\pi \rightarrow \Delta\pi$
$\Delta\pi \rightarrow N\rho$
$\Delta\pi \rightarrow \Lambda K$
$\Delta\pi \rightarrow \Sigma K$

$N\rho \rightarrow N\pi$
$N\rho \rightarrow N\rho$
$N\rho \rightarrow \Lambda K$
$N\rho \rightarrow \Sigma K$

$KN \rightarrow KN$
$KN \rightarrow K\Delta$
$KN \rightarrow KN\pi$
$K\Delta \rightarrow KN$
$K\Delta \rightarrow K\Delta$
⋮

$\bar{K}N \rightarrow \bar{K}N$
$\bar{K}N \rightarrow \Lambda\pi$
$\bar{K}N \rightarrow \Lambda\pi\pi$
$\bar{K}N \rightarrow \Sigma\pi$
$\bar{K}N \rightarrow \Sigma\pi\pi$
$\bar{K}N \rightarrow \bar{K}N\pi$
$\bar{K}N \rightarrow \bar{K}\Delta$
$\bar{K}\Delta \rightarrow \bar{K}N$
$\bar{K}\Delta \rightarrow \bar{K}\Delta$
$\bar{K}\Delta \rightarrow \Lambda\pi$
$\bar{K}\Lambda \rightarrow \Xi N$
$\bar{K}N \rightarrow \Xi K$

⋮

$\pi^+\pi^- \rightarrow \pi^+\pi^-$
$\pi^+\pi^- \rightarrow \pi^0\pi^0$
$\pi^+\pi^- \rightarrow K^0\bar{K}^0$
$\pi^+\pi^- \rightarrow \eta\eta$

$\pi^0\pi^0 \rightarrow \pi^0\pi^0$
⋮

$\pi^+\pi^0 \rightarrow \pi^+\pi^0$
⋮

$\pi^-\pi^0 \rightarrow \pi^-\pi^0$
⋮

$\pi^- p \rightarrow \pi^+\pi^- n$ (OPE) ;
$\pi^- p \rightarrow K^+K^- n$ (OPE);
$\pi^- p \rightarrow K_s K_s n$ (OPE);
$\pi^- p \rightarrow \eta\eta n$ (OPE);

Figure 3.11 (continued): Processes we consider in RANDOM

$\pi K \rightarrow K\pi$	$K^- p \rightarrow K^- \pi^+ n$ (OPE)
$\pi K \rightarrow K\pi\pi$	$K^- p \rightarrow K_s \pi^+ \pi^- n$ (OPE)
$\pi K \rightarrow K\pi\pi\pi$	$K^- p \rightarrow K^- \pi^+ \pi^- \pi^+ n$ (OPE)
$K\overline{K} \rightarrow K\overline{K}$	
$K\overline{K} \rightarrow \pi\pi$	
$K\overline{K} \rightarrow \eta\eta$	$K\overline{K}$ form $f_0(975)$, $a_0(980)$, $\phi(1020)$, $f_2(1270)$
$K\overline{K} \rightarrow \eta\pi$	$a_2(1320)$, $f_2(1525)$
$K\overline{K} \rightarrow \rho\pi$	
$\rho\pi \rightarrow \rho\pi$	
$\rho\pi \rightarrow K\overline{K}$	$\rho\pi$ form $h_1(1170)$, $a_1(1260)$, $a_2(1320)$
$\rho\pi \rightarrow \eta\pi$	
$K^*\pi \rightarrow K^*\pi$	$K^*\pi$ form $K^*(1420)$
$K^*\pi \rightarrow K\pi$	
$a_1\pi \rightarrow \pi\pi$	$a_1\pi$ form $\rho(1700)$, $f_2(1800)$
$a_1\pi \rightarrow a_1\pi$	
$\omega\pi \rightarrow \omega\pi$	$\omega\pi$ form $b_1(1235)$
$\eta\pi \rightarrow \eta\pi$	$\eta\pi$ form $a_0(980)$, $a_2(1320)$
$\eta\pi \rightarrow K\overline{K}$	

Figure 3.11 (continued): Processes we consider in RANDOM

3.3 Results for Si on Si at AGS energies

In order to check whether RANDOM could reproduce some basic features of nucleus - nucleus collisions we tuned the model for Si on Si collisions at the AGS energy domain. RANDOM should be able to explain the features of this type of symmetric systems since its basic assumption, that the two colliding nuclei stick together, should hold. The fragmentation regions for central symmetric collisions between nuclei (where the model is not expected to do very well in explaining the data) should be small. We tuned the number of collisions per event to reproduce the E810 π^- rapidity distribution[6] (Figure 3.12). Figures 3.13 and 3.14 show RANDOM's predictions for the rapidity distribution of K_s and Λ^0, strange particles measured by E810. Figure 3.15 and figure 3.16 show the exponential inverse slopes for the same particles as a function of rapidity. The E810 data are Half Field data (5KG Magnetic field) and were acceptance corrected using the AGSHIJET+N* model.

3.4 Tuning RANDOM for Si on Pb collisions

The next project was to tune the model for Si on Pb interactions. For this type of collisions we cannot simply assume that the two nuclei stick together because there are Pb nuclei that will undergo a very small number of collisions. To get around this we used three particles lists instead of one (the projectile, the target fragmentation list, and the central fireball list), each with a separate number of collisions. We tuned the input parameters to reproduce the proton rapidity distribution of E802 and E814 (total 2000

---

[6] We used 320 collisions/event. AGSHIJET+N* has an average of 170 collisions/event

collisions per event), because the proton rapidity distribution shows clearly the fragmentation regions.

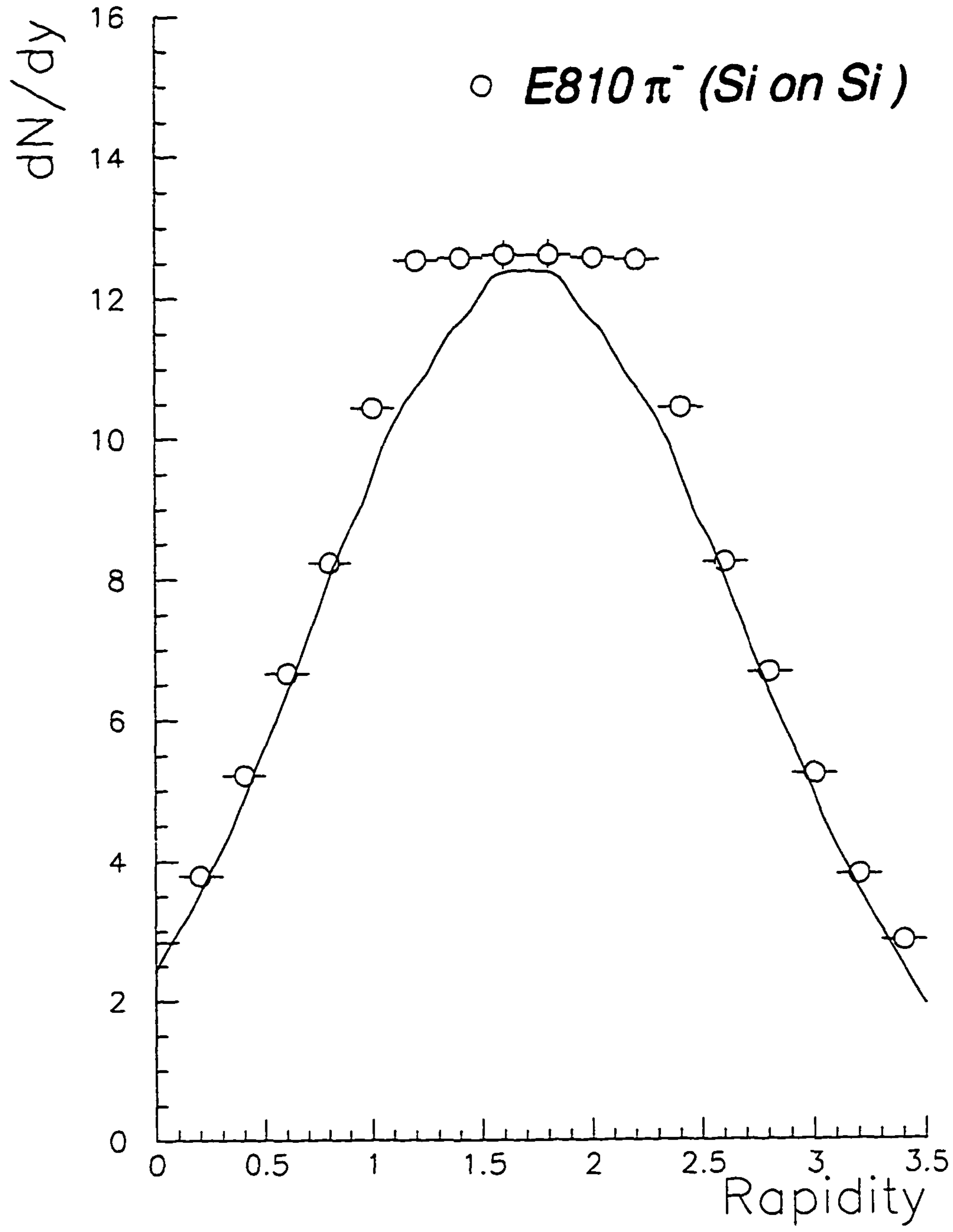

Figure 3.12: Rapidity distribution for π^- from the Si target. The points above a rapidity of 1.7 are the E810 measurements. Errors are statistical only. The solid curve is the prediction of the RANDOM model.

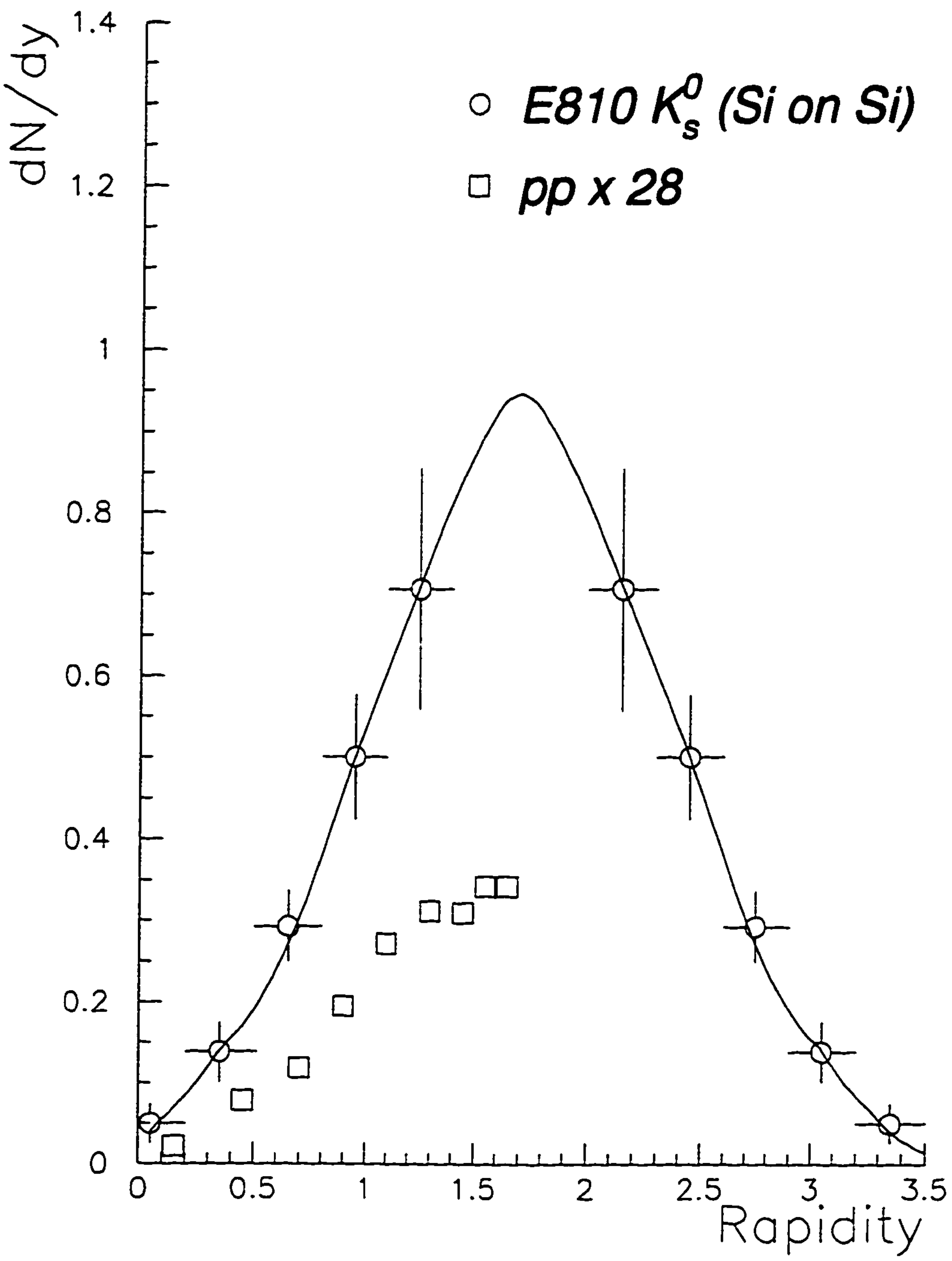

Figure 3.13 : Rapidity distribution for K_s from the Si target. The points above a rapidity of 1.7 are the E810 measurements. Errors are statistical only. The solid curve is the prediction of the RANDOM model. Open squares represent the measurements of [59] scaled by 28.

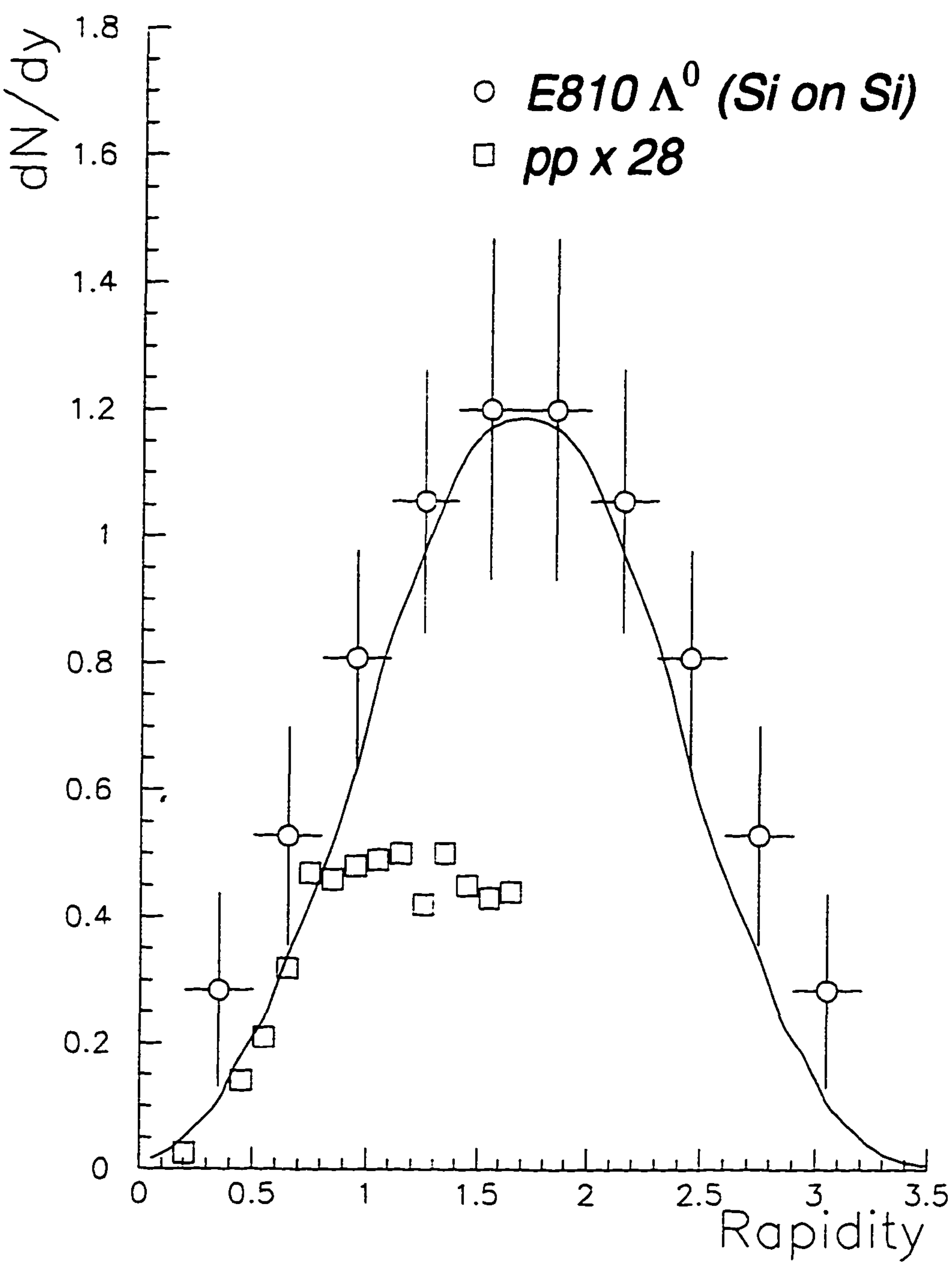

Figure 3.14 : Rapidity distribution for Λ^0 from the Si target. The points above a rapidity of 1.7 are the E810 measurements. Errors are statistical only. The solid curve is the prediction of the RANDOM model. Open squares represent the measurements of [59] scaled by 28.

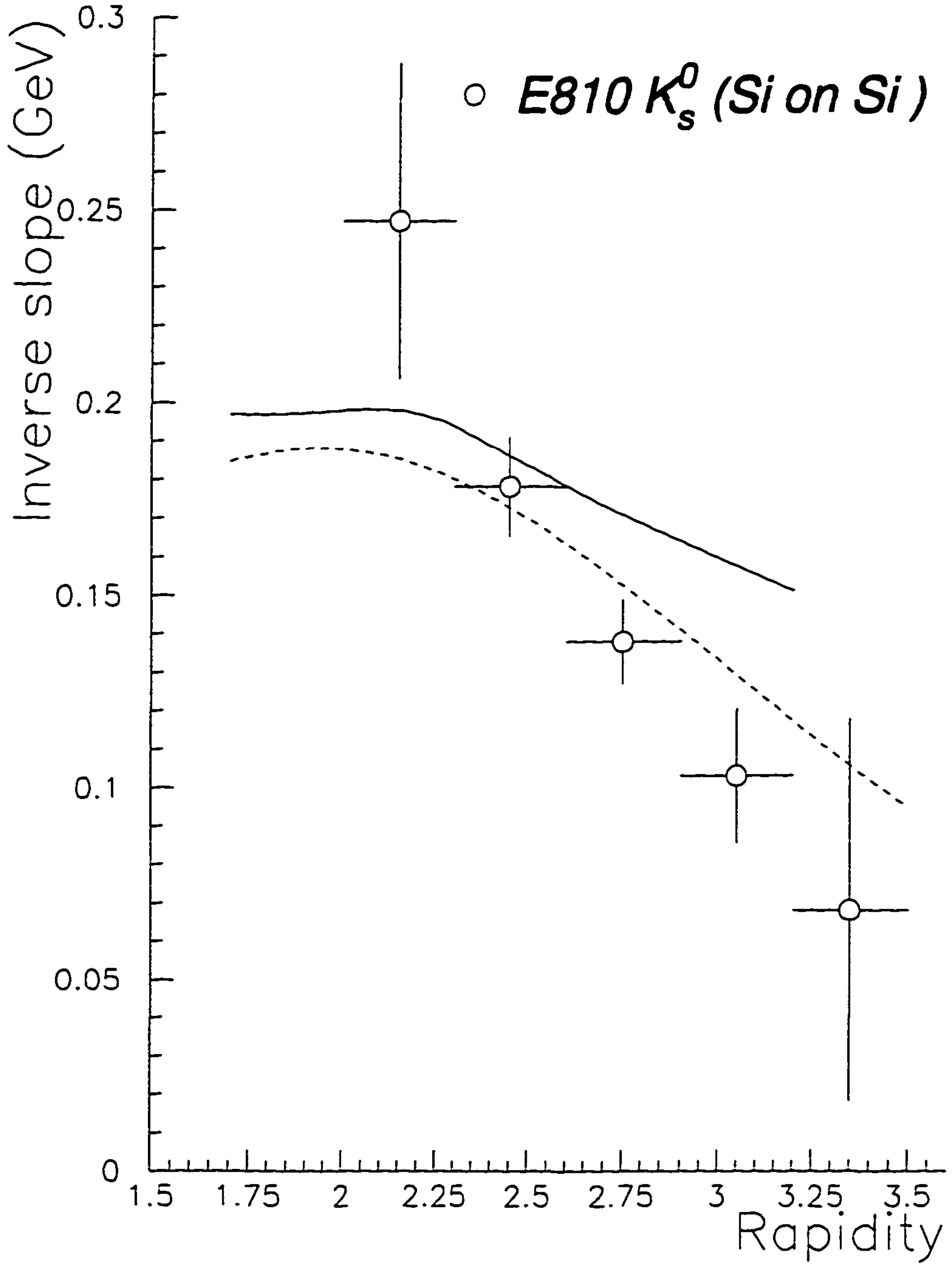

Figure 3.15: Inverse exponential slopes for K_s from the Si target. The solid curves are the predictions of the RANDOM model. The dotted curves are global fits of the form: Aexp(Bm_T) with B = a + b • cosh($y-y_0$).

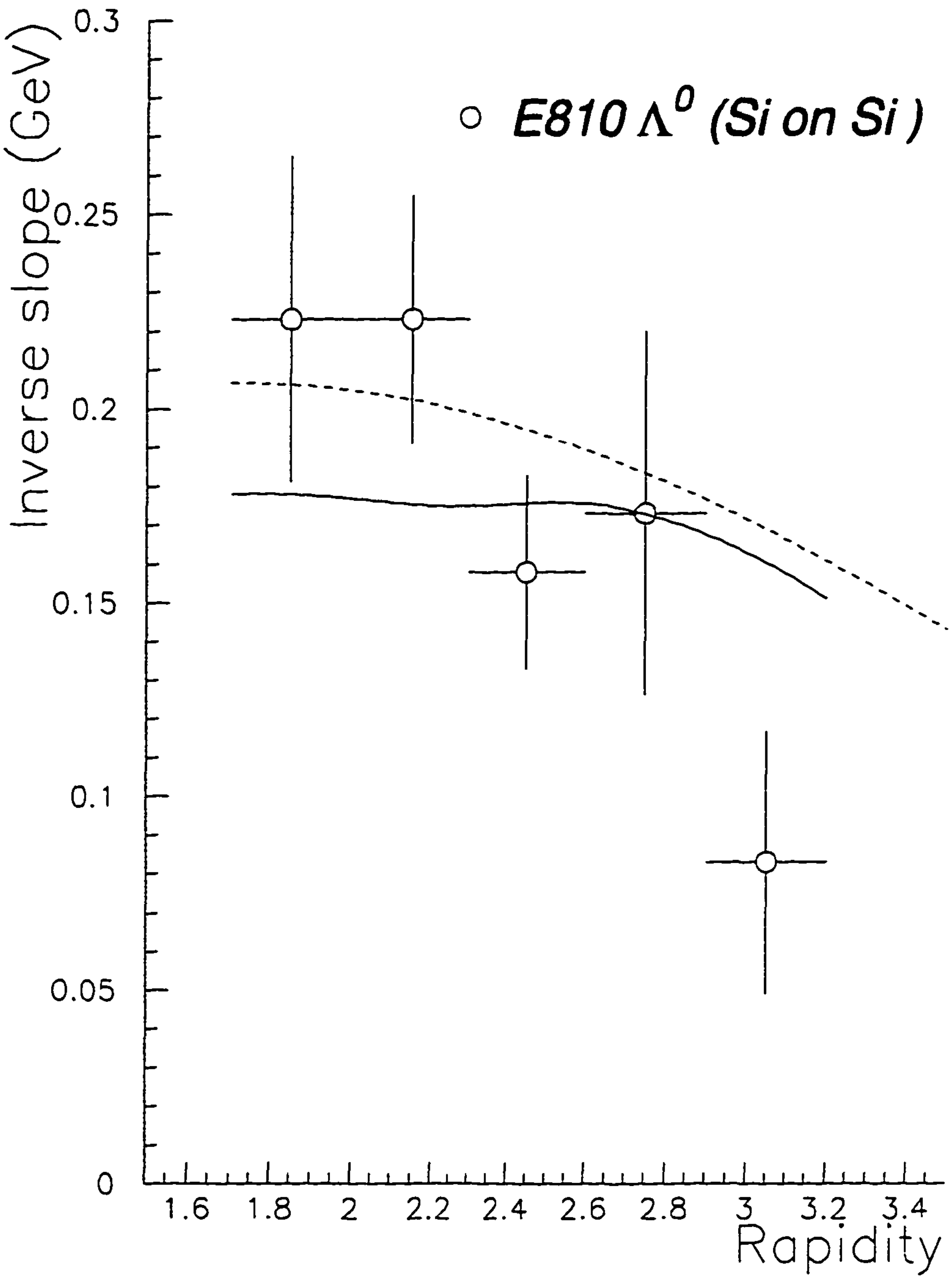

Figure 3.16: Inverse exponential slopes for Λ^0 from the Si target. The solid curves are the predictions of the RANDOM model. The dotted curves are global fits of the form: $A\exp(Bm_T)$ with $B = a + b \bullet \cosh(y-y_0)$.

Figure 3.17 shows the prediction of the model for the rapidity distribution for K^+ and K^- compared to data from experiment E802 for Si on Au interactions. Figure 3.18 and 3.19 show the rapidity distribution for K_s and Λ^0's and figure 3.20 and 3.21 show the exponential inverse slopes for the same particles as a function of rapidity. The data in the last two figures are from experiment E810.

It was pointed out by several authors [61, 62, 63] that the enhancement of particles with single strangeness cannot serve as a clean signature of QGP formation, since it carries out too much background information of the hadronic state. The strangeness enhancement expected in the QGP phase in conduction with a high local strangeness density should favor the formation of multistrange objects, and particularly multistrange antibaryons. In the hadronic gas phase we lack the strangeness density and therefore we should not expect to form these particles abundantly, as a series of unlikely reactions has to occur in their formation, while their destruction is easily possible in collisions with hadronic gas constituents. E810 data were fitted with a fireball consideration, and a Boltzmann term is essential in fitting the E810 K_s data for an acceptable χ^2 [64]. This could mean that mesons are closer to thermal equilibrium than baryons. For the Λ's the fireball aspect was not essential for understanding their characteristics. If QGP is formed and then decayed into such a fireball all strangeness signatures would be washed out. This could be for example the case for slowly, rather than rapidly, decaying QGP. However, hyperons of multiple strangeness provide a better probe of QGP. The experimental challenge of detecting the decay of multiply-strange baryons in the high multiplicity environment of nucleus-nucleus collisions has be taken up by experiment E810 [65]. They observed a Ξ^-/Λ ratio of 0.12 ± 0.02 in $1.4 < y < 2.9$ and $0.0 < p_T < 0.8$ GeV/c. This result challenges the cascade models to include double strange hyperons into their code.

In figure 3.22 we show the rapidity distribution of cascade minus compared to the recent publication by E810. Since no satisfactory model is available to describe the cascade minus production, E810 assumes that the Ξ^-'s obey the same transverse mass distribution as Λ^0's and relying on the fact that the heavier the mass of the particle the smaller the slope of the m_T distribution this approximation is an underestimate. Figure 3.23 shows the comparison of what was used by E810 to RANDOM's prediction. Table 9 shows how the ratio Ξ^-/Λ compares to cascade models and RANDOM. Since when counting hyperons two different charge zero states of different isospin must be counted, the experimental abundances of Λ implicitly include the abundance of Σ^0, arising from the electromagnetic decay $\Sigma^0 \rightarrow \Lambda + \gamma$. In a pure QGP scenario Λ^0 and Σ^0 should be equally formed (same quark content), and thus the ratio Ξ^-/Λ must be corrected by nearly a factor of 2, (exactly 2 when the small difference in mass $m_\Sigma - m_\Lambda = 77$ MeV is neglected). In the Hadronic Gas scenario we expect Σ^0 to be 1/3 of Λ^0, due to isospin considerations (their origin is dominantly N* decays. This is seen in pp collisions at the AGS). The RANDOM model verifies that the Σ^0/Λ^0 ratio is close to 1/3. Table 10 compares the average number of collisions per Si on Pb event at AGS energies for different models. The number of collisions per event in RANDOM is two or three times larger than conventional cascade models. The success of RANDOM in explaining the strange particle production using such a larger number of collisions could be an indication that a central fireball is formed. The other natural explanation would be that we have the creation of some of Quark Gluon Plasma.

Model	Ξ^-/Λ ratio
E810 Data	0.120
AGSHIJET + N*	0.020
RQMD	0.050 [66]
RANDOM	0.090

Table 9: Ξ^-/Λ ratio from various cascade models and RANDOM

Model	Average number of collisions per Si on Pb event at the AGS
AGSHIJET + N*	700
ARC	1,000
RQMD	850
RANDOM	2,000

Table 10: Average number of collisions from different cascade models and RANDOM

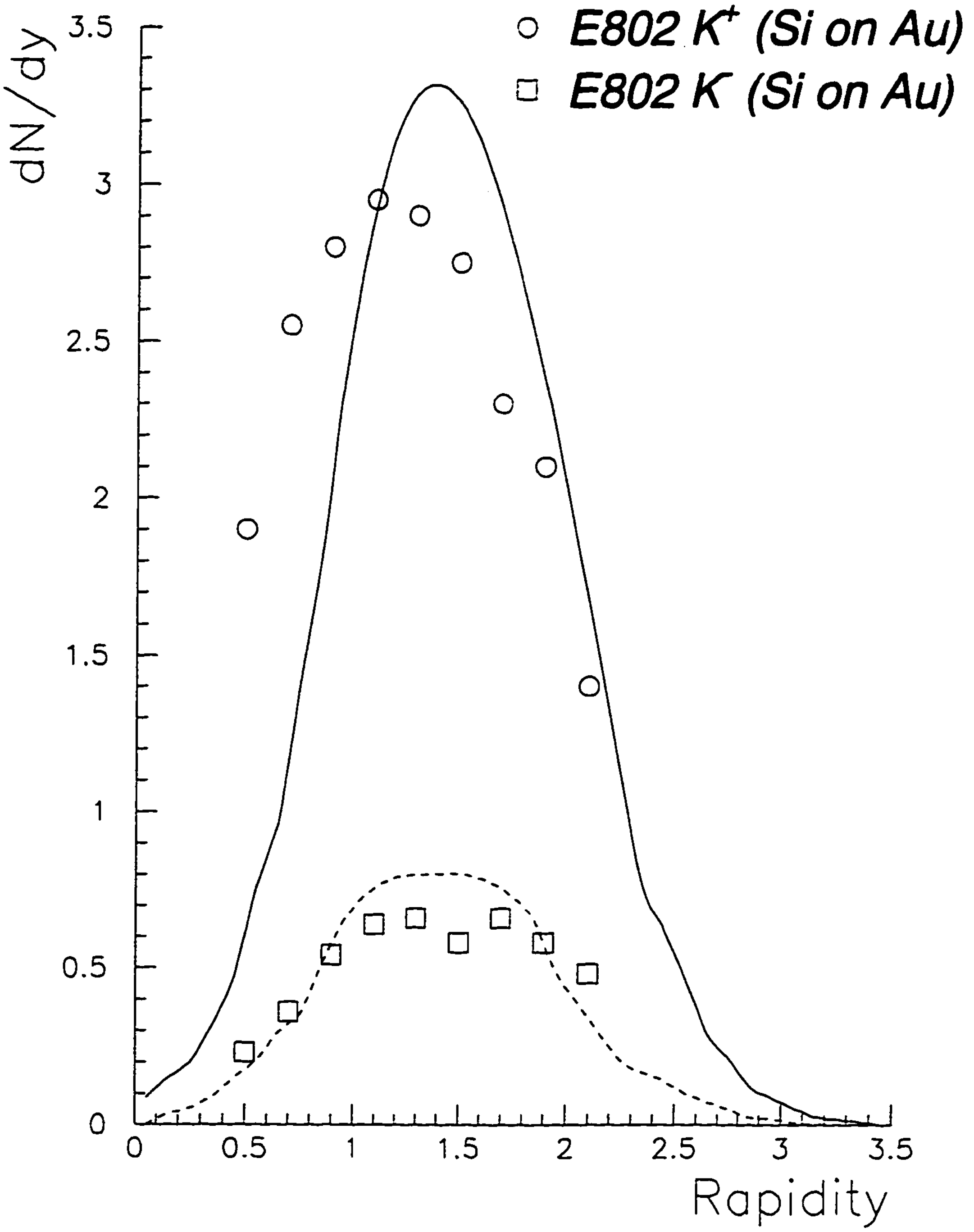

Figure 3.17: Rapidity distribution for K⁺, K⁻. The data points are from experiment E802 (Si on Au), the solid line is the prediction of the RANDOM model.

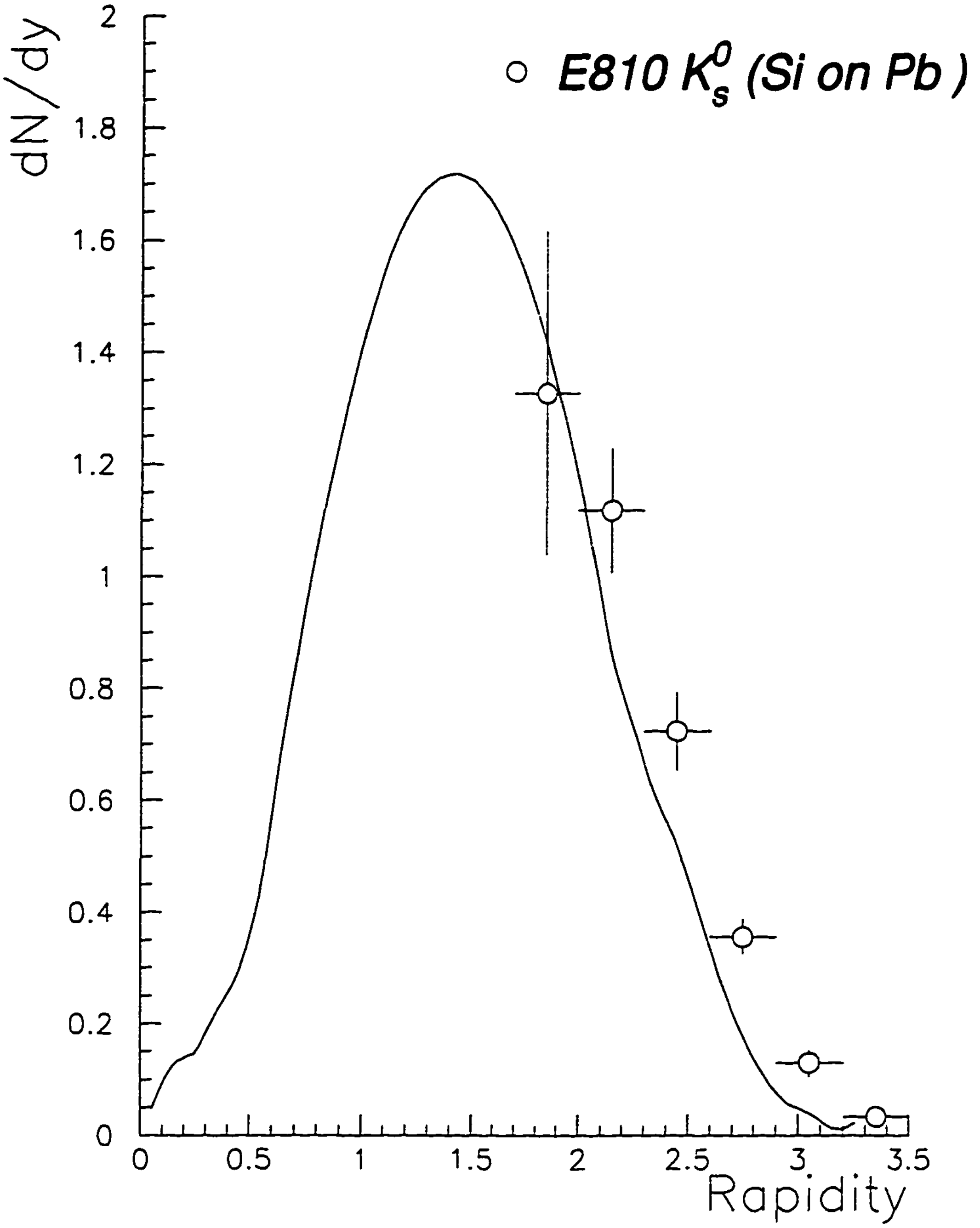

Figure 3.18: Rapidity distribution for K_s from the Pb target. Data points are from experiment E810 (Si on Pb). The solid lines are the predictions of the RANDOM model.

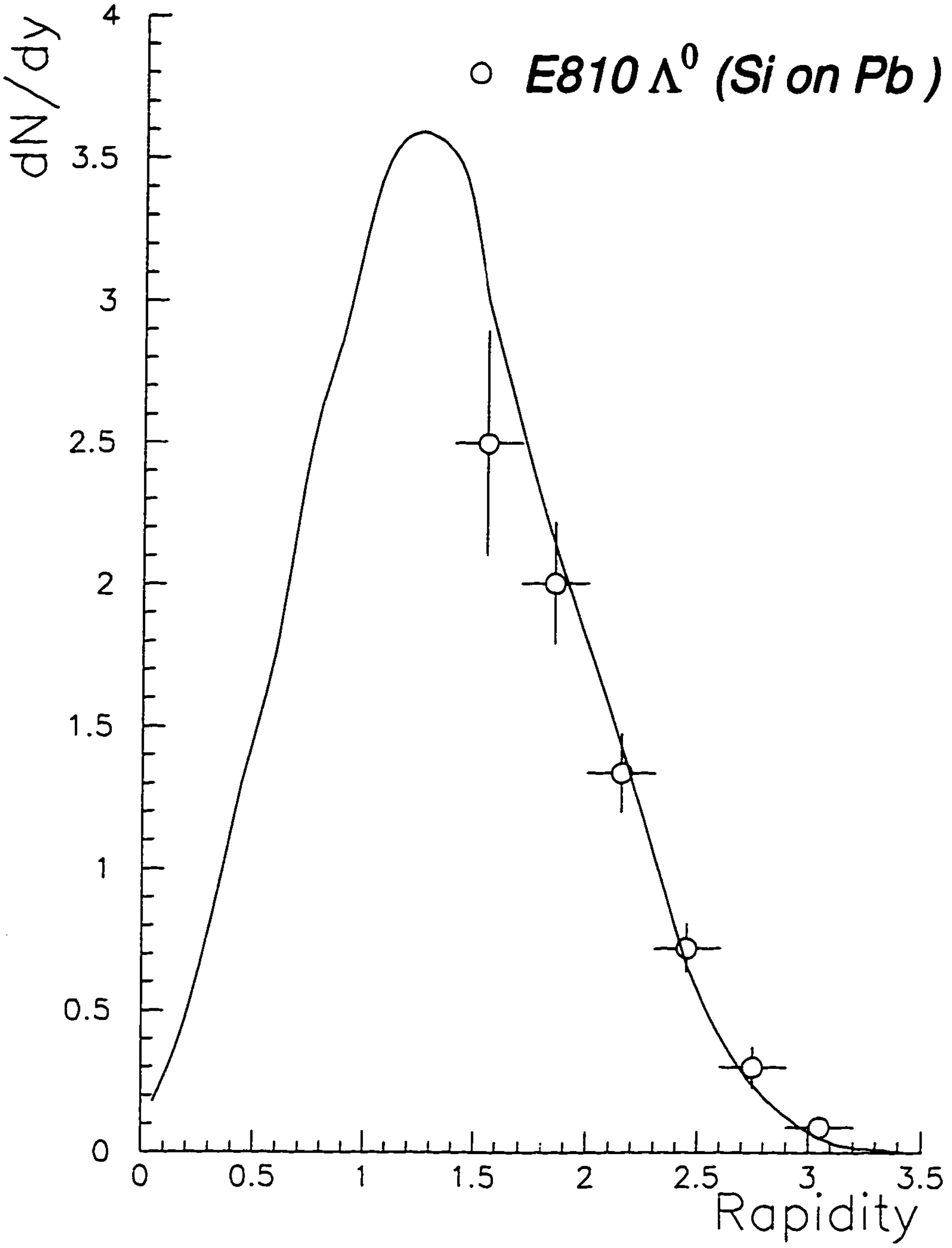

Figure 3.19: Rapidity distribution for Λ^0 from the Pb target. Data points are from experiment E810 (Si on Pb). The solid lines are the predictions of the RANDOM model.

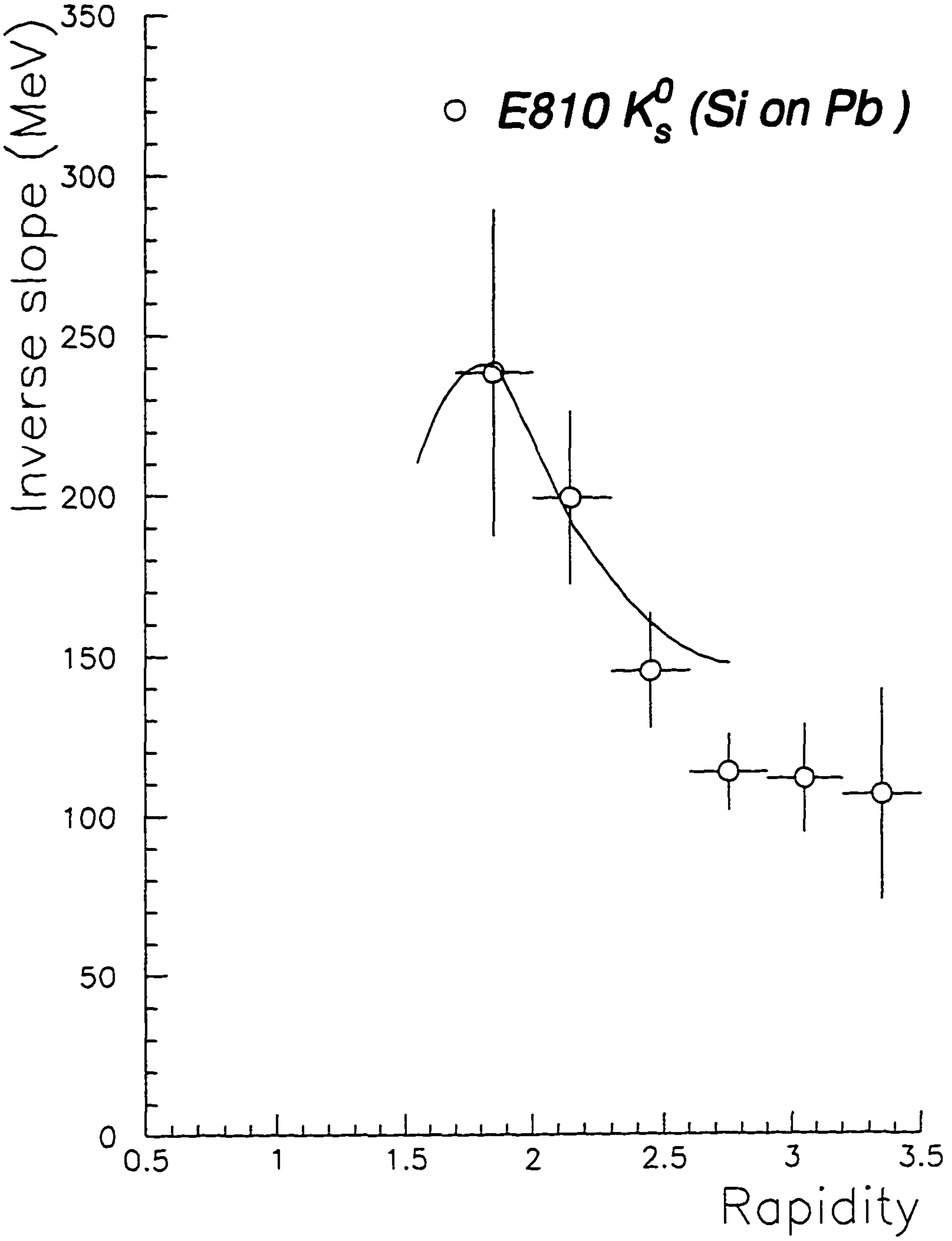

Figure 3.20: Exponential inverse slopes for K_s from the Pb target. Data points are from experiment E810. The solid line is the prediction of the RANDOM model.

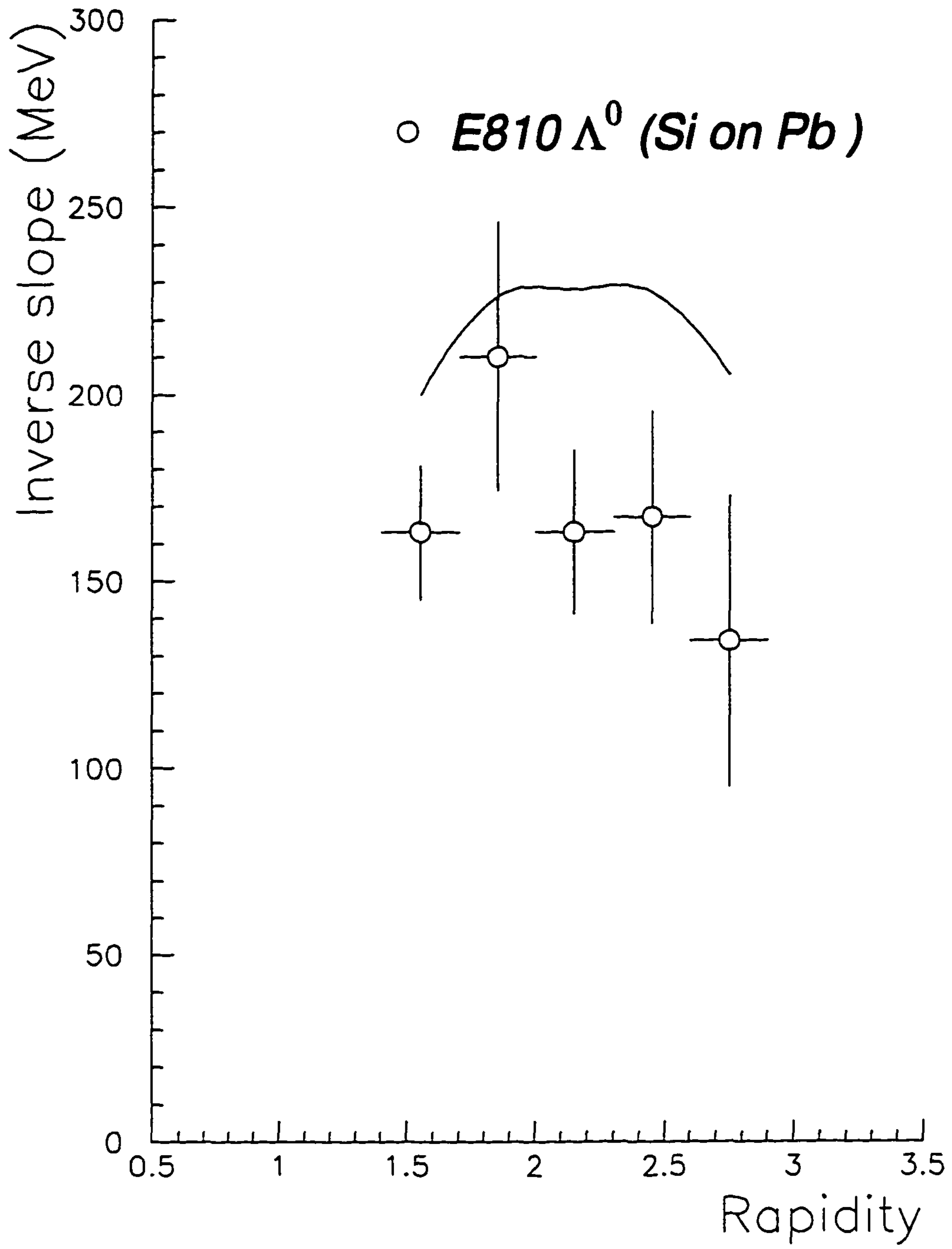

Figure 3.21: Exponential inverse slopes for Λ^0 from the Pb target. Data points are from experiment E810. The solid line is the prediction of the RANDOM model.

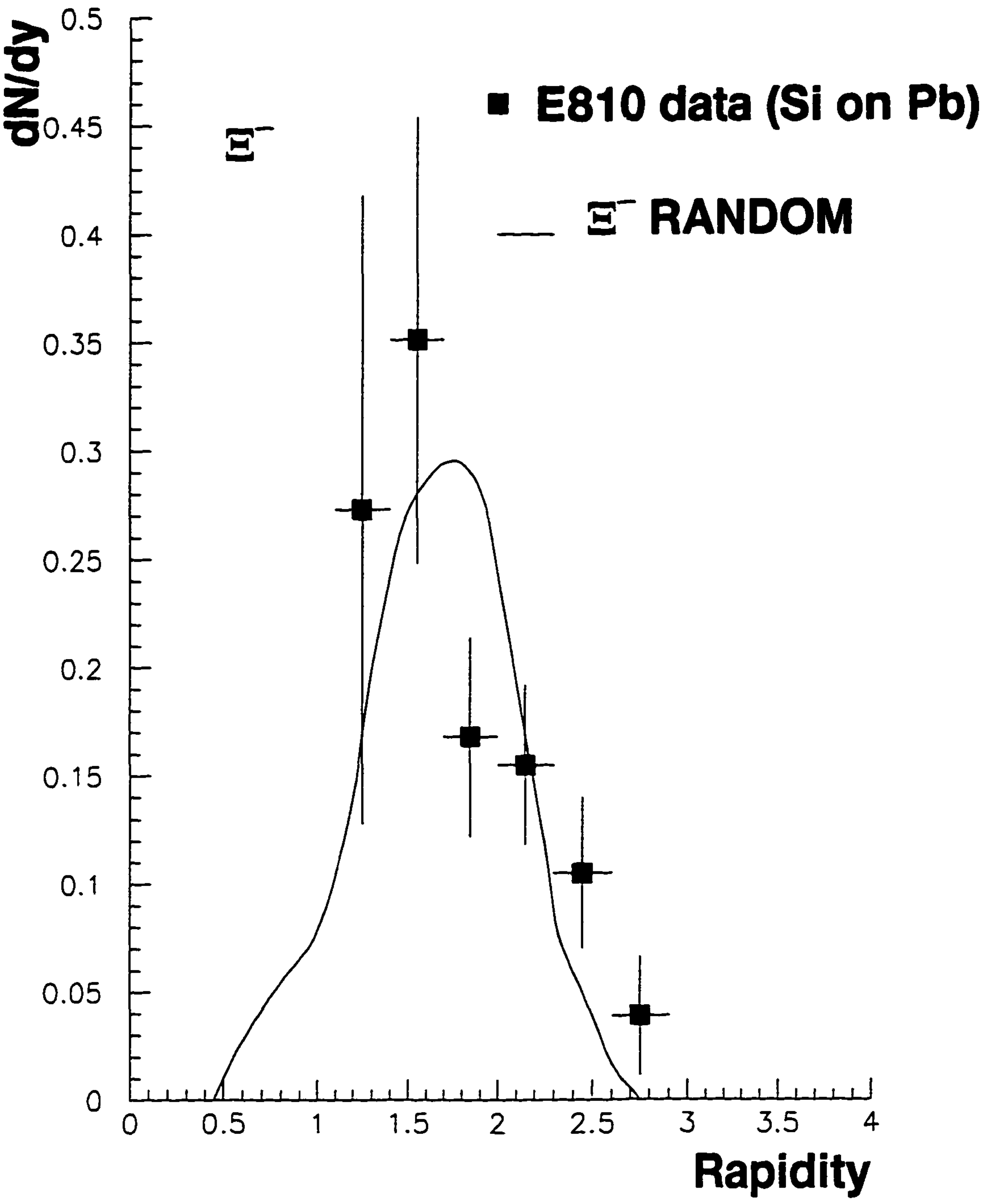

Figure 3.22: Rapidity distribution of cascade minus compared to E810 data.

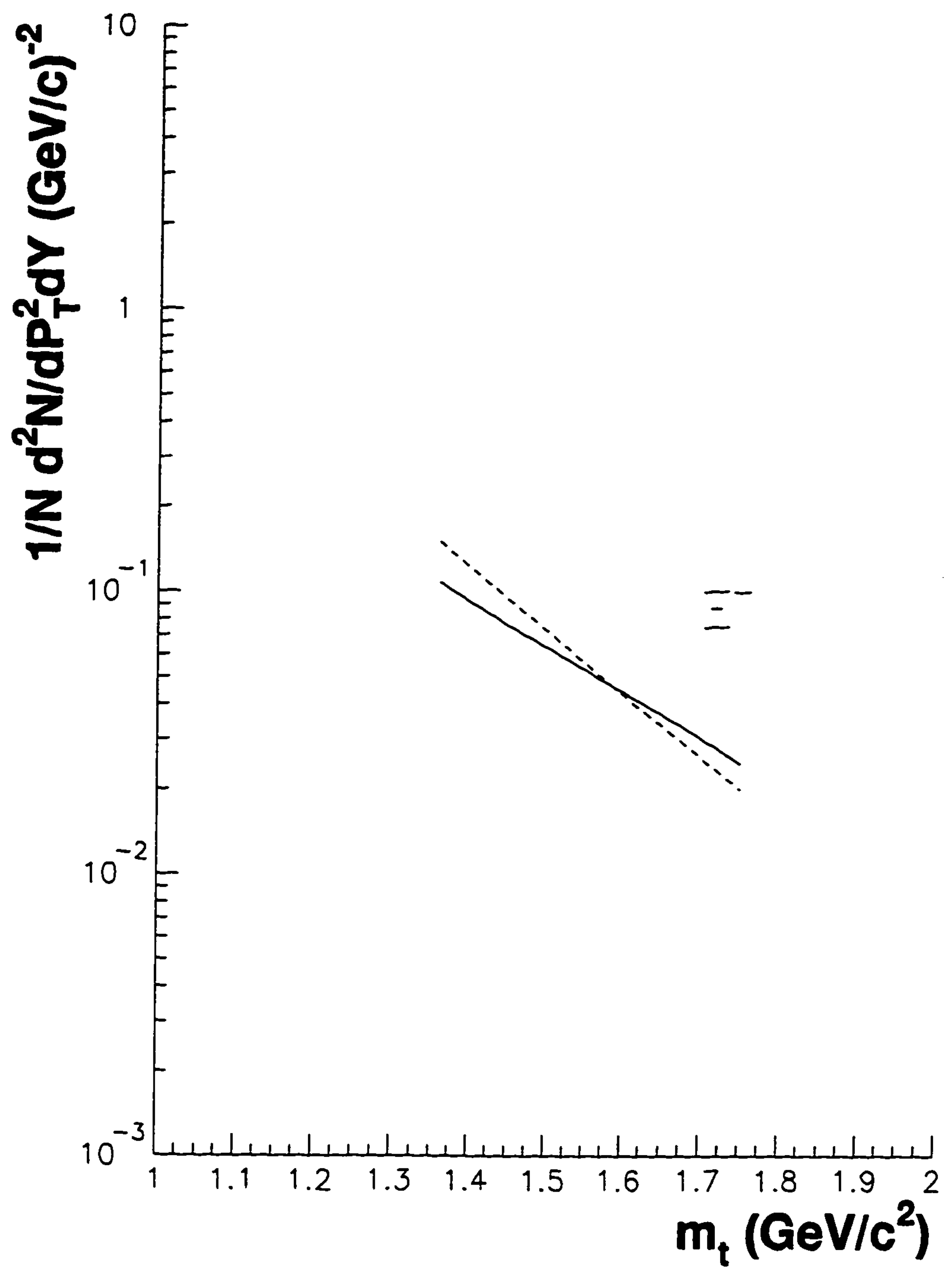

Figure 3.23: The prediction of the RANDOM model for the m_T slope is compared to what was used by E810 in [65].

3.5 Differences between RANDOM and HIJET

Let us summarize now some differences between RANDOM and HIJET:

1. Random doesn't have any space-time information.
2. Different input parameters (formation time vs. number of collisions and probability of decay). In RANDOM the formation time is always zero.
3. Random includes Meson-Meson interactions.
4. HIJET scatters particles when their distance is smaller that R_{int} (using cross sections and geometry). In Random we scatter particles according to their cross sections.
5. The strength of secondary interactions in HIJET depends on formation time.

Always keep Ithaca fixed in your mind.
To arrive there is your ultimate goal.
But do not hurry the voyage at all.
It is better to let it last for long years;
and even to anchor at the isle when you are old,
rich with all that you have gained on the way,
not expecting that Ithaca will offer you riches.
Konstantinos Kavafis ("ITHACA")

4. DATA ANALYSIS AND RESULTS

We present the results of the data analysis on the production of positive and negative tracks. The data were collected during the 1991 run of E810 when Silicon (Si) ions were accelerated at 14.6 GeV/c per nucleon and the target (fixed) was Pb. The thickness of the target was 0.2 mm (3.5% of radiation length) to eliminate the electron-positron tracks that point back to the target, and thus contaminate our charged track samples that point to the primary vertex (target). We selected the most central events by using the total charged track multiplicity in the mid-rapidity region ($1.6 < \eta < 2.5$). Events with total charged track multiplicity in the mid-rapidity greater than 40 were selected as central. This cut yielded 12,051 events, corresponding to a cross section of approximately 250 mb (about 9% of the geometric cross section). The magnetic field was set to 10 KG (1 Tesla). The data set collected with the 10KG magnetic field is called Full Field data set, while the set with the 5KG magnetic field is called Half Field. Most of the data analyzed are from the Full Field data set. Full field data set has the advantage of better momentum resolution, especially for the high momentum tracks.

4.1 Acceptance corrections

The acceptance corrections of the distributions present here were performed with a complete Monte Carlo simulation of the effects of the apparatus and cuts to our final data sample. The procedure is described in figure 4.1. Ten event files (each containing 10,000 Si-Pb events) were generated using the RANDOM event generator. The parameters of the event generator were adjusted to approximate the data in order to minimize any systematic errors in acceptance calculations when an integration was performed over a kinematic variable. Each of these event files (which contained the id's and 4-momenta of the particles) was fed into our simulation package (TPCMC) that used GEANT3.21 to simulate our detector. Our simulation package describes the experimental setup by a structure of geometrical volumes. After accepting an event, it transports the particles of that event through the various regions of the setup, taking into account geometrical volume boundaries and physical effects according to the nature of particles themselves, their interactions with matter and the magnetic field. Figure 4.2 shows the tracks of particles from a Silicon on Lead event in our simulated detector. The simulation package was originally developed on a VAX/VMS platform and later upgraded into a UNIX platform following the upgrade of GEANT (the latest was GEANT3.21). There are running versions of TPCMC on all most popular systems such as VAX/VMS, IRIX5.2, and AIX32 (IBM). The output was in the same format as the real data (fastbus file). The generated hits included all the known effects of detector aperture, efficiencies, resolutions and distortions. This file was then analyzed by the event reconstruction program, the same program used to analyze the actual data. The reconstructed rapidities (y) and transverse momenta squared (p_T^2) for negatives and positives were binned in a 10 by 15 matrix in y and p_T^2 for both the generated (raw) and the surviving (processed) events in the rapidity range $1.7 < y < 3.7$ and range of $0. < p_T^2 < 1.0$. The ratio of these matrices represented our acceptance and were used to correct the analyzed data in a 10 by 15 acceptance grid.

Figure 4.3 and figure 4.5 show the calculated rapidity (y) vs. transverse momentum (p_T^2) acceptance for negative tracks using pion mass and proton mass respectively. Figure 4.4 shows the acceptance for positive tracks using proton mass.

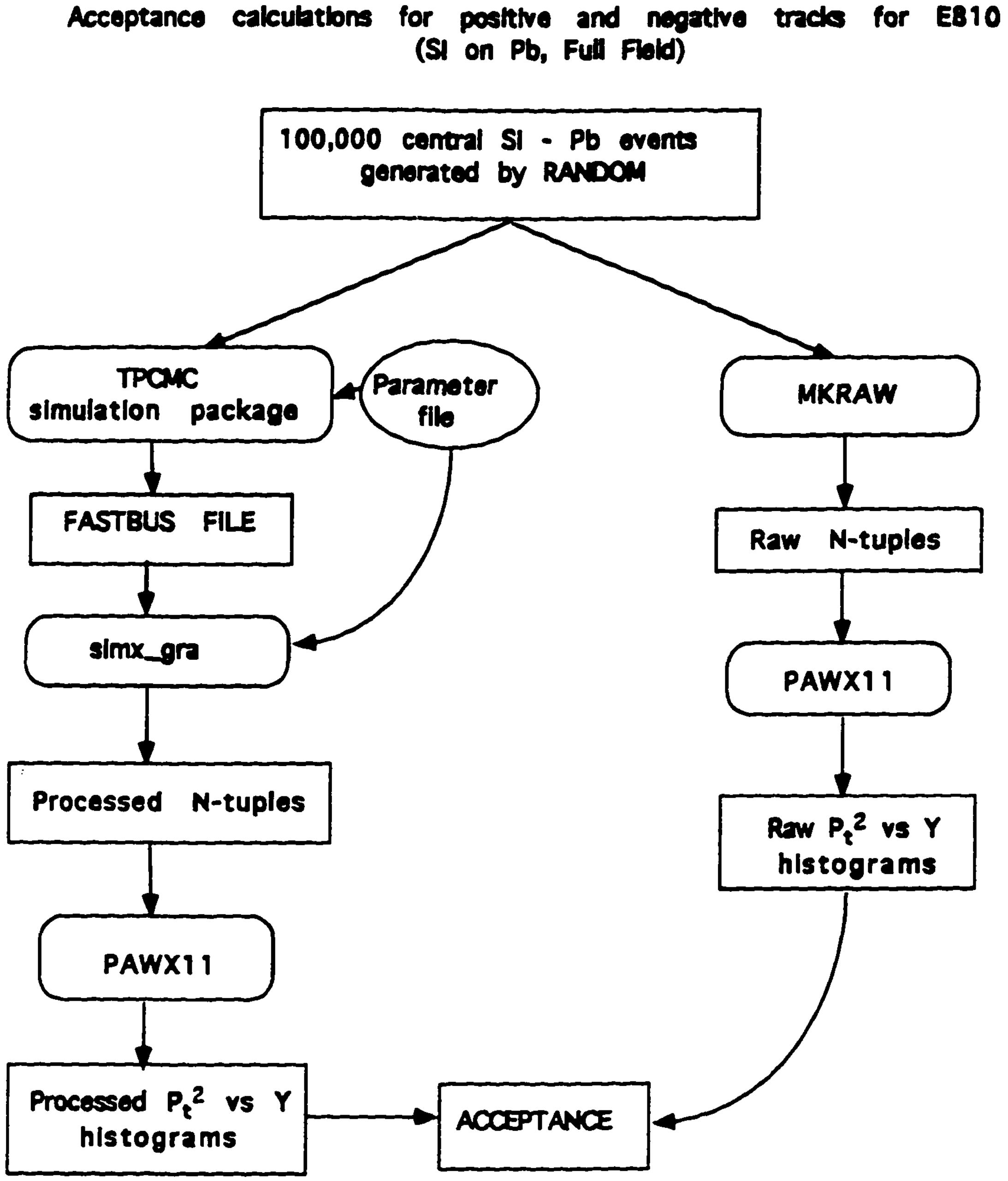

Figure 4.1: General procedure to determine acceptance.

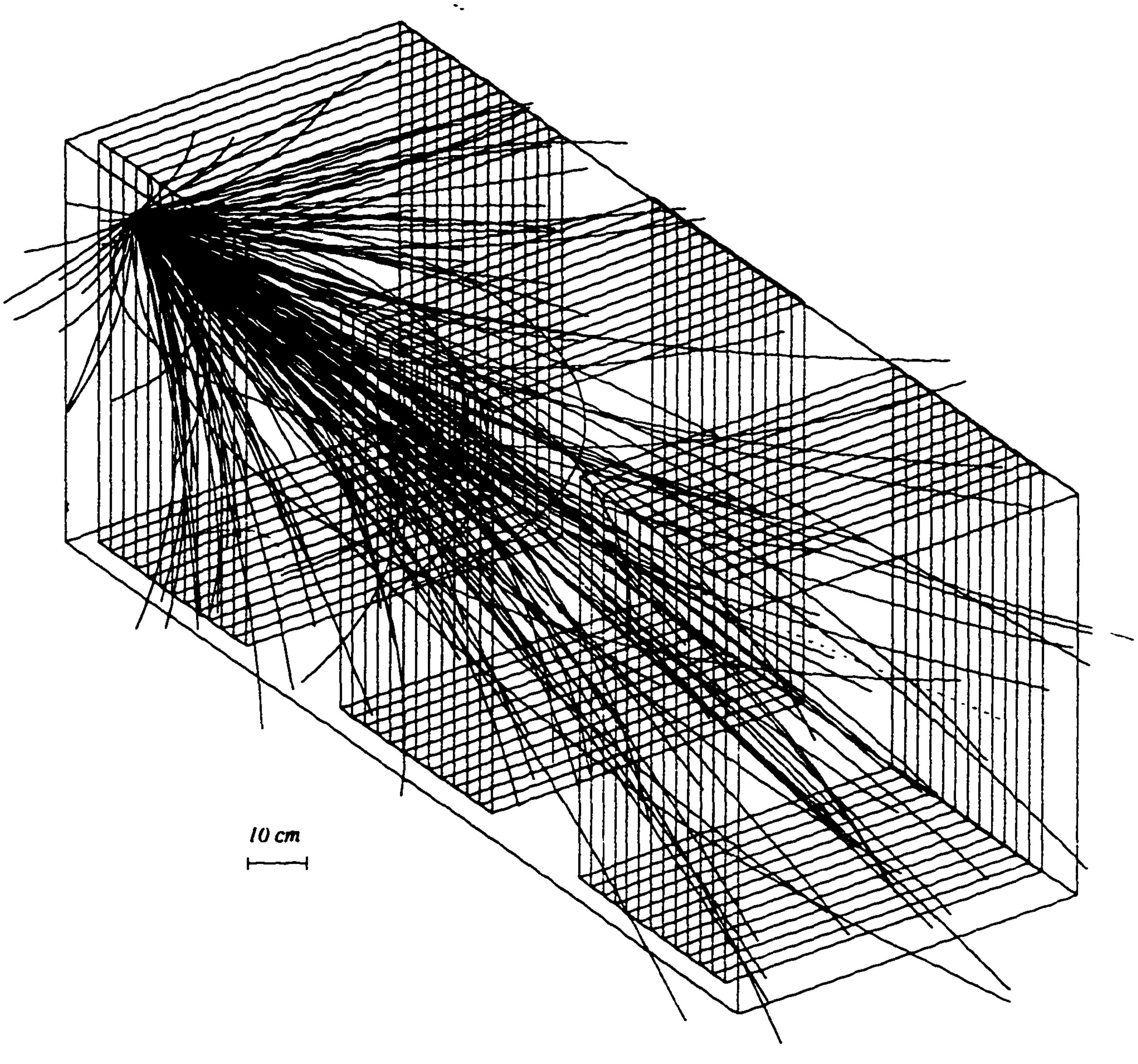

Figure 4.2: A Si on Pb event generated by HIJET in our detector. The tracks of the particles and the detector were simulated using GEANT3.21

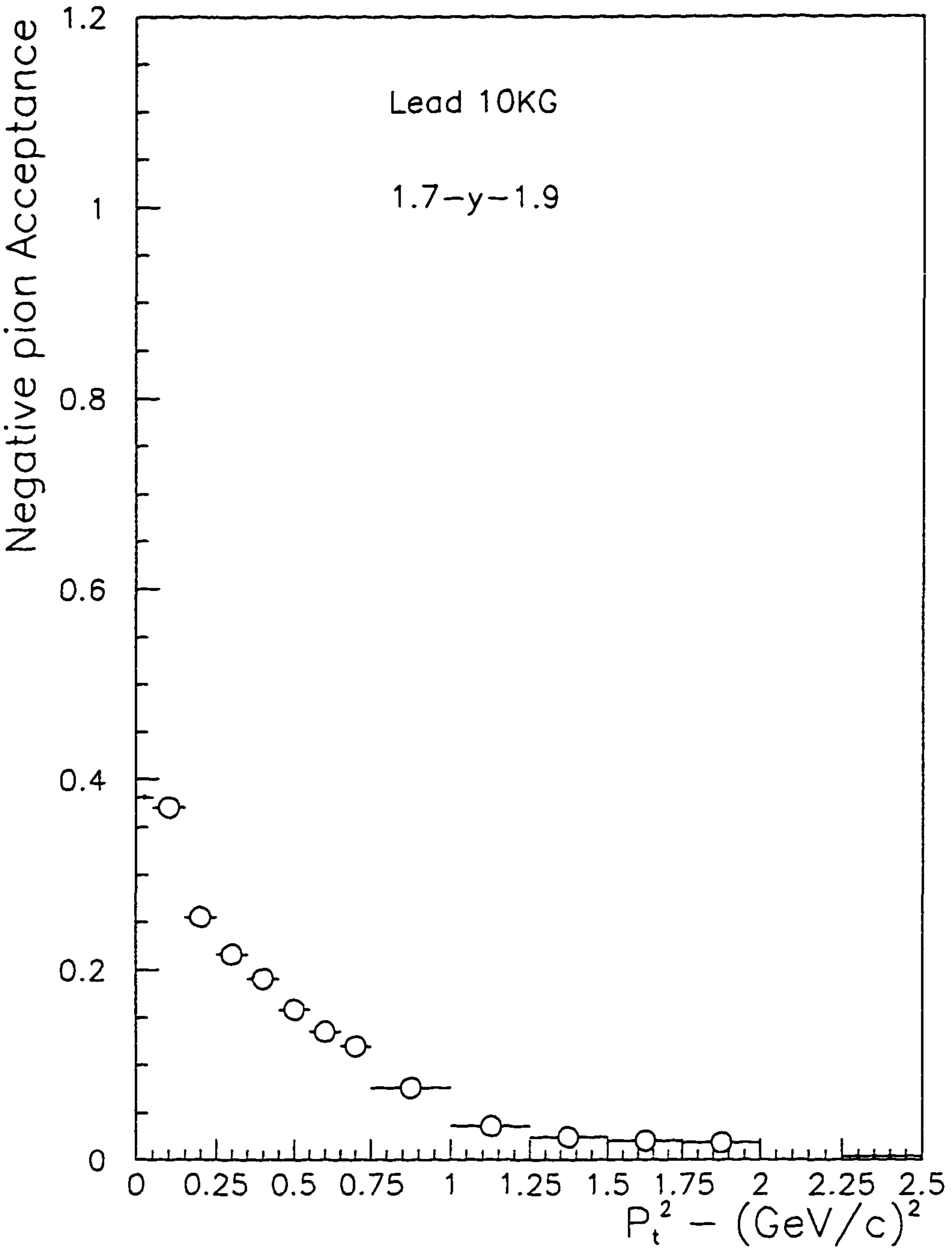

Figure 4.3: Acceptance of negative tracks using the pion mass to calculate their rapidity.

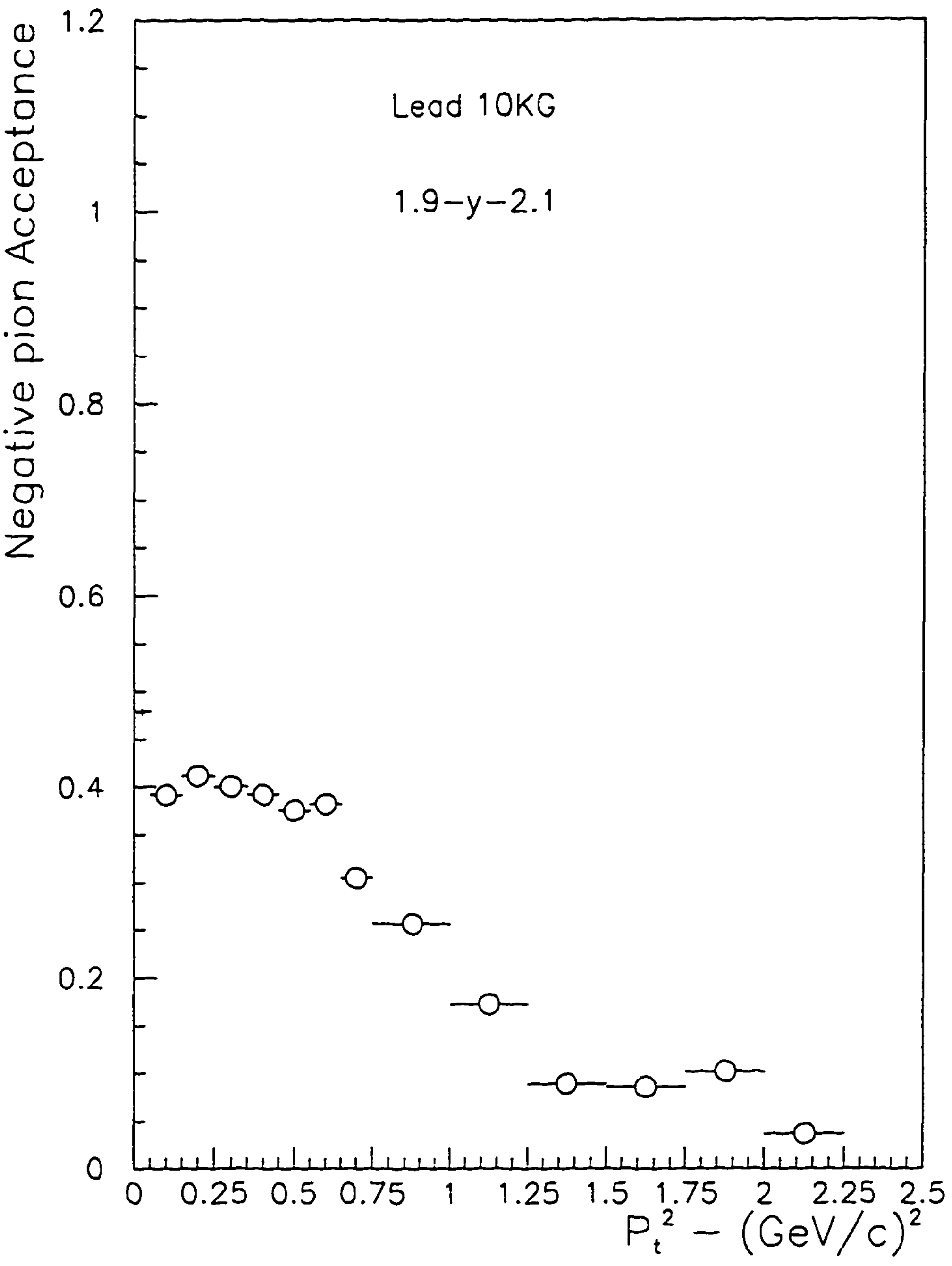

Figure 4.3 (continued)

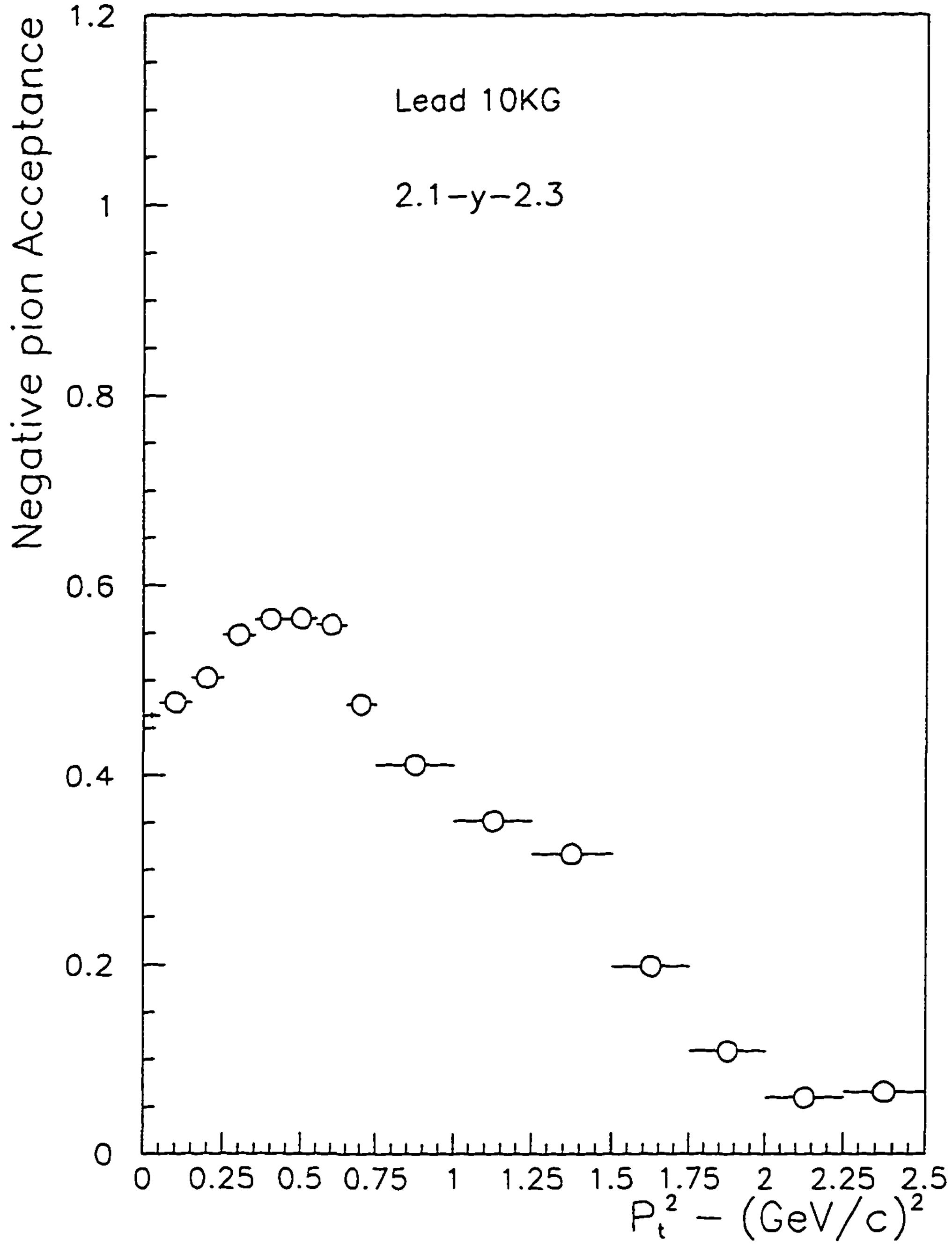

Figure 4.3 (continued)

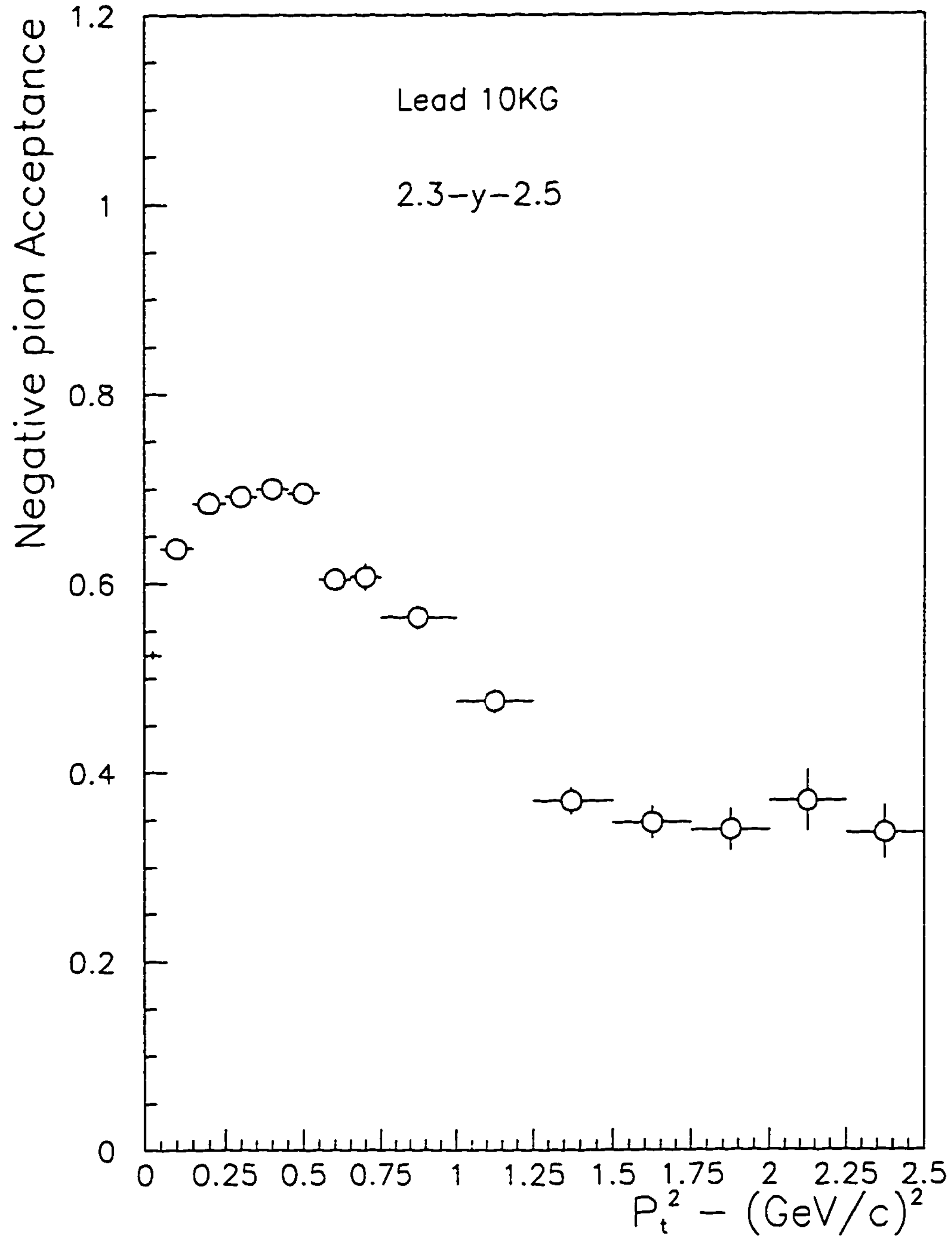

Figure 4.3 (continued)

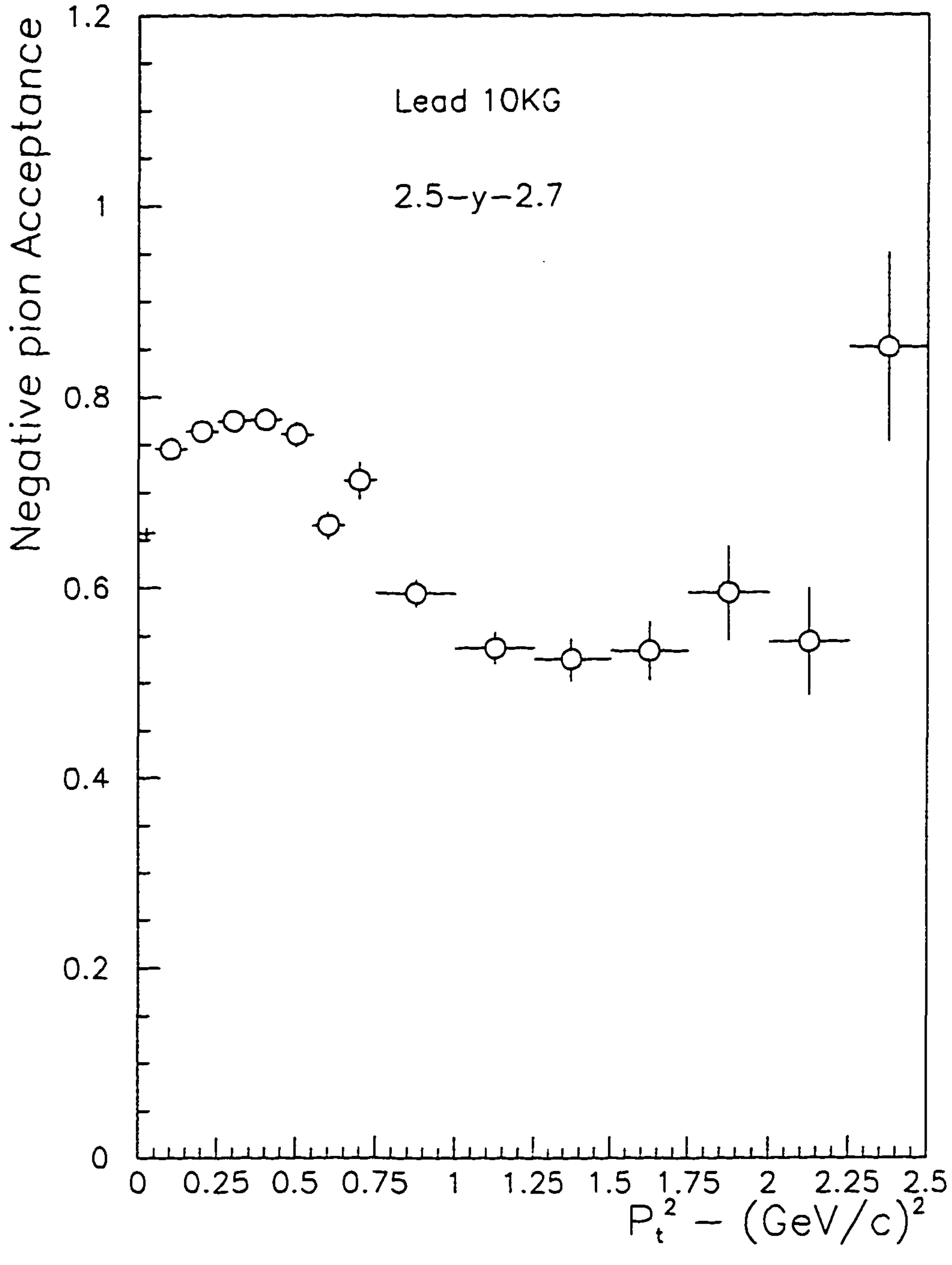

Figure 4.3 (continued)

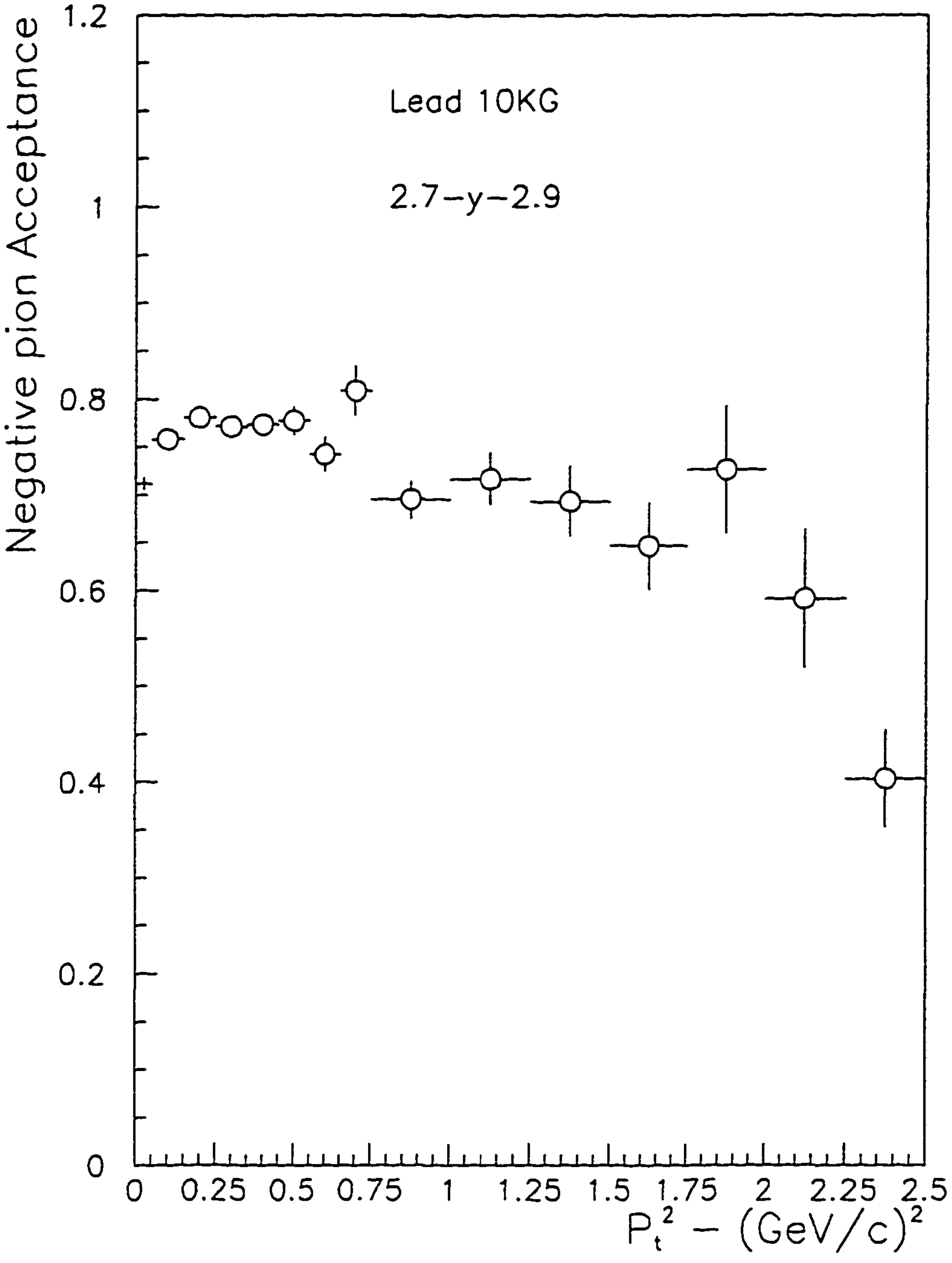

Figure 4.3 (continued)

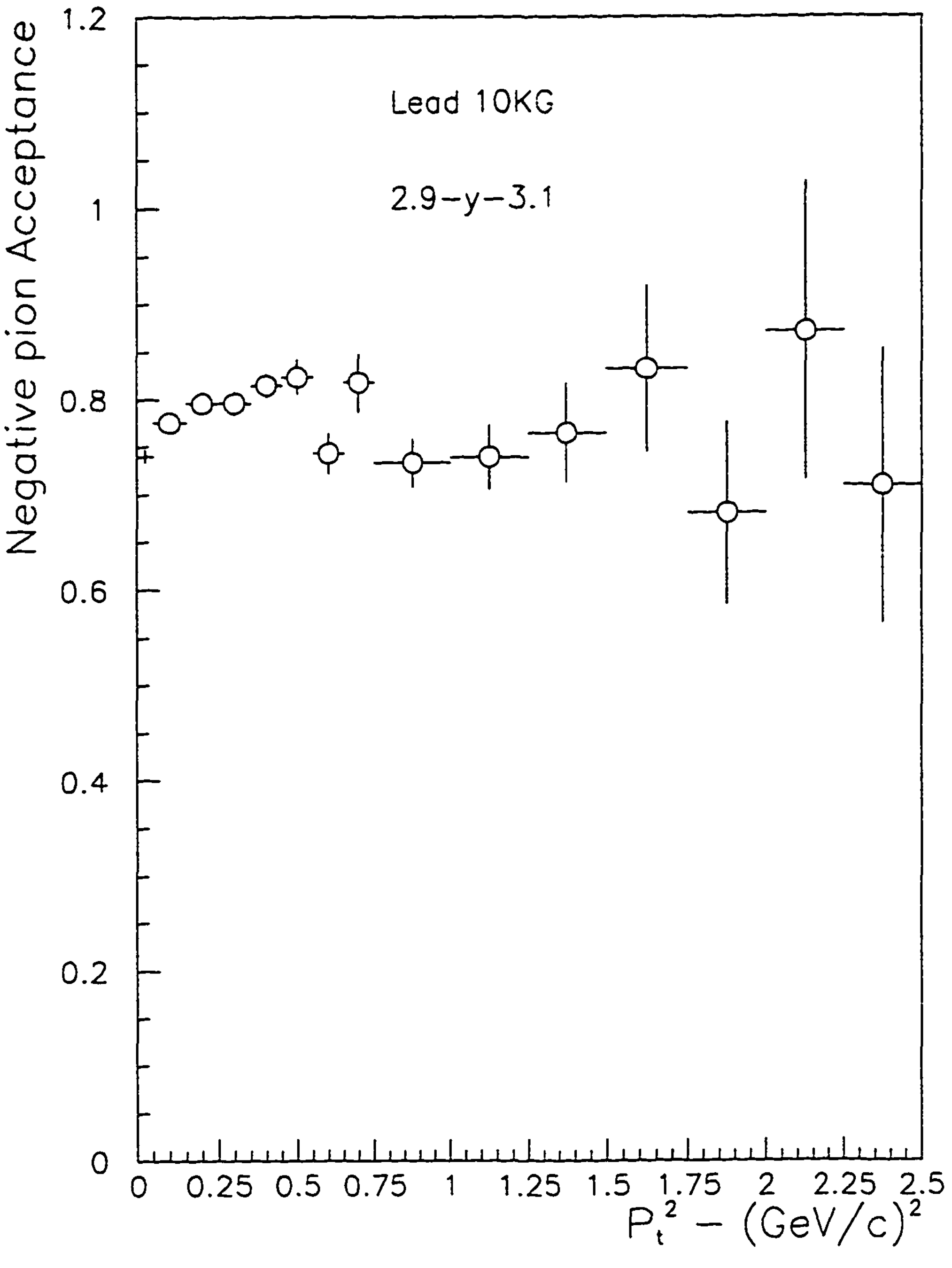

Figure 4.3 (continued)

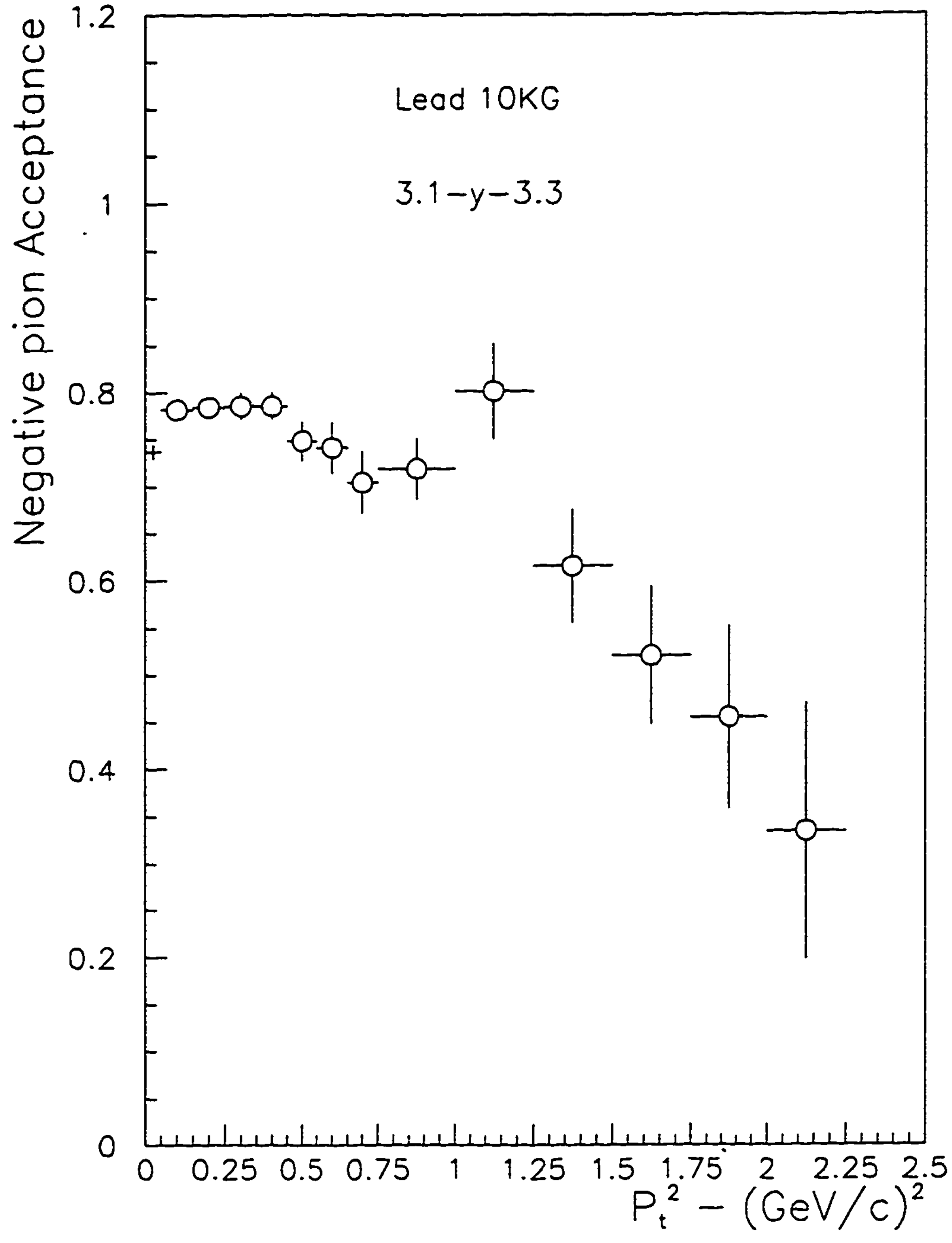

Figure 4.3 (continued)

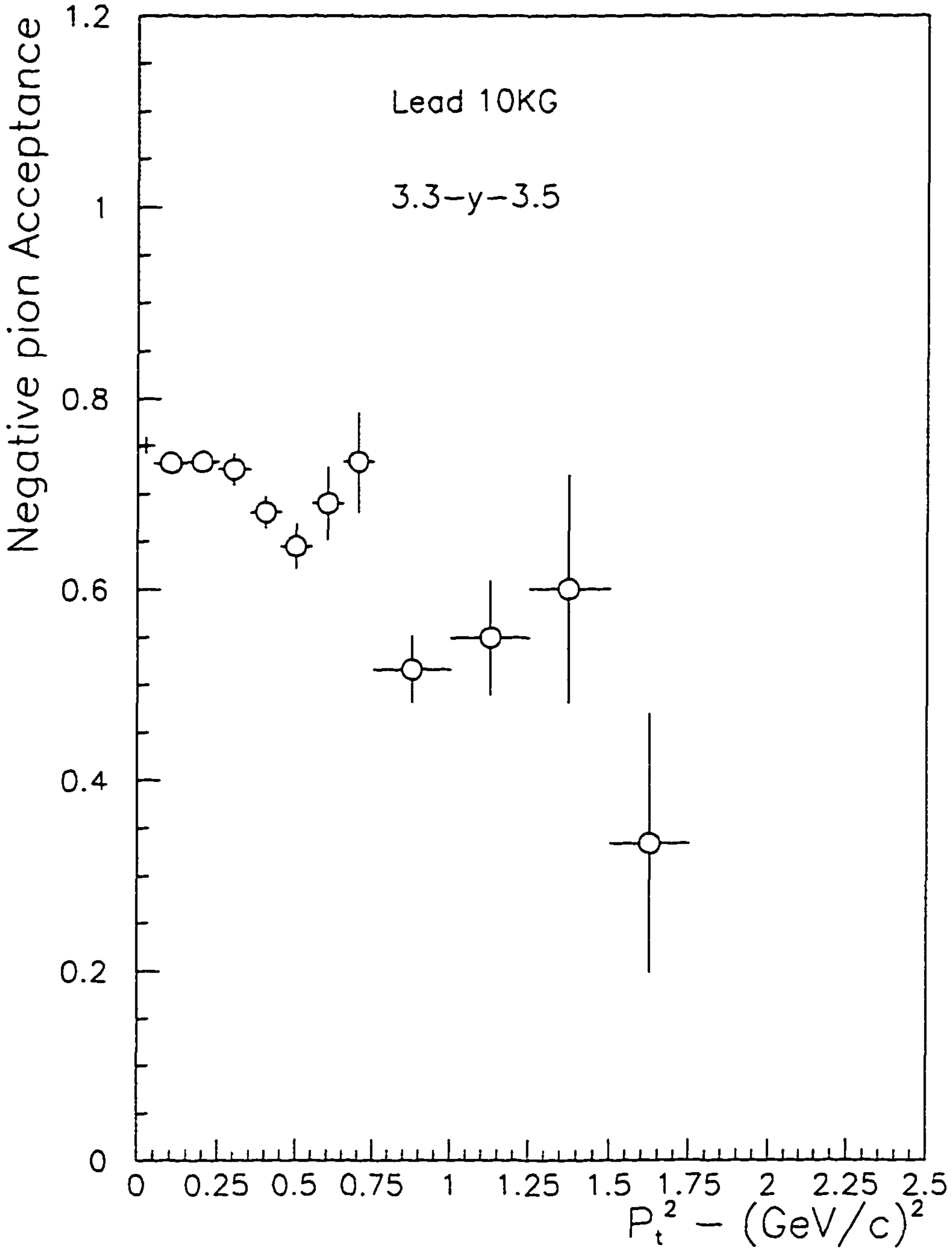

Figure 4.3 (continued)

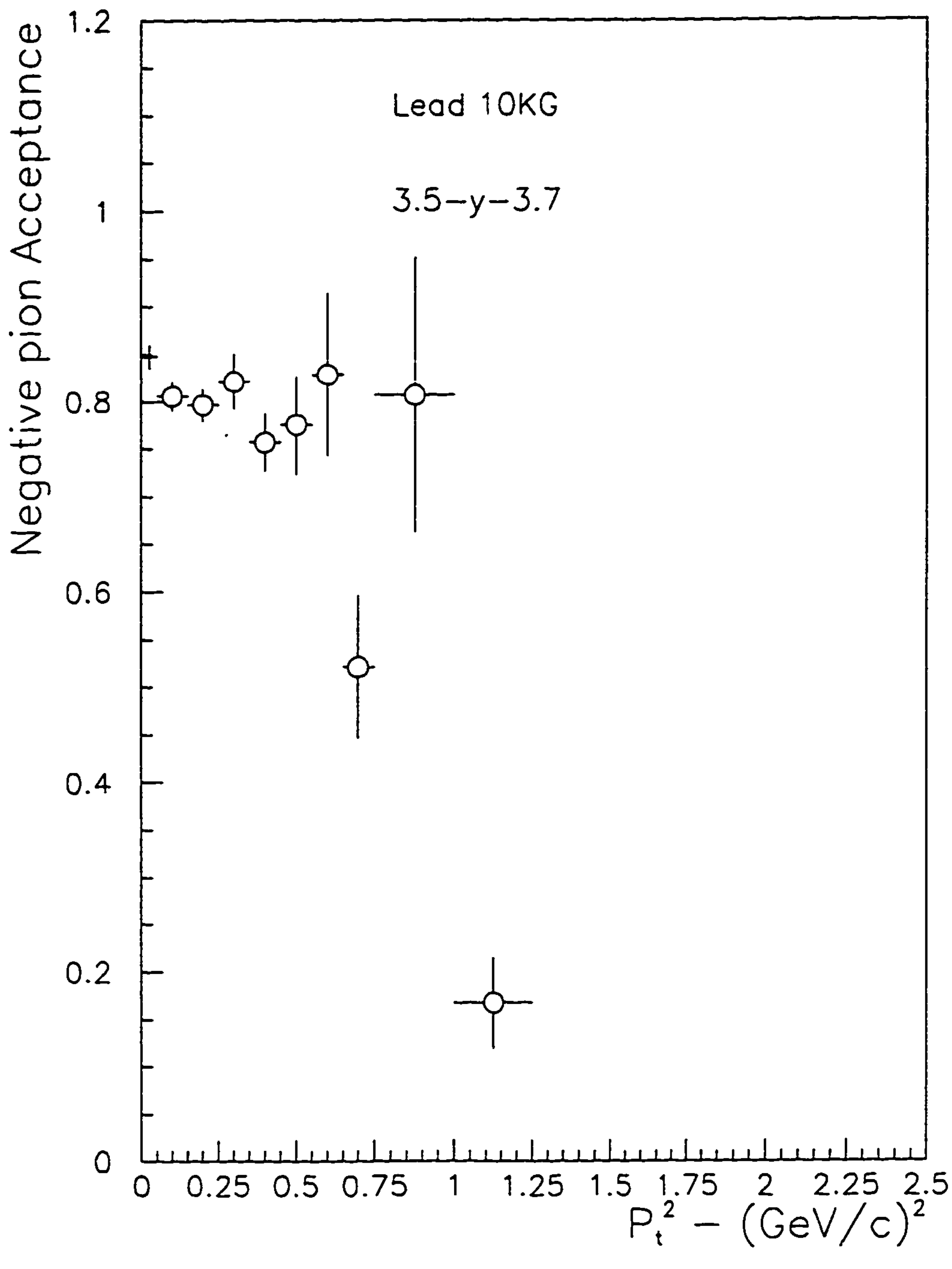

Figure 4.3 (continued)

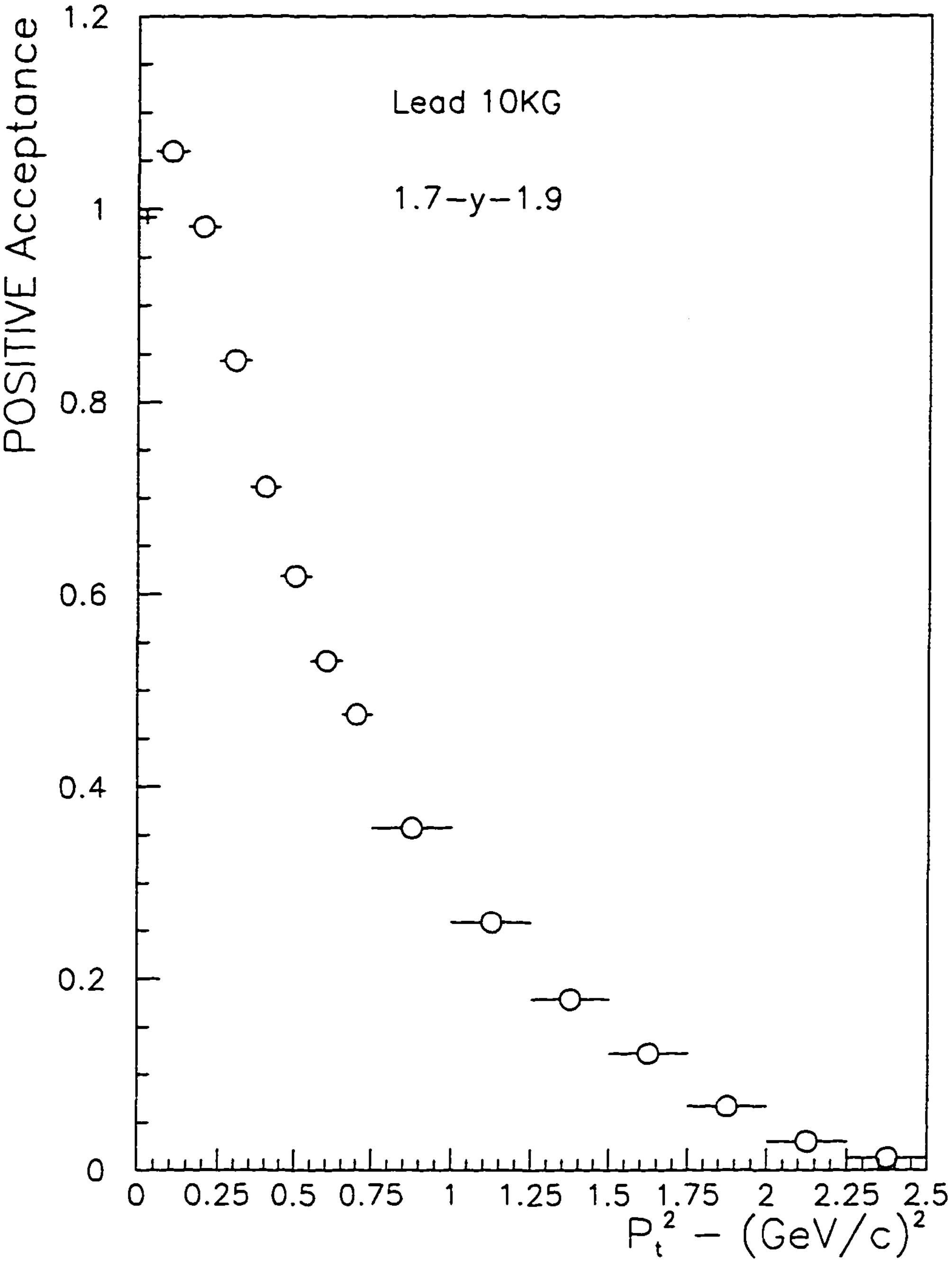

Figure 4.4: Acceptance of positive tracks using the proton mass to calculate rapidity

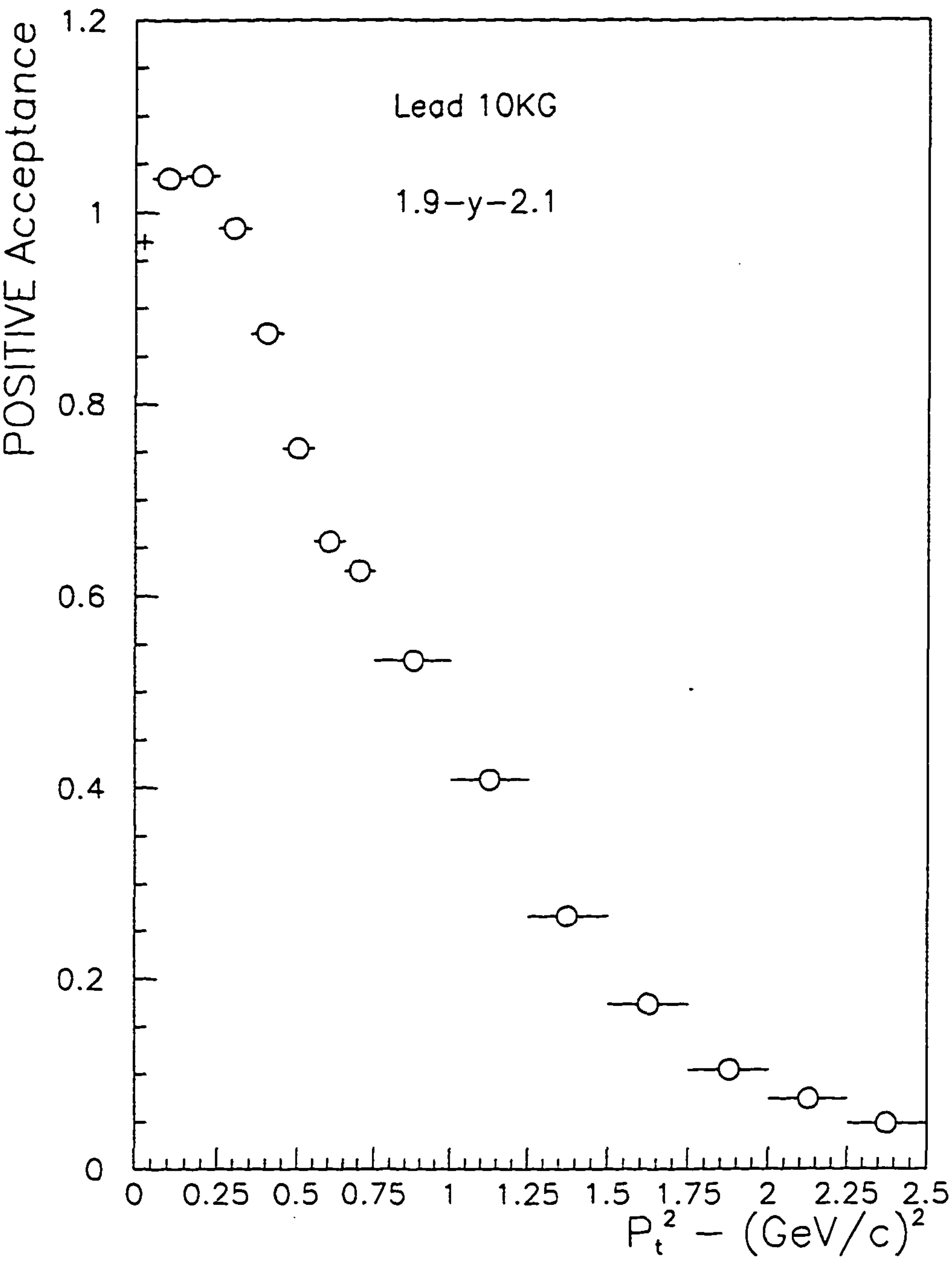

Figure 4.4 (continued)

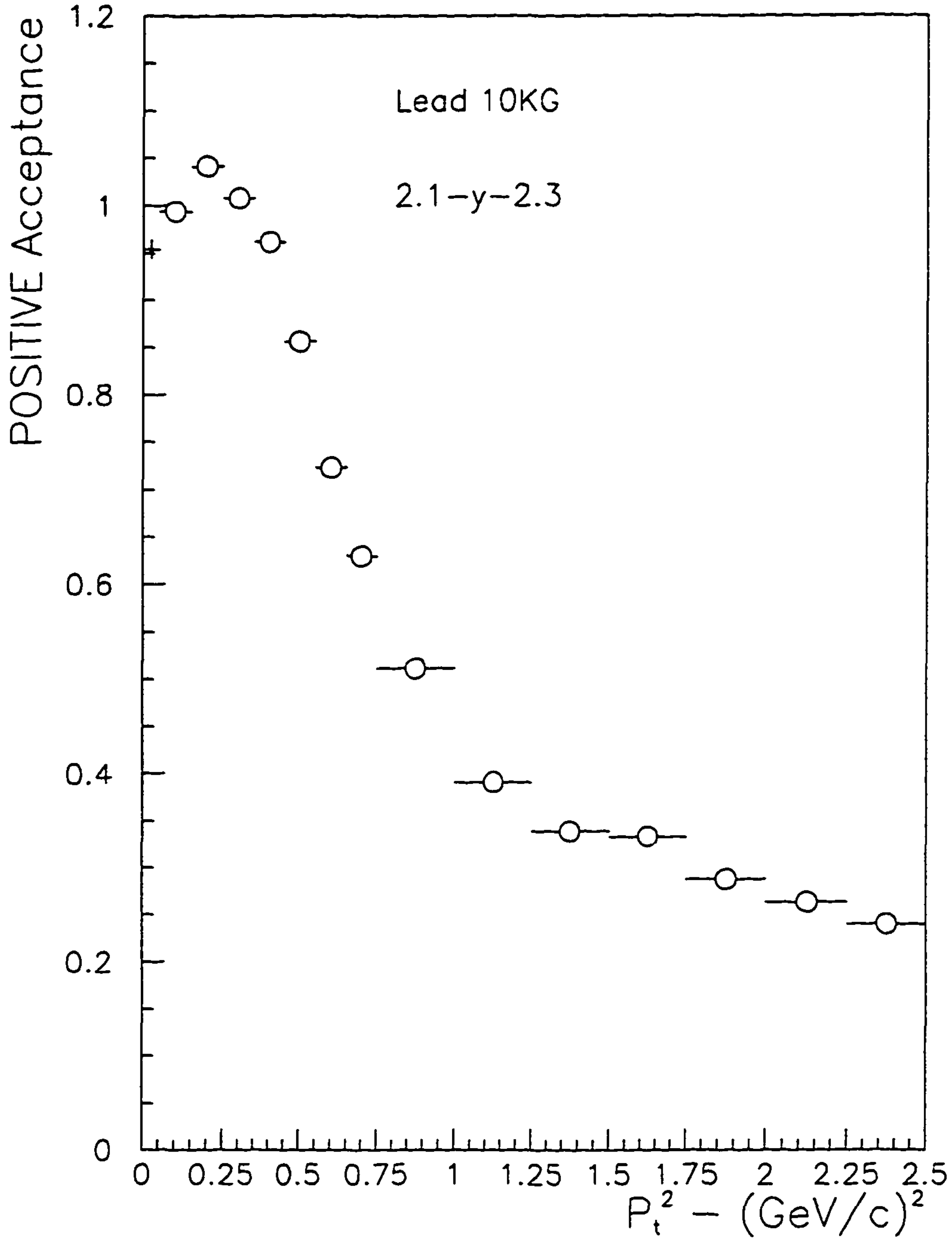

Figure 4.4 (continued)

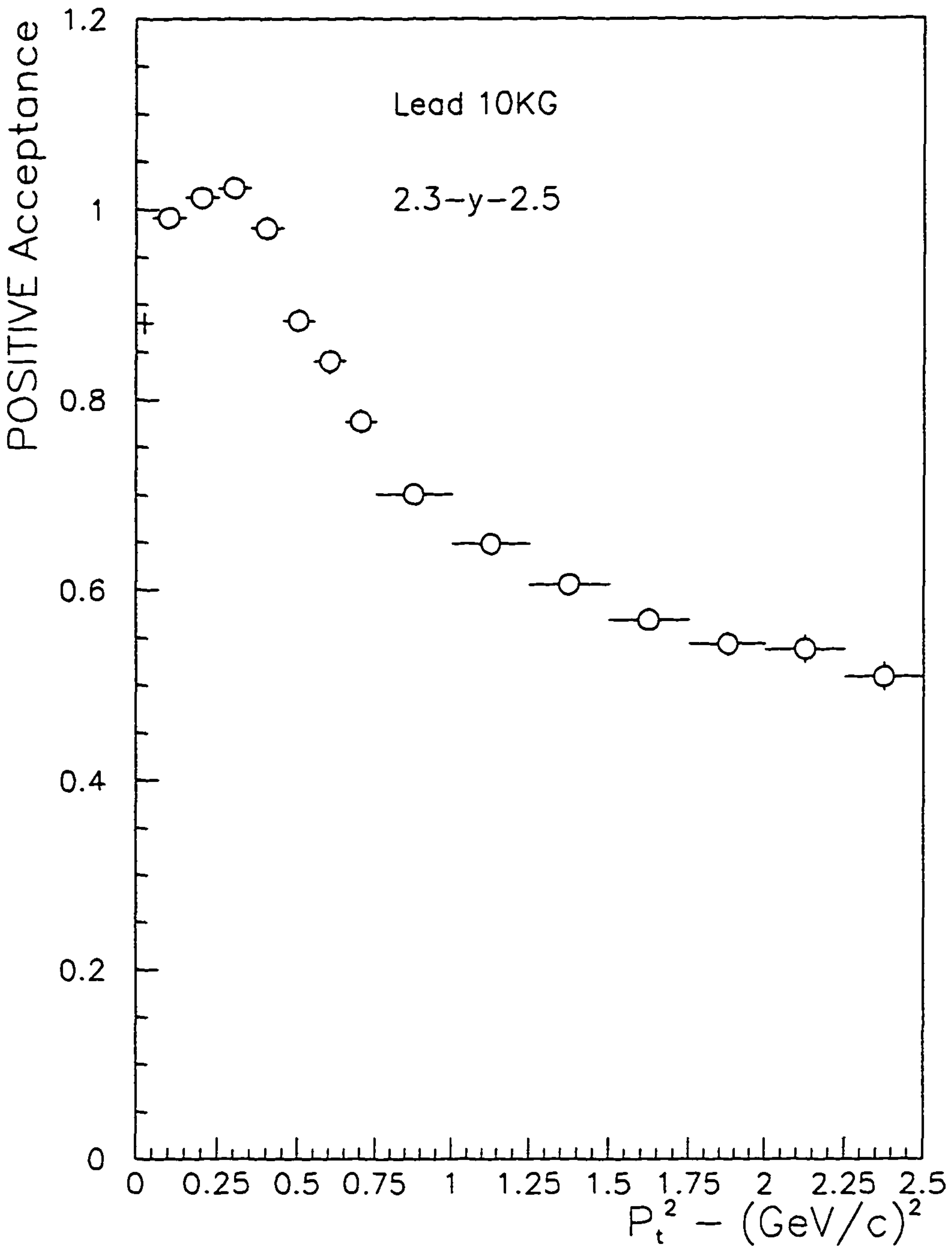

Figure 4.4 (continued)

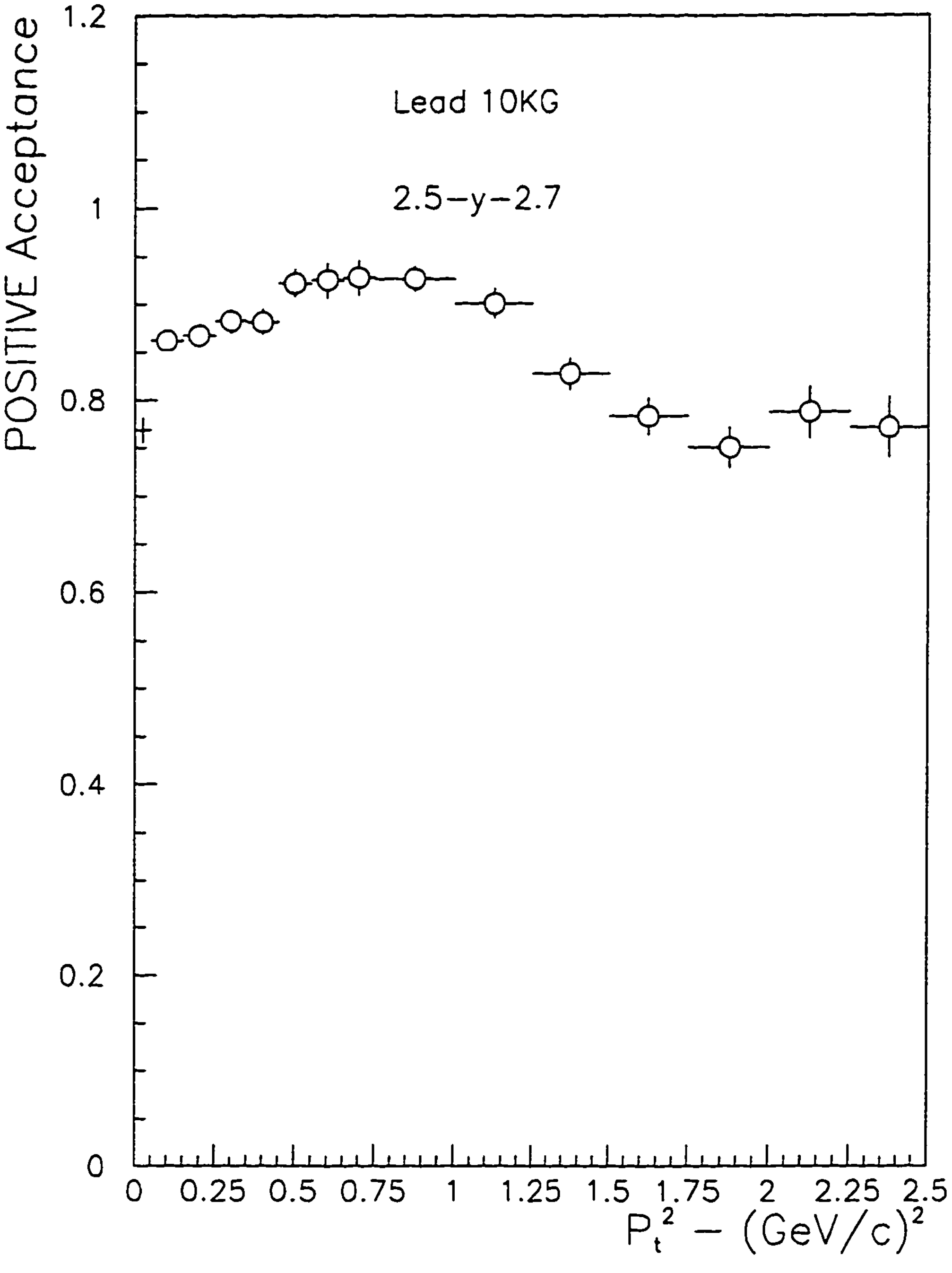

Figure 4.4 (continued)

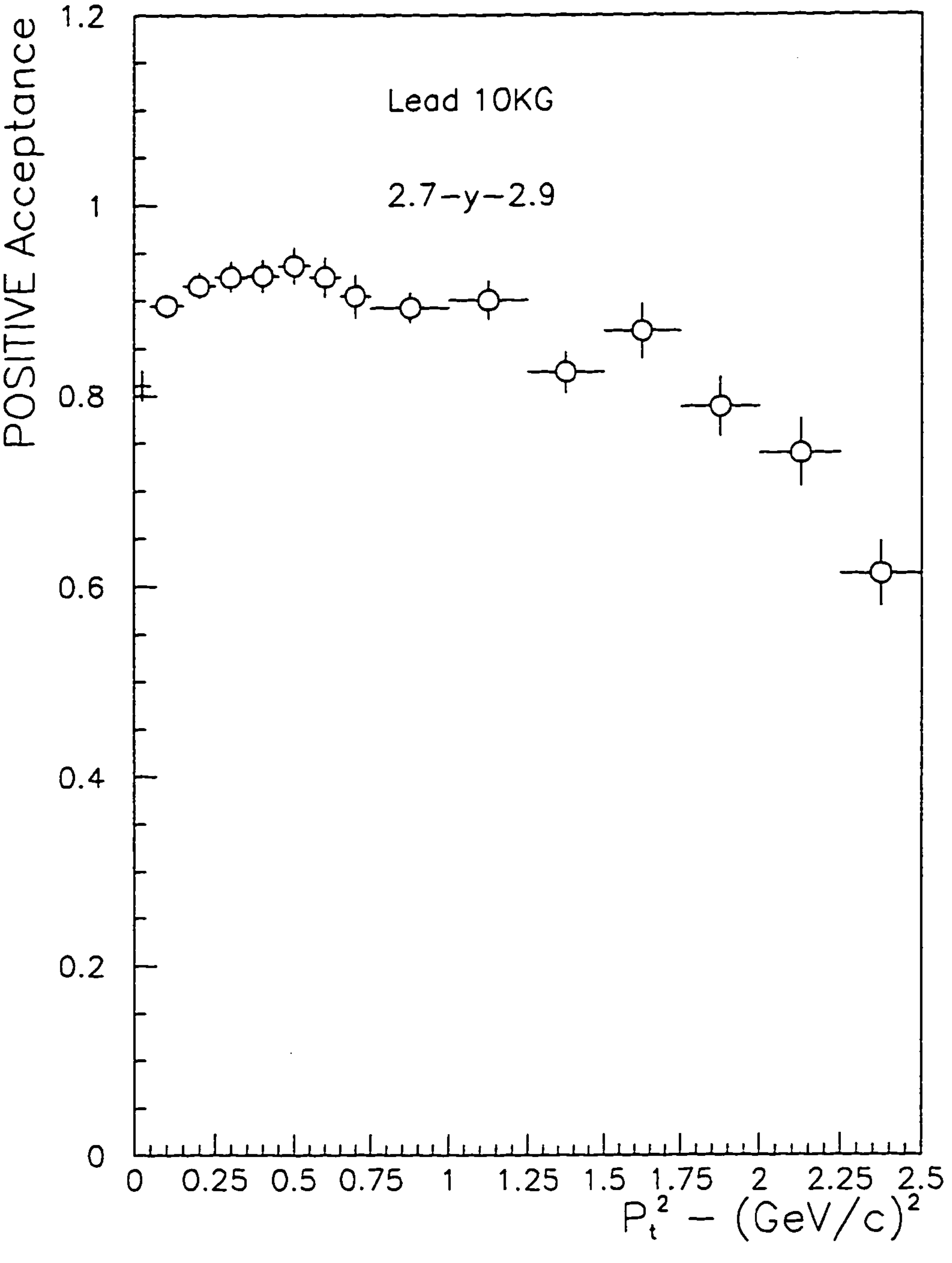

Figure 4.4 (continued)

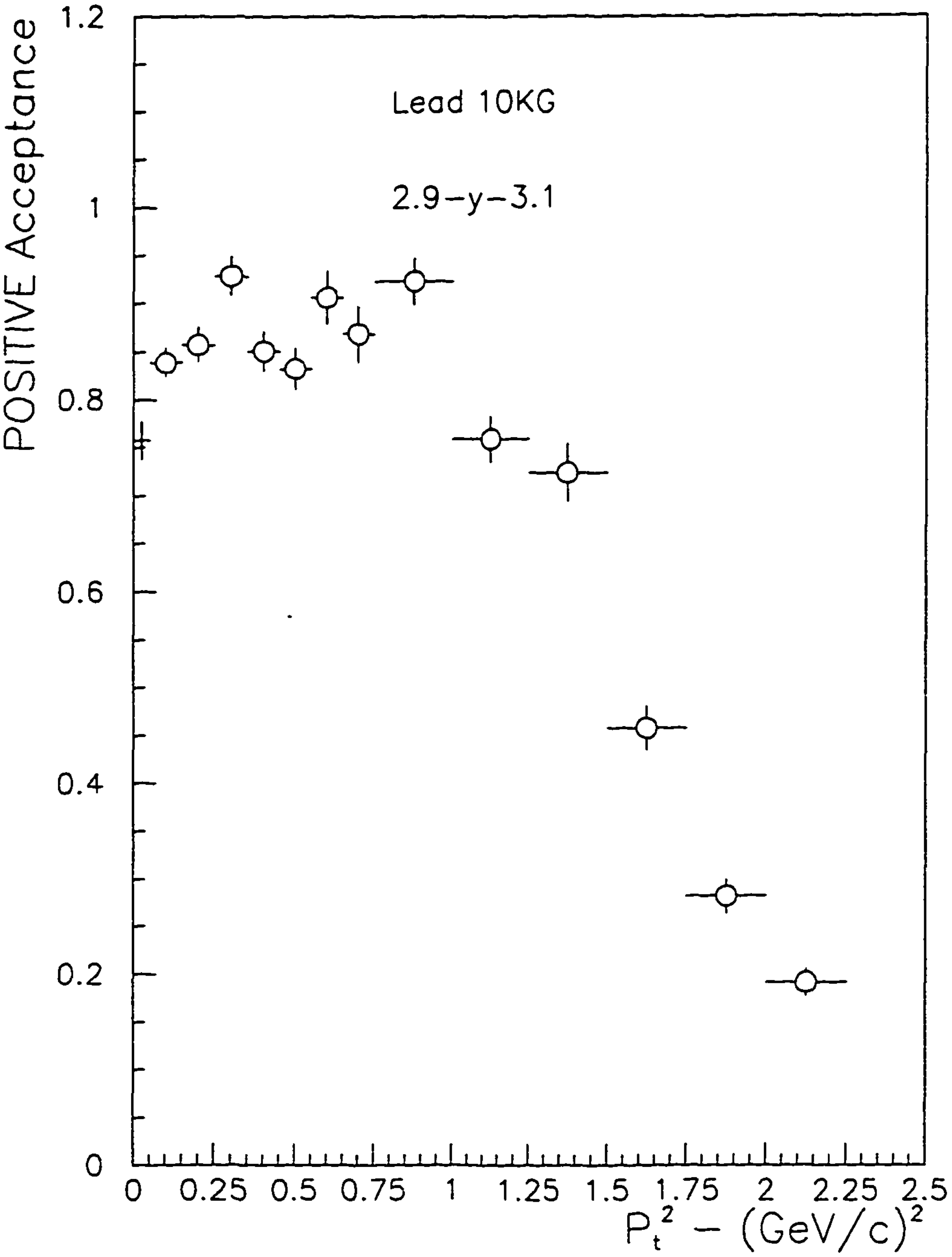

Figure 4.4 (continued)

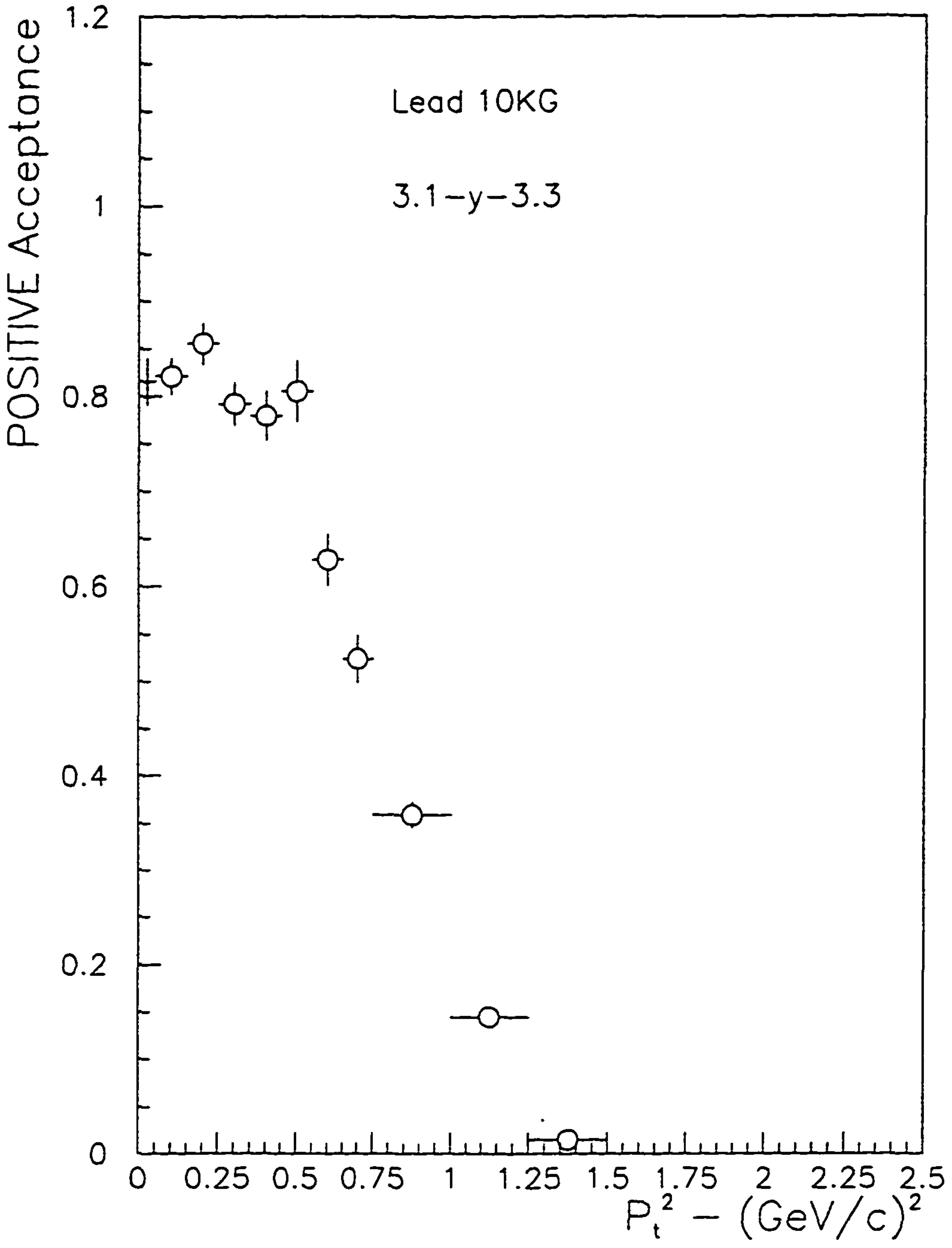

Figure 4.4 (continued)

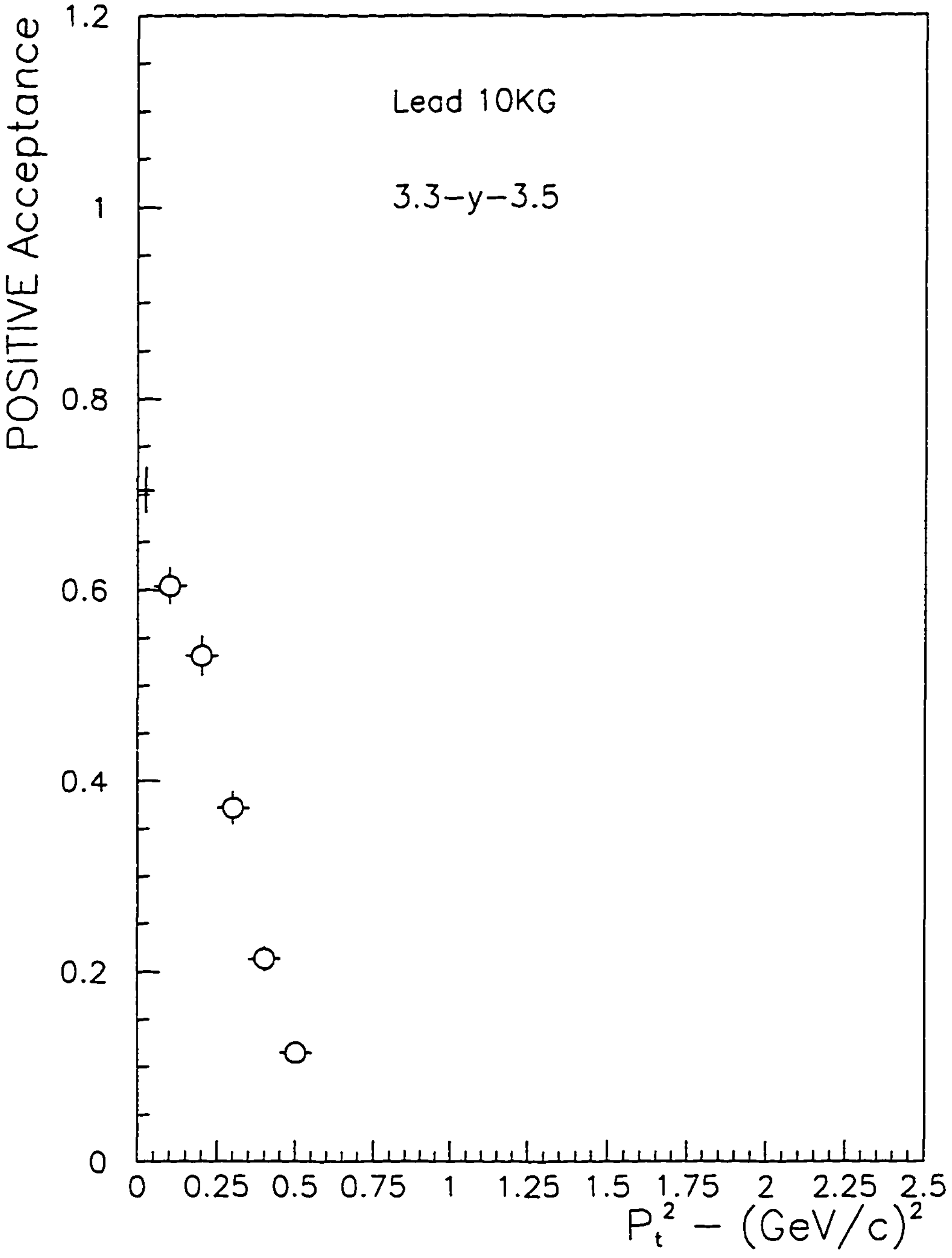

Figure 4.4 (continued)

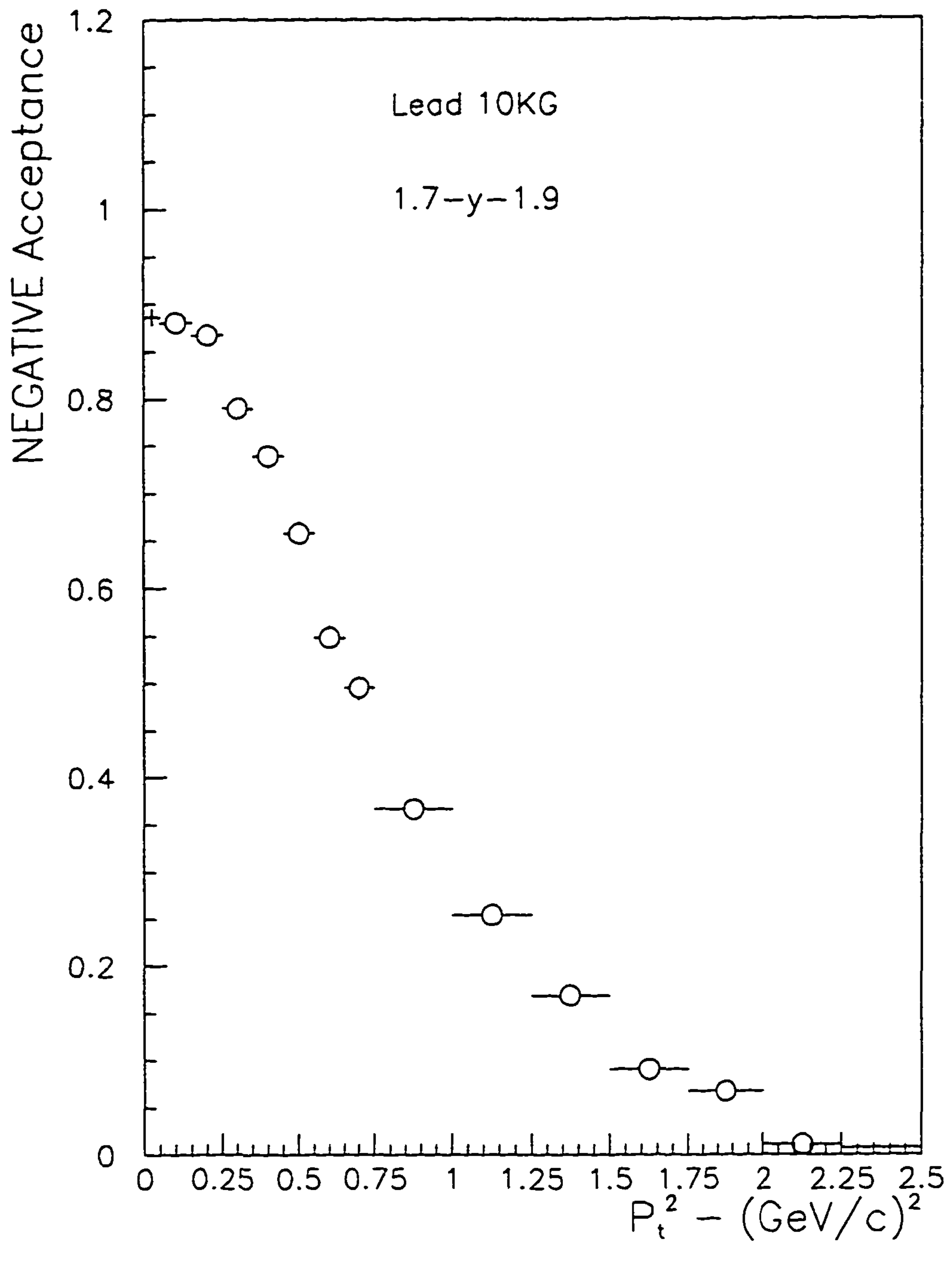

Figure 4.5: Acceptance of negative tracks using the proton mass to calculate their rapidity

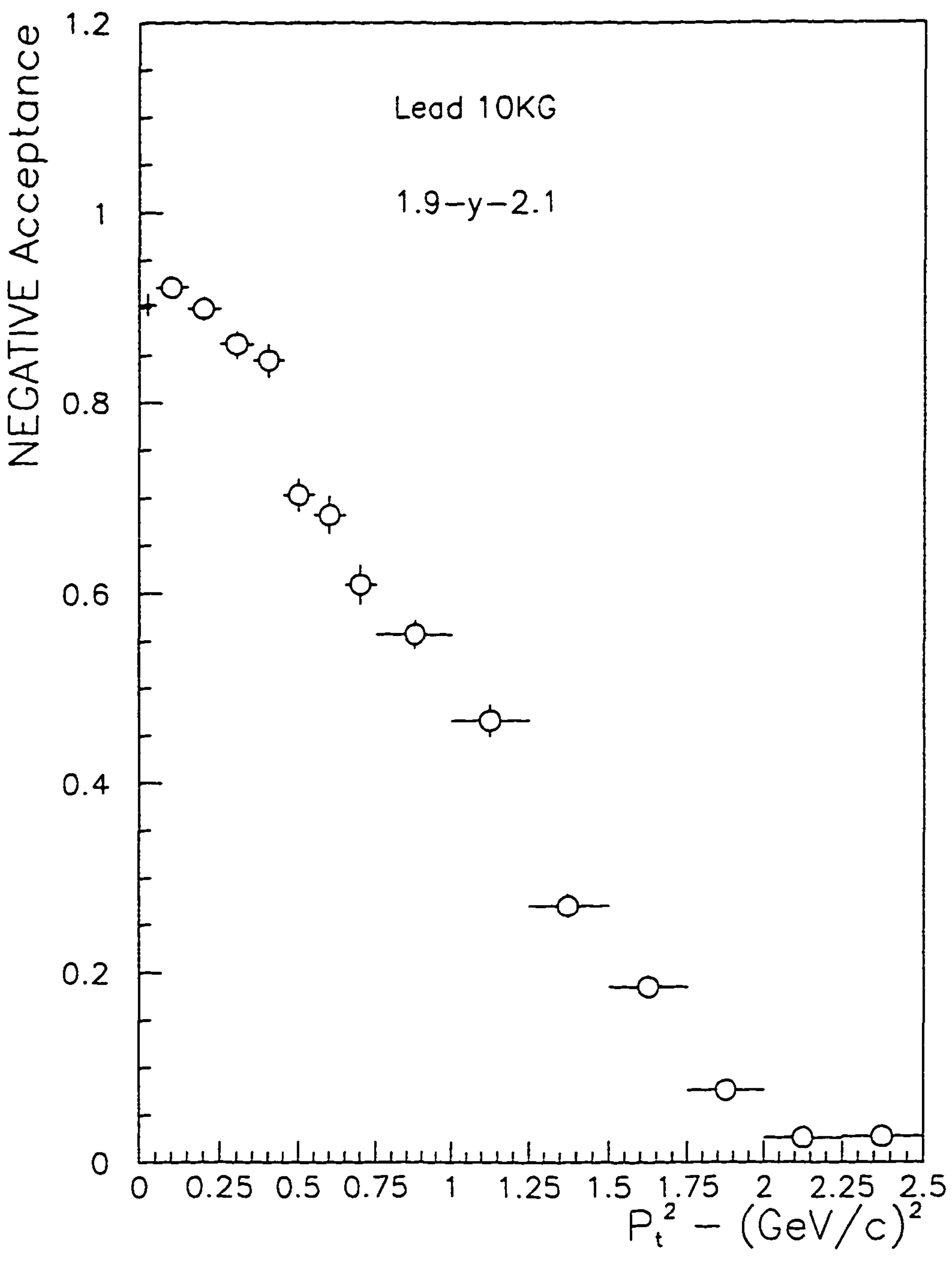

Figure 4.5 (continued)

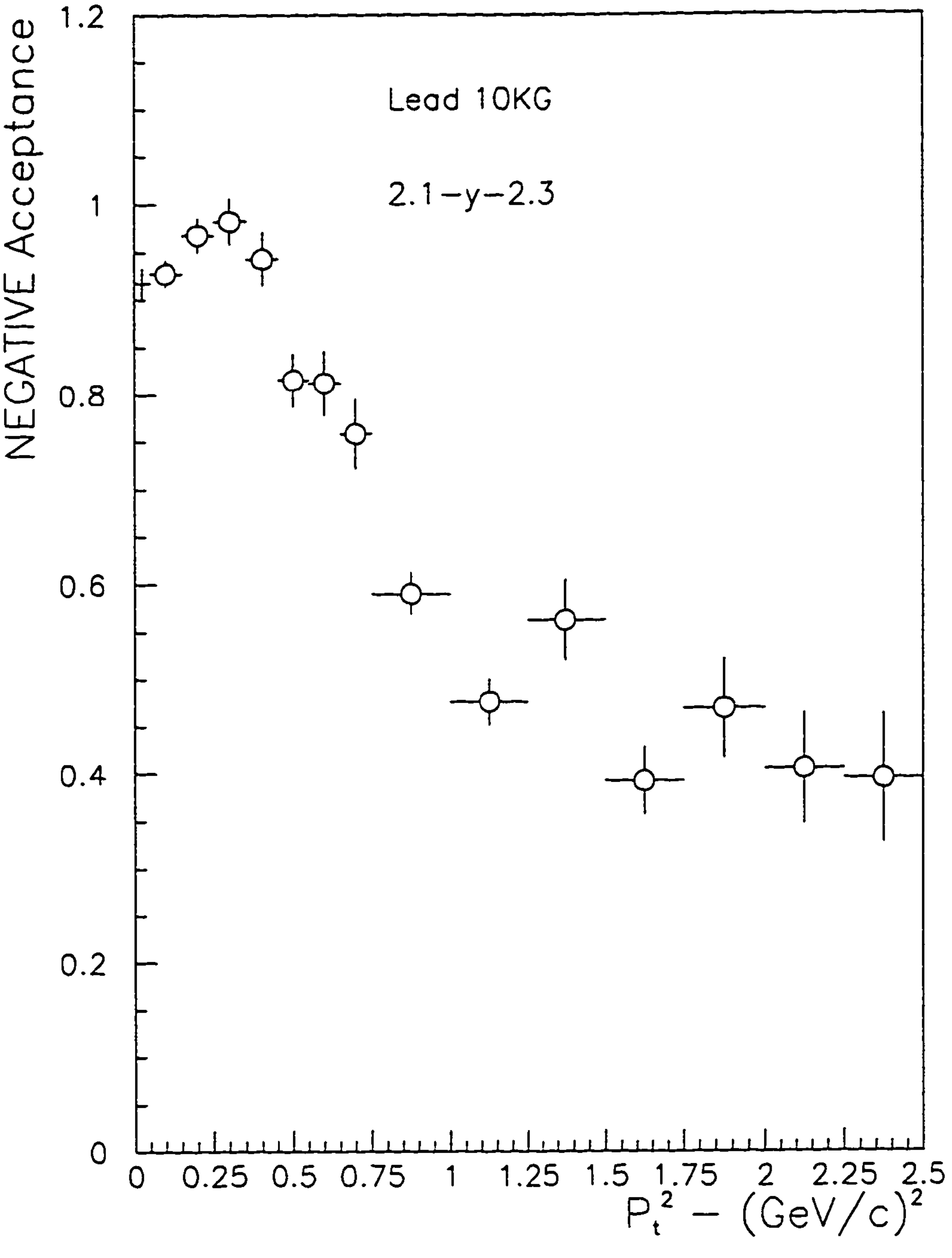

Figure 4.5 (continued)

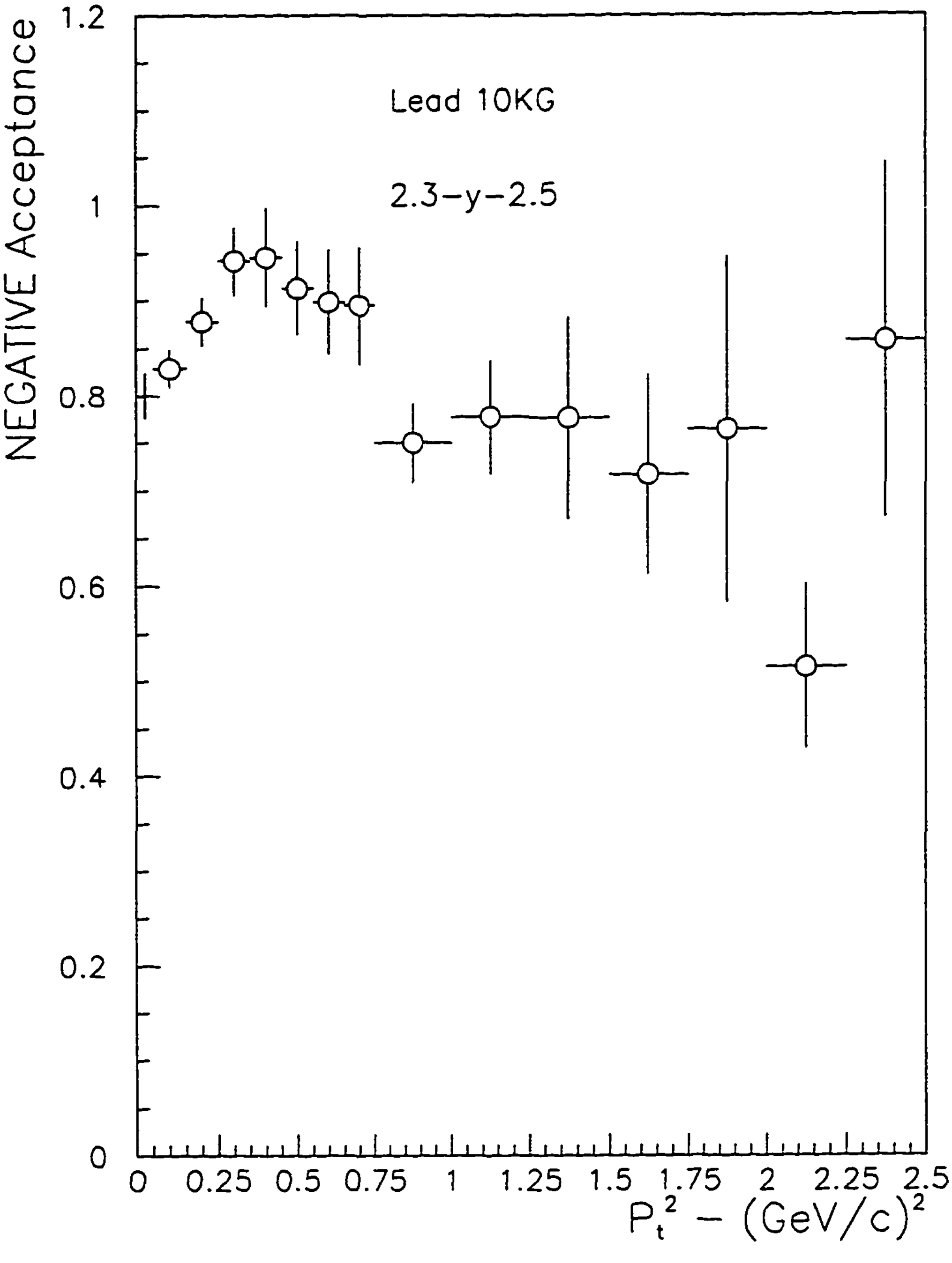

Figure 4.5 (continued)

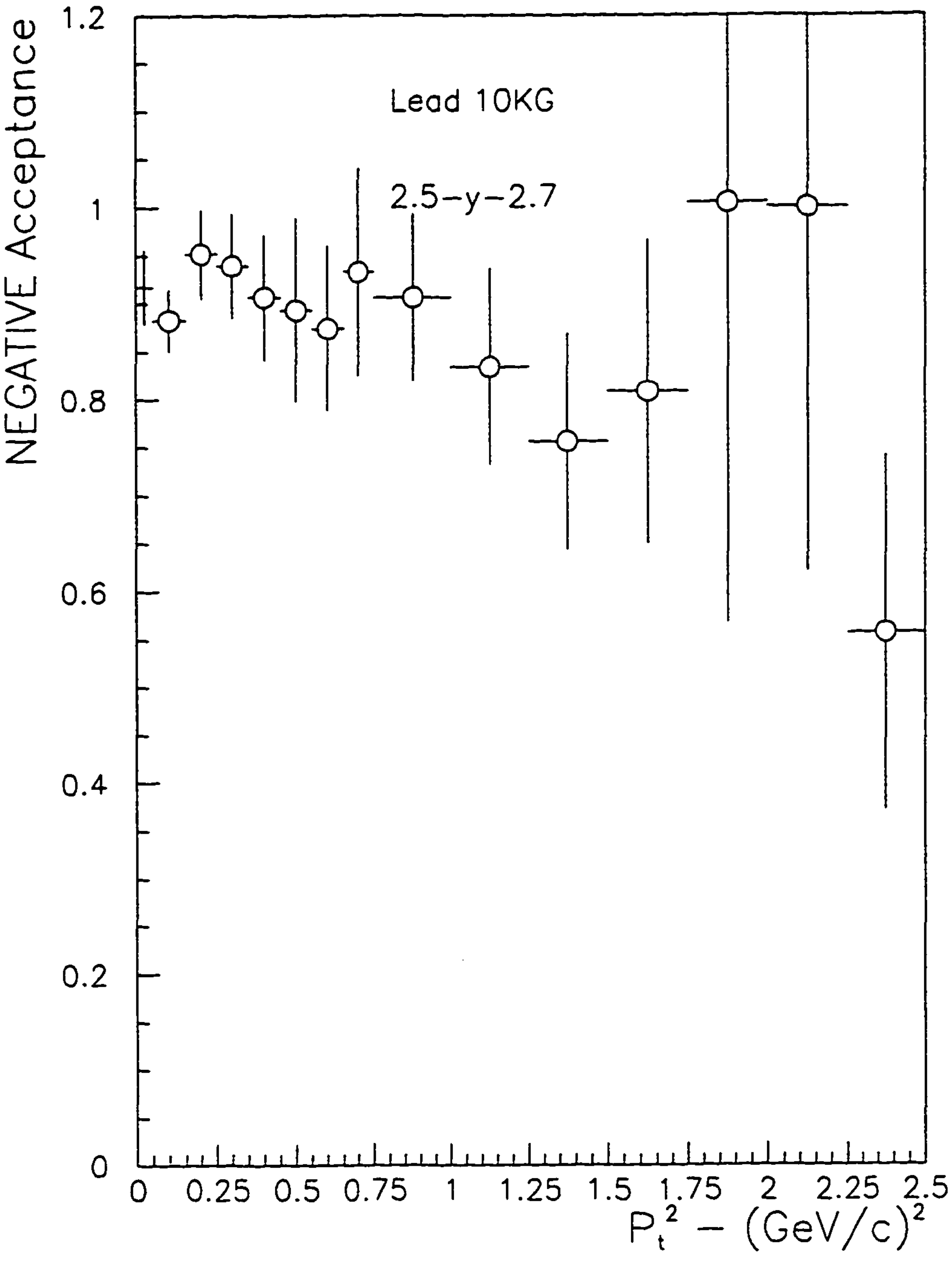

Figure 4.5 (continued)

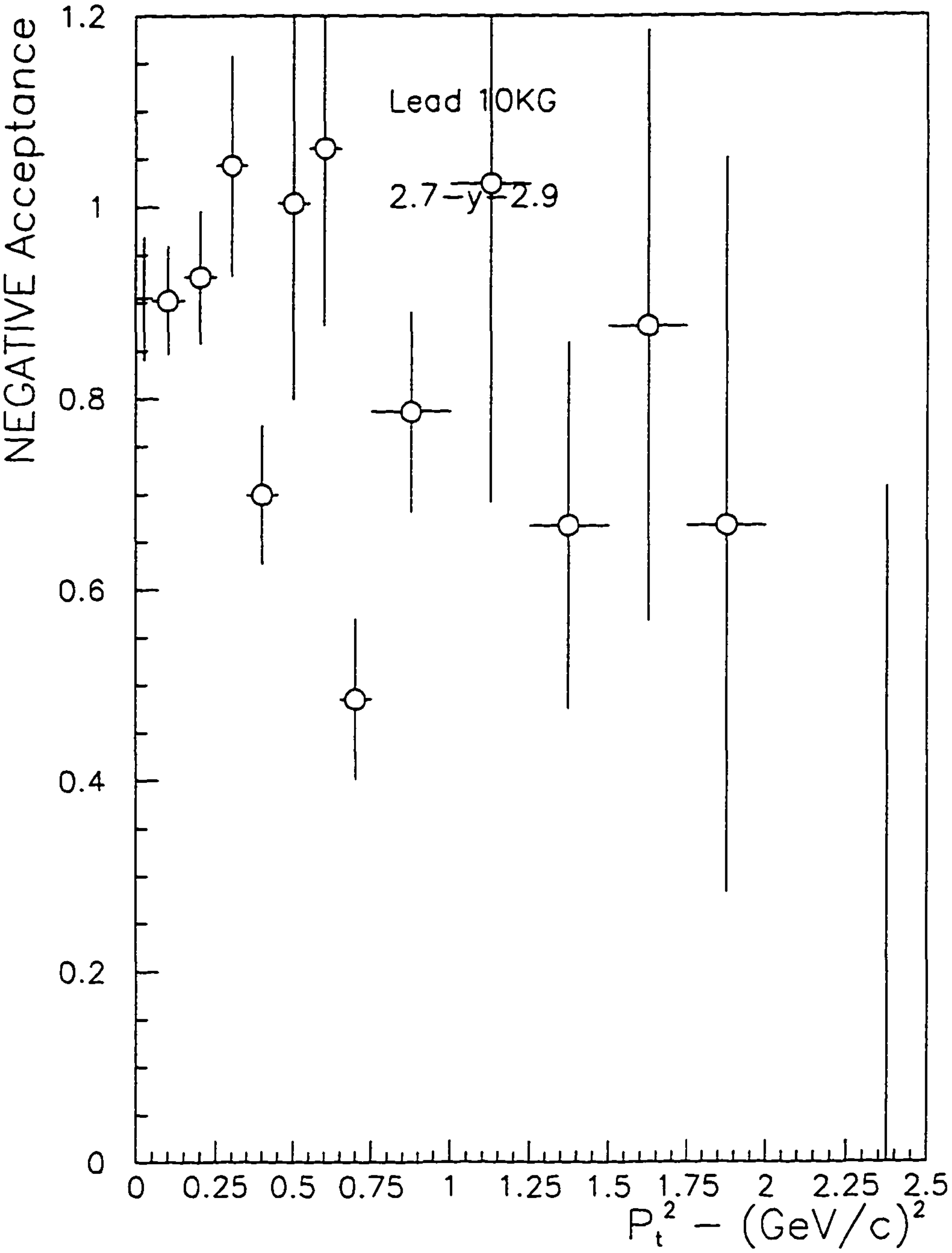

Figure 4.5 (continued)

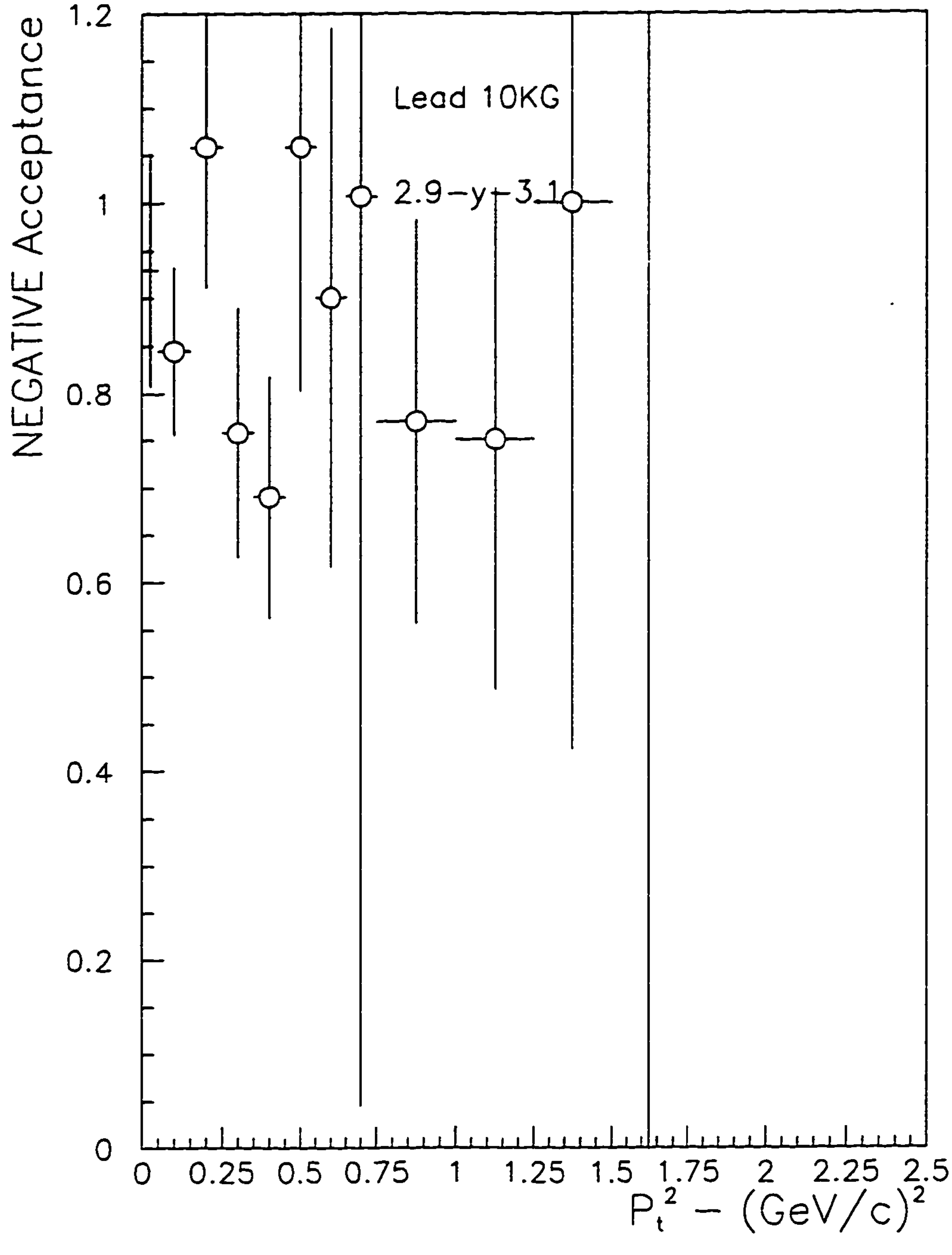

Figure 4.5 (continued)

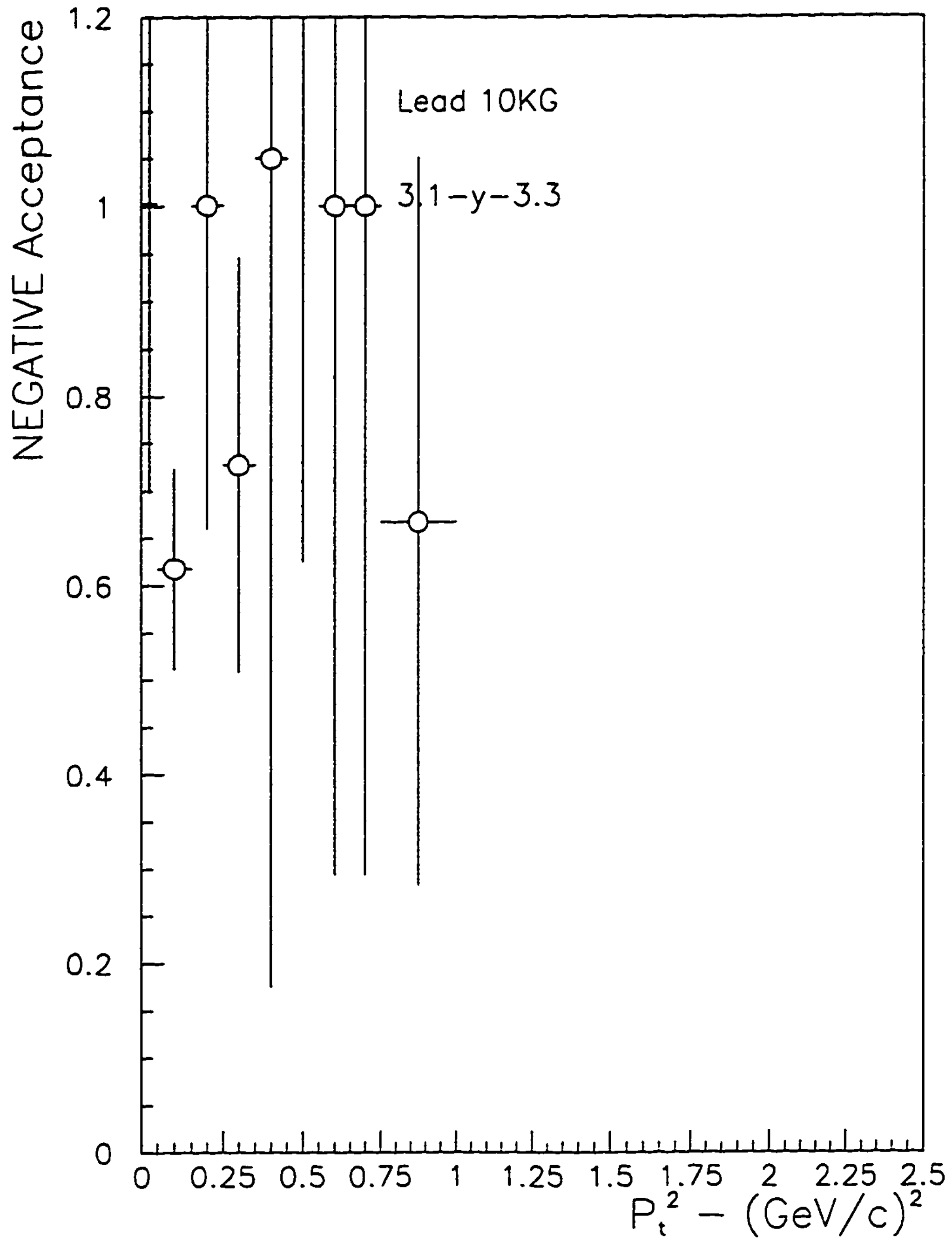

Figure 4.5 (continued)

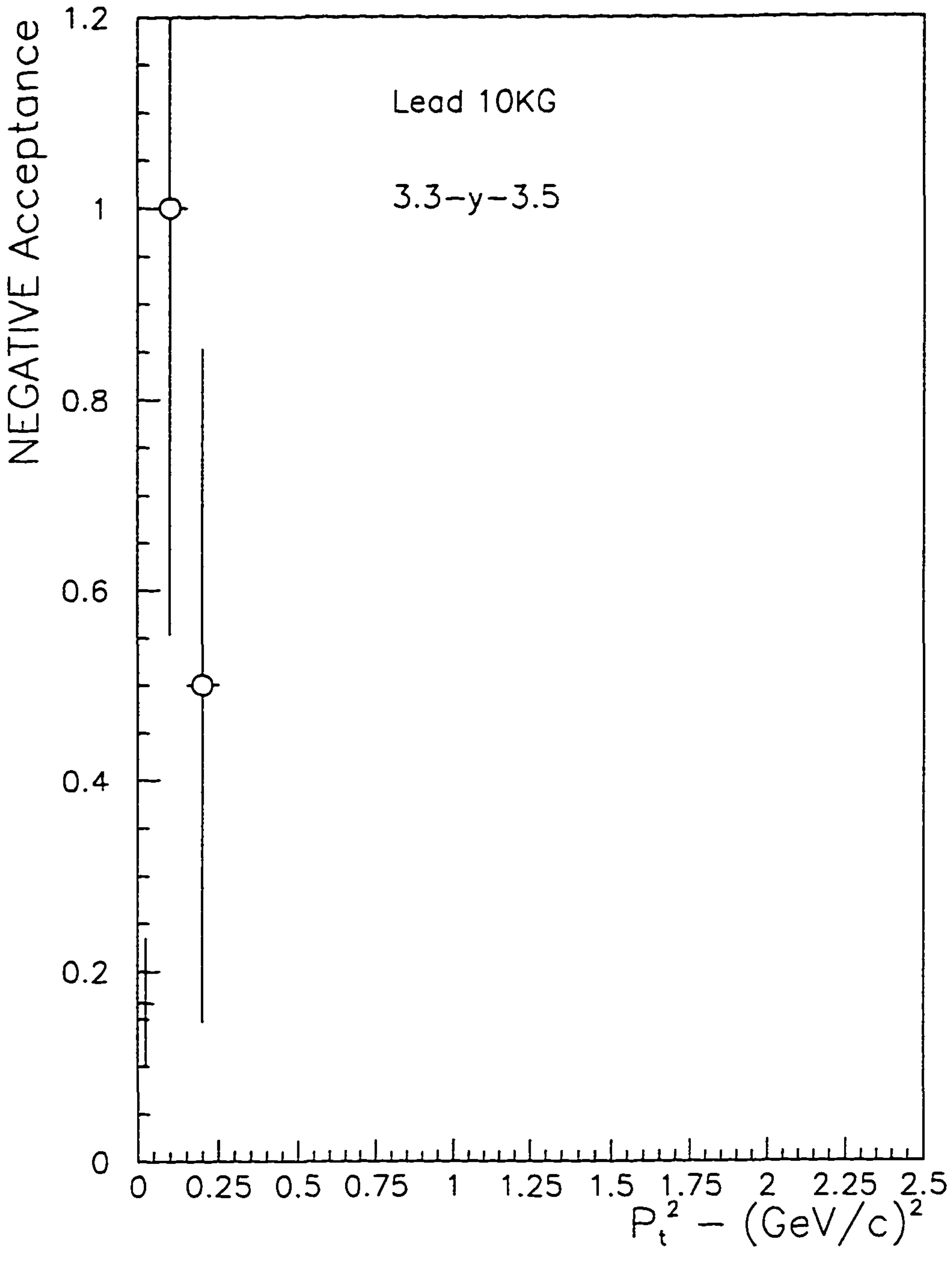

Figure 4.5 (continued)

4.2 Corrections and assumptions

Let us list here the corrections and the assumptions that we made before we present the results of the analysis. First of all we are interested in central Si on Pb events. From all the events written on tape we selected the most central by requiring the total charged track multiplicity at central rapidities to be greater than 40. We checked using Monte Carlo events that the charged track multiplicity is a good measurement of centrality. The Monte Carlo generated events were processed by our simulation package. By keeping track of the impact parameter of each event, we observed that events with large charged track multiplicity in our detector were events with small impact parameter (central). This cut yielded 12,051 events, corresponding to a cross section of approximately 250 mb (about 9% of the geometric cross section).

For our analysis we selected only well measured tracks. Well measured tracks are those with good momentum resolution. The selection of well measured tracks is based on the following:

1. Tracks with large sagitta have good momentum resolution. Sagitta is a measure of the bending of the track in the magnetic field and is defined as:

$$s = \frac{1}{2664}\frac{l^2}{p} \tag{4.1}$$

   where l is the projection of the track along the beam direction and p is the momentum of the track. The larger the momentum of the track, the smaller the sagitta. Tracks in our final sample have sagitta greater than 0.75 cm.

2. Tracks with a small number of hits were discarded. Those were low momentum tracks which were swept by the magnetic field. These tracks exited early from our detector producing a small number of hits in the first TPC module only. Tracks with a small number of hits have bad momentum resolution. Tracks with track length less than 38.0 cm were discarded.

3. Tracks with very large momentum were discarded. The upper limit in momentum was set to 20.0 GeV/c. This cut is explained in the next section about momentum resolution.

4. Only particles that point back to the primary vertex (target) were selected. If V_x, V_y, and V_z are the coordinates of the primary vertex assigned to the track, then only those that satisfied the following cuts were selected:

   $$-3.5 < V_x < 3.5 \quad -3.5 < V_y < 3.5 \quad 44.0 < V_z < 46.0 \tag{4.2}$$

   The target position is at $z = 45$cm

5. For the above cut number 3, there are tracks that point back to the target accidentally. Such tracks are, for example, decays of Λ^0, K_S, Σ. Since we study positive and negative tracks coming from the target we should correct for these decays. From simulation studies it turns out that this is a small correction, mainly due to the fact that most of these particles are produced at central rapidities. To the extent that our Monte

Carlo generator, correctly produces the same amount of Λ^0, K_S, Σ, their decays are taken into account.

6. We examined the contamination of e^+e^- tracks coming from the target. The origin of these tracks are photons (mainly from π^0 decays) through pair production. It turns out that the choice of thin targets (a few per cent of the radiation length) was very effective in eliminating the contamination coming from pair production at the target.

7. In acceptance calculations, we would like to do a model independent calculation. Unfortunately this is not practically possible because we would need to have infinitesimally small bins and an infinite number of events. Since this is not possible there is always a systematic error introduced due to the specific event generator used in acceptance calculations. This effect was seen in our acceptance calculations at the very forward rapidity bins. Since RANDOM does not reproduce well the proton rapidity distribution at very forward rapidities there was an underestimate of the effect of track merging. The merging effect is the following: as mentioned in the previous chapter the track reconstruction program starts from downstream where the hit density is less and moves towards the more crowded environment in the first TPC module. It is possible that when the track reconstruction program gets to the more crowded environment that hits have been assigned to other tracks, because the were merged into one hit for both tracks. By using RANDOM this effect was underestimated since RANDOM underestimates the forward going protons. We made a corrections for this effect by

using another event generator (AGSHIJET) that reproduces well the forward going protons.

8. In extracting the proton distributions from the data, we use the assumption that the π^- and the π^+ distributions are the same. By using this assumption we get the distributions of all the positives using the proton mass and the distribution of all negatives using again the positive mass and then by subtracting the negatives from the positives we get the proton distributions. The above assumptions has been checked by Monte Carlo and has been verified with data from other experiments. We expect that this assumption is correct since we are looking at the forward rapidity region, the projectile region, where the number of protons and neutrons are equal (Si has 14 protons and 14 neutrons). Unfortunately when we get to the data from the Au beam (Au on Au collisions) this assumption does not hold. The Au nucleus has more neutrons than protons (Z=79) and the neutrons-neutron interactions are more effective in producing π^-. We will have to rely on other methods to extract the distributions of protons.

9. Finally we made corrections for the contaminations of K^+ and K^- in the positive and negative distributions respectively. Details about these corrections will be given when we present the results.

4.3 Momentum resolution

The value of $\Delta p/p^2$ in general should be constant (independent of momentum) and during test runs it was measured using beam tracks. The beam tracks are high momentum tracks and thus cross all three TPC modules producing hits to all 36 TPC rows. When it comes to low momentum tracks, we see that value of $\Delta p/p^2$ is not constant anymore due to multiple scattering which is more effective at low momentum. Besides, low momentum tracks exit part way through the TPC's or have otherwise missing hits, the resolution will be worse early. For particles with hits in all 36 rows of the TPC's the momentum resolution is given by $\frac{\Delta p}{p^2} \approx 0.01(GeV/c)^{-1}$. In order to use only reasonably accurate data for momentum dependent variables, we have removed tracks whose measured momentum exceeds a limit chosen for each track to correspond to an expected resolution given by $\frac{dp}{p} \approx 25\%$. (This means, for example, that full length tracks had an upper limit of 20 GeV/c). This cut is applied to the data and to the Monte Carlo events to compensate the effect of the acceptance (this is cut number 3 in the previous section).

Momentum resolution can be determined using Monte Carlo. Tracks generated by Monte Carlo (HIJET) were tracked through our detector using GEANT which included all the inefficiencies and distortions of our detector. By keeping track of the track number we could compare the momentum of the track before (generated by Monte Carlo) and after (after going through our detector). Inefficiencies and distortions of our detector were determined by specialized runs using an upstream target. Drift chambers placed downstream of the TPC's were used to determine tracks. Many such runs were done during the run because the response of our detector (especially with our long drift distances) changes with temperature and quality of gas.

The magnetic field plays an important role in the momentum resolution. Using a high magnetic field (10KG) we can measure high momentum tracks within the required momentum resolution. In a low field, these high momentum tracks do not bend enough and thus the momentum resolution is bad. To get an idea how this works, let us just use some simple geometrical considerations and a maximum value for transverse momentum of 1 GeV/c (figure 4.6). We estimate that tracks with momentum up to 2.9 GeV/c will cross the first TPC module only. Tracks with momentum up to 5.6 GeV/c will cross the first two TPC modules while those with momentum 9.6 GeV/c will cross all three TPC modules.

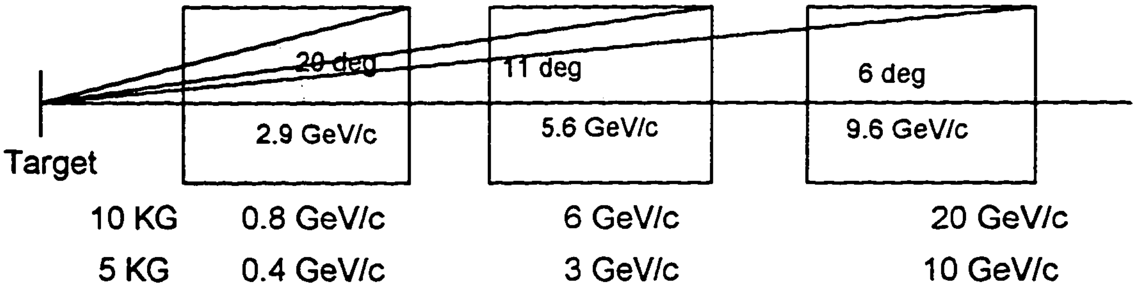

Figure 4.6: Full magnetic field provides better momentum resolution. By requiring a better than 10% momentum resolution, we can measure higher momentum tracks with the full field than with the low field.

Using Full field (10KG) and the fact that we want to have momentum resolution better than 10% we can measure tracks that cross all three TPC modules with momentum up to 20 GeV/c, those crossing the first two modules with momentum up to 6 GeV/c and those that cross the first module momentum up to 0.8 GeV/c. The corresponding measurements using the Half field are 10., 3., and 0.4 GeV/c. The advantage of the Full Field is more obvious for the tracks that cross the first two modules. It is possible to have in the data tracks with momentum 5.6 GeV/c crossing the first two TPC modules. Using Half Field (and requiring a 10% momentum resolution) we can only measure tracks with momentum up to 3 GeV/c. In other words we lost tracks with momentum greater than 3 GeV/c. Using the Full Field we can measure tracks with momentum up to 6 GeV/c, eliminating a number of lost tracks.

4.4 Results for negative pions

An understanding of pion production in relativistic heavy ion collisions is needed for several reasons [67, 68, 69, 70, 71]. Pions are copiously produced at AGS energies and are expected to be easily thermalized due to their large cross section (100 - 200 mb) in dense nuclear matter. A comparison between pion and proton energy spectra has been suggested as a method of identifying the presence of collective flow effects [72] in the expanding nuclear system. Although many attempts have been made to fit the results (such as collective flow, pion absorption and different thermal freeze out times for the pions and the protons) the most successful method is based upon Δ dominance in the production mechanism. The $\Delta(1232)$ resonance is expected to be the major source of pion enhancement at low transverse momentum and has been proposed as an alternative measure of the system temperature [73]. Low transverse momentum enchantment in the spectrum of pions has been observed at the AGS [47, 49, 74, 75], $\sqrt{s} = 5.4 GeV$ and at CERN $\sqrt{s} = 19.4 GeV$ (in the nucleon - nucleon frame) [76, 77].

In our data sample all negatives are treated as negative pions. The pion mass is assigned to them to calculate rapidity and transverse mass. The biggest contamination comes from negative kaons. Both event generators and data (E802) [42, 52, 78] give a K^- over π^- ratio of the order of 4%. We can give an estimate of this type of contamination in our pi minus sample by using K^- distributions from other experiments that use particle identification in their experimental set up to separate K^- from π^-, or by using event generators that reproduce the K^- and π^- distributions. Knowing the four-vectors of K^- we assigned the pion mass to them to see how these distributions change.

4.4.1 Transverse mass distributions

We start from the differential invariant multiplicity distribution or transverse mass distribution of negative pions:

$$E\frac{d^3N}{dp^3} = \frac{1}{N_{trig}}\frac{1}{m_T}\frac{d^2\sigma}{dm_T dy} \tag{4.3}$$

Transverse mass is defined as $m_T = \sqrt{p_T^2 + m_\pi^2}$ where p_T is the transverse momentum of the pion (p_T = psinθ) and m_π is its rest mass. In (4.3) N_{trig} is the number of events (=12051) and dy = 0.2. In figure 4.7 we show the distribution at different rapidity bins. Each rapidity bin was multiplied by an extra factor of ten in order to put them all in one plot.

We fitted the large m_T part with an exponential ($0.3 < m_T - m_\pi < 1.0$ GeV/c^2):

$$\frac{1}{N_{ev}}\frac{d^2N}{m_T dm_T dy} = A\exp[B(m_T - m_\pi)] \tag{4.4}$$

where N_{ev} is the number of events (=12,051) and dy = 0.2. We observe an enhancement in the production of negative pions over the above exponential fits (large m_T fits) at low m_T-m_π. We find that our data can be described by a sum of two exponential, one for the large slope region (cold component in the pion spectrum) and one for the large m_T - m_π region. Very similar behavior was observed in our older data (E810) for Si on Au and Si on Si and also in Si on Au and Si on Al by other experiments (E814) at the AGS and at CERN. The enhancement has been observed in a wide range of energies and systems involved, from cosmic rays experiments to Fermi and CERN energies. Monte Carlo event generators were able to produce this effect by including Δ's and other excited N*'s in their code.

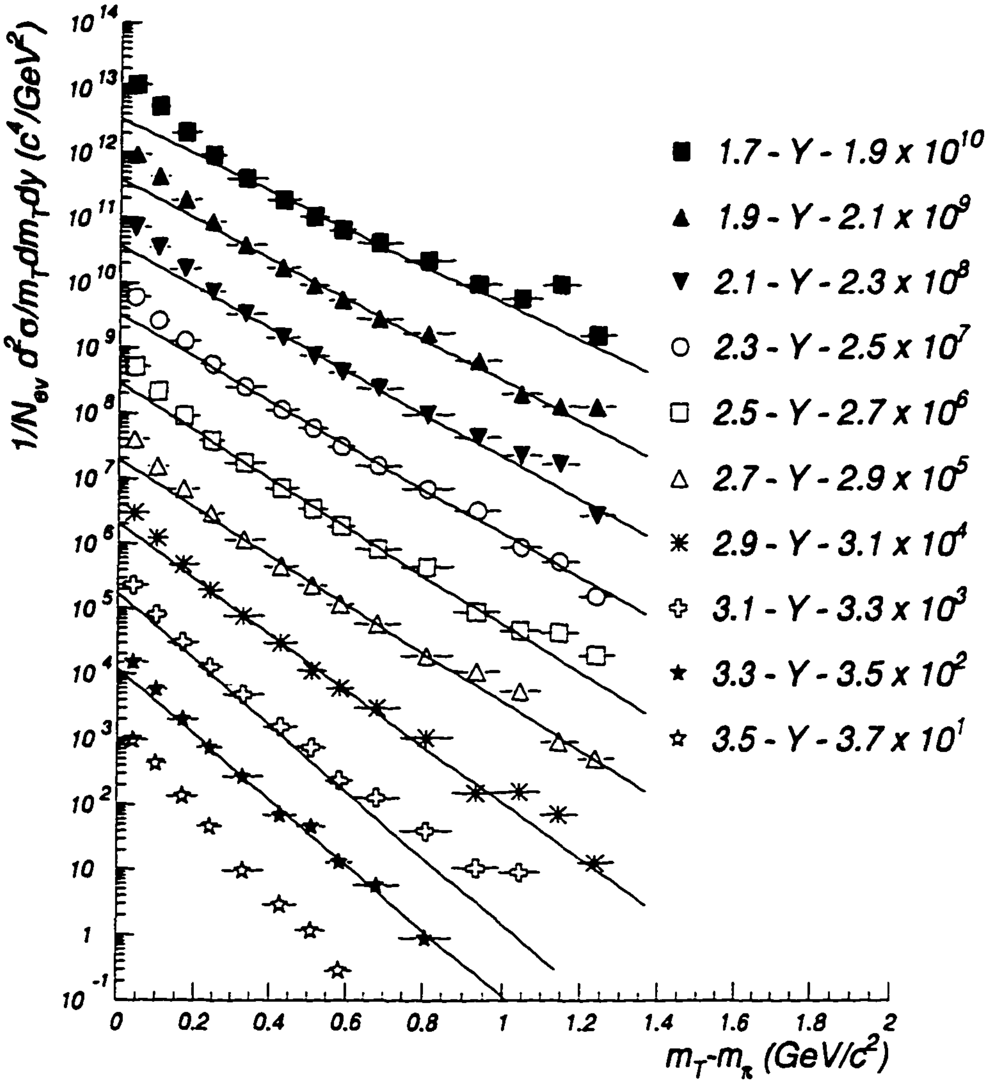

Figure 4.7: Transverse mass distributions for pions. Each rapidity bin has been multiplied by factors of ten to fit all the distributions in one plot. Lines are exponential fits in $0.3 < m_T - m_0 < 1.0$ GeV/c^2.

Of course, baryon resonance decays may not be the only possible source of the enhancement. Some theoretical ideas include the existence of collective effects, such as transverse flow, creation of small plasma droplets, the system could be out of chemical equilibrium and that there is an excess of pions with respect to chemical equilibrium at freeze out, and finally that the system could be in a partial thermal equilibrium due to longitudinal expansion leading to additional soft pions [79]. Shuryak proposes the existence of attractions between constituents leading to a modification of the pion dispersion relation. This makes it difficult for the constituents to leave the system, trapping the low p_T pions in a potential well. So the pions must climb out of the potential and thus will be cooled.

For each rapidity bin we determine the values of A and B. The inverse of negative B is also known as the inverse slope or "Temperature". We do not regard the values of inverse slopes as having physical significance but only as providing an adequate description of the transverse mass behavior of the data.

In order to compare our data to widely accepted event generators we took 1537 Si on Au RQMD1.07 events with impact parameters between 0.0 and 4.0 fm. (Experiment E802 used the same set of RQMD events to compare to their data [78]). First we should try to put trigger effects into those events; in other words we should try to see which of these events would be selected by our trigger. In order to see which particles would make it into our detector it is not just a simple geometrical cut because the target is in the magnetic field and the particles as soon as they are formed they bend before they reach the detector. So, instead of putting a complicated geometrical cut in order to take the magnetic field into account, we processed the RQMD events with our simulation package and we put on the processed events the same cuts as in the data. Figure 4.8 shows the impact parameter distribution of these events. The shaded region shows the distribution of the events that pass our centrality cuts. We see that the cuts get rid of many large impact parameter events and very few small impact parameter events. Since we cut in about 9% of the geometric cross section we end up needing larger impact parameter RQMD events. The RQMD curves are from all the 1537 events. Figure 4.9 shows the comparison of our data with the predictions of the model. Only three representative rapidity bins are used. The linear plots are also shown to emphasize the low transverse mass enhancement. The lines are sums of exponential fits to the data (solid line) and to RQMD (dashed line). Figure 4.10 shows the rapidity dependence of the inverse slopes for our data (large m_T) and for E802. We compare only the large m_T region because E802 measures in the large m_T region only. We obtained acceptable values of χ^2 for our fits (χ^2 per degree of freedom was around 0.7 - 1.7). RQMD seems to have a smaller slope for large m_T than the data. RQMD reproduces the low m_T -m_π enhancement by including excited baryons like Δ's, N*'s in the code. For the low m_T -m_π we get inverse slopes that do not vary with rapidity as much as the large m_T part. The temperatures are between 70 and 90 MeV. The fact that the inverse slopes do not vary much with rapidity may have to do with the fact that baryon resonances are evenly distributed with rapidity and dominate over meson resonances such as ρ and strange resonances. Pions from meson resonances contribute in the midrapidity region.

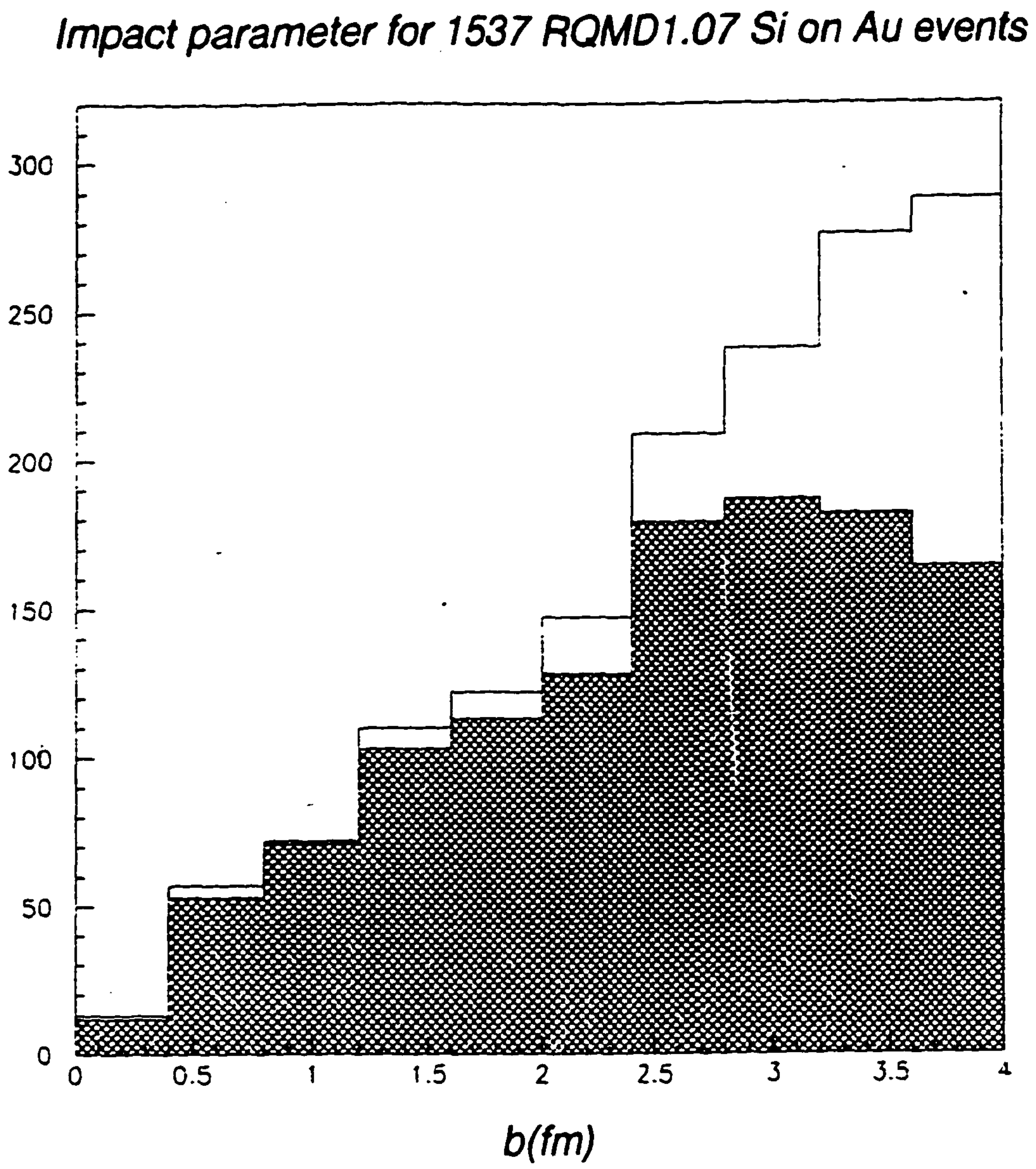

Figure 4.8: Impact parameter (b) distribution of the 1537 RQMD events [78] used to compare to our data. The shaded region shows the events that passed the same cuts we imposed on the data. The cuts are effective in getting rid of events with large impact parameter.

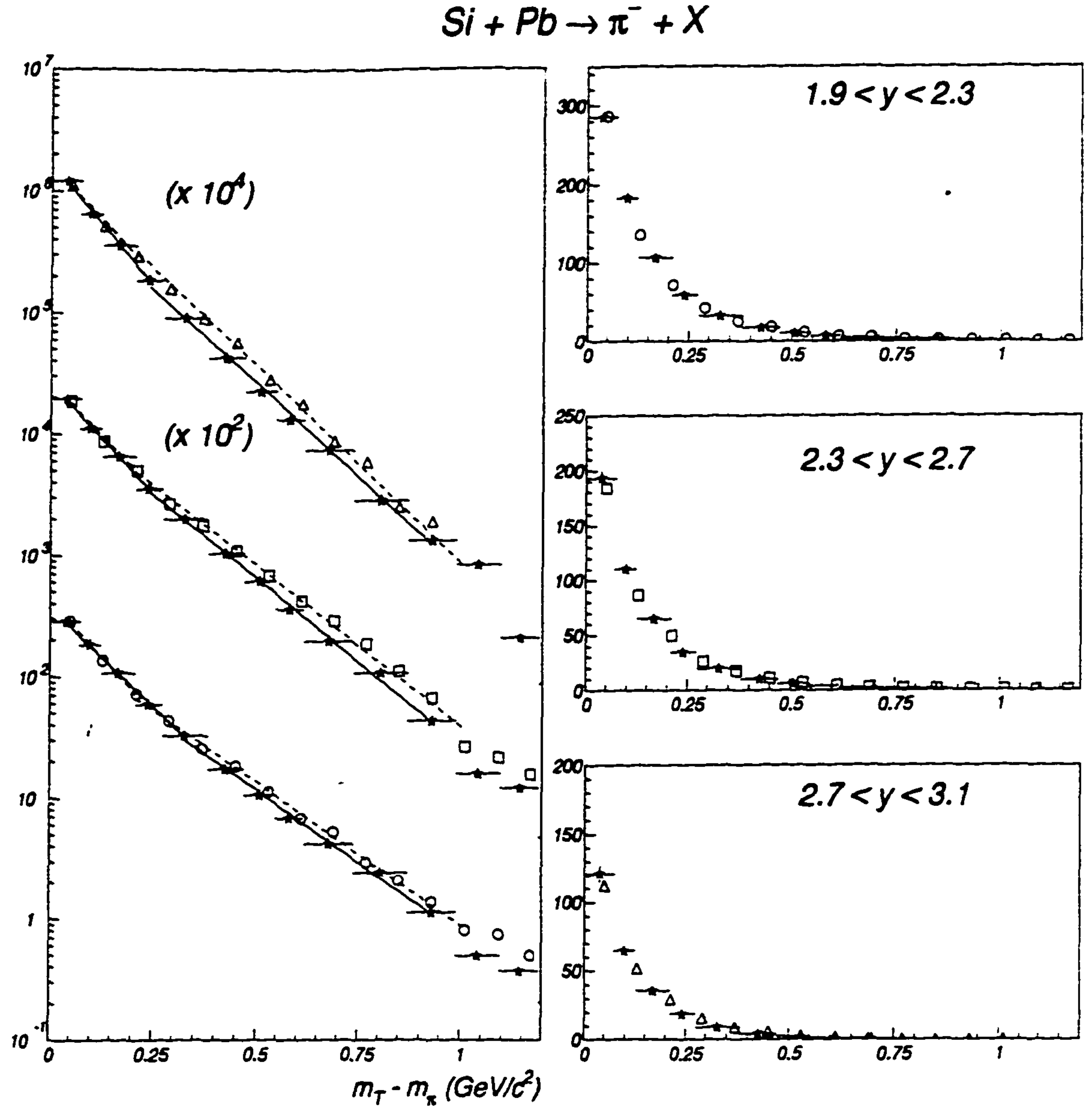

Figure 4.9: Comparison of our data with the predictions of the RQMD model. Only three representative rapidity bins are shown. The linear plots are also shown to emphasize the low transverse mass enhancement. The lines are sums of exponential fits to the data (solid line) and to RQMD (dashed line).

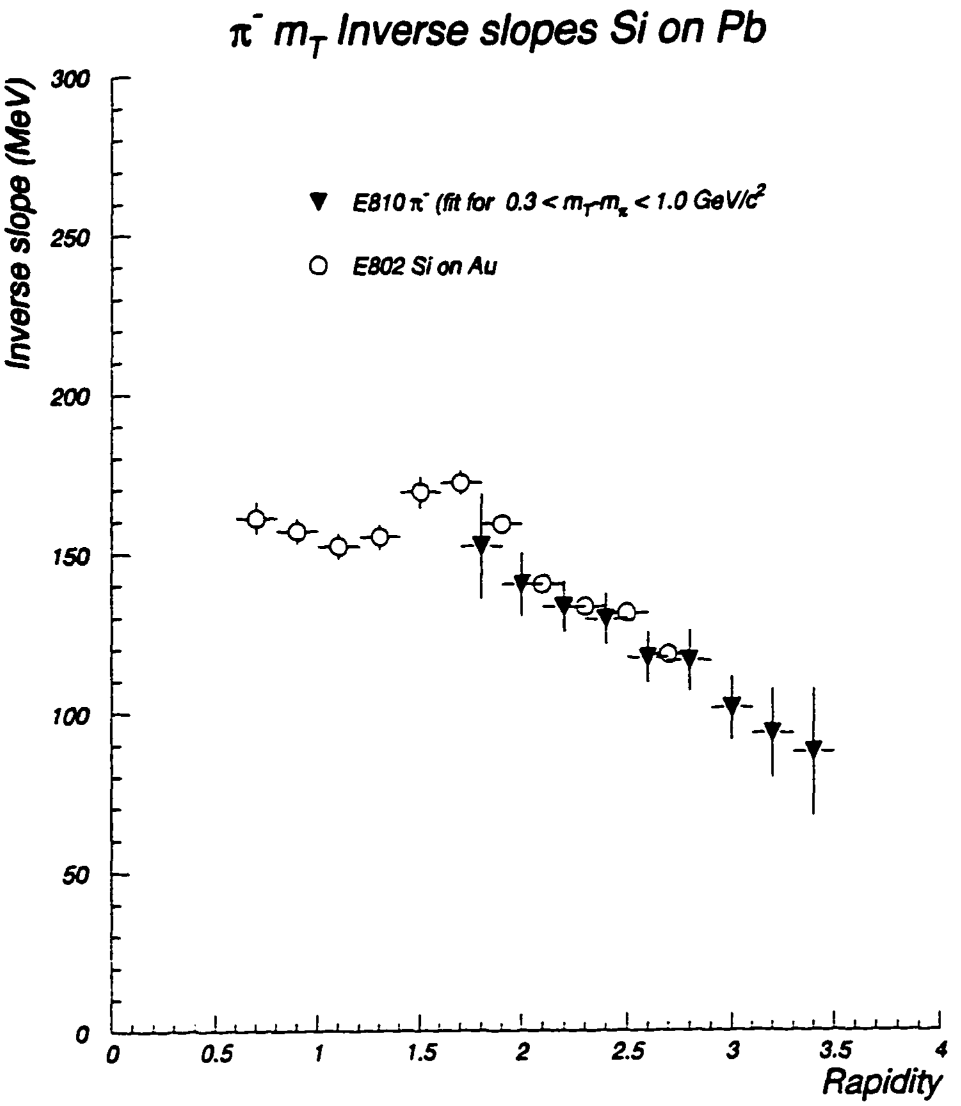

Figure 4.10: Rapidity dependence of the inverse slopes for our data in the large m_T region (inverted triangles) and for experiment E802 (Si on Au) from [80] (open circles).

At CERN baryons dominate over meson and strange resonances at target rapidities. At midrapidities meson and strange resonances dominate over baryon resonances. This different resonance domination at different rapidity bins leads to a rapidity dependence of the low m_T dependence enchantment in the pion spectrum. On the other hand, at the AGS baryon resonances dominate at all rapidities; thus we expect only a weak dependence of the enchantment [67].

We calculated that about 30% of all pions are at the low m_T region. Of course the question is not only how many pions we have at low mt but how many of them came from excited baryons. The ratio of excited baryons (especially $\Delta(1232)$) to ground state nucleons (protons and neutrons) have been proposed as an alternative method to calculate the temperature of the system.

The error bars in the "Temperature" were determined by the 1σ variation of χ^2. We selected as acceptable fits to our data those that yielded χ^2 within 1σ of the original value. Thus, there is a 70% (68.3%) probability that the temperature at a certain rapidity bin will be within error bars, and 30% probability (to be more accurate 31.7%) that the temperature will be outside the reported error bars.

4.4.2 Rapidity distributions

By integrating over m_T we obtain the rapidity distribution dN/dy for negative pions. Since we cannot measure out to infinite m_T we use the exponential fits for large m_T to extrapolate to unmeasured region. Figure 4.11 shows the rapidity distribution for negative pions, compared with RQMD model and with E802. The RQMD points are from the 1537 events. The fact that the E802 measurements are below our data and RQMD points was expected since E802 extrapolates to unmeasured low $m_T - m_\pi$ regions using exponentials and not taking into account the lot $m_T - m_\pi$ enhancement. Figure 4.12 shows the comparison of our Si on Pb data with our Si on Si measurements and p-p collisions scaled by 28.

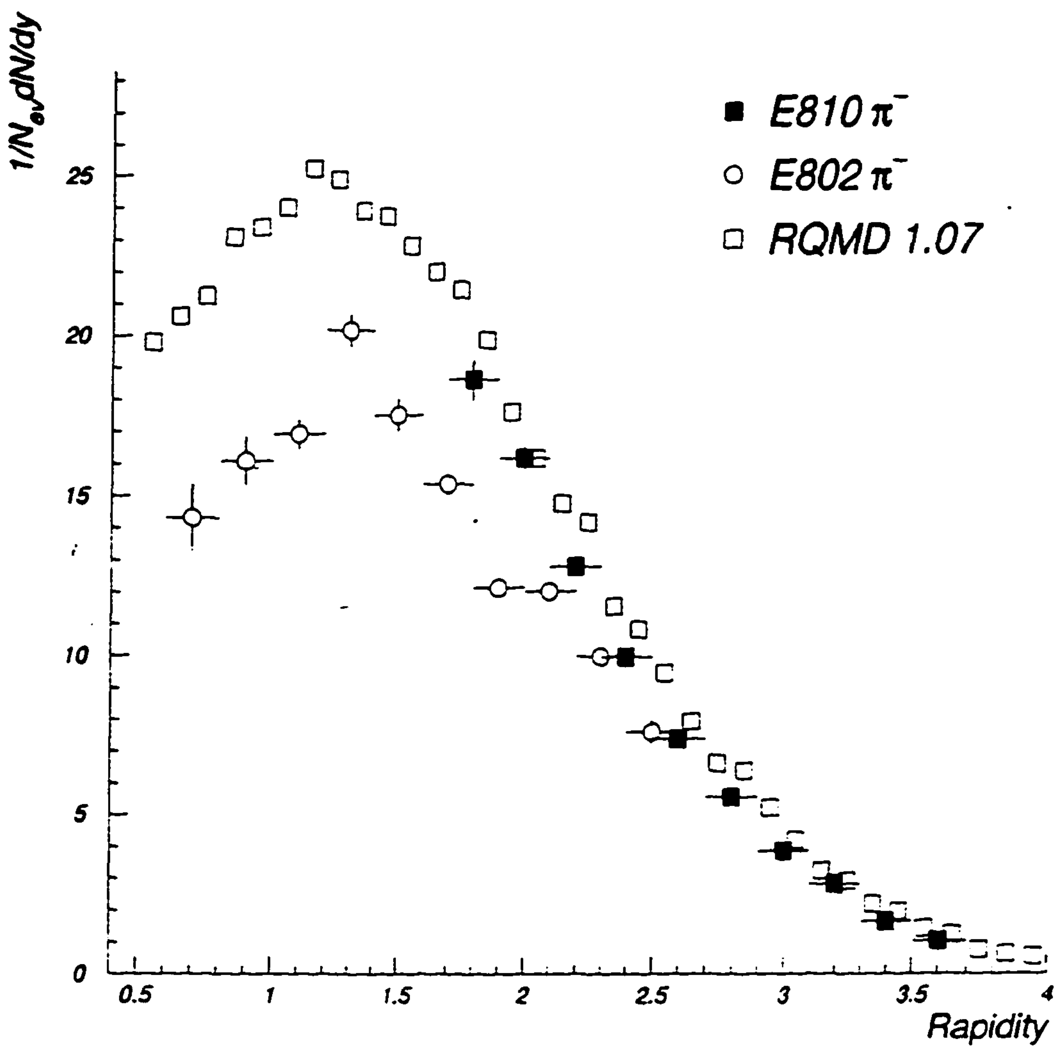

Figure 4.11: Rapidity distribution for negative pions, compared with the RQMD model and with E802 [80]. The RQMD points are from the 1537 events [78].

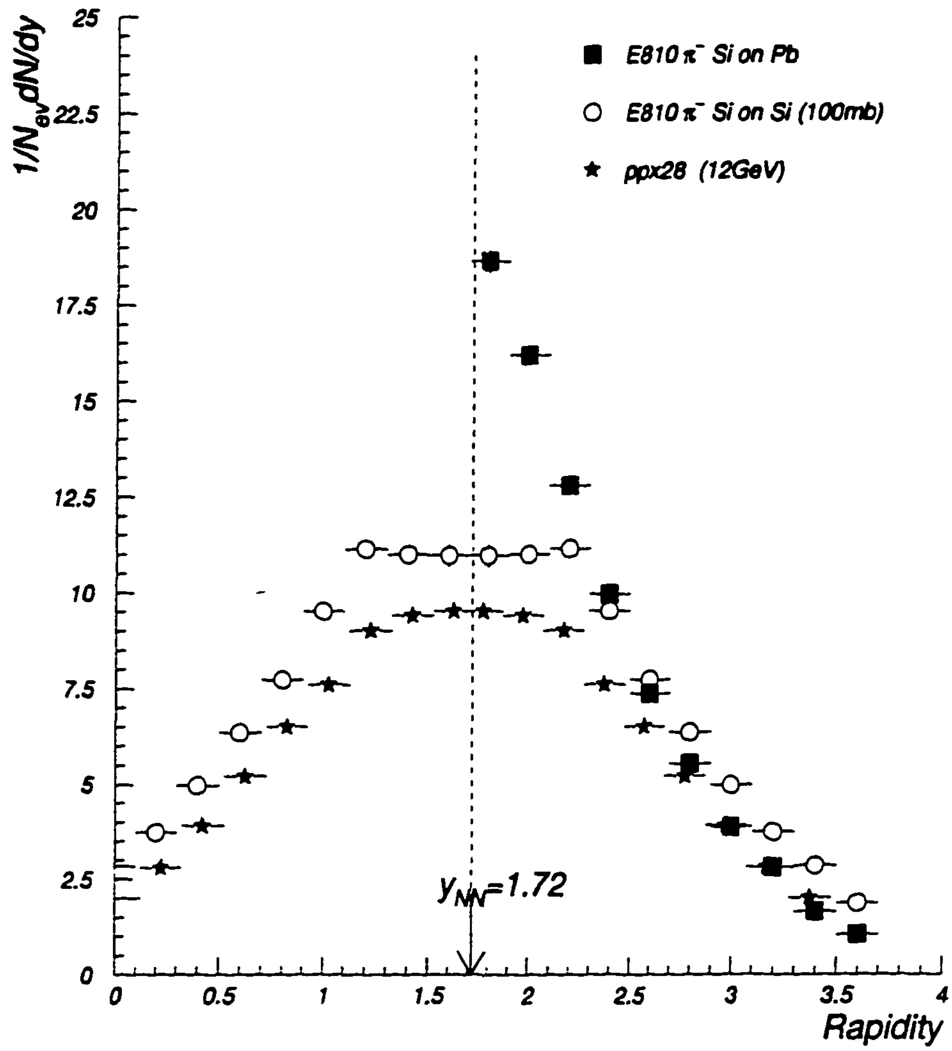

Figure 4.12: Comparison of our Si on Pb pion distribution (solid squares) with our Si on Si measurements [47] (open circles), and p-p collisions [59] scaled by 28 (stars).

We observe an increase in the pi minus production from the Si target to the Pb target. By comparing pi minus production in p-p and Si on Si we observe a suppression in the pi minus production. Due to the fact that the Si nuclei has neutrons and thus in a Si on Si collisions we would expect many n-n collisions and using the fact that n-n collisions produce more pi minus than p-p collisions due to isospin effects, we would expect to see more pi minus produced in Si on Si than in p-p. Thus, although the total number of pi minus in Si on Si (area under the curve) is larger than the number of pions produced in p-p, we were expecting still more pions in Si on Si. To make this statement more quantitative we use the mean multiplicity of negatively charged hadrons produced in pp collisions $<h^->_{pp}$ and in pn collisions $<h^->_{pn}$ in similar energies [81]. Data for pn collisions are from p+d or d+p events. For the number of negatively charged hadrons produced in neutron - neutron collisions, $<h^->_{nn}$, there are poor data due to problems with neutron beams. In general we expect the number of pi minus produced in nn collisions to be similar to pi plus in pp collisions. This is true for low energies, below the K^- threshold. Above the K^- threshold K^- are produced and thus the above assumption stops to hold. For higher energies the we use an empirical formula : $<h^->_{nn} = <h^->_{pp} + (0.7 \pm 0.1)$. We now try to get the number of negative hadrons produced in nucleus nucleus collisions by counting the number of pp, pn, np, and nn collisions. Thus the number of negatively charged particles produced in collisions of identical nuclei (like Si on Si) is:

$$<h^- >_{NN} = (\frac{Z}{A})^2 \cdot <h^- >_{pp} + 2 \cdot \frac{Z}{A} \cdot (1 - \frac{Z}{A}) \cdot <h^- >_{pn} + (1 - \frac{Z}{A})^2 \cdot <h^- >_{nn} \qquad (4.5)$$

Since there are no data for $\langle h^- \rangle_{nn}$, $\langle h^- \rangle_{pp}$, and $\langle h^- \rangle_{pn}$ at AGS energies we extrapolate linearly. Thus we get $\langle h^- \rangle_{pp} = 0.836$, $\langle h^- \rangle_{pn} = 1.136$, and $\langle h^- \rangle_{nn} = 1.536$. For collisions between Silicon nuclei we have Z=14 and A=28. Thus, from the above formula we get

$$\langle h^- \rangle_{NN} = 1.162 \tag{4.6}$$

This is the number of negatively charged particles produced for nucleon - nucleon weighted to take into account the Si nucleus. From our Si on Si rapidity distribution we estimated about 27 negative hadrons produced. Thus the number of negatively particles produced per participants nucleon is 27/56 = 0.482. It makes sense to assume that the number of participant nucleons is less than 56. E802 has estimated the number of participants using the energy deposited in the zero degree calorimeter for Si on Al systems to be 44. Since the Si target has one more proton than Al we say 45. Thus 27/45 = 0.600. The number of participants for nucleon - nucleon interactions is 2. Thus 1.162/2 = 0.581. Thus we do observe a suppression in the number of produced hadrons per participating nucleon in Si - Si than in nucleon - nucleon. The numbers above are from [81]. The total number of pions produced in Si on Si , assuming $\pi^+ = \pi^-$ and $\pi^0 = (\pi^+ + \pi^-)/2$ is 27x3 = 81. Thus the number of pions per participant is 81/45 = 1.8. $N_\pi = 1.8 \mathrm{x} N_{part}$. E802 for central collisions estimates a total of 19x3=57 pions and thus $N_\pi = 1.1 \mathrm{x} N_{part}$ for very similar centrality cuts (8% for E810, 7% for E802). The difference could be due to the fact that E802 does not measure at low m_T region where the pion enhancement is.

4.5 Results on protons

Positive tracks were assigned the proton mass. Assuming that the negative pion and the positive pion distribution are the same, as discussed in section 4.2, we were able to subtract the positive pions from the positives and thus extract the proton distributions.

4.5.1 Transverse mass distributions

Figure 4.13 shows the differential cross sections $\frac{1}{N_{ev}}\frac{d^2N}{m_T dm_T dy}$ for protons as a function of $m_T - m_0$ ($m_T = \sqrt{p_T^2 + m_0^2}$). The lines are exponential fits (the same form was used for the pions, but now we assign the proton mass) for $m_T - m_0 < 1.0$ GeV/c^2. For all cases we obtain a good χ^2 to our parametrization (χ^2 per degree of freedom was between 0.2 and 3.9). We used RANDOM to correct the data for K^+ and K^- contamination (the most important contamination) in the proton spectrum. We used the proton mass to calculate the transverse mass of all the positives ($p + \pi^+$) and then subtracted the negatives π^- using again the proton mass. Thus the resulting spectrum $p + \pi^+ - \pi^-$, represents the proton spectrum under the assumption that $\pi^+ = \pi^-$, an assumption which is supported by both Monte Carlo and experiment, [78]. (Actually we do expect an excess of negative pions in the target region since we have more neutrons than protons in the target and so we'll have more n + n collisions than p + p. n + n collisions are more effective in producing negative pions).

Table 10 below shows the values of the inverse slopes using exponential and Boltzmann fits. The inverse slopes obtained using Boltzmann fits are slightly smaller but we obtain a better χ^2. The errors in the temperature were calculated by estimating the change in the parameter B of the fit that would change χ^2 by 4 units. This change in χ^2 corresponds to a change of the Confidence Level (C.L) from 50% to 15%, which in turn corresponds to a change from 1σ to 2σ in a Gaussian distribution.(For many degrees of freedom the χ^2 distribution becomes a Gaussian distribution, [82]).

Rapidity (y)	Exponential Inverse slopes (MeV)	χ^2/d.o.f	Boltzmann (MeV)	χ^2/d.o.f.
1.7 - 1.9	224 ± 10	2.25	188 ± 4	0.41
1.9 - 2.1	223 ± 10	2.41	189 ± 4	0.51
2.1 - 2.3	192 ± 7	3.91	167 ± 3	0.78
2.3 - 2.5	160 ± 3	0.64	141 ± 3	0.16
2.5 - 2.7	145 ± 6	1.74	129 ± 3	0.37
2.7 - 2.9	140 ± 8	0.49	126 ± 3	0.04
2.9 - 3.1	135 ± 17	0.39	121 ± 6	0.15
3.1 - 3.3	106 ± 10	0.74	97 ± 8	0.20
3.3 - 3.5	70 ± 10	0.29	66 ± 12	0.29

Table 10: Inverse slopes using exponential and Boltzmann fits to our proton transverse mass spectrum

Figure 4.14 shows the comparison of the data with RQMD. The RQMD curves are from all the 1537 events. Only three representative rapidity bins are used. The linear plots are also shown to emphasize that there is no low transverse mass enhancement as in the case of negative pions. The lines are exponential fits to the data (solid line) and to RQMD (dashed line). Finally we compare our inverse slopes to published results from other experiments, figure 4.15.

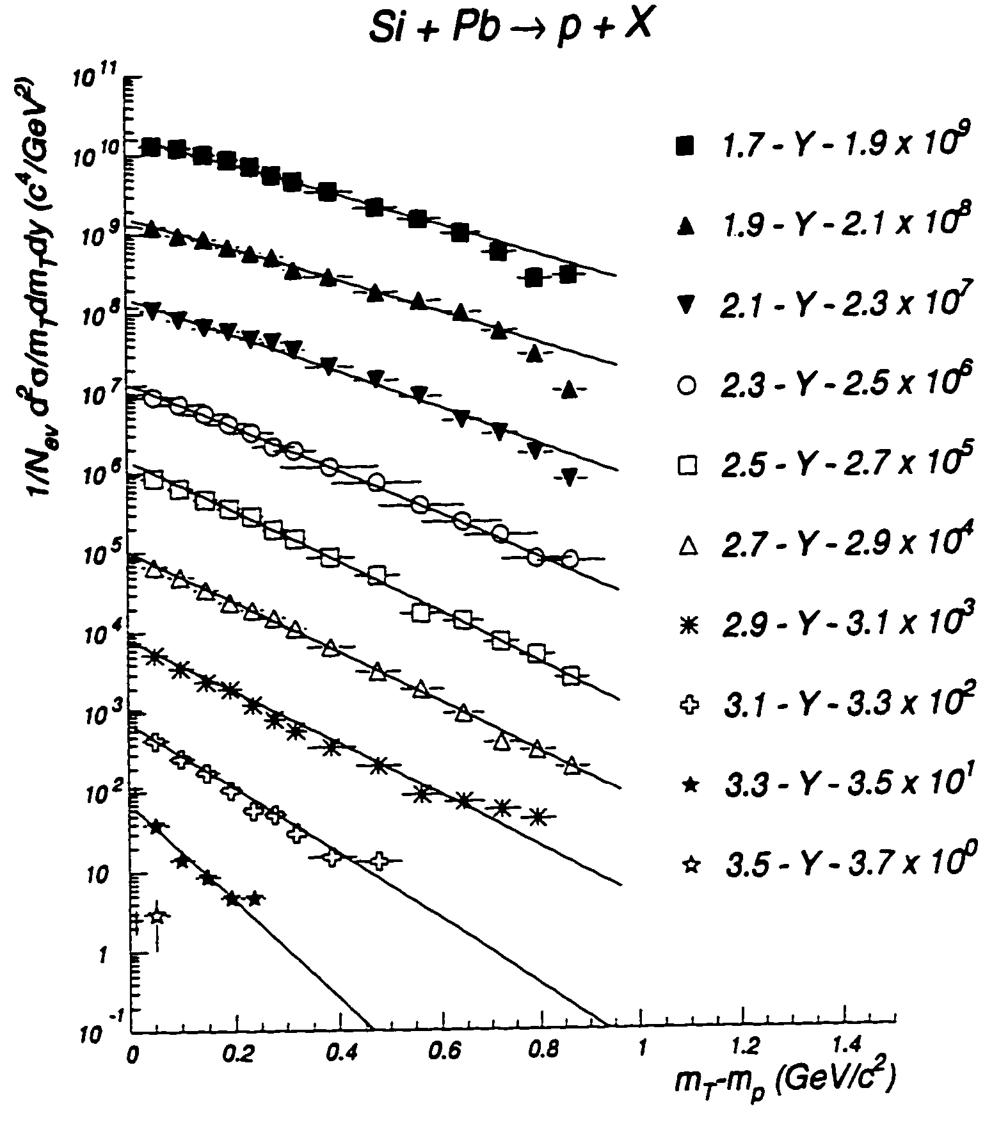

Figure 4.13: Transverse mass distributions for protons. Lines are exponential fits as described in the text.

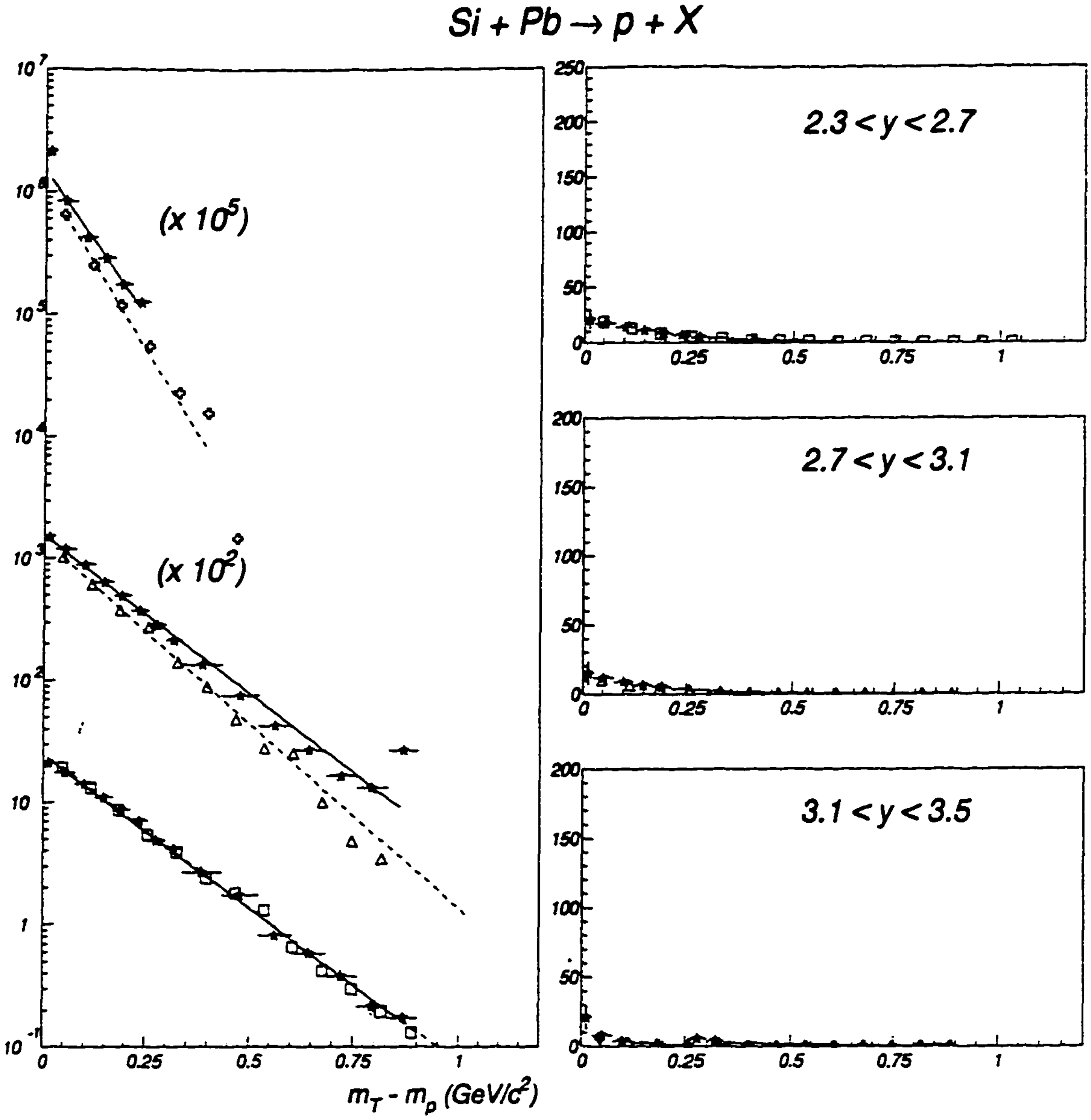

Figure 4.14: Comparison of our proton data with the RQMD model [78]. Only three representative rapidity bins are used. The linear plots are also shown to emphasize that there is no low transverse mass enhancement as in the case of negative pions. The lines are exponential fits to the data (solid line) and to RQMD (dashed line).

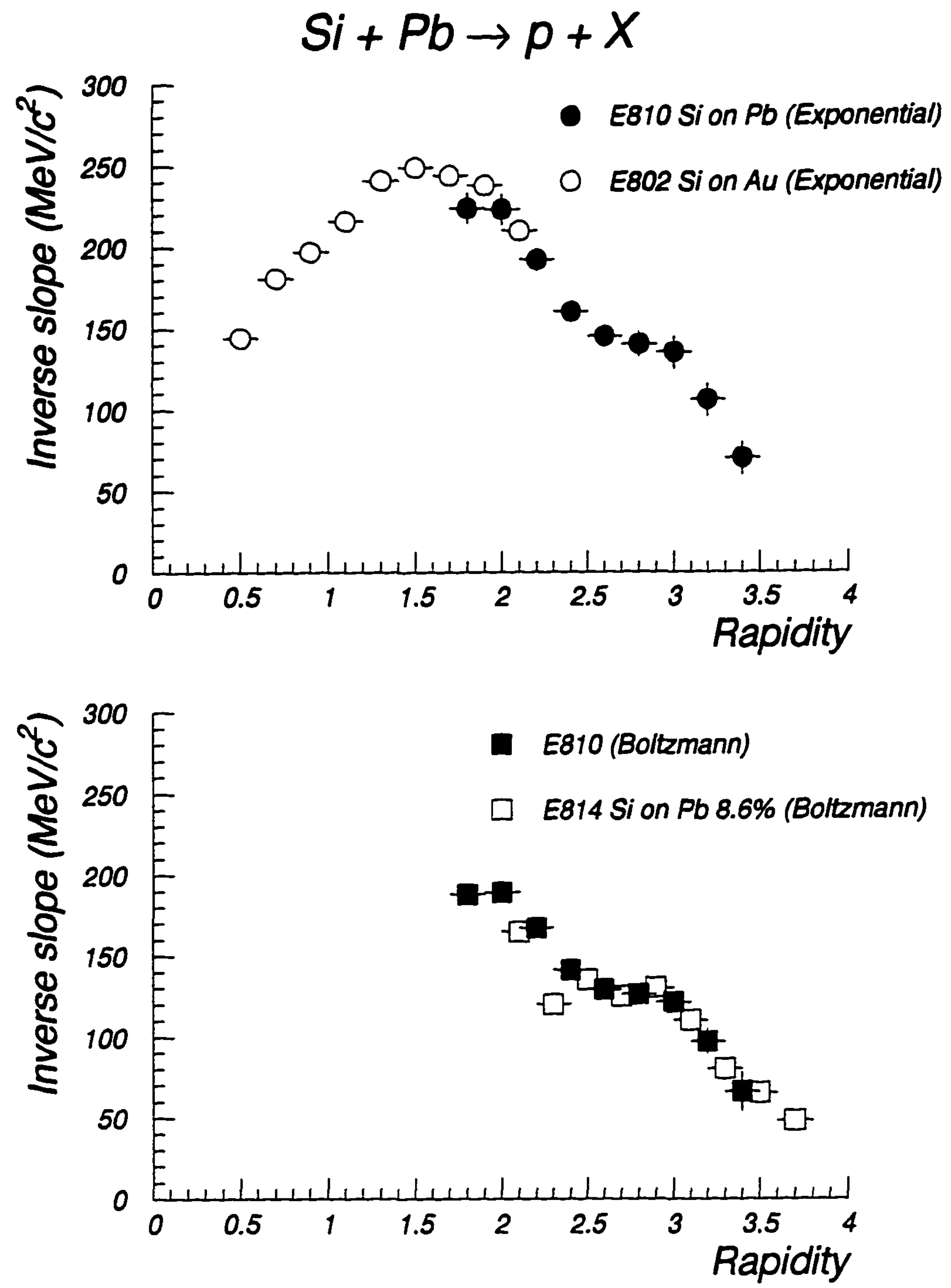

Figure 4.15: Comparison of our exponential inverse slopes (solid circles) to those from experiment E802 [80] (open circles), and our Boltzmann inverse slopes (solid squares) to those from experiment E814 [83] (open squares). Considering the differences in the acceptance and centralities of the experiments the agreement is reasonable.

4.5.2 Rapidity distribution for protons

Our measurements cover a wide enough region so that we can obtain an integrated rapidity distribution by summing over the differential cross sections. We used the functional form A·*exp*(-Bm$_T$) to extrapolate to unmeasured regions of m$_T$ (m$_T$ - m$_p$ > 1.0 GeV/c^2). The contribution of the extrapolated part to the rapidity spectra is negligible. Figure 4.16 shows the rapidity distribution for protons. Also shown in figure 4.16 is the proton rapidity distributions including contamination from K^+ and K^- and the prediction of RANDOM. At large (very forward) rapidities RANDOM underestimates the number of protons. It is at this region that the effect of merging was underestimated and we had to make corrections in our acceptances by using HIJET. Figure 4.17 shows our results along with proton rapidity distributions from E802 (Si + Au) and E814. Considering the differences in centrality selection and the different range of kinematic variables covered in the two experiments, we observe reasonably good agreement.

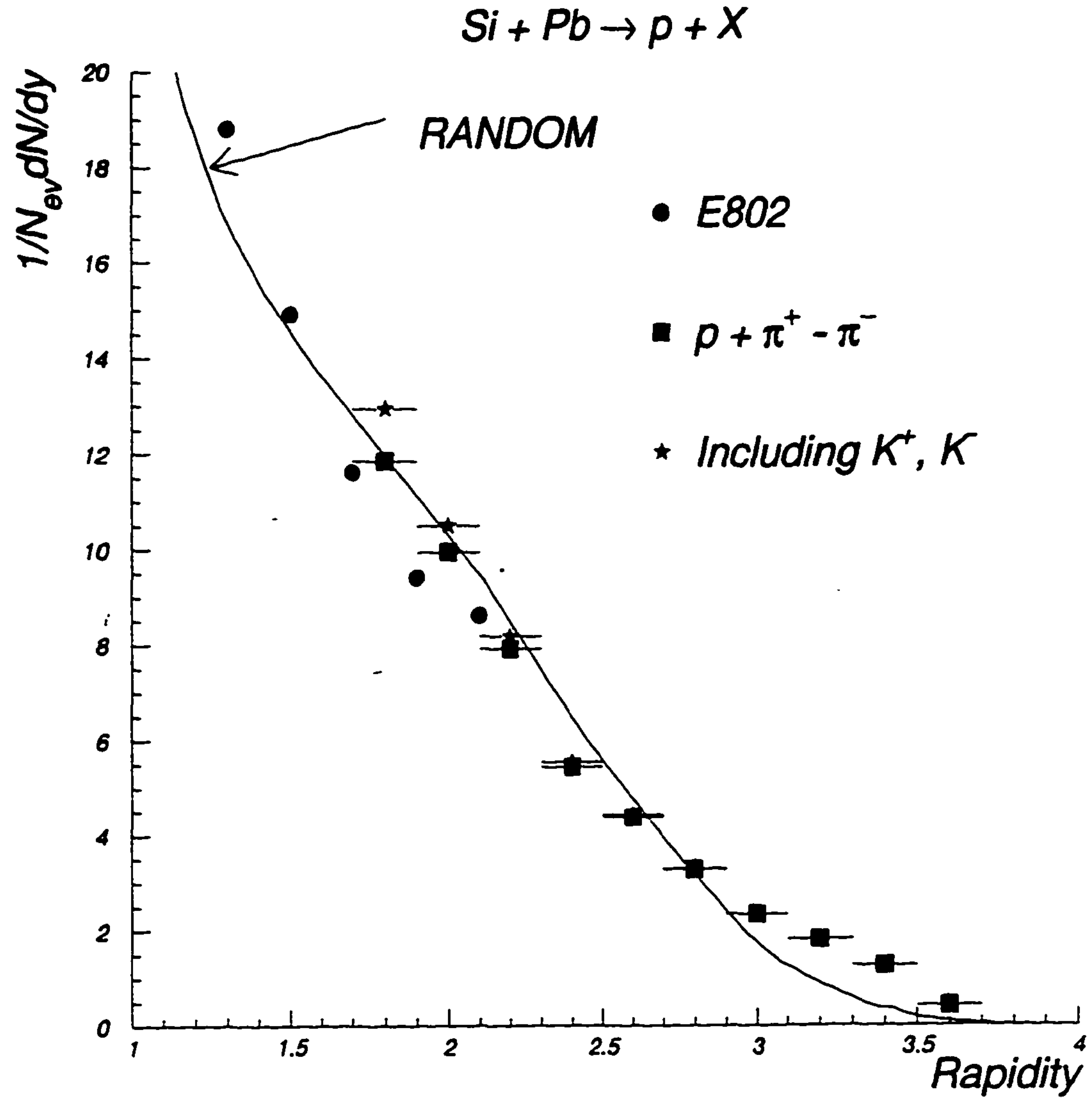

Figure 4.16: Rapidity distributions for protons. We also show the rapidity distribution including K^{+}, K^{-} contamination (solid stars). The E802 points (solid circles) are for Si on Au collisions from [80]. Errors are statistical only.

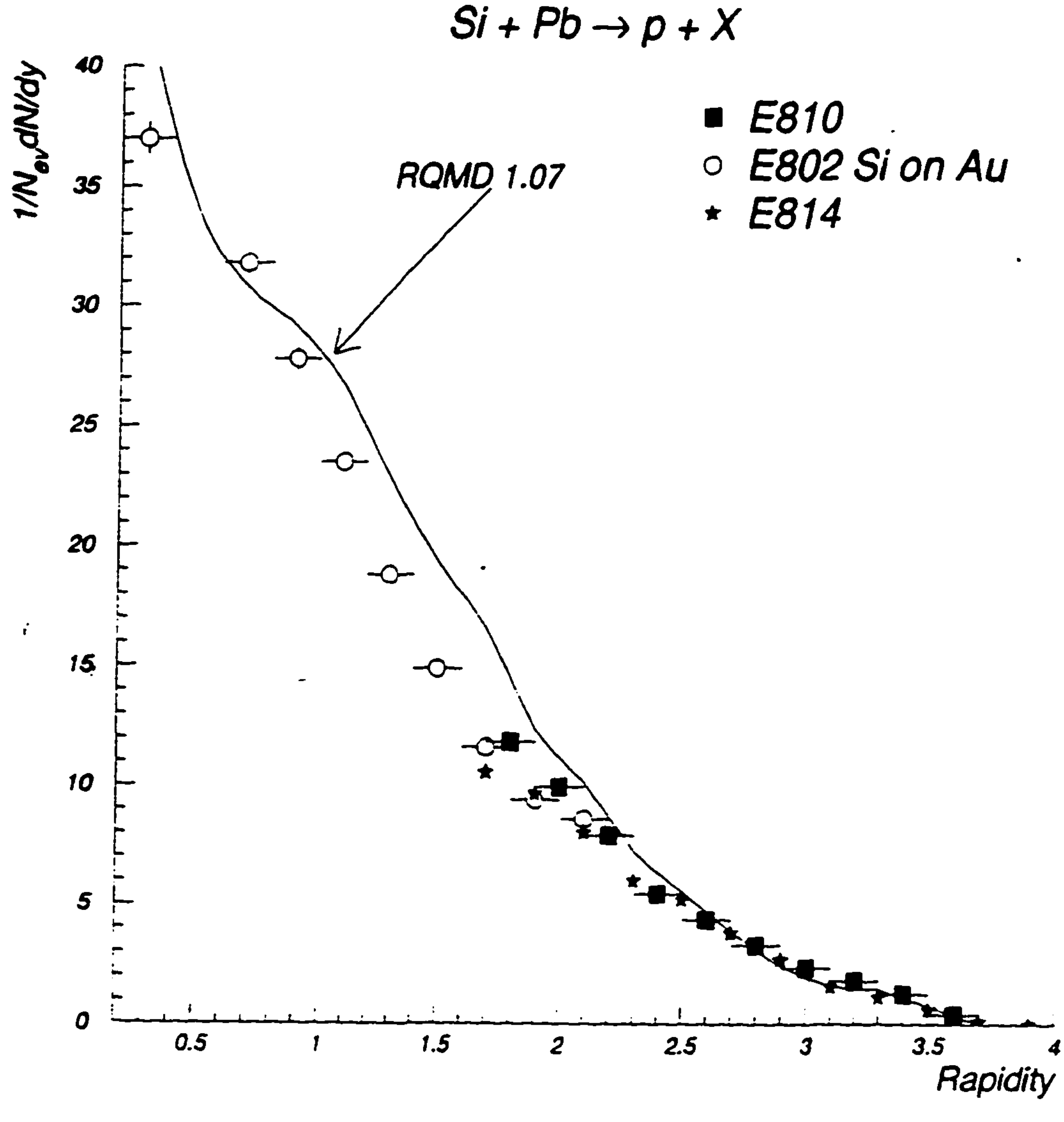

Figure 4.17: Comparison of our proton rapidity distribution with E802 Si on Au [80] and E814 [83]. The solid line is the prediction of RQMD1.07 [78].

4.6 Nuclear stopping

The issue of nuclear stopping is a paramount element in estimates of the temperature, energy density and baryon density of the large volume of hot compressed, nuclear matter after a central nuclear collision. Rapidity distributions and transverse energy distributions play an important role in the discussions of nuclear stopping [83, 84, 85, 86].

To get an idea of the amount of energy that can be deposited in Si-Pb collisions at the energy region of the AGS lets assume that the maximum energy that can be deposited is limited kinetically by the total kinetic energy in the center of mass of the participating nucleons:

$$E_T^{\max} = \sqrt{s} - m_N(B_P + A_P) \tag{4.7}$$

where m_N is the nucleon mass, A_P is the number of participating target nucleons, B_P the number of projectile participants, and s the cm energy squared:

$$s = 2m_N B_P A_P E_{lab} + (B_P^2 + A_P^2)m_N^2 \tag{4.8}$$

E_{lab} is the lab projectile energy per nucleon.

Lets assume that the projectile drills a tube through the target nucleus leaving the spectators in the target nucleus initially undisturbed. For a central collision the number of target participants in this tube is :

$$A_P = \frac{3}{2}B^{\frac{2}{3}}A^{\frac{1}{3}} \tag{4.9}$$

One effect not included above is the rescattering of secondaries on target spectators (and participants), which tends to increase A_P thus increasing the maximum deposited energy.

The mean free path of a nucleon in nuclear matter is:

$$\lambda = \frac{1}{\sigma \cdot n} \cong 1.5 fm \qquad (4.10)$$

where $\sigma = 30$ mb and n = 0.15 nucleons/fm^3.

The radius of a Pb nucleus is ≈ 7fm, thus all nucleons incident on a Pb nucleus will suffer 5-6 inelastic collisions. If the incident nucleons retain enough energy to penetrate the target nucleus, then the target appears "gray". On the other hand, if the incident nucleon loses its entire energy after a few inelastic collisions, the target appears "black". The incident nucleon will be slowed down inside the nucleus ("stopping") and the formation of a baryon-rich high density region is expected.

The shape of proton rapidity distributions reflects directly the degree of nuclear stopping, and the onset of nuclear transparency expected in high energy nucleus-nucleus collisions. Initially the target and projectile nucleons have very narrow rapidity distributions centered at y=0 and y=3.44 respectively, and dN/dy=0 in between these two peaks. If the nuclei were highly transparent to one another, one might expect to see some broadening and small shift toward midrapidity of the initial distributions and a sparse population of the central region in the final state; On the other hand, if the colliding nuclei were fully stopped, one would expect to see most of the nucleons at midrapidity, with the width of the distribution determined by thermal and possibly hydrodynamic motion, and no peaks in the beam and target regions. Based on p + A → p + X data at energies Elab≥ 100 GeV, we expect that in central Si + Au collisions the average rapidity of projectile baryons would be shifted downward by $\Delta y \approx 2.5$ while the rapidity of participant target baryons should be shifted upward by $\Delta y \approx 1.0$ .Therefore a substantial amount of equilibration between projectile and target baryons is expected to occur at 14.5 GeV where the total rapidity gap is only 3.5 . As can be seen in our proton rapidity distribution figure 4.18 the peak at y=3.44 (projectile fragmentation region) has completely disappeared, indicating a high degree of nuclear stopping. Chapman *et al.* [87] published an analysis based on extrapolation of the E802 data and concluded that there is evidence of high nuclear transparency, largely because the extrapolation yielded too little longitudinal momentum. After adding a component to protons at $y \approx 3$ they obtained the curves shown in figure 4.18. The peak predicted at $y > 2.4$ in [87] does not appear in the data.. Based on their curve Chapman et al. concluded that 6.4 out of 14 incident protons stay in the region $2.4 < y < 3.4$. HIJET and RANDOM give $N_P = \int_{2.4}^{3.4} \frac{dN}{dy} dy = 3.$ protons in this region indicating a much larger stopping power than suggested in [87].

Measurements of transverse and forward energy provide another way of measuring nuclear transparency. E802 measurements of E_T show that the maximum value of E_T does not increase with target mass after a certain mass number ($A \approx 100$). Naively one would expect that the thicker the matter of the target, the more energy can be deposited into the matter to induce a larger transverse flow E_T. The saturation seen in figure 4.19 seems to be related to nuclear stopping. If the Cu (or Ag) nucleus is already "black" as viewed by the projectile, then, even if the target thickness (in terms of nuclear matter thickness) were increased further, the energy deposited in the matter would remain constant. This would induce a saturation feature in the E_T distribution. Similar results were obtained by the E814 collaboration, figure 4.20. Forward energy measurements E_F support the above considerations.

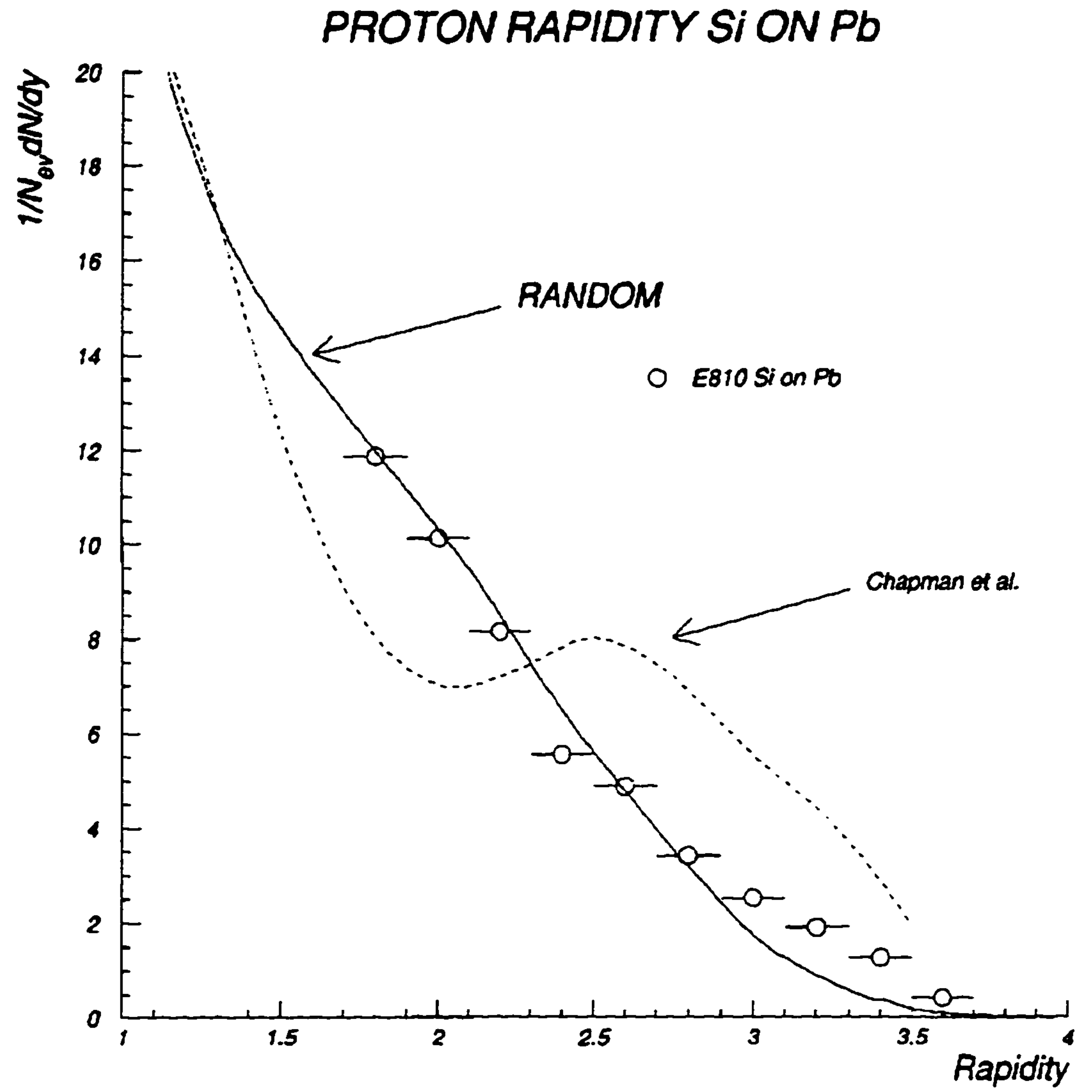

Figure 4.18: Proton rapidity distribution and the curve from [87]. The solid line is the prediction of RANDOM

For the Au target a sharp peak is observed at $E_F \cong 0$, implying that no energy flows in the forward direction, presumably due to the fact that the Au nucleus is black. On the other hand, a finite energy flow is observed for the Al target, due to two possible reasons:

a) A complete overlap between Si and Al can hardly be expected so that some of projectile remnants are emitted at forward angles, and b) the Al nucleus is not thick enough so that the projectile could still penetrate through it.

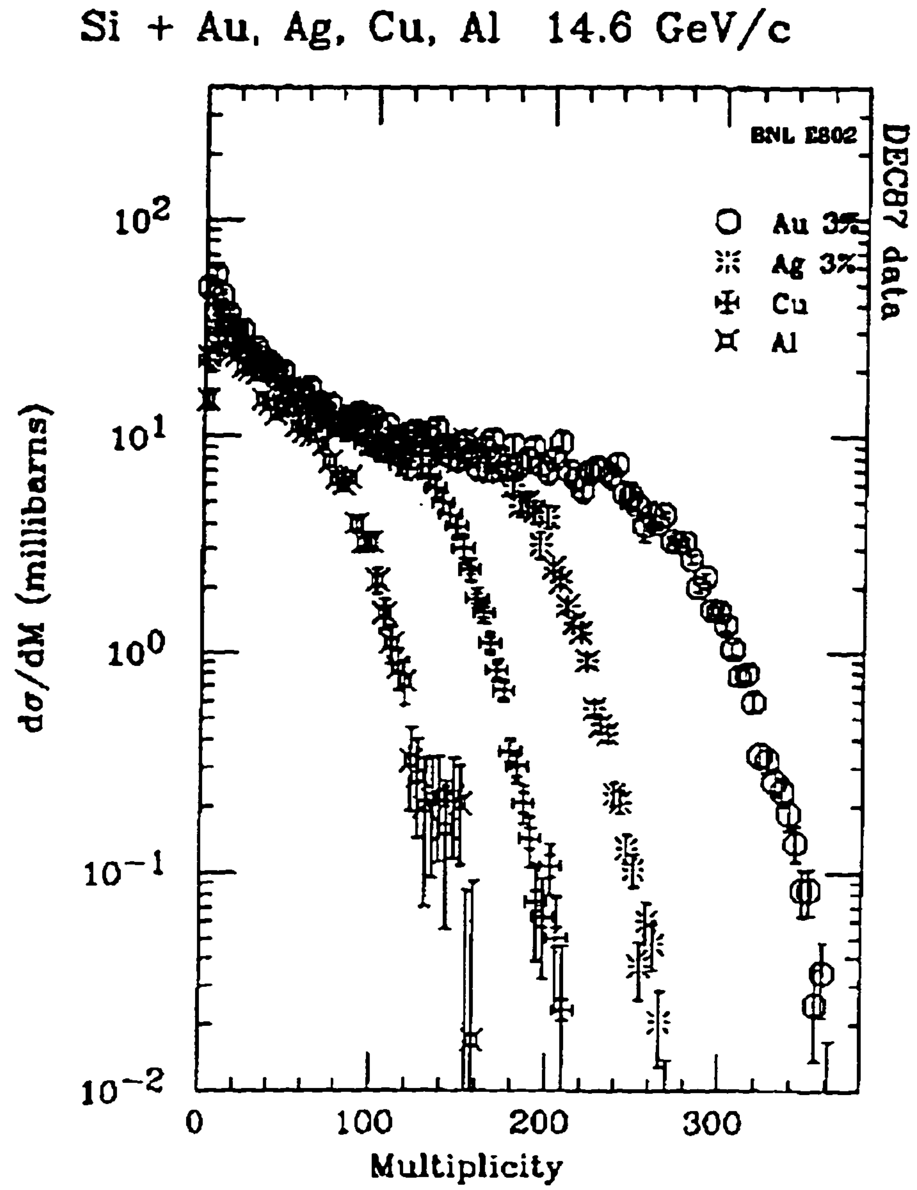

Figure 4.19: Target mass dependence of the transverse energy (E_T) flow (E802).

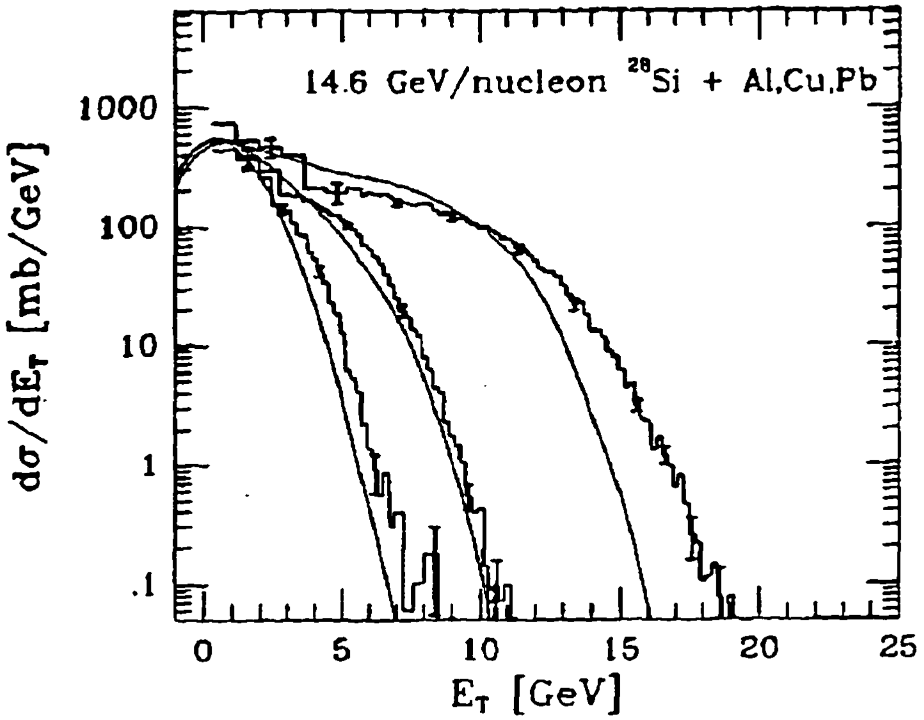

Figure 4.20: Experimental transverse energy distributions from E814 for 14.6 GeV/nucleon Si beams for pseudorapidities of $-0.5<\eta<0.9$. The lines are the results from the Landau fireball [88].

4.7 Positive - negative track correlations

In a central Si on Pb collision at the AGS (14.6 GeV/c per nucleon) we expect to form a fireball which expands, cools, freezes out and the particles leave the composite system and reach the detector. By studying the properties of the particles at freeze out, such as their composition and momentum distribution, we try to deduce the earlier history of the system.

Earlier we calculated the “temperatures” (inverse slopes) of negative pions and protons and we would like to use this information and try to come up with a “freeze-out temperature”. We call the “temperatures” we presented earlier as “apparent” temperatures. Those apparent temperatures are not necessarily the freeze out temperatures.

Looking at the temperatures of protons and negative pions we observe that the proton inverse slopes vary more rapidly with rapidity than pions. Many [73] have pointed out that much of the apparent temperature may come from flow. Such complications (flow) may be present at the AGS. Flow could give an explanation for the difference in the inverse slopes of protons and negative pions since flow has a relatively small effect on the relativistic pions but a substantially larger effect on the not yet relativistic protons Some flow would have greater effect on protons than in pions. If the pions and the protons are emitted from a common thermal bath, they have the same kinetic energy but since protons are much heavier than pions, flow should have greater effect on the protons than the already relativistic pions. One method of deducing the freeze out temperature would be to study a system of pions and protons at equilibrium and add at the end a flow effect such that the final apparent temperatures would be the same with those observed in the data. Such attempts have been carried out in [73] and the freeze out temperature was determined to be around 110 MeV.

The above explain the difference in the temperature between protons and pions (also the K^+ temperature is in between the proton and pion temperature). In pp and pA collisions we have seen : $T(p) \approx T(K^+) \approx T(\pi)$. Thus in pp and pA collisions we do not see the difference in the temperature as we do in Heavy Ion collisions. This is not inconsistent with the flow effect. But this does not explain the temperature of K_s and Lambda being not much different. The above explanation of flow does not take into account the fact that there are final state interactions among the emitted particles created in the collision. A way to include these effects is to introduce the mean-free path for all particle species. Due to the fact that $\sigma_{NN} = 40$ mb and $\sigma_{\pi N} = 100\text{-}200$ mb the mean free path for protons is much larger than that of pions; for K^+, $\sigma_{KN} = 10$mb. So, the created fireball expands until freeze out. As it expands it cools off. So if one assumes that the kaons and the protons leave the expanding fireball earlier than the pions due to different mean free paths then the kaons and the protons must have a higher temperature because they probe an earlier and hotter stage of the fireball. In the case of thermal equilibrium we would expect to have the same temperature for all particle species, provided they all freeze out at the same time. To summarize, some possible reasons to explain the different temperatures for different particle species are : outward flow, different mean-free paths, resonance decay, even QGP.

All the above "temperatures" were obtained by an exponential fit to the transverse mass distributions of the particles. Maybe we should try to get to the temperatures using a different approach. A method of determining the freeze out temperature is making use of the low m_T enhancement in the pion distribution [73]. The source of the low m_T pions seen at various experimental data has been identified as the Δ decay. Pions from the decay of Δ's show a different transverse mass distribution than direct pions. From the low m_T enhancement of pions the number of Deltas can be estimated and from the ratio of Deltas to nucleons the freeze out temperature can be deduced. They conclude that the freeze out temperature of pions is around 150 MeV. Thus in [73] the low p_T pions from Δ decay are proven to be a good thermometer for the true temperature reached in relativistic heavy ion collisions at the AGS. In what follows we try to determine the pion temperature in a similar way: using proton - pi minus correlations.

4.7.1 The method

The method to extract the freeze out temperature using proton - pi minus correlations is the following: we use the thermal model to determine the relative populations of excited nucleon states as a function of the temperature. We are considering the following states: ground state nucleons (protons and neutrons), Δ(1232), N*(1500) and N*(1700). Considering a system with the above states in thermal equilibrium, the population of each state is given by:

$$\rho_i = \frac{g_i}{2\pi^2}\int_0^\infty \frac{p^2}{\exp(\beta(\varepsilon_i - \mu)) + 1} dp \qquad (4.11)$$

where g_i in the degeneracy of each energy level, ε_i the corresponding energy and μ the chemical potential. Figure 4.21 shows the population of excited and ground state of nucleons as a function of temperature. Using Clebsch - Gordon coefficients and data we determine the decays of Δ and N*'s. We decay Δ's to Nπ and N*s to Nπ and Nππ. If f_1 is the fraction of nucleons in the Δ(1232) state, f_2 in N*(1500), f_3 in N*(1700) and f_0 in the ground state, then the ratio of correlated proton - pi minus pairs to protons, the ratio of correlated proton - pi plus pairs to protons and the ratio of negative pions coming from excited nucleons to protons are given as a function of temperature (appendix 6) by:

$$\frac{p\pi^-}{p} = \frac{1}{6} f_1 + 0.73 f_2 + 0.77 f_3 \tag{4.12}$$

$$\frac{p\pi^+}{p} = \frac{1}{2} f_1 + 0.22 f_2 + 0.30 f_3 \tag{4.13}$$

$$\frac{\pi^-}{p} = \frac{\pi^+}{p} = \frac{2}{3} f_1 + 0.94 f_2 + \frac{16}{15} f_3 \tag{4.14}$$

$$f_0 + f_1 + f_2 + f_3 = 1 \tag{4.15}$$

At low temperatures most of the nucleons are in the ground state and only a few in excited states. Figure 4.22 shows the dependence of (4.12) - (4.14) on the temperature. Our goal is to determine in the data the ratio of π^- that come from excited baryons to protons, and using figure 4.22, to extract the freeze out temperature. Since in the data we don't know which pions are directly produced and which come from the decay of excited nucleons the use of a model (event generator) is essential. Thus, the temperatures extracted are model dependent.

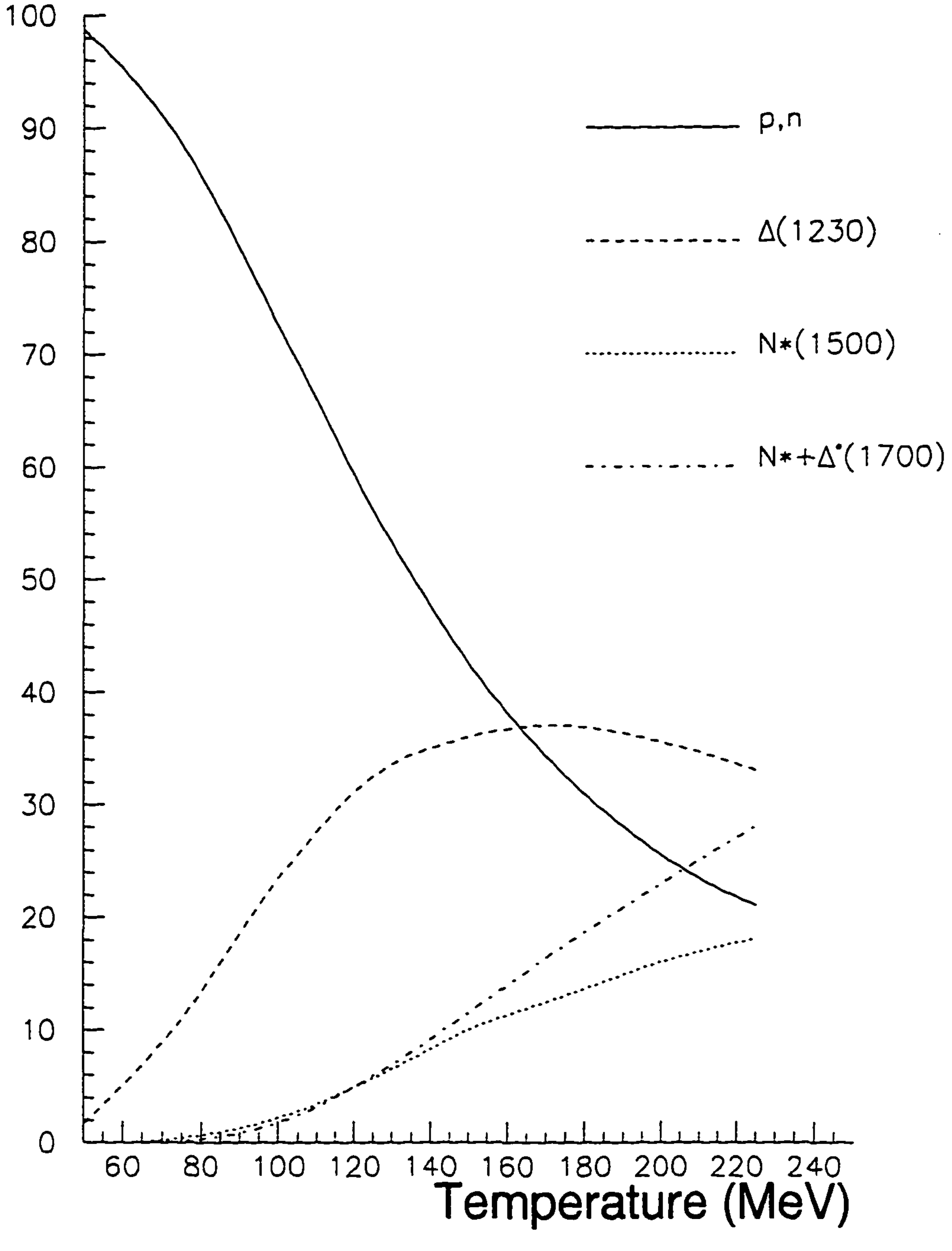

Figure 4.21: Relative population of excited and the ground state of nucleons as a function of the temperature.

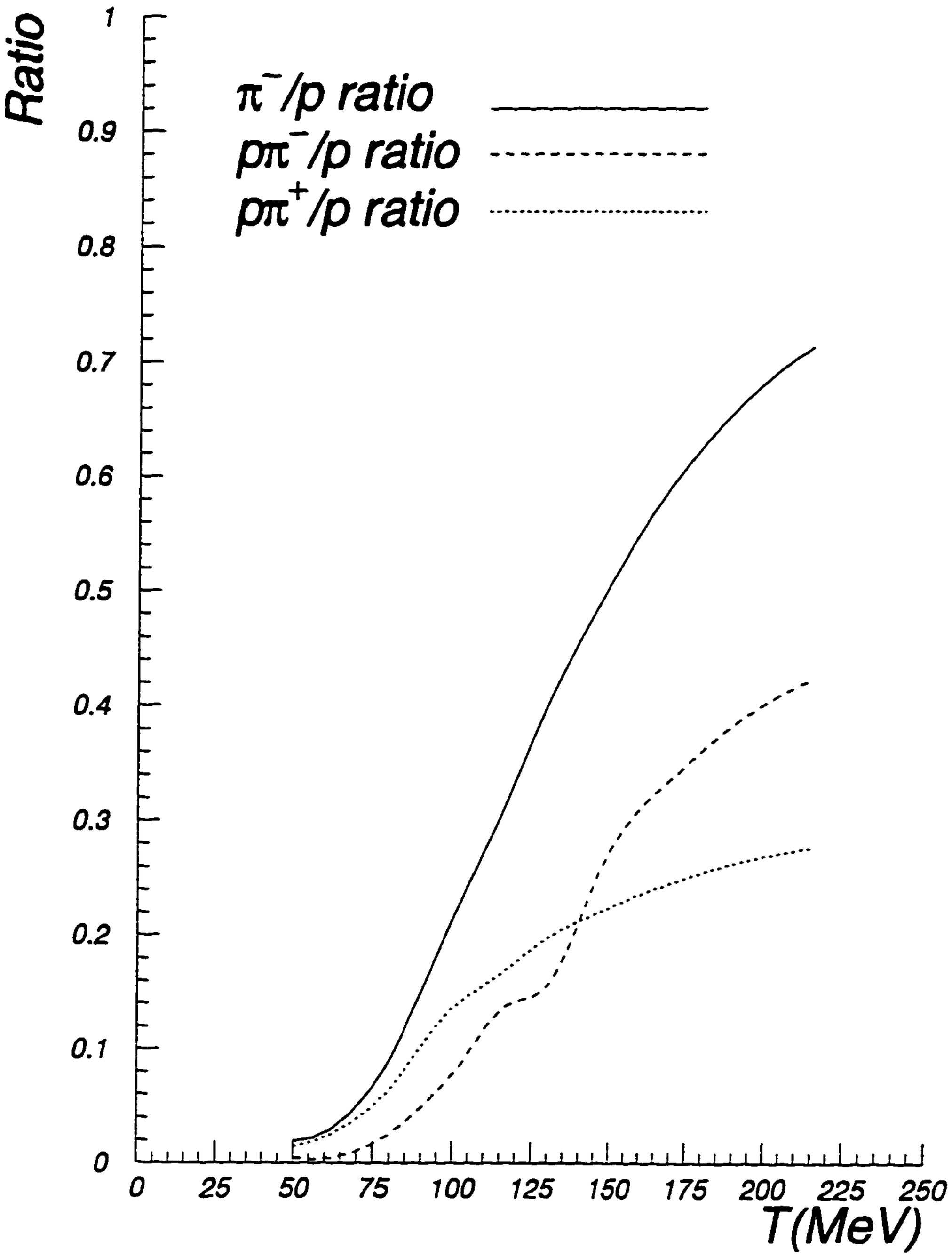

Figure 4.22: Dependence of the π^-/p, π^-p/p and π^+p/p ratios on the temperature.

4.7.2 Analysis

First we extract and try to understand the proton - pi minus correlation in the data. Since our detector did not provide particle identification, to study proton pi minus correlations we selected as negative pions all the negatives and all the positives with rapidity greater than 2.7 as protons. We checked our assumption for the protons with both data and Monte Carlo and we concluded that is a safe assumption since we found only a small contamination (around 7%), mostly from positive pions. Proton - pi minus pairs within the same event were treated as signal, while pairs from different events were used to estimate the background. The tails of background and signal effective mass distributions with $m_{eff} > 1.5$ GeV/c^2 were used to normalize our signal. The correlation is shown in figure 4.23.

A first interpretation for the observed correlation is that it comes from the correlation of pions with forward going protons. It is possible that the observed correlation may be a result of a multibody correlation. This idea came after we separated the data events into two groups: one with more stopping (2 or less protons in the forward region with rapidity greater than 2.7, 75% of all the data events) and one with less stopping (3 or more protons in the forward region, the remaining 25% of the data). The correlation was mainly driven by the data sample with the less stopping. We believe that the correlation is driven by pions which are emitted by forward moving excited nucleons.

To check the idea we started extensive Monte Carlo simulations. We observed that the rapidity distribution of pions in the data follows that of the protons. For the data sample with the more stopping the pions were distributed around mid-rapidity, while in the less stopping events the pion distribution was spread over a larger range in y. Since the correlation is driven by the less central events, one naively could get the number of pions emitted by forward moving excited nucleons by simply subtracting the two pion distributions (normalized for the same number of events). Of course it is also possible that the change in the rapidity distribution of pions is not only due to the decay of excited nucleons but the distribution of directly produced pions (from rescattering) could change. Using the HIJET [57, 58] event generator we studied the emission of pions from excited nucleon states. We reduced the nucleon - nucleon cross section by 30% in 25% of the events to study the forward moving excited nucleons. Although the observed proton - pi minus correlation was reproduced, we discovered that the above subtraction of the two pion rapidity distributions is not guaranteed to give us the correct number of pions. Which means that the directly produced pions (not coming from decays) could contribute to the correlation and thus, in order to determine the ratio of pi minus over proton, a simple subtraction of the rapidity distributions of negative pions for the two data sets would be inaccurate.

We decided to use the widely accepted RQMD1.08 [89]. Si on Pb RQMD events were generated and the observed correlation was reproduced. In order to study the source of the negative pions that lead to the correlation we stopped the excited nucleons from decay and we decayed them at the end of the event. The number of negative pions were counted and from the p minus over proton ratio we determined the temperature. We would like to develop a method of counting the pions that we could apply to the data, since in the data we cannot know the source of the emitted pions. Using RQMD1.08 we separated the Si on Pb event into two different groups (with less and with more stopping). From the rapidity distribution of pions for the two event sets, we scaled the the rapidity distribution of the more stopping set to equal that of the less stopping at y = 1.7. Subtracting the two rapidity distributions we get $(\Delta\pi) = 4300$. We repeat the same procedure for direct pions, pions that come from the decay of forward baryon and pion that come from the decay of central baryons. We get: $(\Delta\pi)_{dir} = 2200$; $(\Delta\pi)_{forw.} = 1500$ and $(\Delta\pi)_{centr.} = 800$. We get $\Delta\pi \approx (\Delta\pi)_{dir} + (\Delta\pi)_{forw.} + (\Delta\pi)_{centr.}$. We know that there are 4400 decay pions from the forward going baryons in the total event sample (all the RQMD events). With this study we show that the substraction procedure gives the total number of negative pions coming from the decay of excited baryons. We went back to the data and we counted the number of negative pions by subtracting the two rapidity distributions. Then we did acceptance corrections and the final result is shown in figure 4.24.

π^-/p ratio		Temperature (MeV)
E810 data	0.102 ± 0.003	82
RANDOM	0.122	85
RQMD	0.158 ± 0.012	90

Table 12: π^-/p ratios and the corresponding temperatures.

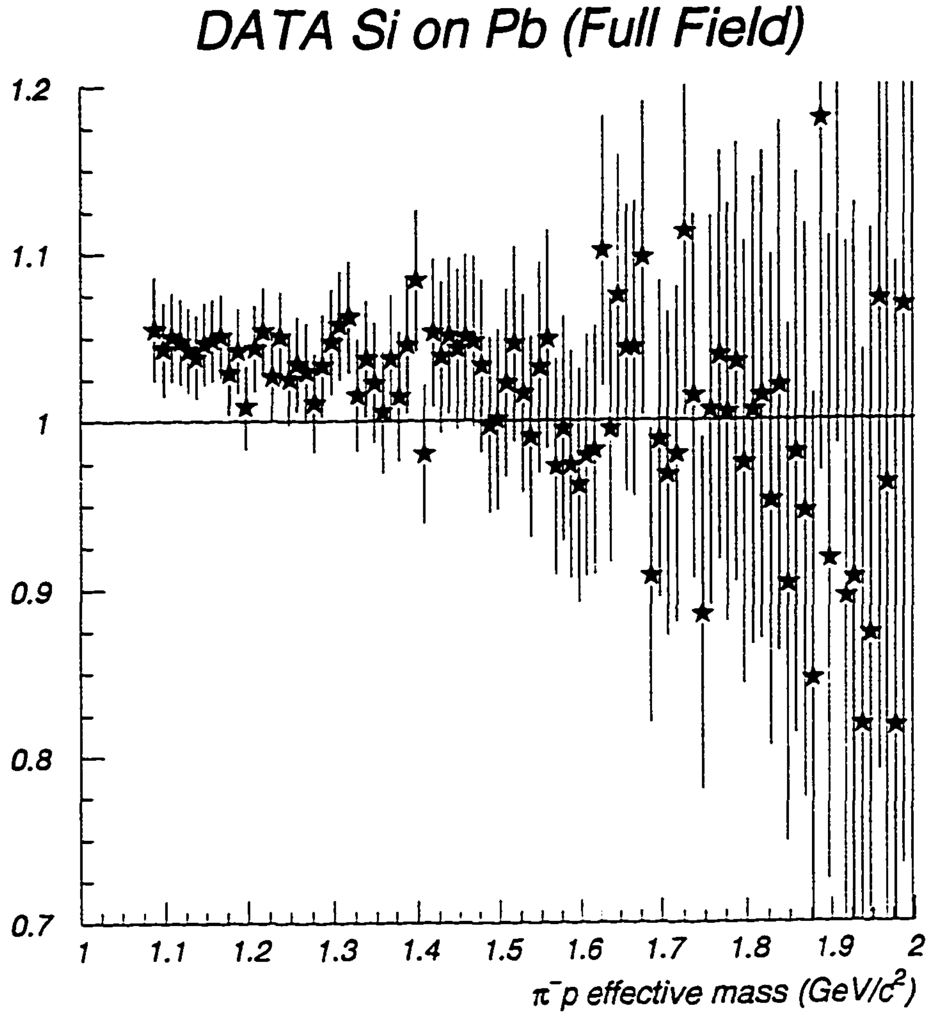

Figure 4.23: Correlation of protons with negative pions in the E810 data (Si on Pb).

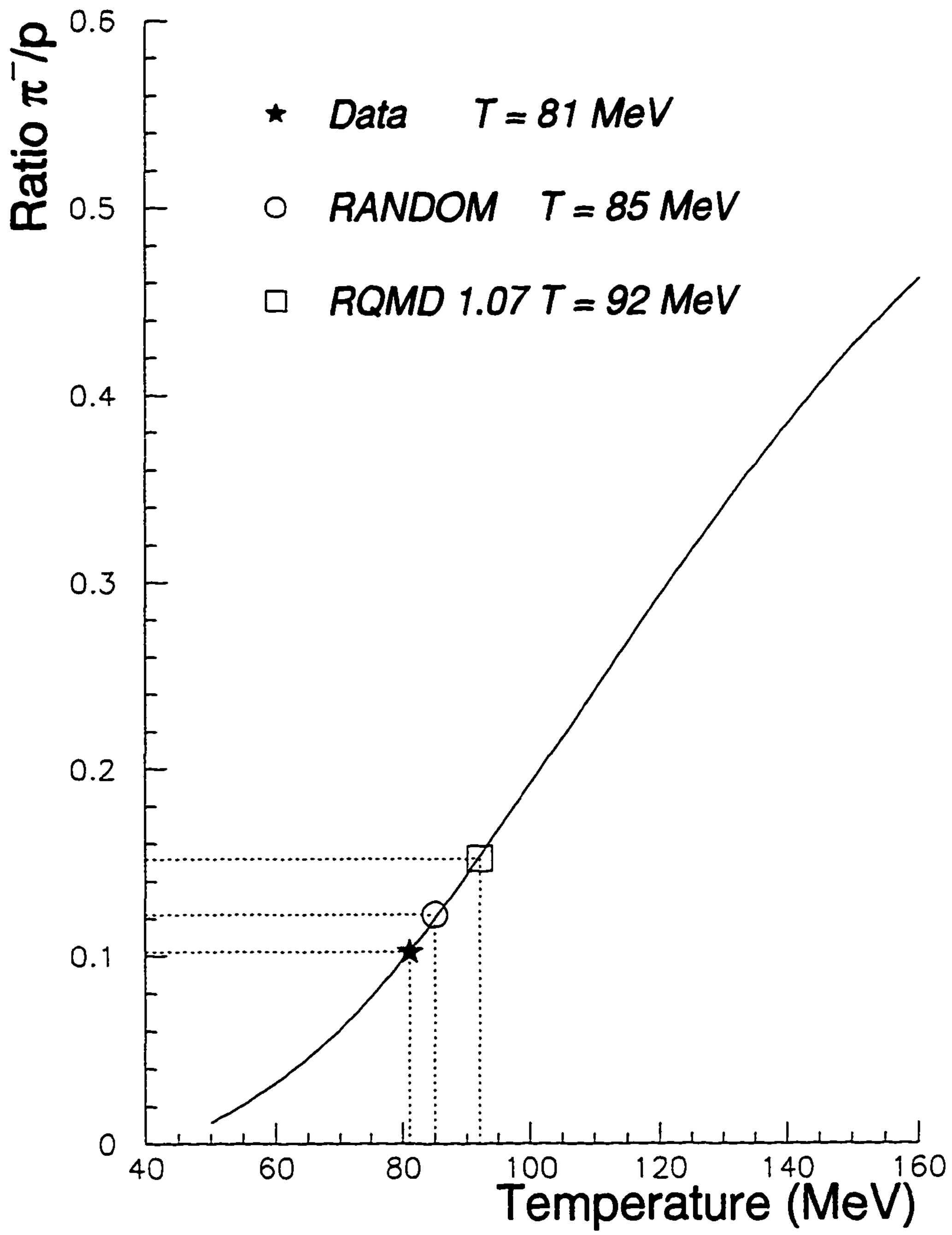

Figure 4.24: Temperature calculations based on proton - negative pion correlations for E810 data and event generators RANDOM and RQMD.

Ithaca has given you the beatiful voyage.
Without her you would never have taken the road.
But she has nothing more to give you.

And if you find her poor, Ithaca has not defrauded you.
With the great wisdom you have gained, with so much experience,
you must surely have understood by then what Ithacas mean.
Konstantinos Kavafis ("ITHACA")

5. CONCLUSIONS

This thesis work was concentrated on the production of positive and negative particles in Si on Pb collisions at the Alternating gradient Synchrotron (AGS) at Brookhaven National Laboratory (BNL). Relativistic heavy ion collisions, such as those of Si on Pb at the AGS, provide a unique experimental tool to study matter at extreme conditions of density and/or temperature. The goal of such experimental studies is to observe a theoretically predicted phase transition from normal nuclear matter to a phase of deconfined quarks and gluons, known as Quark-Gluon Plasma (QGP). I must point out that as of today there have been proposed several signals of such a phase transition, but there is no ultimate signal, that when seen, would guarantee that such a phase transition has occurred. The lack of such an ultimate signal, represents the need for a better understanding of the dynamics involved in relativistic heavy ion collisions. Studies of the characteristics of the production of positive and negative particles, such as the one performed in this thesis, are needed to give us some insight on the mechanisms involved in heavy ion collisions.

In this thesis, I presented the results of the analysis of 12051 central (high multiplicity) Si on Pb events. The Si and the Pb nuclei collided at an energy of around 5.4 GeV per nucleon at the center of mass. Si on Pb collisions are not symmetric and thus we cannot take advantage of the symmetry of the system, as we would in Si on Si or Au on Au collisions. At the time of the experiment the AGS could not provide Au beam. The E810 experimental setup covered the forward hemisphere in the nucleon-nucleon center of mass frame. Since no particle identification techniques were used to identify particles, all negatives were treated as pions by assigning the pion mass to them to calculate their variables, such as rapidity and transverse mass. The source of contamination to our pion sample was mainly due to negative kaons. We applied techniques involving measurements of other experiments and Monte Carlo event generators to get an estimate of this type of contamination. The pions observed in these events have the characteristics of pions emitted from a thermal source. This was supported by the fact that their rapidity distribution is peaked at midrapidity. Collective effects, such as flow, may be present, but in order to study such effects one should look in the heavier protons rather than the light pions. If pions and protons are emitted from a thermal bath, collective effects have a greater impact on the heavy protons than the already relativistic pions. The thermalization of pions was expected since the pion - nucleon cross section is large and thus pions do not escape easily the hot dense fireball created in these collisions. Using the observed rapidity distribution of pions, we compared to the production of pions in other systems (such as Si on Si, proton on proton) and other energies. One of the conclusions of the comparison is that rescattering plays an important role in the production and absorption of pions in heavy ion collisions. Pions are absorbed by being retained in excited nucleons (such as Δ's and N*s). This effect was verified in our pion transverse mass distribution. The source of the low transverse mass enhancement in the pion spectrum is Δ's and N*s resonances (this is how event generators reproduced the observed enhancement, although this does not necessarily mean that this is the only source of the pion enhancement). As far as the multiplicity of negative pions is concerned, we estimated an average of 0.6 negative pions (or 1.8 pions) produced per participating nucleon in Si on Pb collisions at the AGS.

The same variables were studied for the protons. The proton spectrum was extracted after subtracting the negatives (with proton mass) from the positives. Inverse slopes were extracted by fitting the transverse mass spectra with exponential and Boltzmann functions. The proton rapidity distribution reflects the amount of stopping. Our data indicate that there is a large amount of stopping at the AGS. The projectile Si protons are stopped in the target depositing their energy and creating a region of high baryon density. Although the baryon density at the AGS has reached large values none has ever claimed to have seen, beyond any reasonable doubt, signals of a phase transition to QGP. Strangeness enhancement, which has been proposed as a signal of such a transition, has been observed by several experiments at the AGS including E810. Most of the “unusual” phenomena seen at the AGS have been reproduced by event generators using regular hadronic physics. The retention of pions in excited nucleons, mentioned earlier, could lead to enchanted strangeness production.

The RANDOM event generator was mainly developed to help us understand the production of strangeness at the AGS. RANDOM reproduced many of the characteristics of the production of strangeness at the AGS by adjusting the number of collisions per event at the decay time of resonances. The large number of collisions (2000 collisions per event) required to reproduce the strangeness production in Si on Pb collisions may be an indication that chemically equilibrated fireball is created or that some QGP scenario is required to explain the data (in particular the Ξ^-/Λ ratio measured in our data).

Many have pointed that the estimates of the “Temperature” of the system by using exponential and Boltzmann fits to transverse mass spectra are inaccurate (figures 4.10 and 4.15). These estimates may of decay pions. In other words, temperatures extracted based on the decay of excited nucleons give model dependent answers.

Before closing this last section of my thesis I would like to note that we are all looking forward to the beginning of the RHIC era (Relativistic Heavy Ion Collider). At RHIC we will have the opportunity to study matter at energy densities that approach 100 times that of regular hadronic matter. As we are getting closer to collecting data with RHIC, we need to get a better understanding of the Physics that we expect to study at RHIC, understand what our capabilities are with the available facilities and get the prerequisite training to be able to study exciting new Physics.

Appendix 1

System of natural Units

The right choice of units for describing a certain set of phenomena has the advantage to simplify the analysis of the phenomena, to simplify the calculations involved, and to estimate a characteristic scale by the order of magnitude. At the same time, unusual units are a hindrance for an outsider trying to understand special literature. Here I present some characteristics of the system of natural units that is being used extensively in particle physics (in which $\hbar$=c=1) and compare it to the International System of units (SI).

The physics of elementary particles deals with quantum relativistic phenomena, so it is natural to use the quantum of action $\hbar$ for the unit of action and the velocity of light c for the unit of velocity. Since both these quantities are universal constants, it is natural to take the next step and assume them to be unities. From $c = \mathbf{r}/t$ we see that the dimensions of the spatial coordinates **r** and time t are identical: $[\mathbf{r}] = [t]$[*]. The dimension of Energy E, momentum **p** and mass m are also identical: $[E] = [\mathbf{p}] = [m]$. Moreover, if we take into account the relation between momentum and wavelength: $\mathbf{p} = 2\pi\hbar/\lambda$, then it is obvious that:

$$[\mathbf{r}^{-1}] = [t^{-1}] = [\mathbf{p}] = [E] = [m]$$

Also, $\hbar c \cong 197\, MeV fm = 1 \rightarrow \boxed{1\, fm = (200\, MeV)^{-1} = (0.2\, GeV)^{-1}}$

Cross sections are measured in barns: $1\ barn = 10^{-24}\ cm^2 = 100\, fm^2$.

And from $\hbar \cong 0.7 \cdot 10^{-24}\ GeV\, sec \rightarrow \boxed{1\ GeV^{-1} \cong 0.7 \cdot 10^{-24}\, sec}$

---

[*] Square brackets designate the dimension of the enclosed physical quantity.

The Boltzmann constant k_B is the factor for converting from Kelvin degrees (K) to energy units: $k_B \cong 1$ eV/ 11604K. Setting $k_B = 1$ we get: $\boxed{1\text{eV} \cong 11604 \text{ K}}$

Lets consider the motion of an electron with momentum p (GeV/c) along an orbit with radius ρ meters in a transverse magnetic field with strength H (Tesla). In SI units:

$$p = e H \rho$$

Then, multiplying both sides by c, we have:

$$\boxed{pc \text{ (GeV)} \cong 0.3 \text{ H (Tesla) } \rho \text{ (meters)}}$$

We used: $1 \text{ e Tesla m} = 1 \text{ e V sec m}^{-2} \text{ m} = 1 \text{ eV s m}^{-1}$ and $10^{-9}\, c\, sec\, m^{-1} \cong 0.3$

Appendix 2

Energy density of gluons

Assuming that the gluons and the light quarks are essentially massless particles, at least on the scale of energies available in the hot plasma, i.e. 200 MeV, and neglecting the interactions among the constituents of the plasma (except for the assumption of thermalization which is a result of their presence) we can get an estimation of the energy density of the gluons in the plasma state [18]. The number of degrees of freedom for the gluons are :

$$N_g = 2\ (\text{spin}) \times 8\ (\text{colour}) = 16$$

We now calculate the energy density residing in each degree of freedom. The gluons form an ideal relativistic Boson gas at temperature $\beta = 1/T$.

$$\begin{aligned}
E_g &= \int \frac{d^3p \cdot d^3r}{h^3} \frac{E}{e^{\beta E} - 1} \\
&= V\int_0^\infty \frac{4\pi p^2 dp}{(2\pi)^3 \hbar^3} \frac{cp}{e^{\beta cp} - 1} \\
&= \frac{V}{2\pi^2} \int_0^\infty \frac{p^3 \cdot dp}{e^{\beta p} - 1} = \frac{VT^4}{2\pi^2} \int_0^\infty \frac{x^3 dx}{e^x - 1} \\
&= \frac{VT^4}{2\pi^2} \int_0^\infty \frac{x^4}{e^x + 1} dx \\
&= \frac{VT^4}{2\pi^2} \Gamma(4)(\frac{1}{1^4} + \frac{1}{2^4} + \frac{1}{3^4} + \ldots.) \\
\varepsilon_g &= \frac{T^4}{2\pi^2} \Gamma(4) \frac{\pi^4}{90} = \frac{T^4}{2\pi^2} 6 \frac{\pi^2}{90} = \frac{\pi^2 T^4}{30}
\end{aligned}$$

Thus for 16 degree of freedom we get : $\varepsilon_g = \frac{8}{15}\pi^2 T^4$

Using $\hbar c \cong 200$ MeV fm, then in natural units: $\hbar c=1$ and thus: 200 MeV = 1/fm. So at T = 200 MeV we get: $\varepsilon_g \cong 5$ MeV/fm^3.

<u>NOTE</u>: For <u>pions</u> in high temperature (so that we consider them as massless, $T \gg m_\pi$) we get, for 3 degrees of freedom:

$$\varepsilon_\pi = \frac{\pi^2}{10}T^4$$

Appendix 3

Calculation of Fermi Energy for Nucleons and quarks

If N$_f$ are the number of degrees for nucleons, then:

$$\int_0^{p_F} N_f \frac{d^3N}{h^3} V = N$$

For N$_f$ = 2, we get:

$$2\int_0^{p_F} \frac{4\pi p^2 dp}{h^3} = \rho_{num}$$

$$2\frac{4\pi}{h^3}\frac{p_F^3}{3} = \rho_{num}$$

$$p_F = \sqrt[3]{\frac{3h^2}{8\pi}\rho_{num}}$$

$$cp_F = \hbar c\sqrt[3]{3\pi^2\rho_{num}}$$

Using $\hbar$c ≅ 200 MeV fm and ρ_{num}= 0.15nuclons/fm^3 we get E$_f$=350 MeV

Fermi energy for quarks:

Using the procedure for light quarks we get:

$$\frac{N_q}{h^3}\frac{4\pi p_F^3}{3} = \rho_{num}^q$$ for light quarks, and

$$\frac{N_N}{h^3}\frac{4\pi p_{F,N}^3}{3} = \rho_{num}^N$$ for nucleons, where N$_q$ and N$_f$ are the number of degrees of freedom for quarks and nucleons respectively, and $p_{F,N}$ is the Fermi momentum for nucleons calculated above. Dividing the above relations we get:

$$p_F^q = p_F^N \left(\frac{\rho_{num}^q}{\rho_{num}^N}\right)^{\frac{1}{3}} \left(\frac{N_N}{N_q}\right)^{\frac{1}{3}}, \quad \text{or } p_F^q = p_F^N \left(\frac{\rho_0^q}{\rho_0^N}\right)^{\frac{1}{3}} \left(\frac{3}{2\times 3}\right)^{\frac{1}{3}}$$

For $\rho \cong 10\ \rho_0$ we get $p_F^q \cong 500$ MeV at T=0. So, at T=0 $p_F^q > m_s + m_{\bar{s}}$

Appendix 4

List of particle id numbers used in RANDOM

Particle	Symbol	id
proton	p	1120
neutron	n	1220
pion +	π^+	120
pion -	π^-	-120
pion 0	π^0	110
rho +	ρ^+	121
rho -	ρ^-	-121
rho 0	ρ^0	111
eta	η^0	220
omega	ω	221
Kaon +	K^+	130
Kaon -	K^-	-130
Kaon 0	K^0	230
Kaon 0 bar	$\bar{K}^0$	-230
Kaon *+	K^{*+}	131
Kaon *–	K^{*-}	-131
Kaon *0	K^{*0}	231
Kaon *0 bar	$\bar{K}^{*0}$	-231
Lambda	Λ^0	2130
Sigma +	Σ^+	1130
Sigma –	Σ^-	2230
Sigma 0	Σ^0	1230
Cascade 0	Ξ^0	1330
Cascade –	Ξ^-	2330
Omega –	Ω^-	3331

Table 13: List of particle id numbers used in RANDOM

Appendix 5

Cross sections in RANDOM

Here we list cross sections of various processes in RANDOM. Cross sections in the code of RANDOM are calculated in subroutine *rsigma.f.* The same subroutine is used by HIJET and its extensions (like AGSHIJET, HISTAR e.t.c.).

For many of the processes that cross sections are not known or are difficult to calculate we use the Additive Quark Model (AQM). The AQM assigns a factor to each particle (Table 14). Whenever two particles collide their cross section is the product of their factors if their Center of Mass energy is above threshold, and zero otherwise.

Particle	AQM factor
π	4.2
N	6.3
K	3.2
Y (Λ, Σ)	5.3
ϕ	2.5
Ξ	4.3
Ω	3.3

Table 14: AQM factors assigned to particles

Examples of cross sections calculated using the AQM:

NN: $\sigma_{NN} = 40$ mb

πN: $\sigma_{\pi N} = 26$ mb, KN: $\sigma_{KN} = 20$ mb, $\pi\pi$: $\sigma_{\pi\pi} = 17$ mb

πK: $\sigma_{\pi K} = 13$ mb, πY: $\sigma_{\pi Y} = 22$ mb, KY: $\sigma_{KY} = 17$ mb

ϕN: $\sigma_{\phi N} = 16$ mb, $\phi\pi$: $\sigma_{\phi\pi} = 10$ mb, $\phi\phi$: $\sigma_{\phi\phi} = 6$ mb

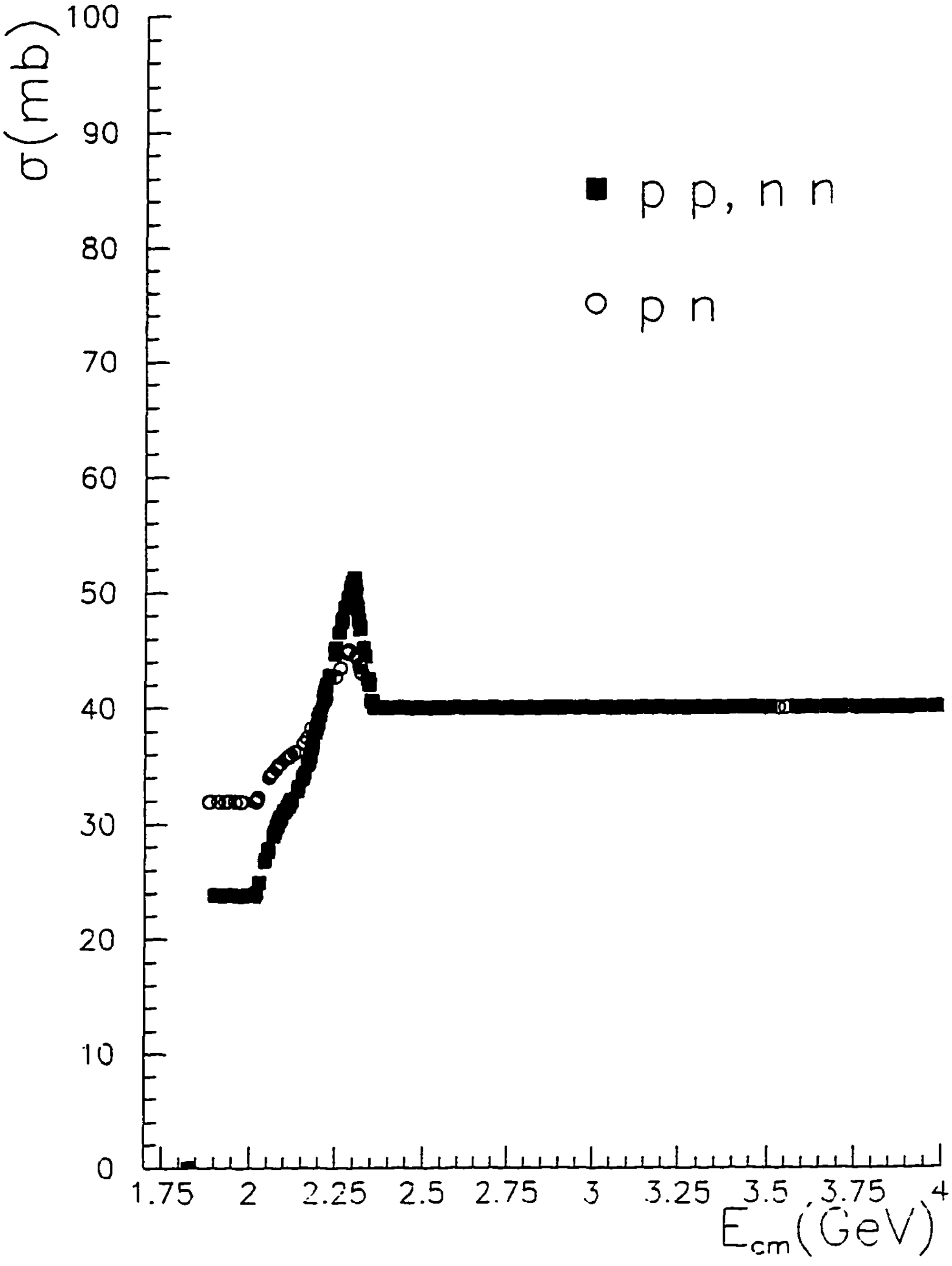

Figure A5.1: Nucleon - Nucleon cross sections.

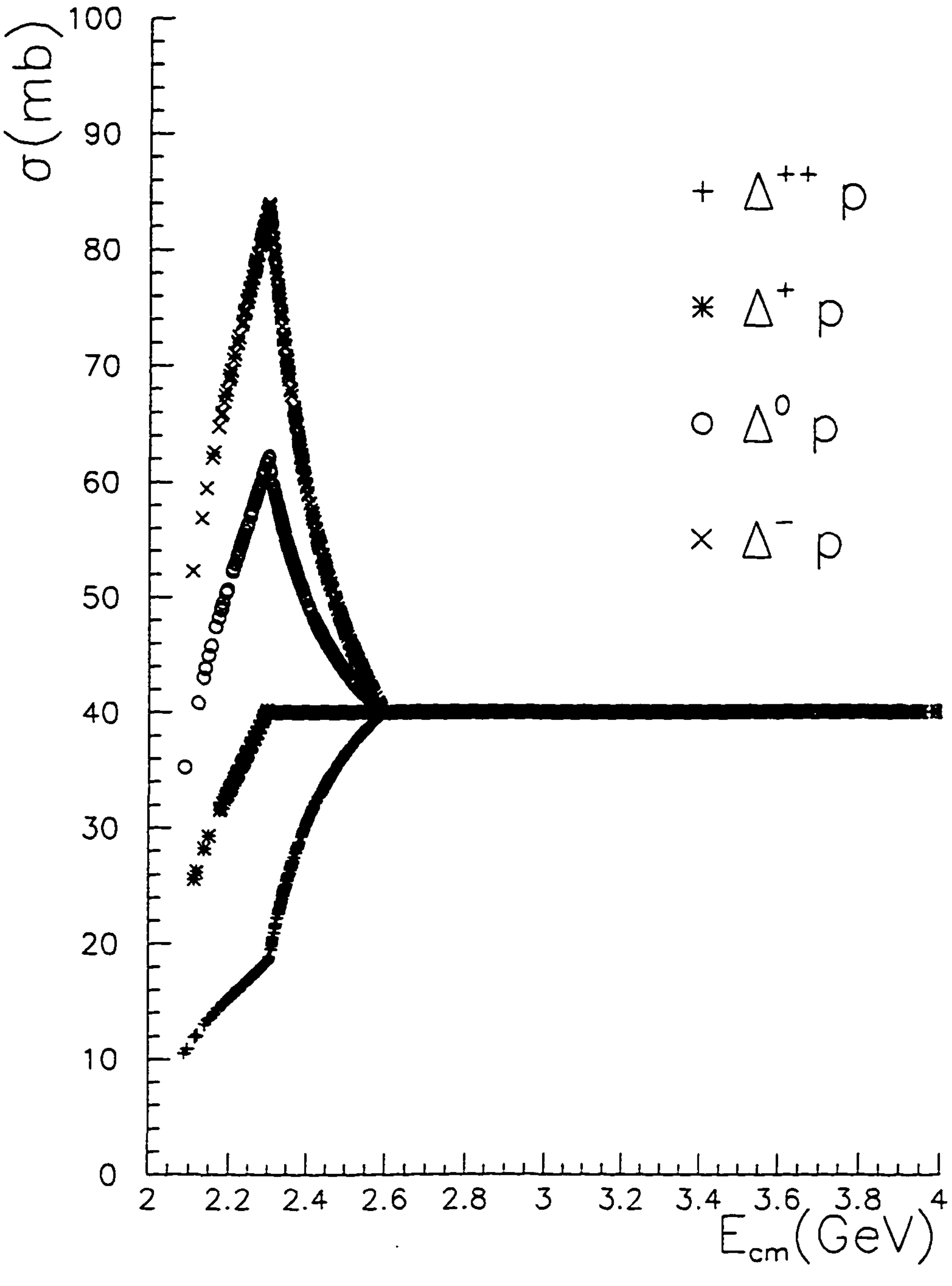

FigureA5.2: Proton - Delta cross sections

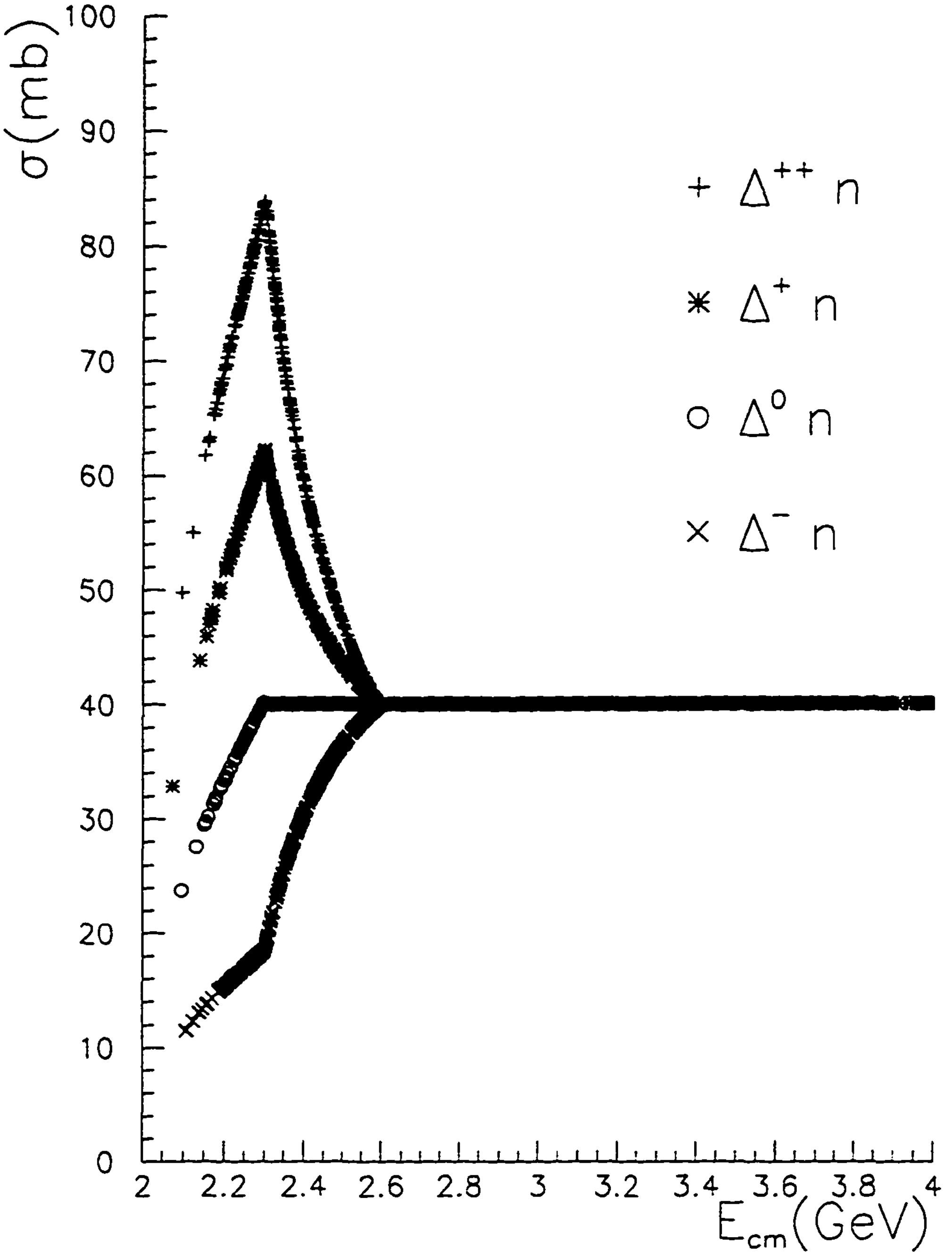

Figure A5.3: Neutron - Delta cross sections

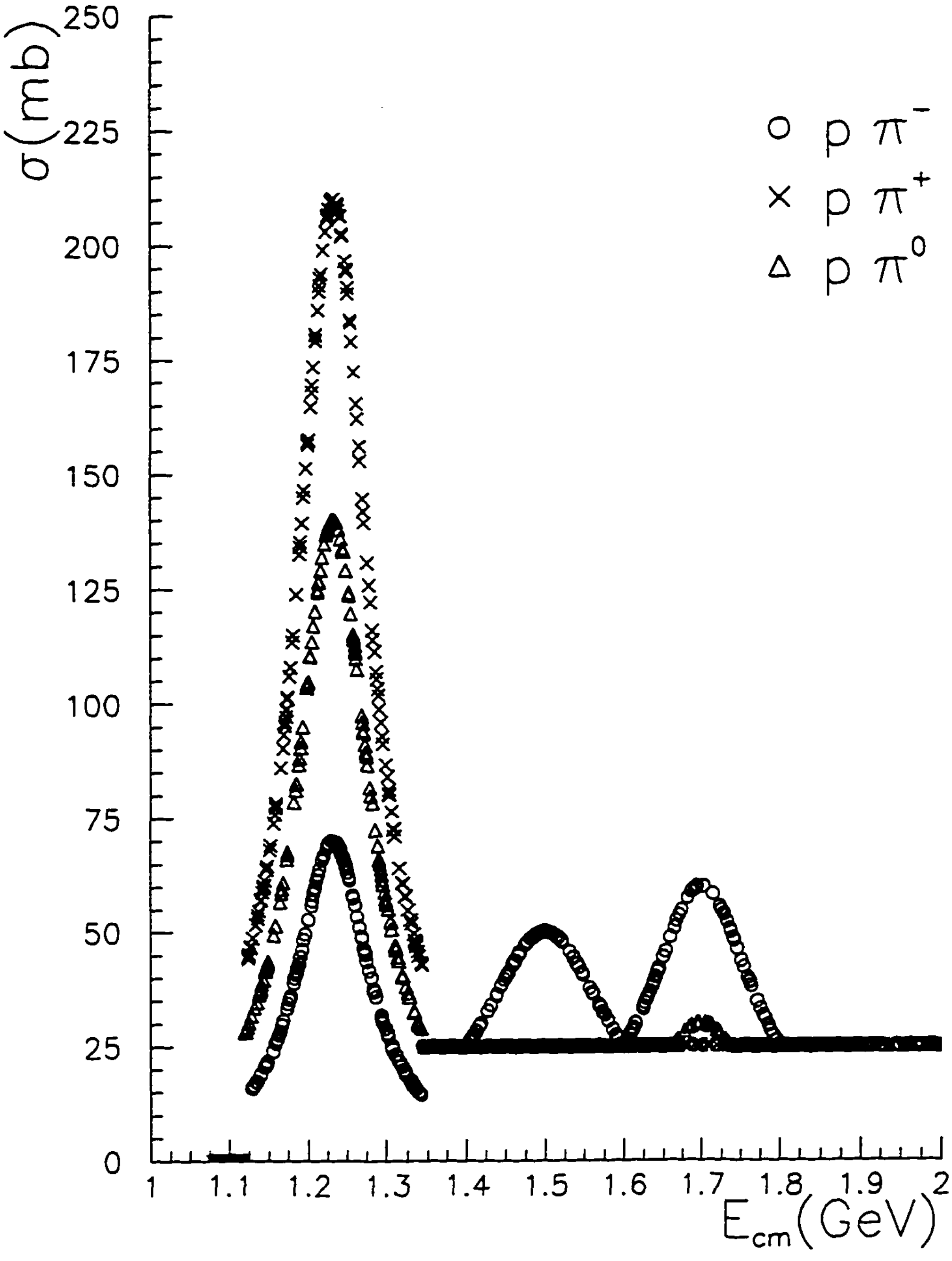

Figure A5.4: Proton - pion cross sections

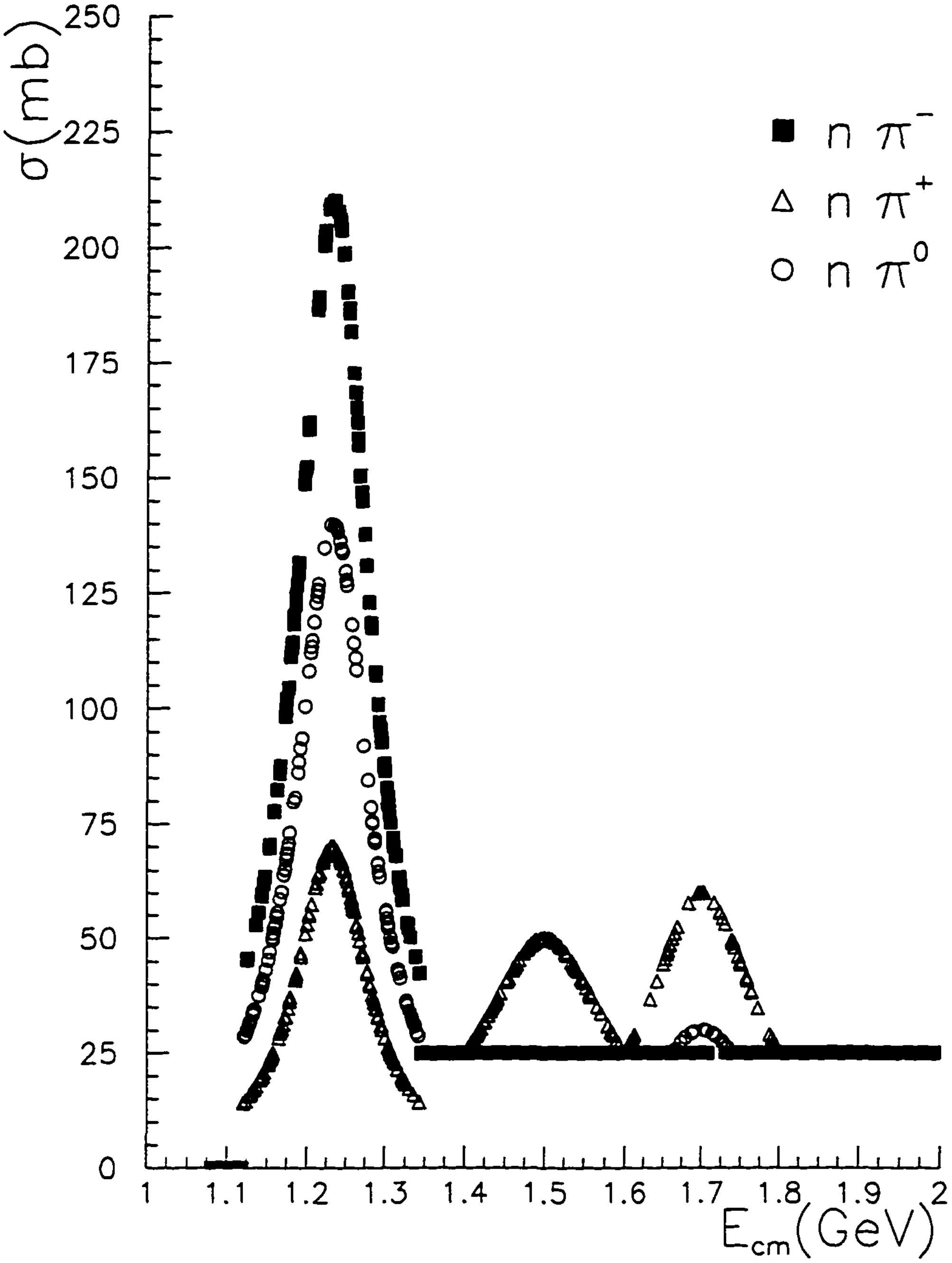

Figure A5.5: Neutron - pion cross section

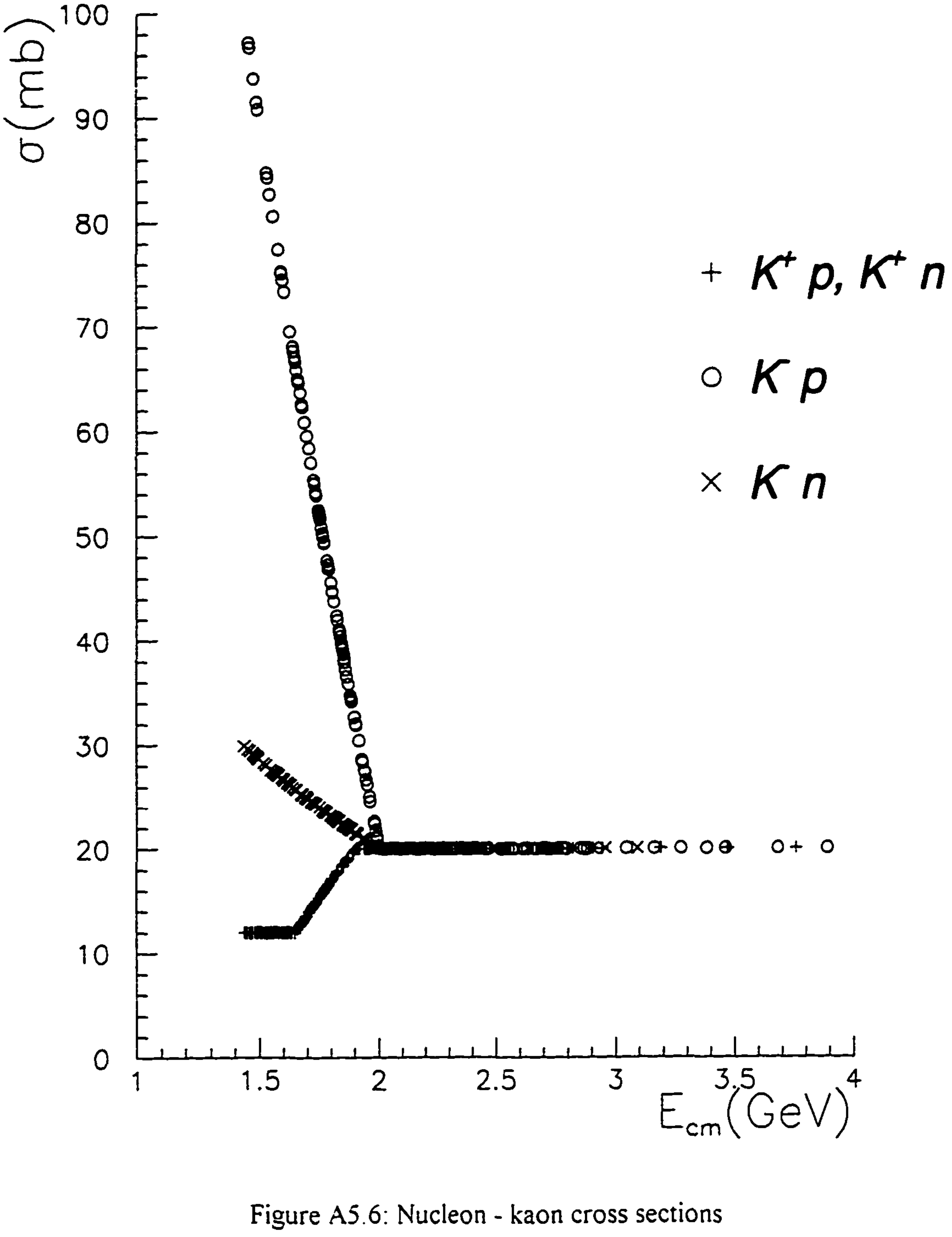

Figure A5.6: Nucleon - kaon cross sections

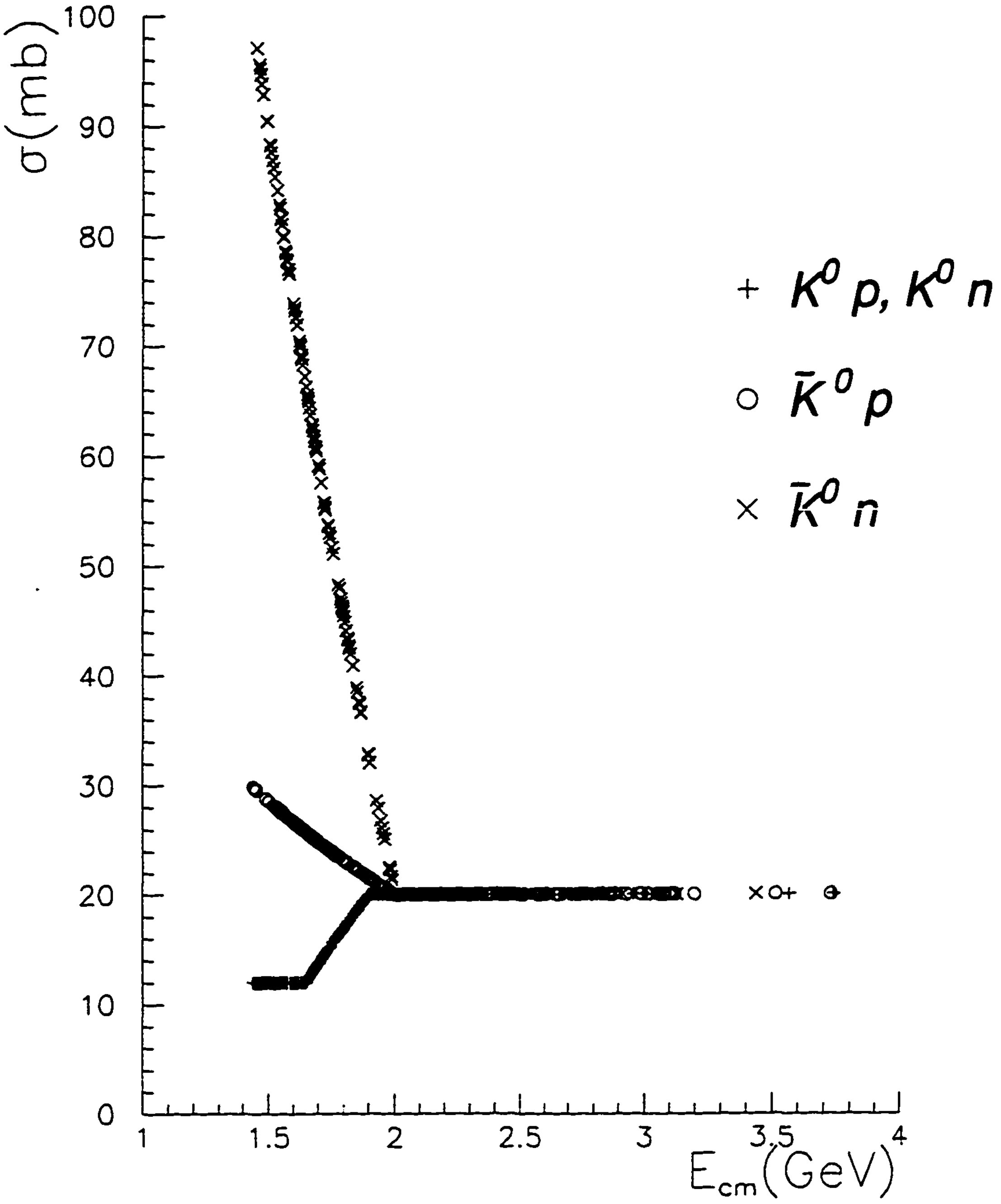

Figure A5.7: Nucleon - Kaon cross sections

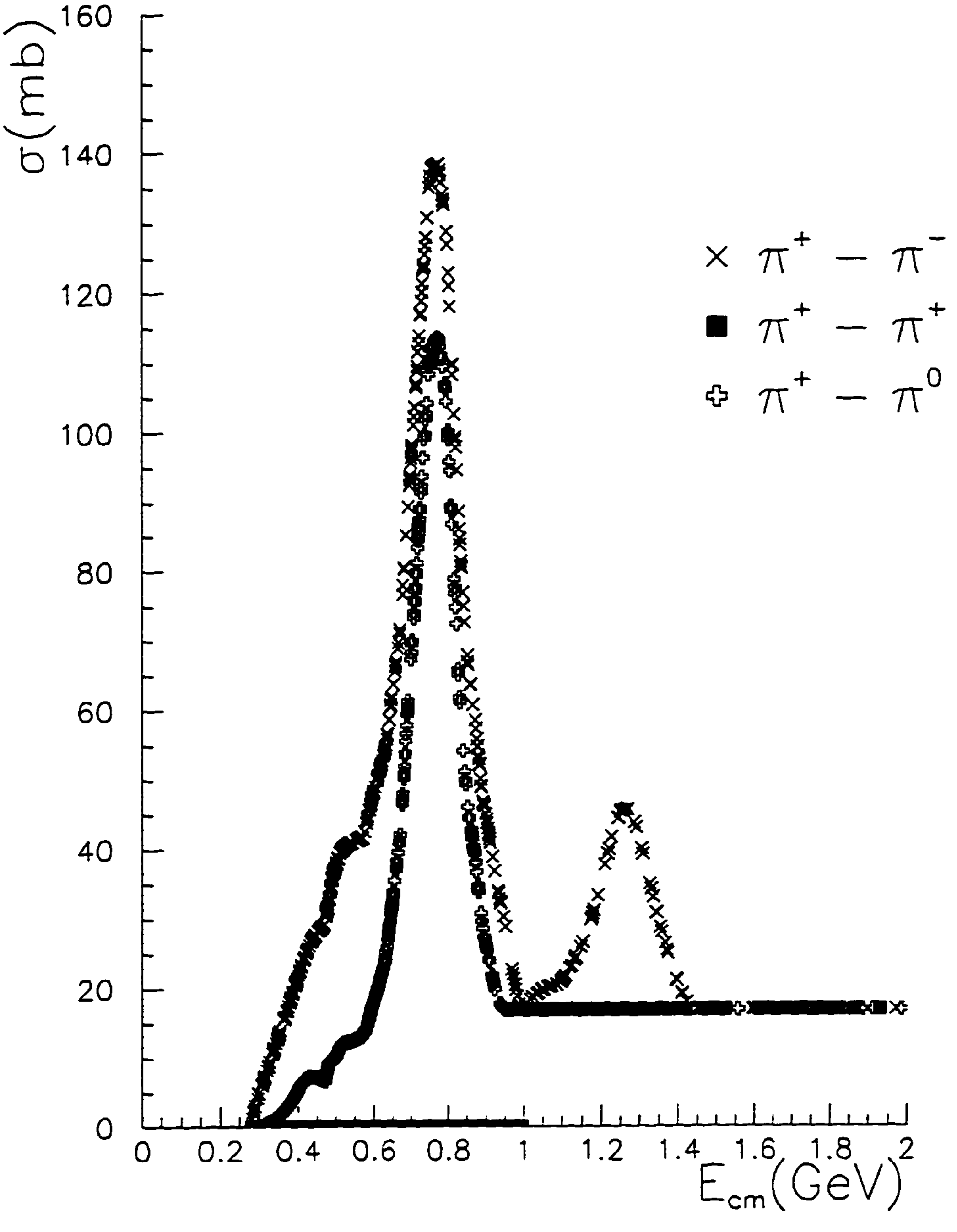

Figure A5.8: Pion - Pion cross sections

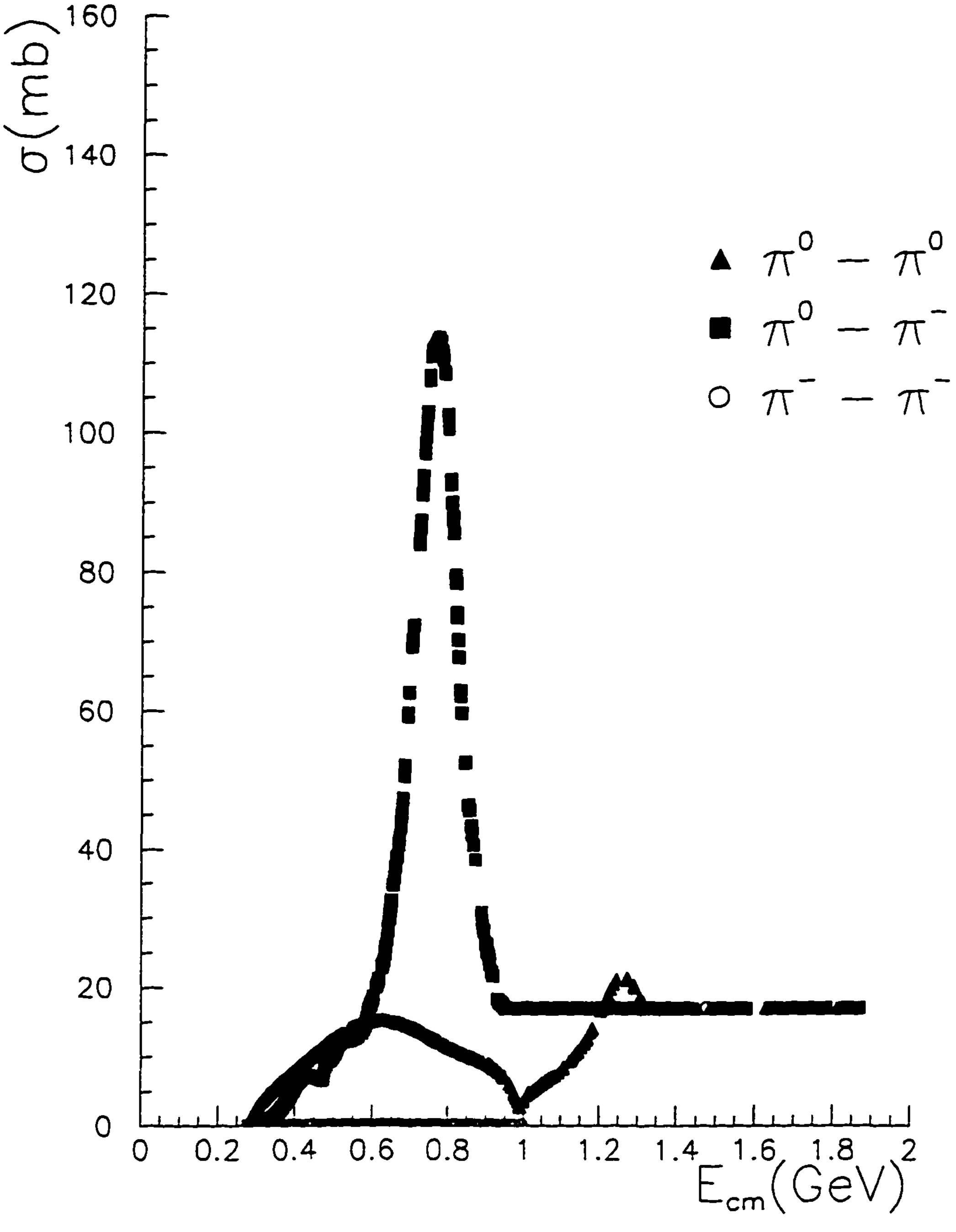

Figure A5.9: Pion - Pion cross sections

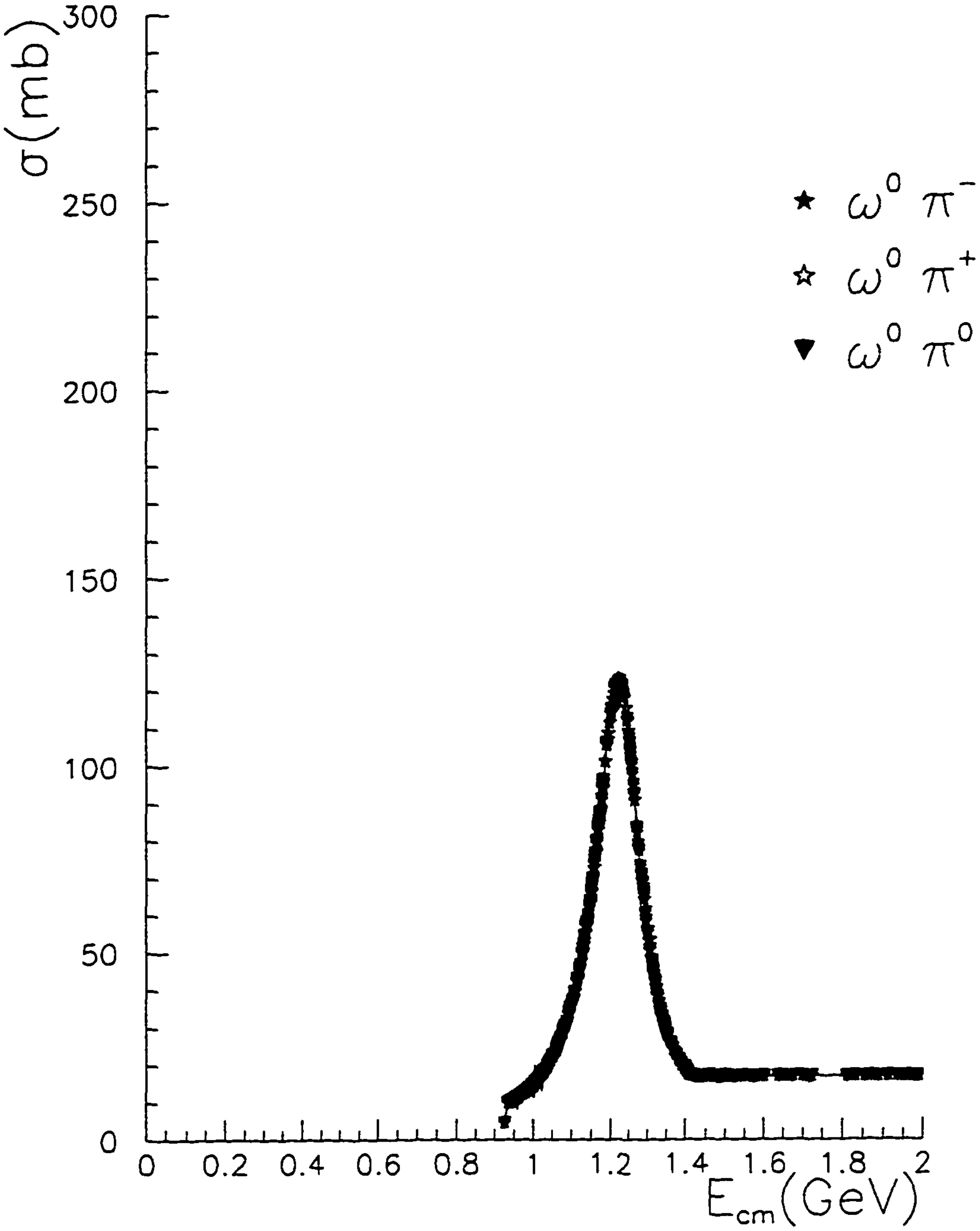

Figure A5.10: Omega - Pion cross sections

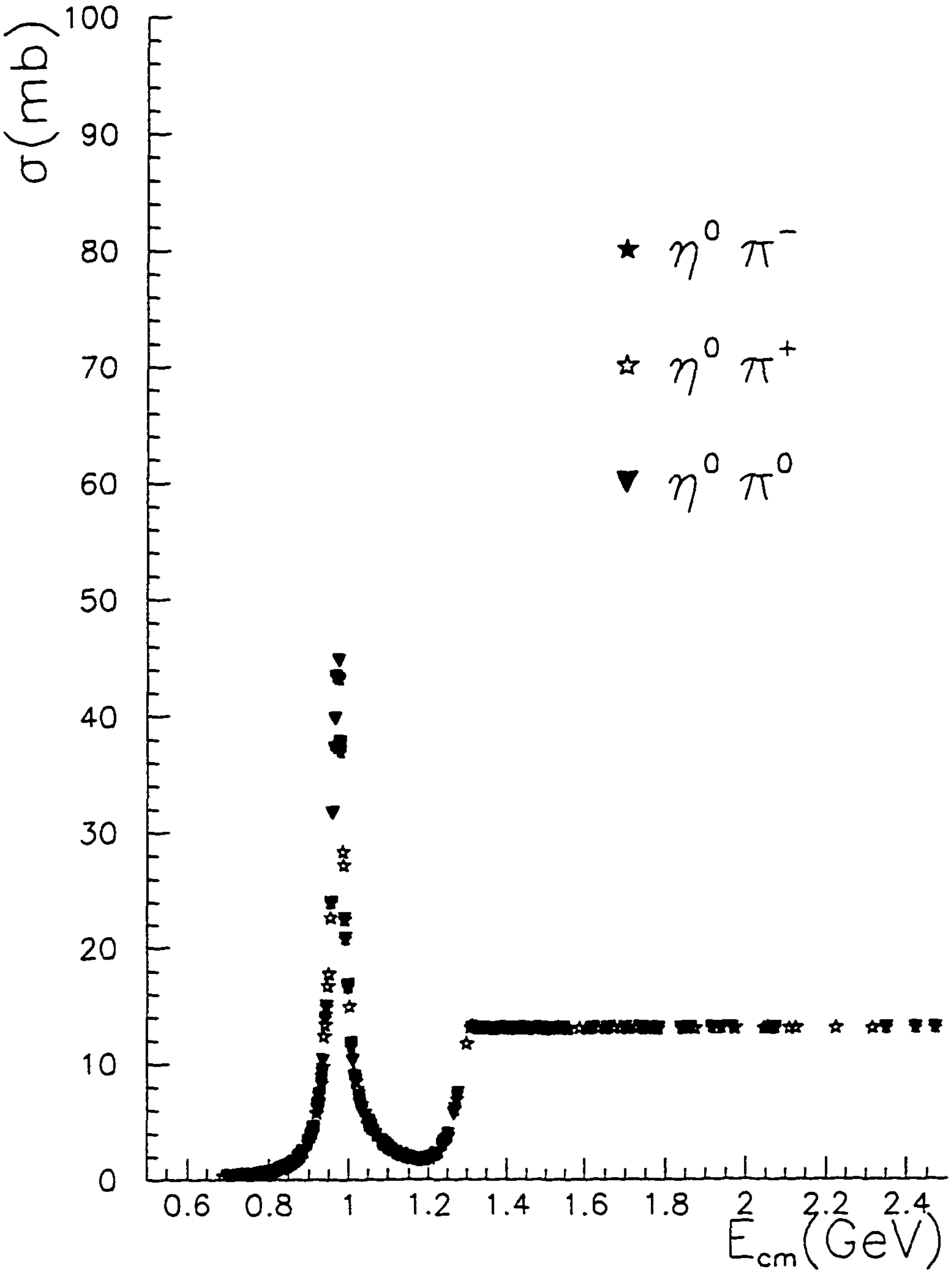

Figure A5.11: Eta - Pion cross sections

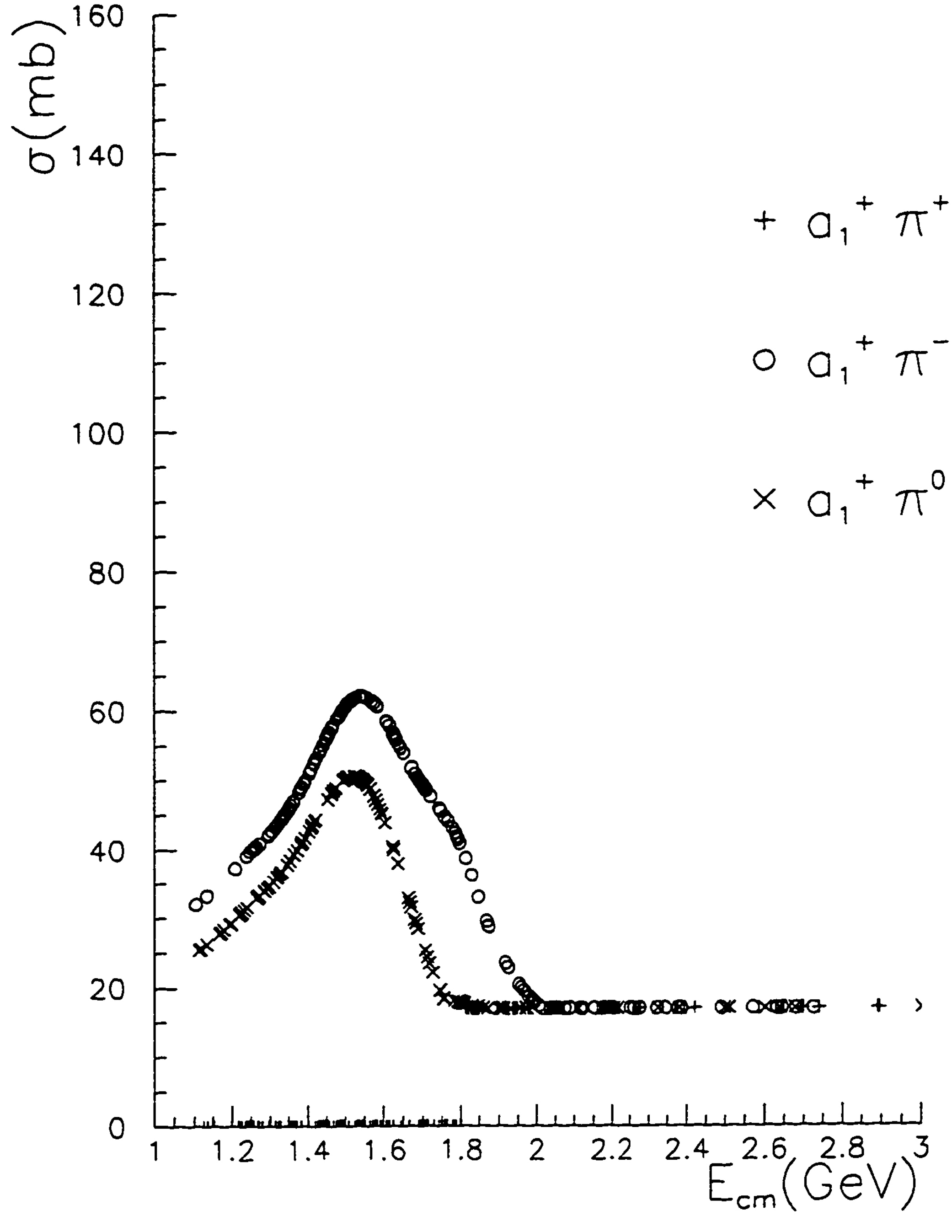

Figure A5.12: a_1^+ - Pion cross sections

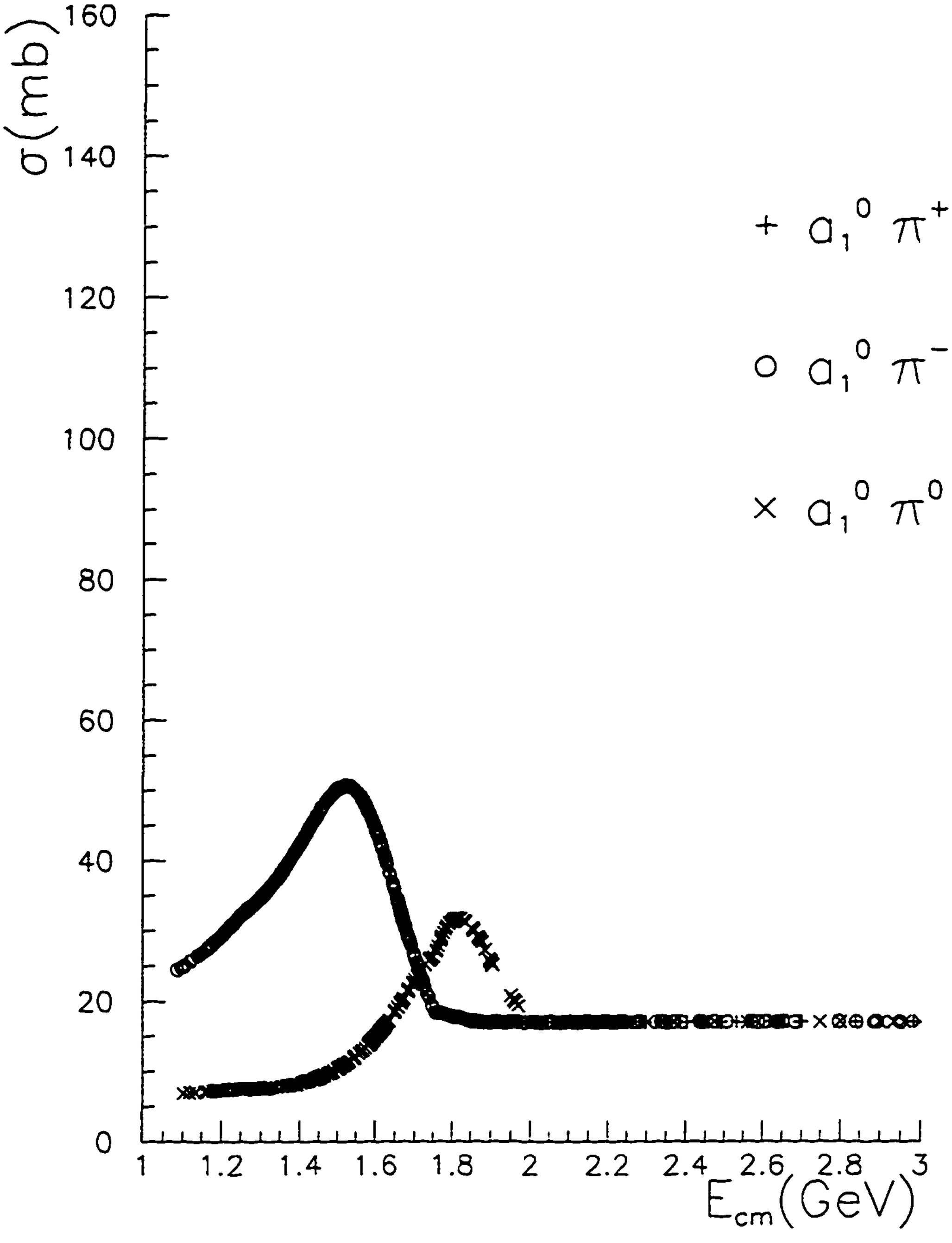

Figure A5.13: a_1^0 - Pion cross sections

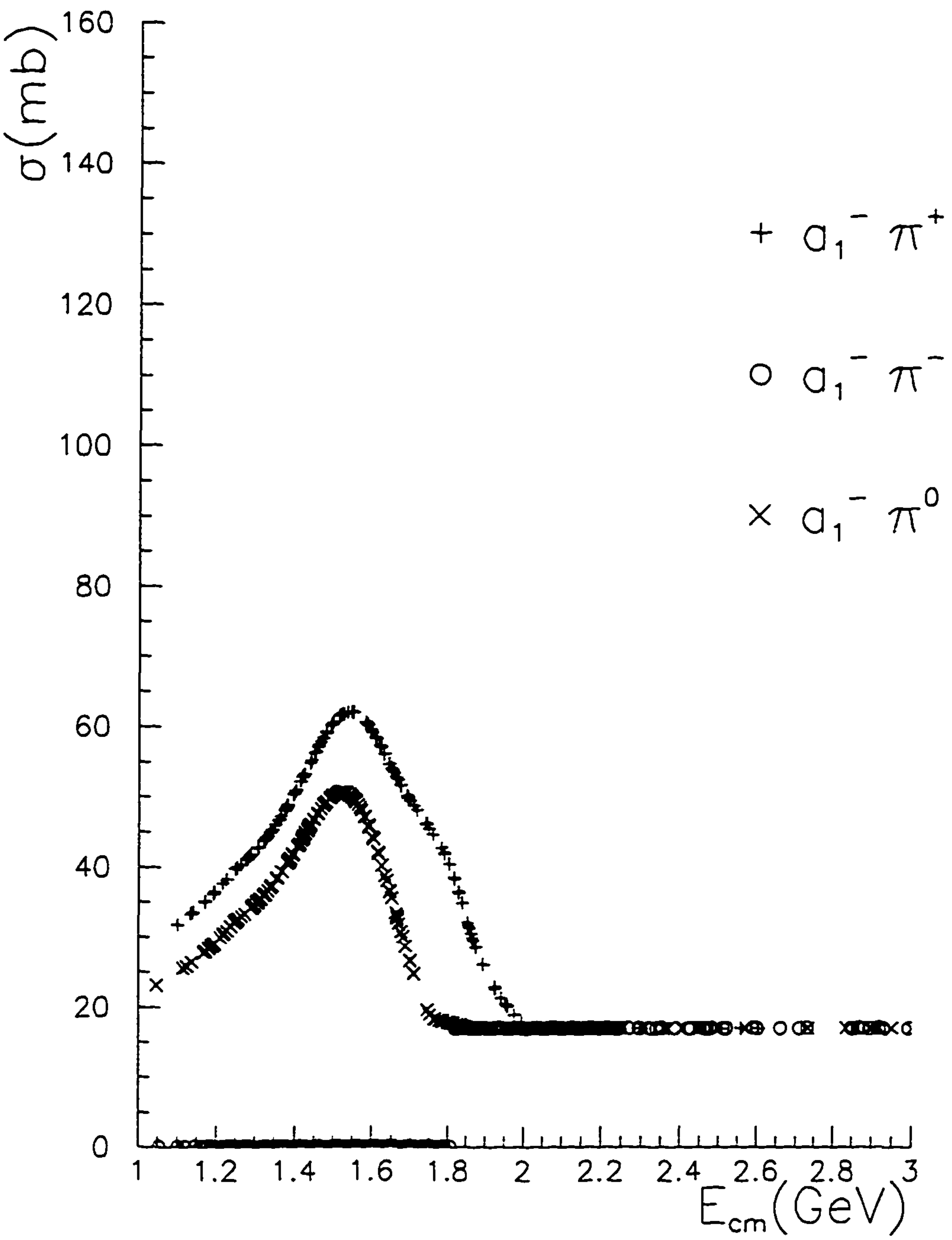

Figure A5.14: a_1^- - Pion cross sections

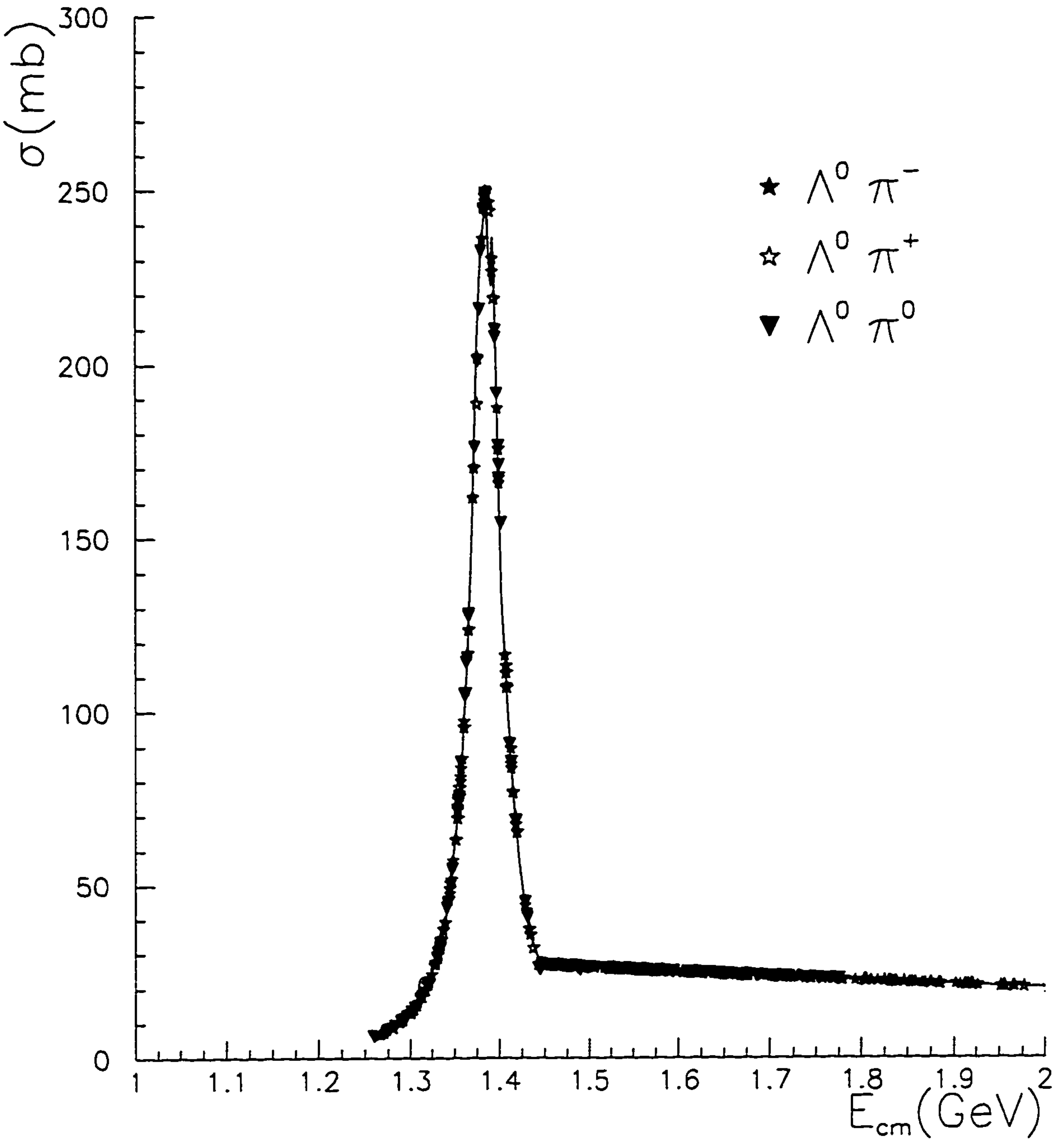

Figure A5.15: Lambda - Pion cross sections

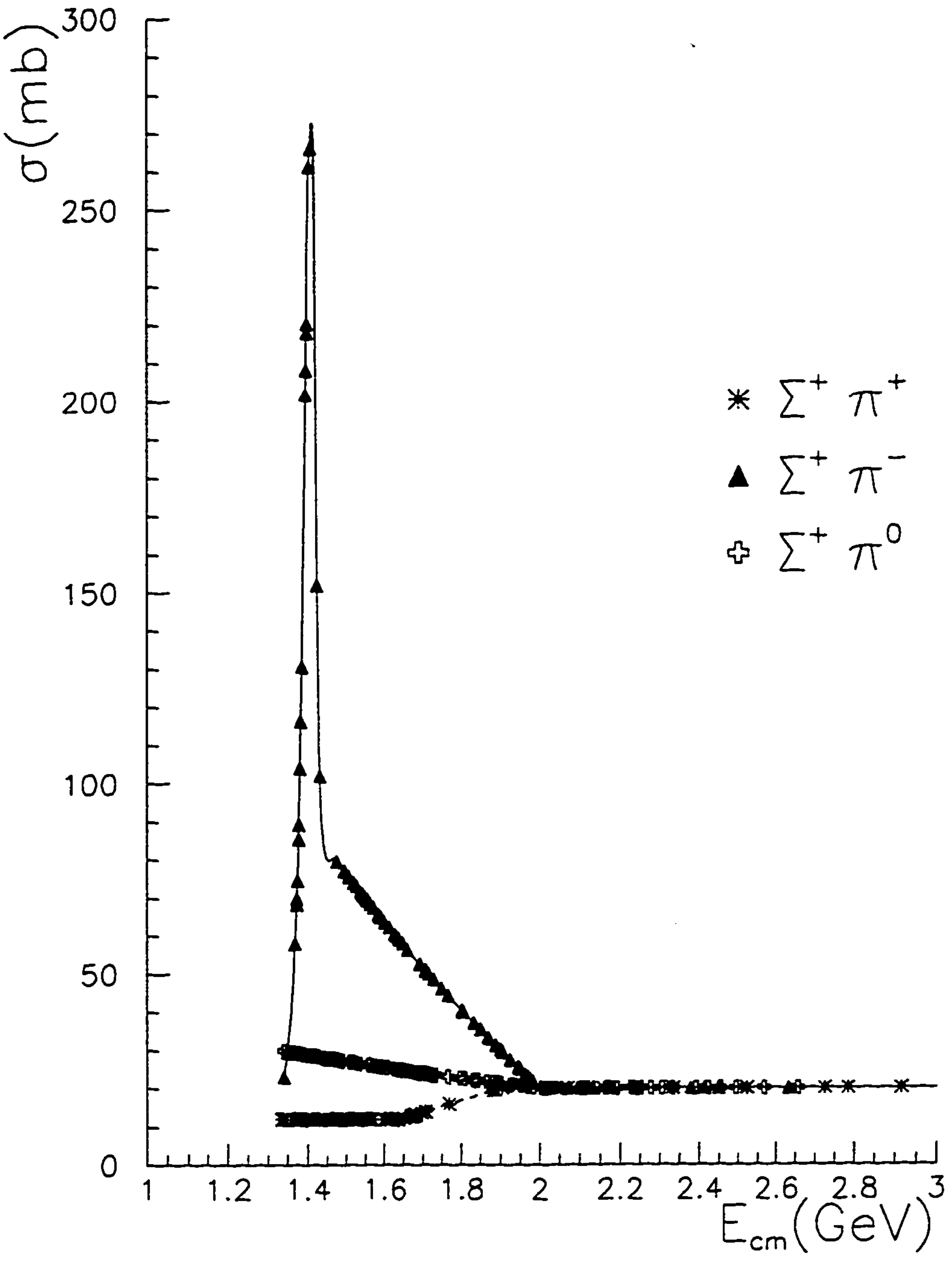

Figure A5.16: Σ^- - Pion cross sections

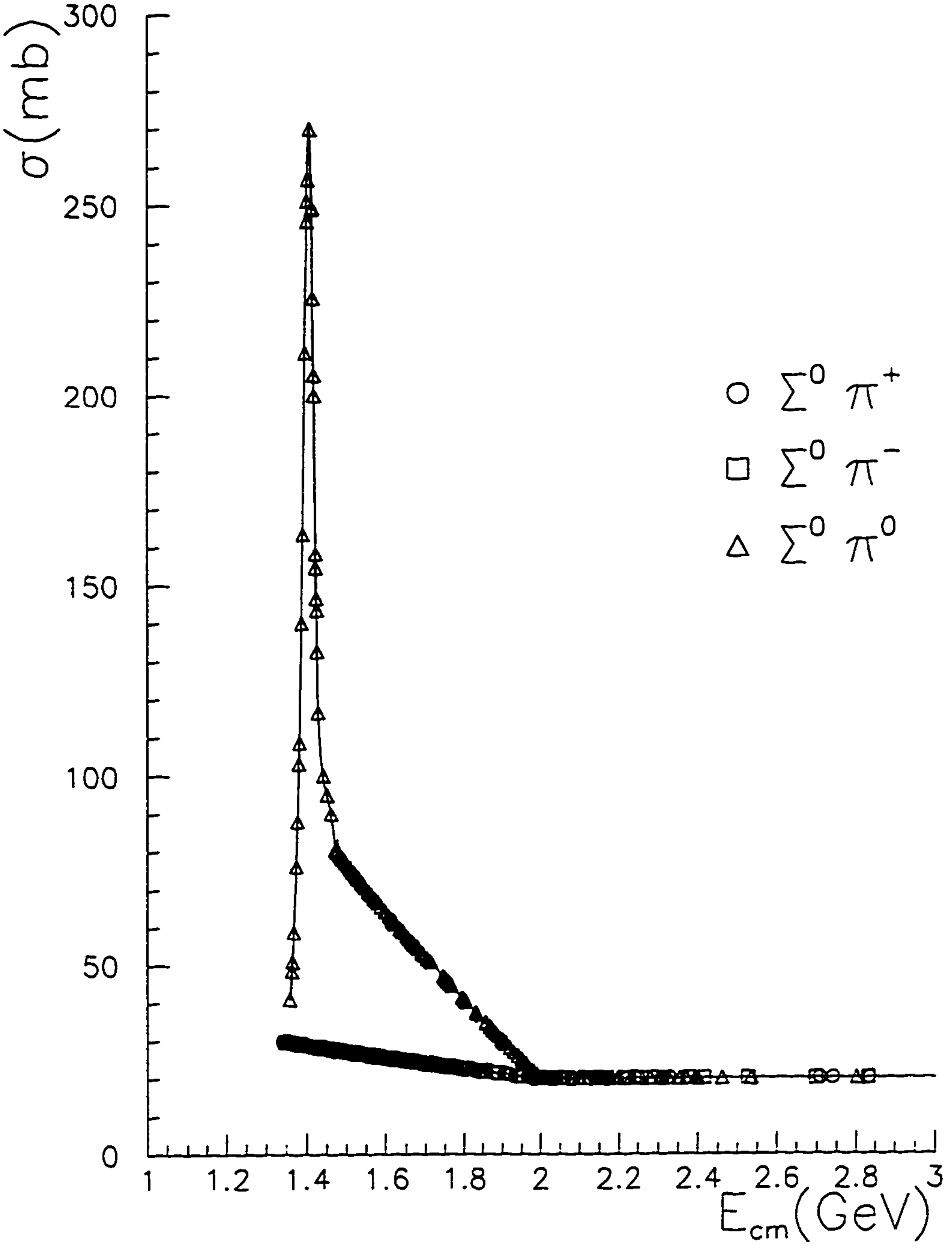

Figure A5.17: Σ^0 - Pion cross sections

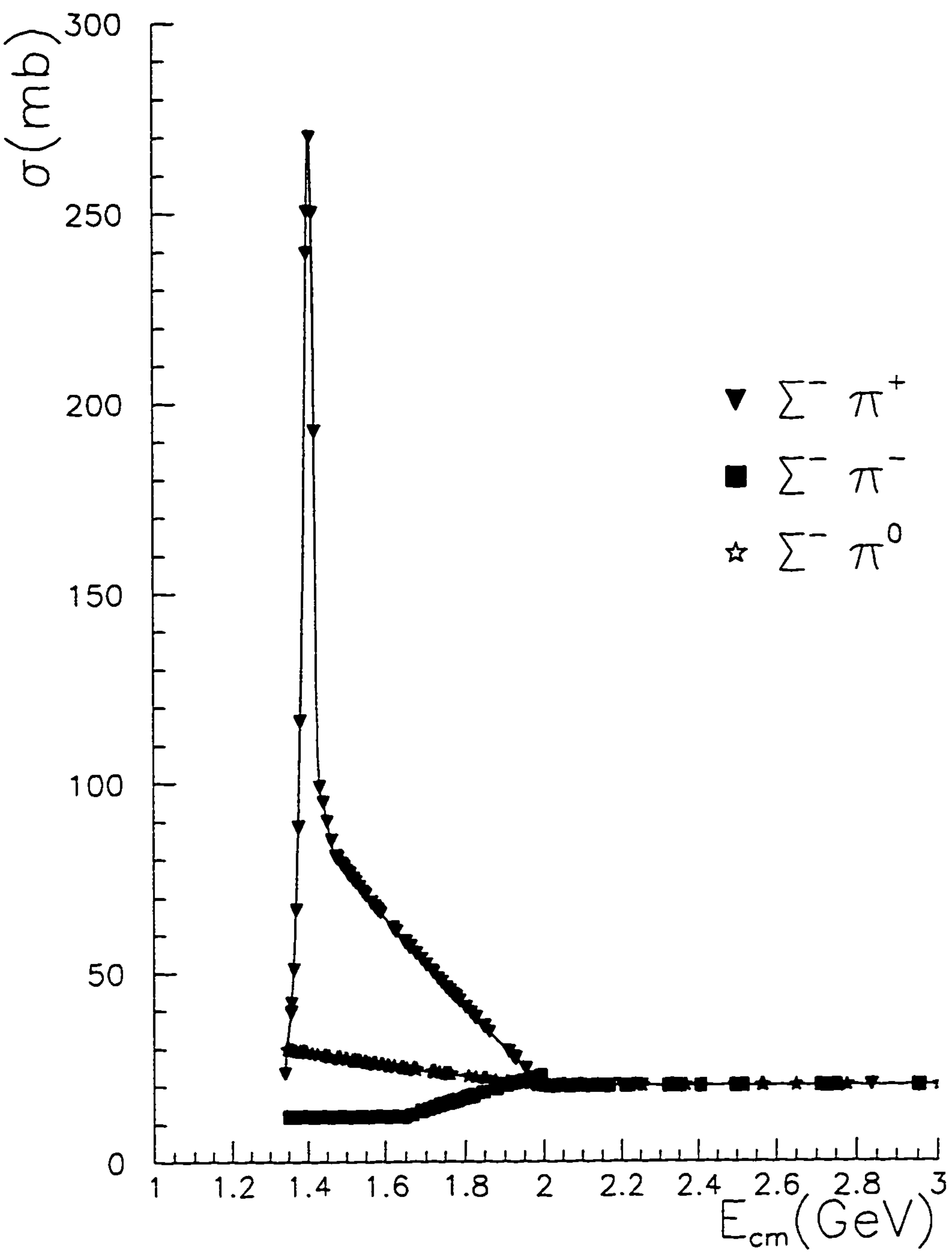

Figure A5.18: Σ^- - Pion cross sections

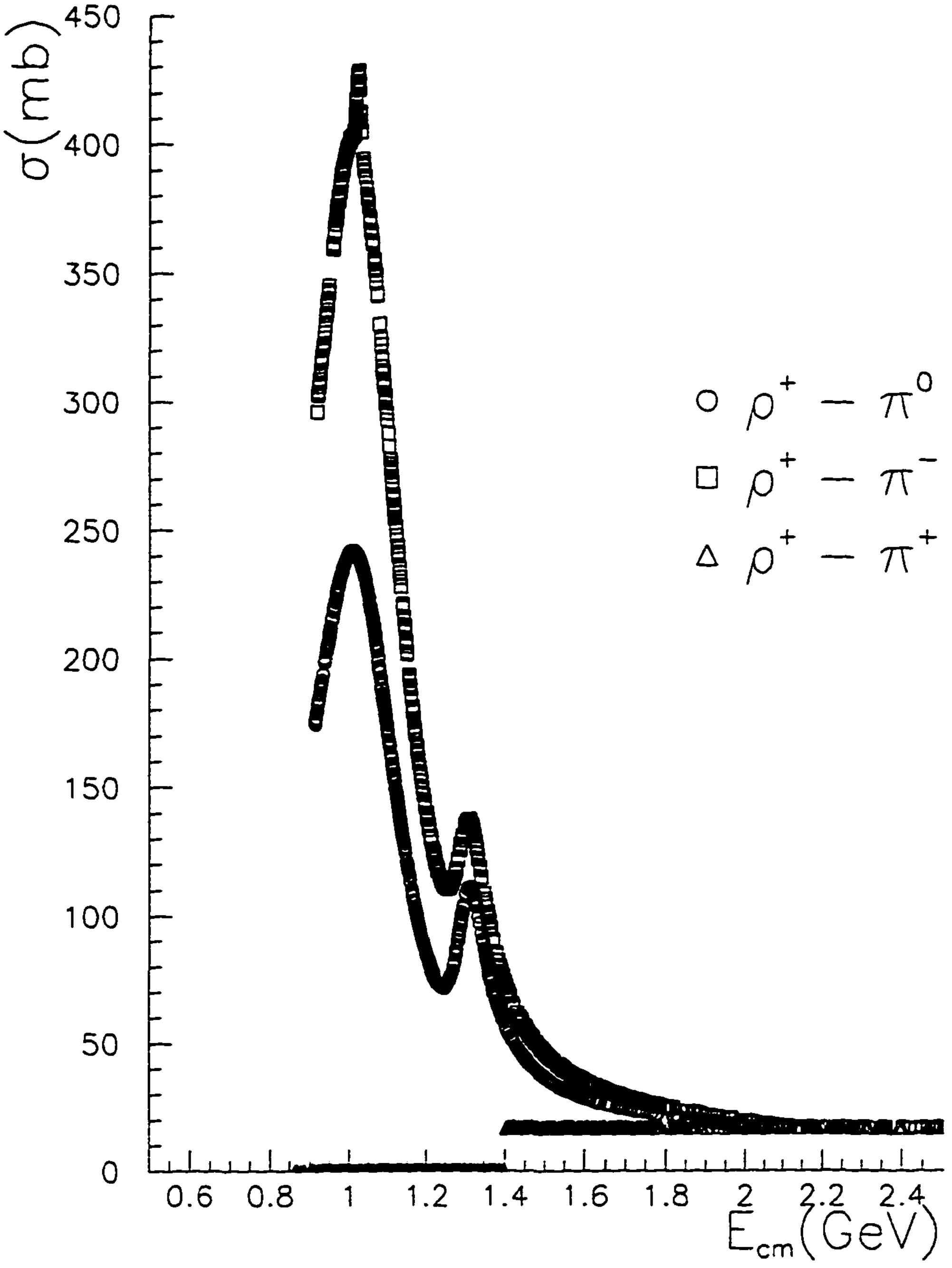

Figure A5.19: ρ⁺ - Pion cross sections

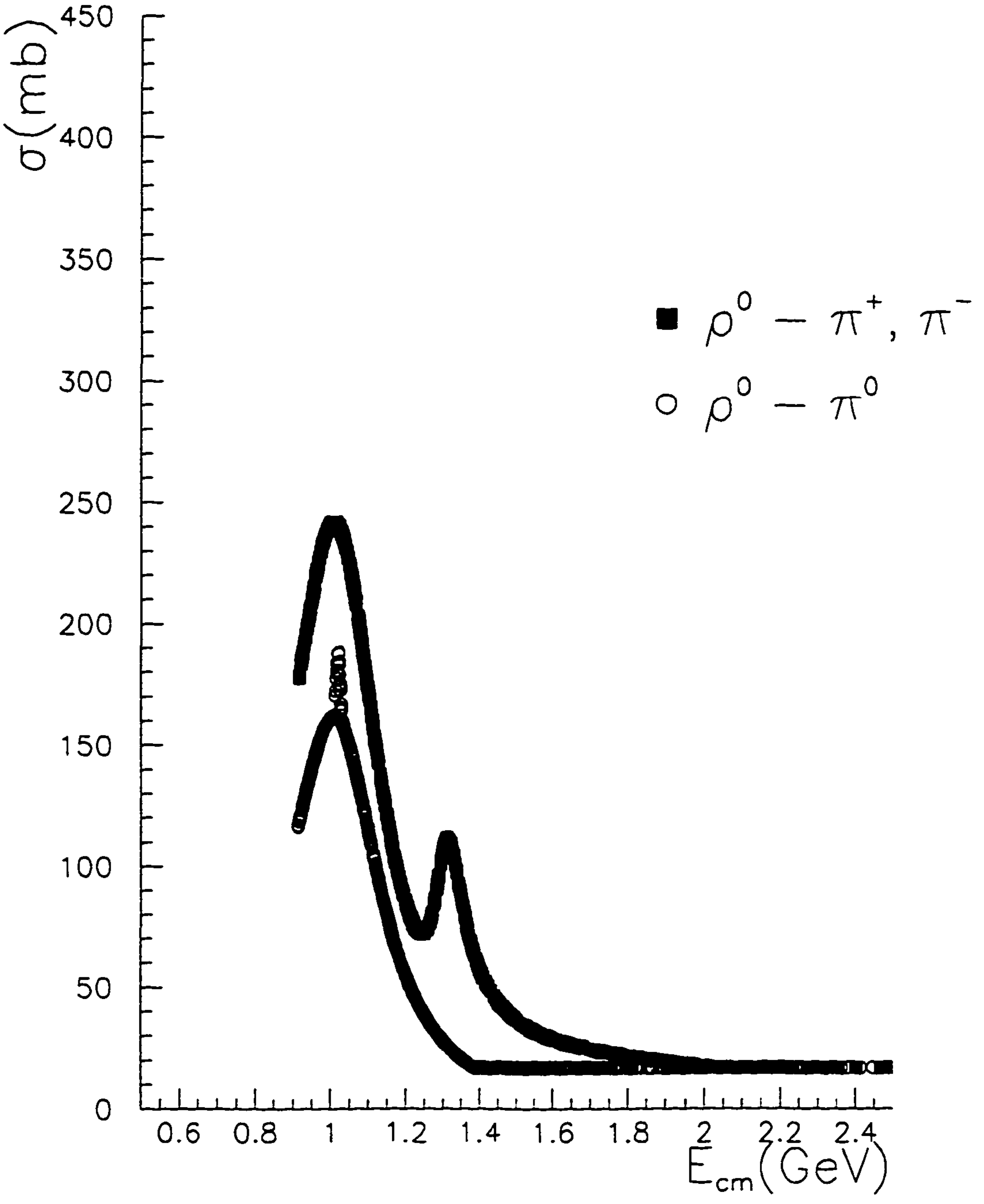

Figure A5.20: ρ^0 - Pion cross sections

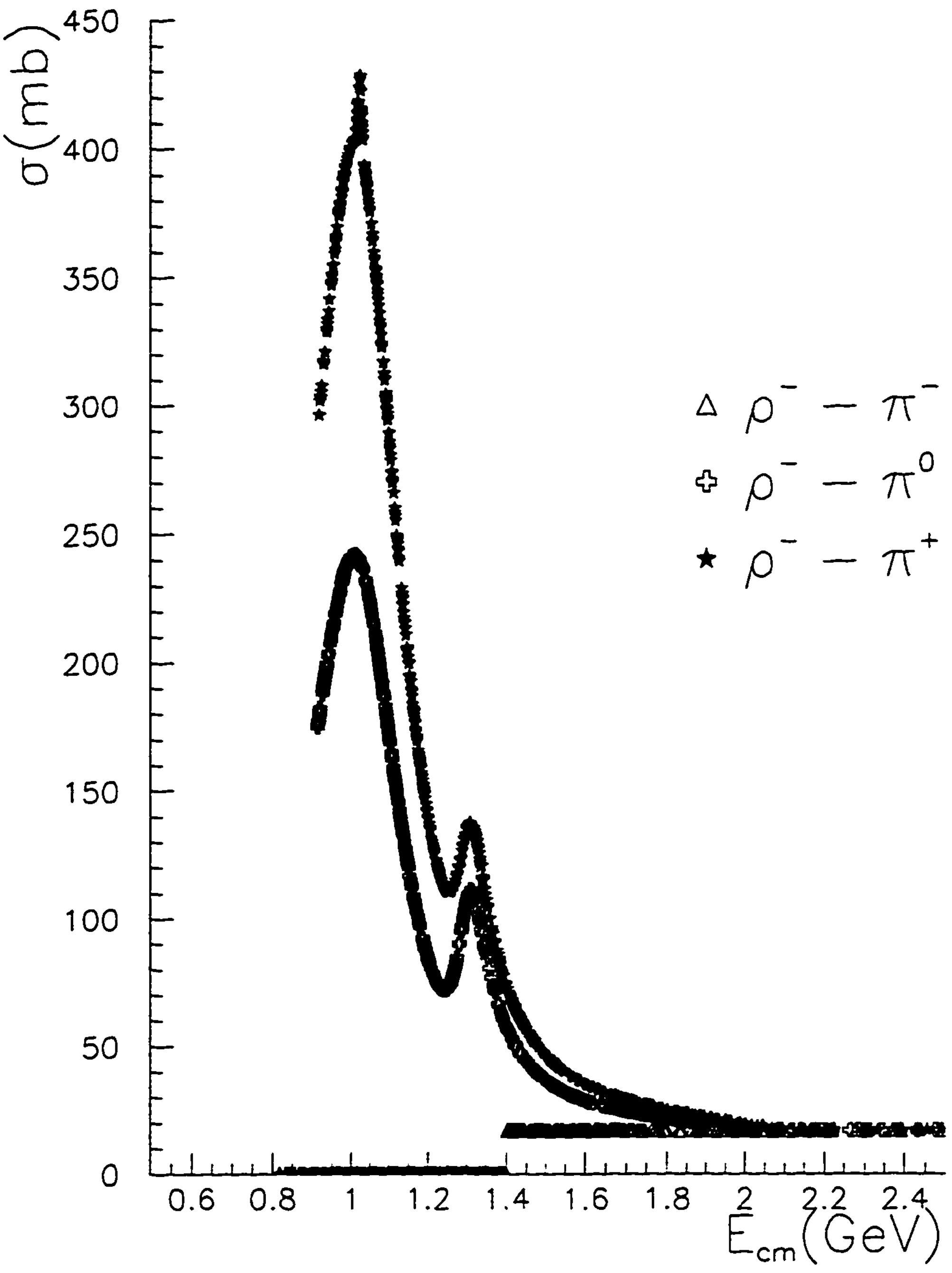

Figure A5.21: ρ^- - Pion cross sections

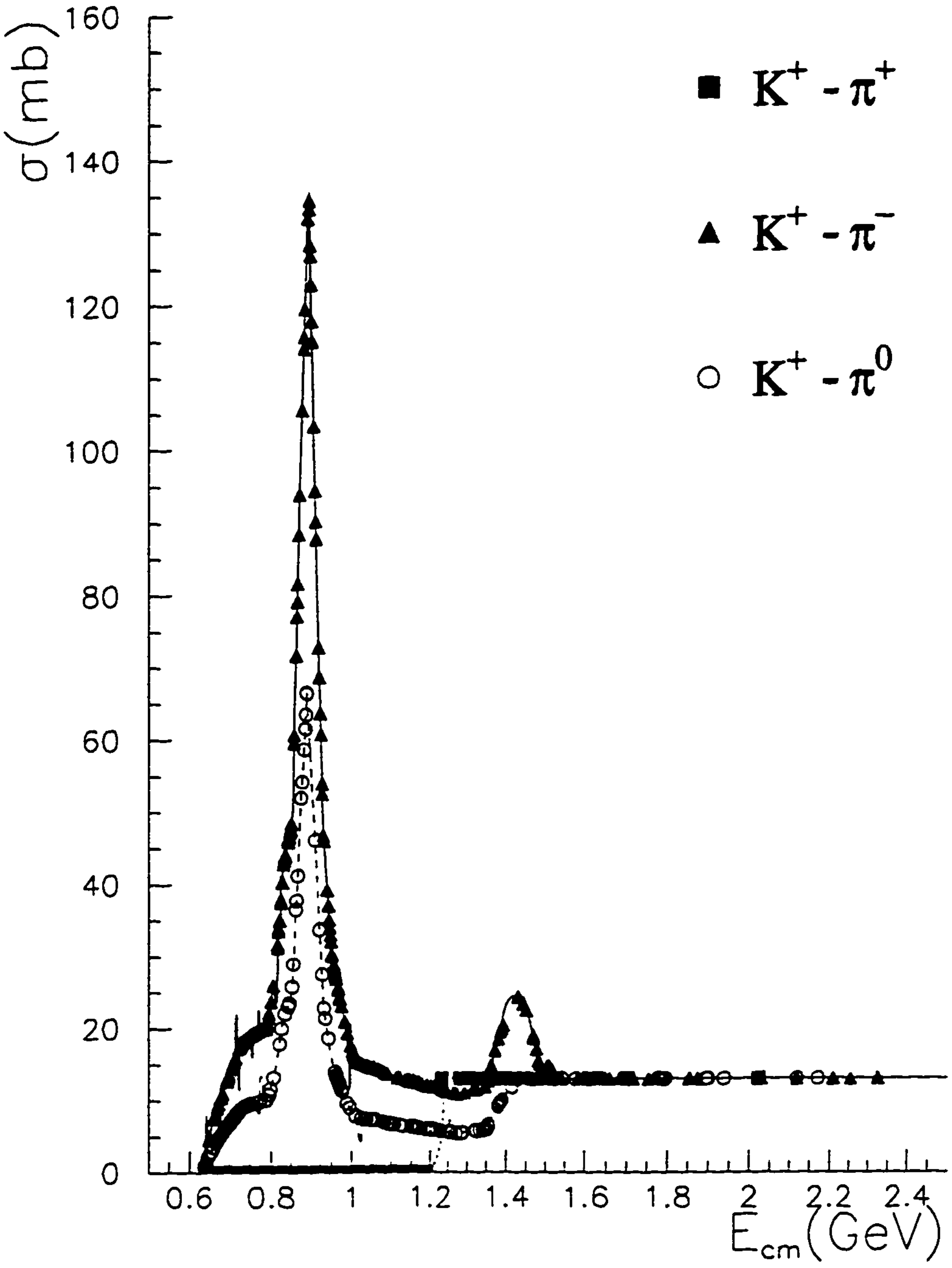

Figure A5.22: K⁻ - Pion cross sections

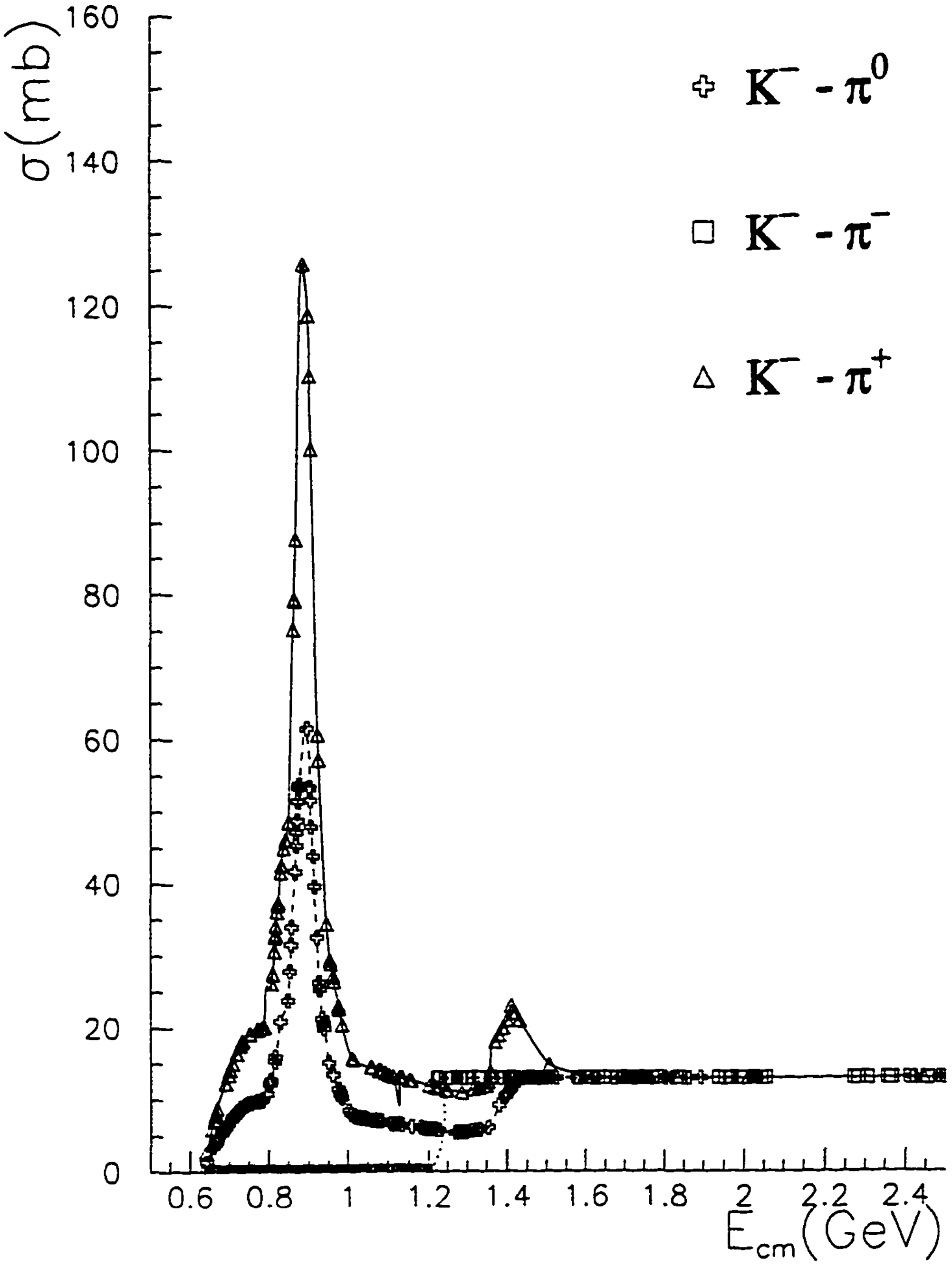

Figure A5.23: K - Pion cross sections

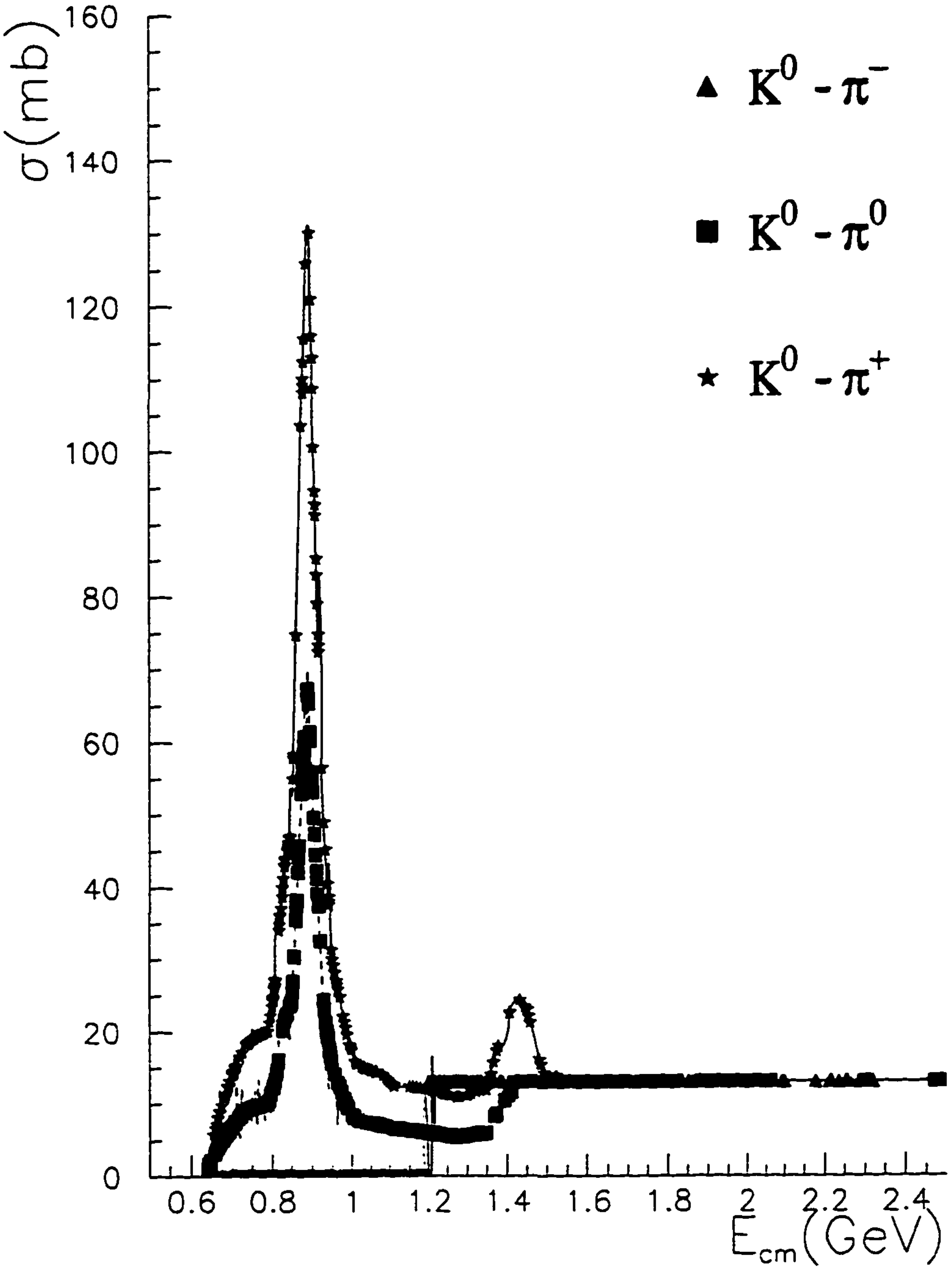

Figure A5.24: K^0 - Pion cross sections

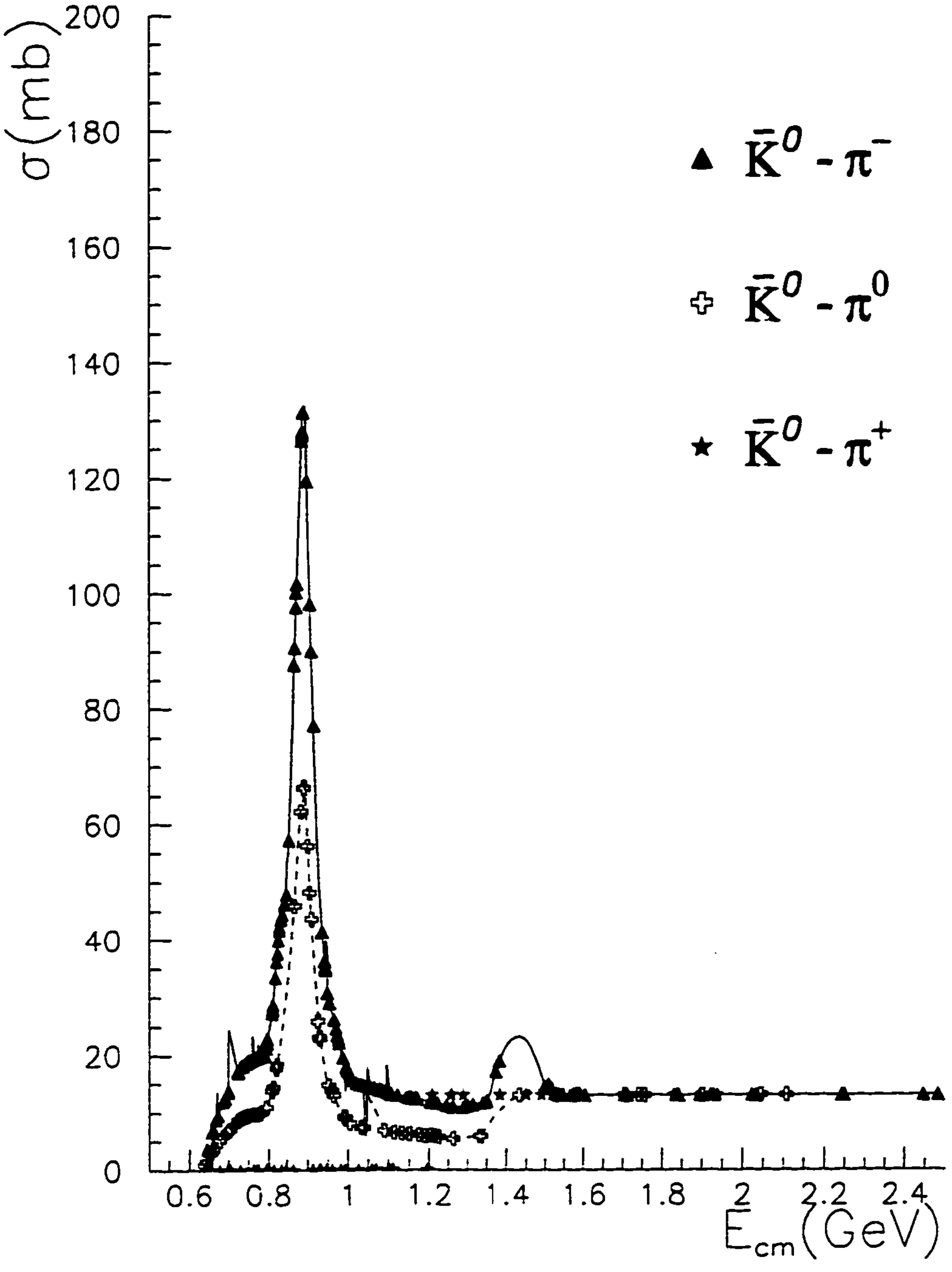

Figure A5.25: $\bar{K}^0$ - Pion cross sections

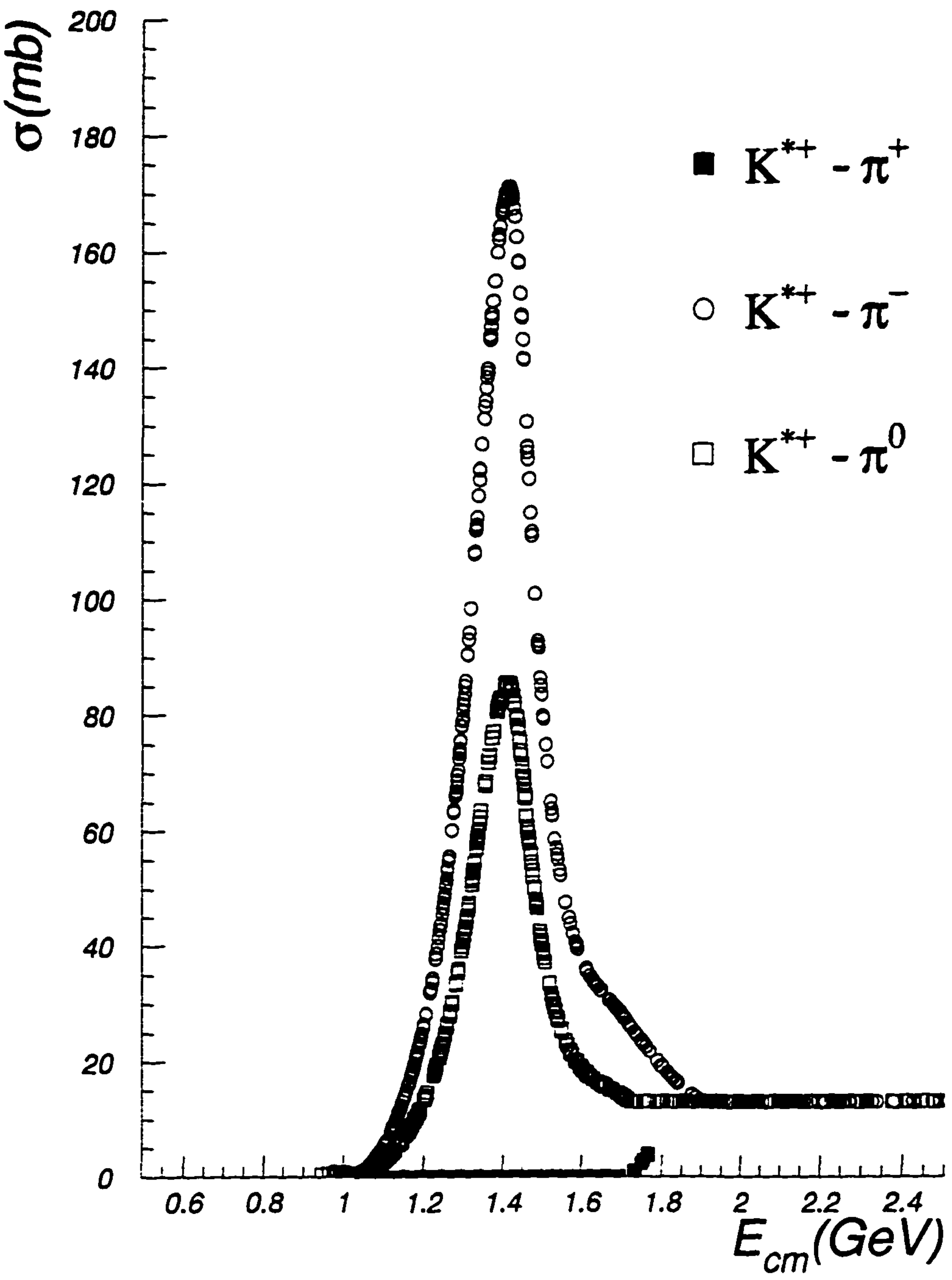

Figure A5.26: K^{**} - Pion cross sections

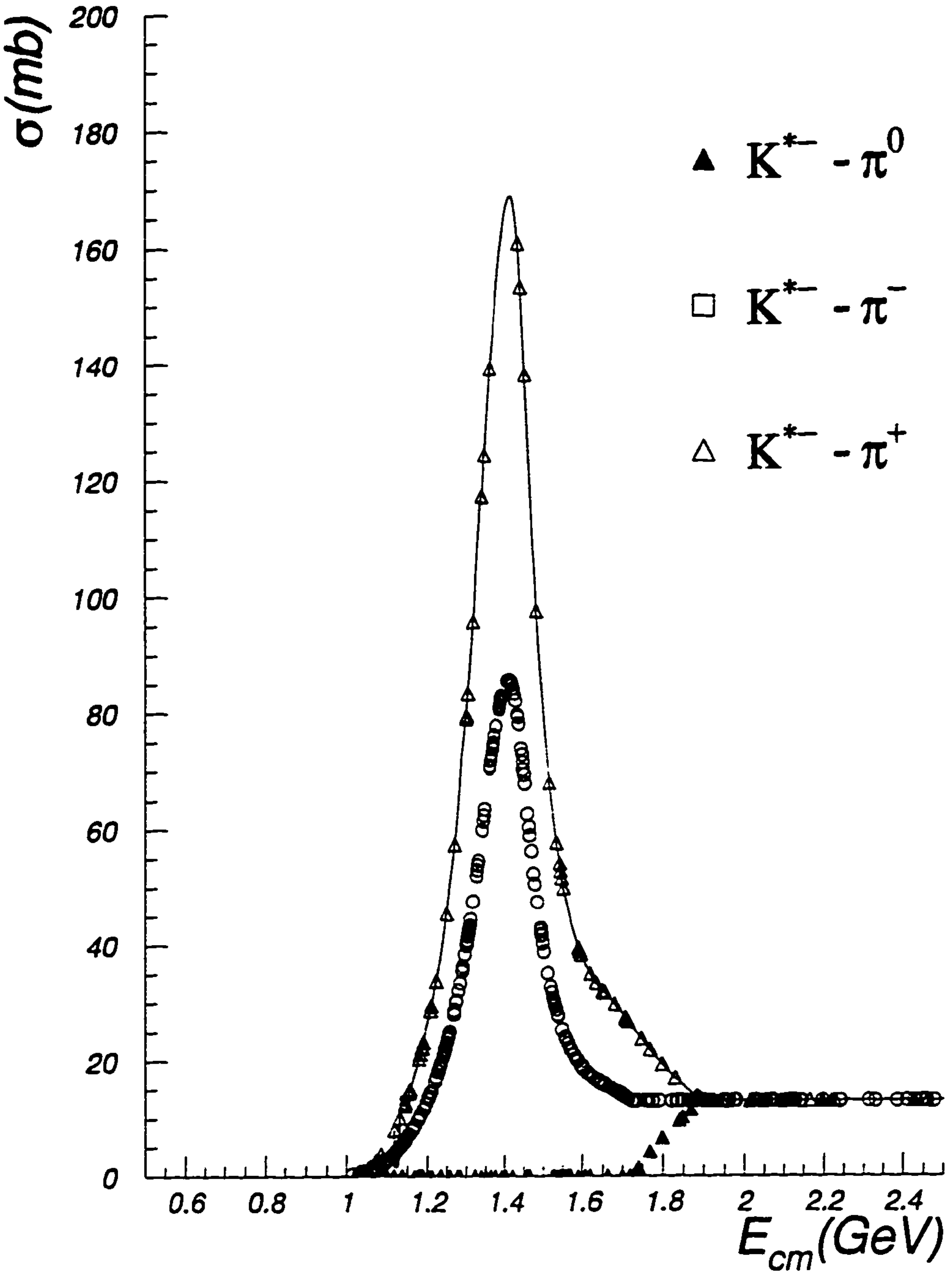

Figure A5.27: K^{*-} - Pion cross sections

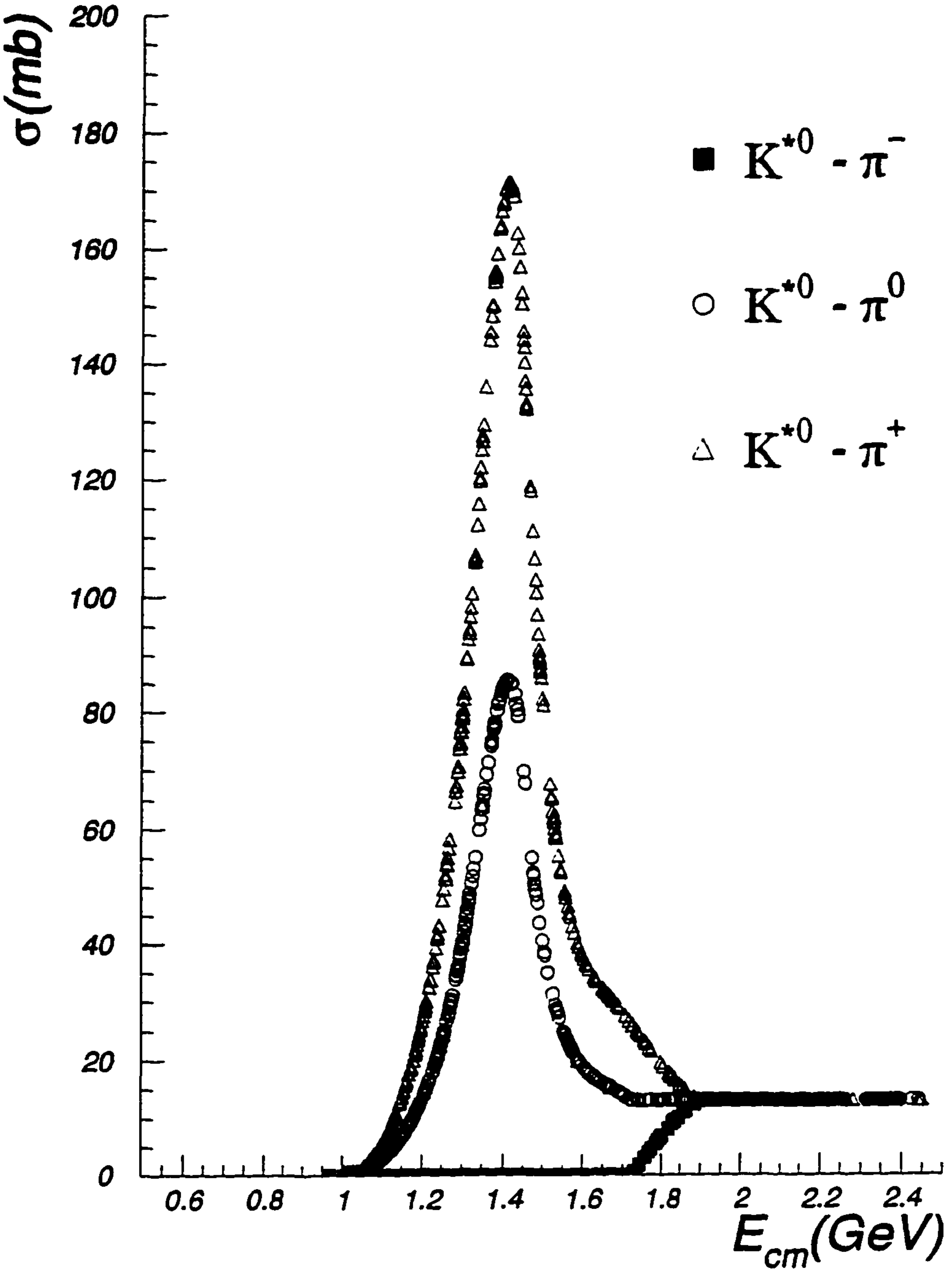

Figure A5.28: K^{*0} - Pion cross sections

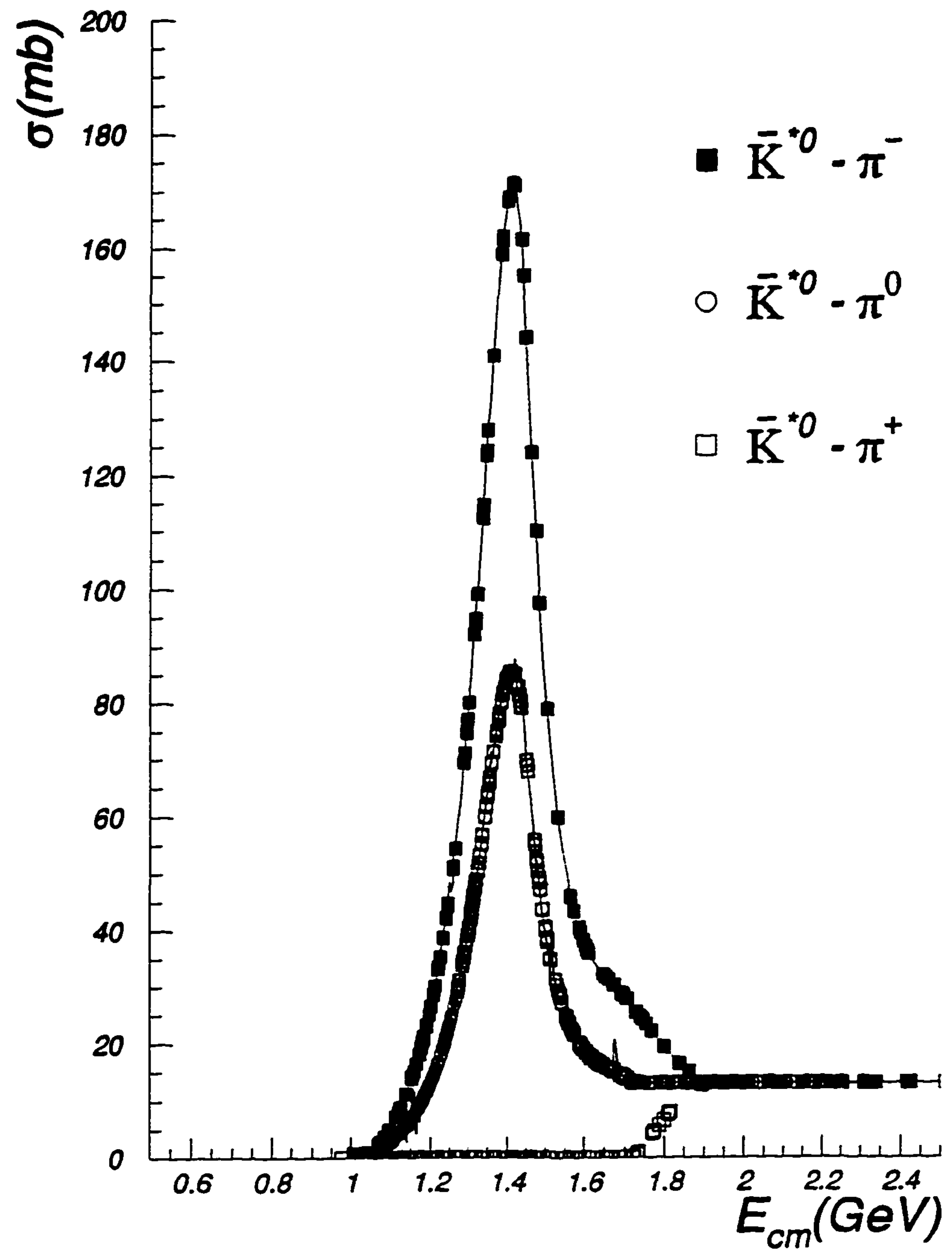

Figure A5.29: $\bar{K}^{*0}$ - Pion cross sections

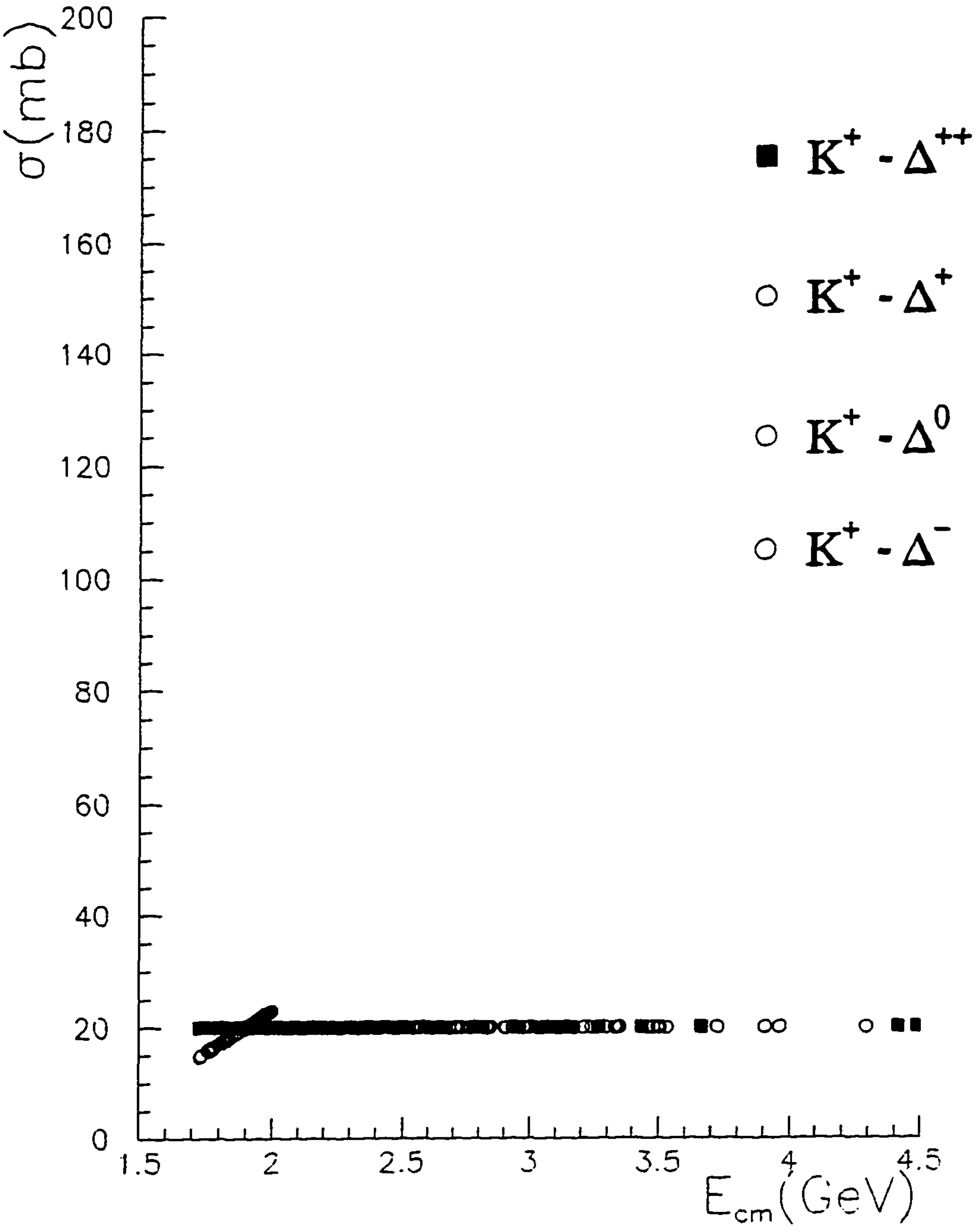

Figure A5.30: K^- - Delta cross sections

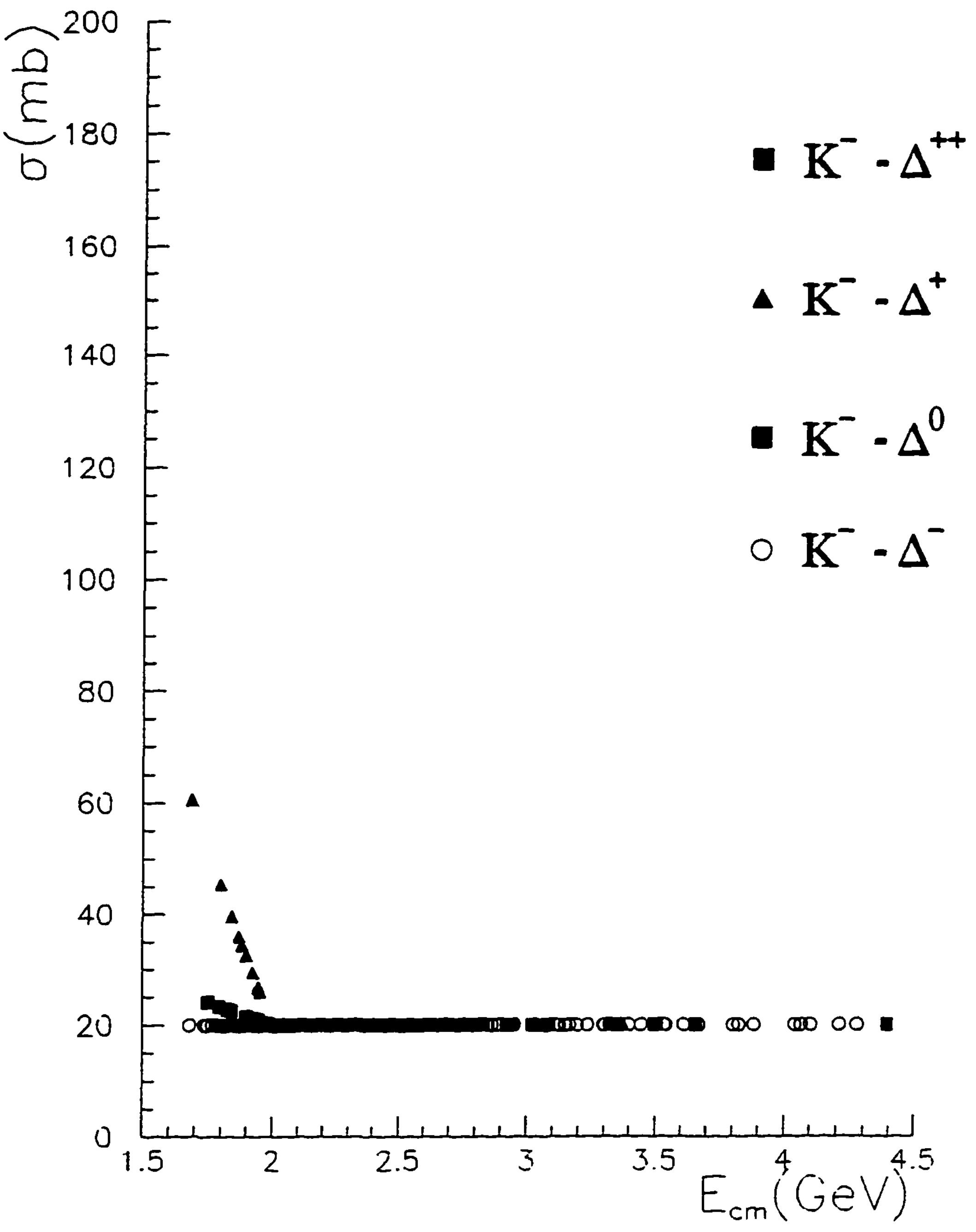

Figure A5.31: K - Delta cross sections

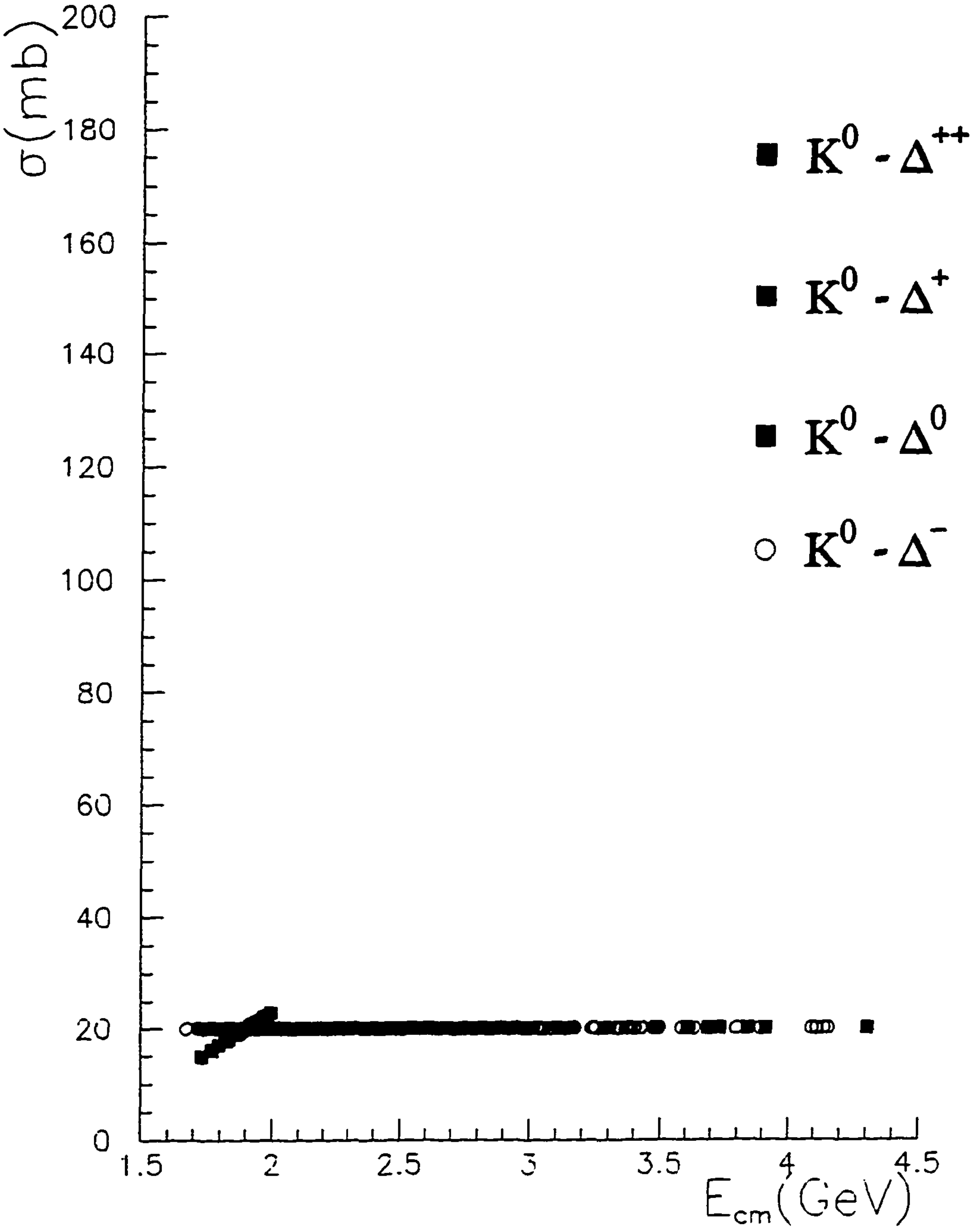

Figure A5.32: K^0 - Delta cross sections

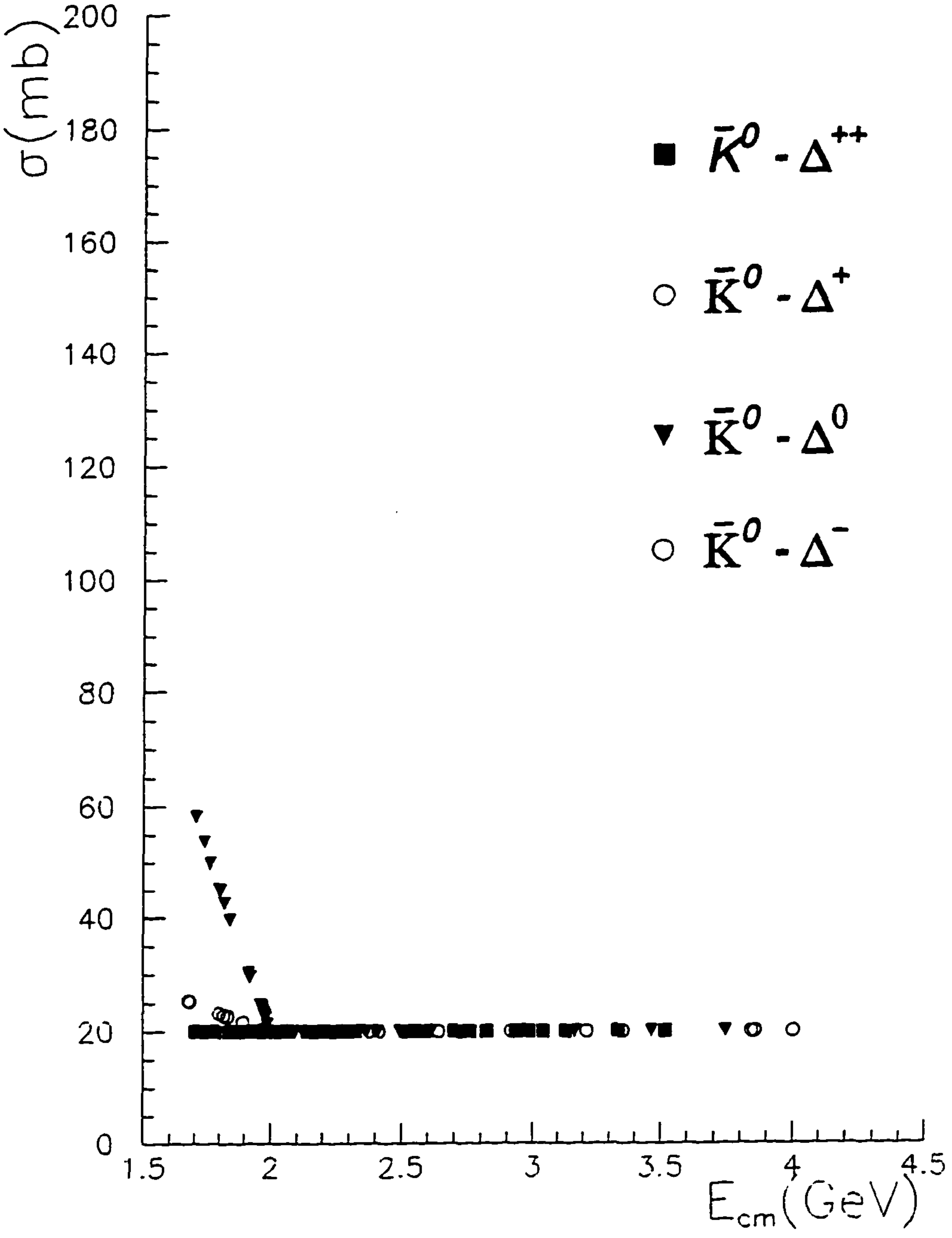

Figure A5.33: $\bar{K}^{*0}$ - Delta cross sections

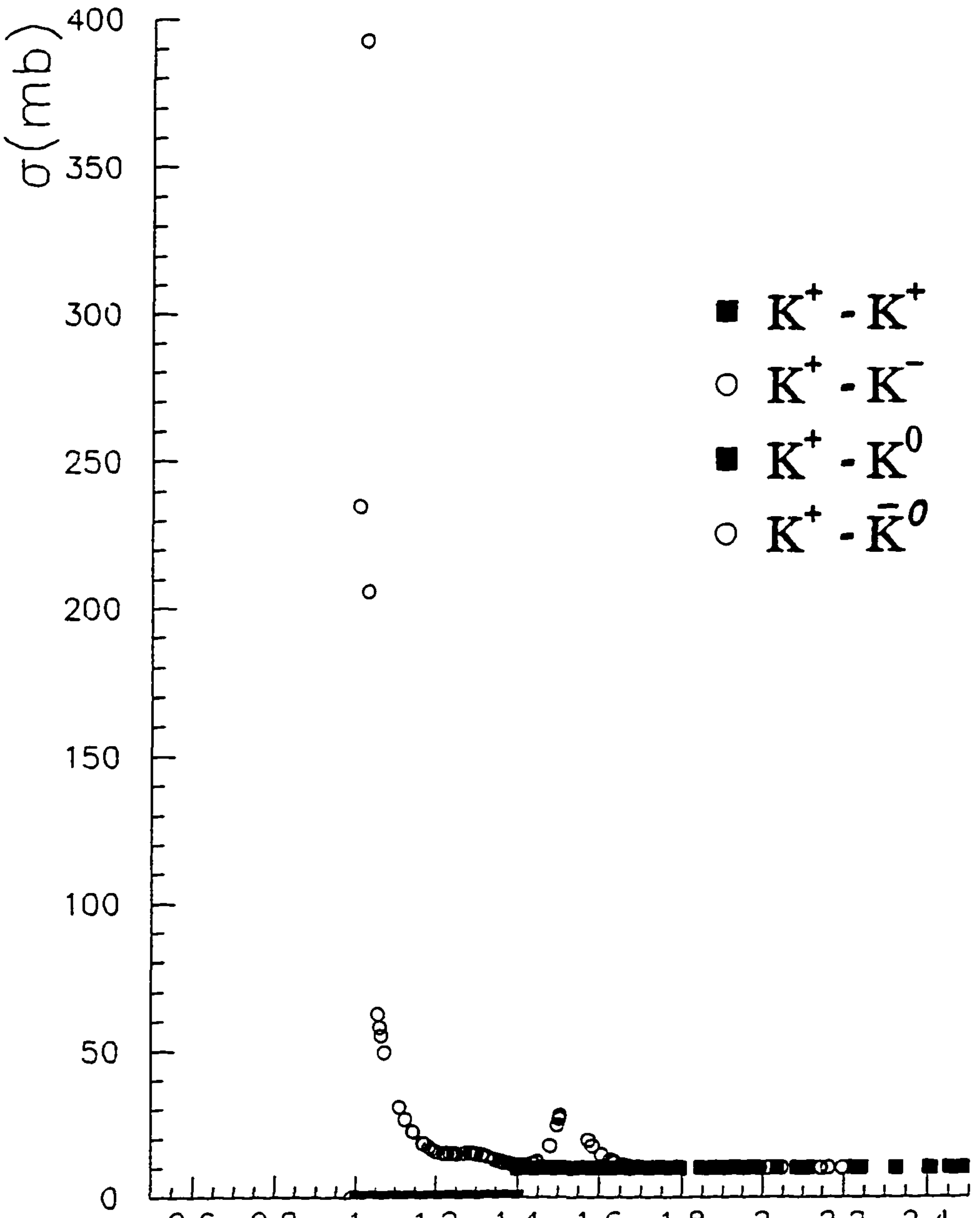

Figure A5.34: K - K cross sections

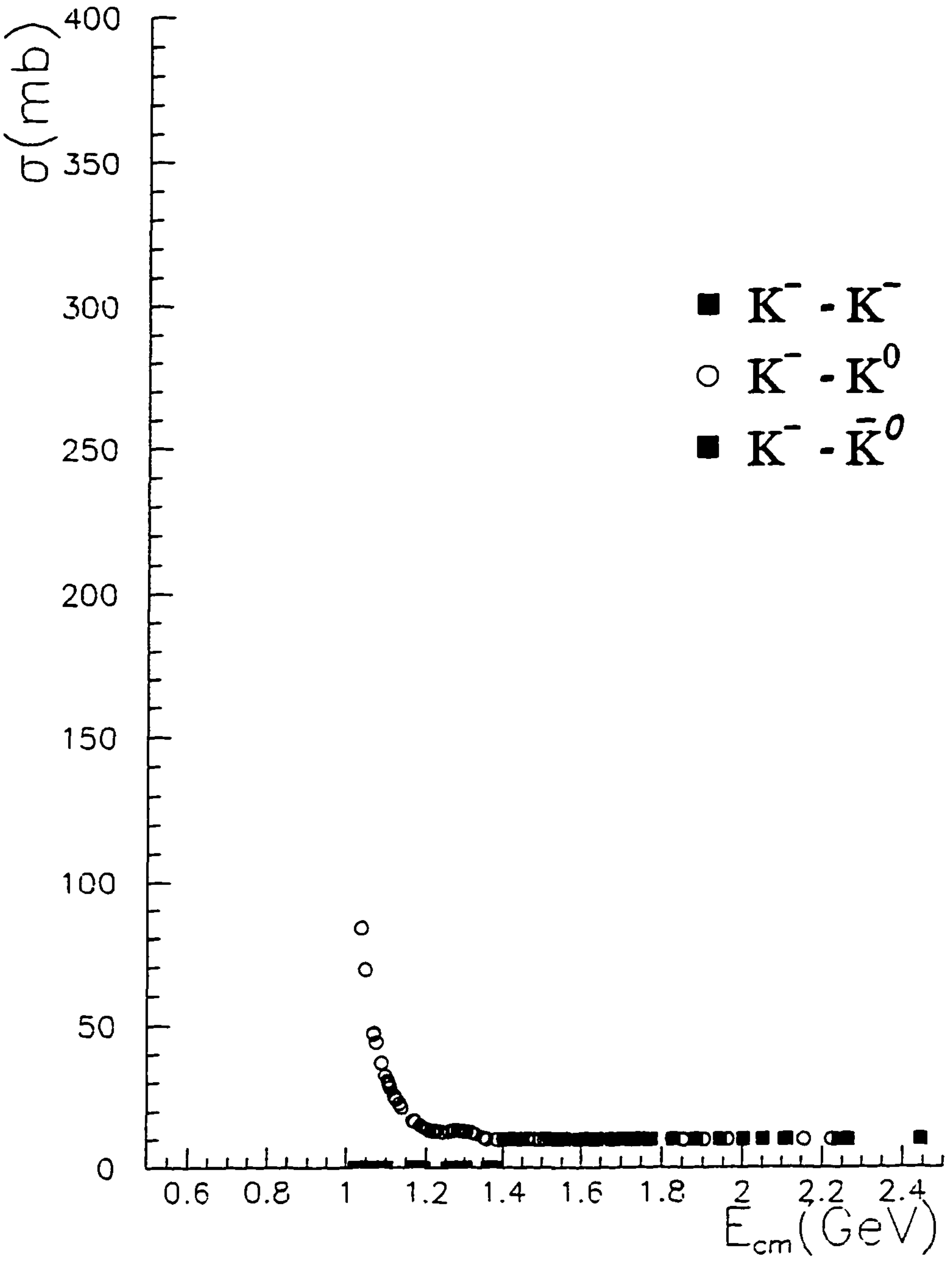

Figure A5.35: K - K cross sections

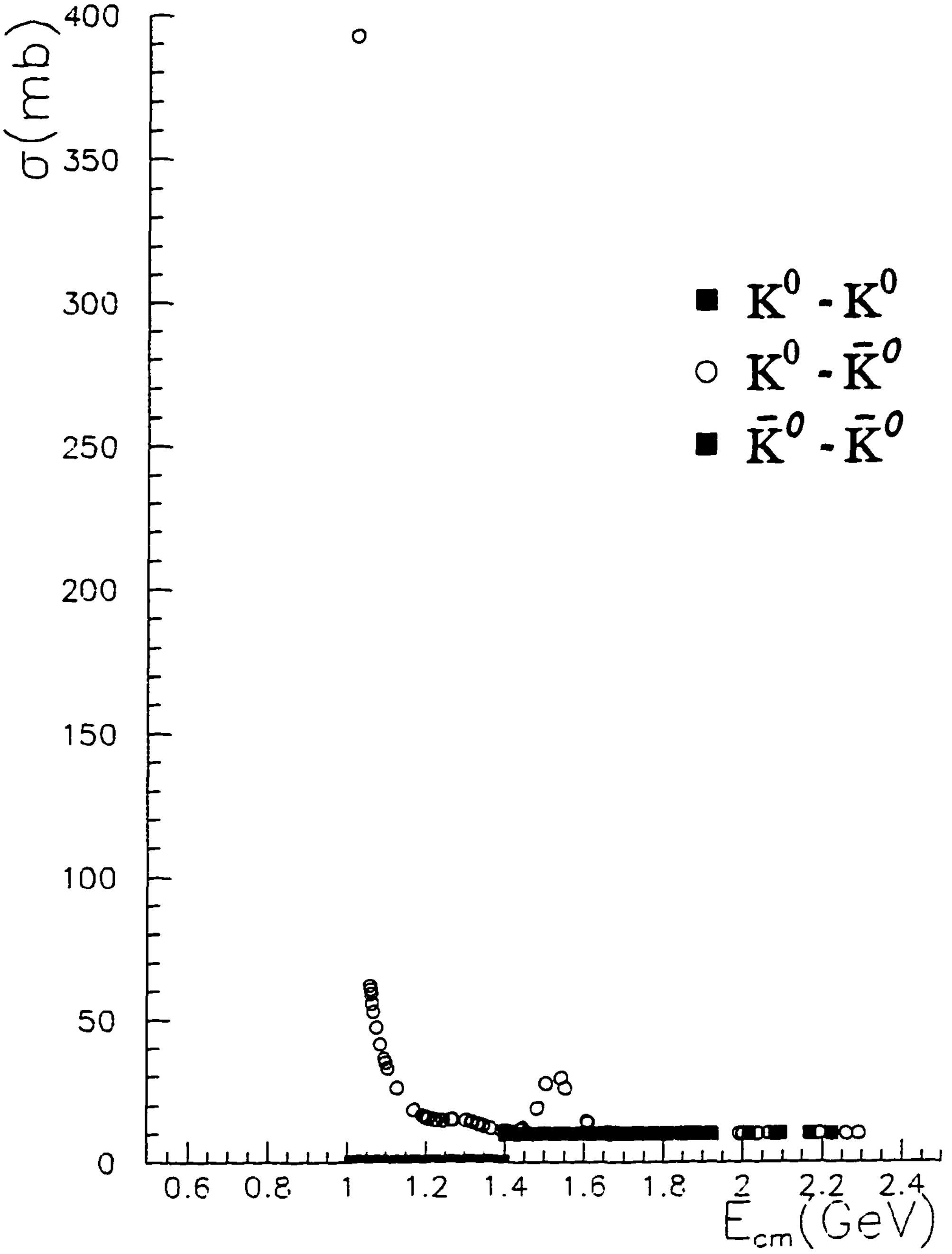

Figure A5.36: K - K cross sections

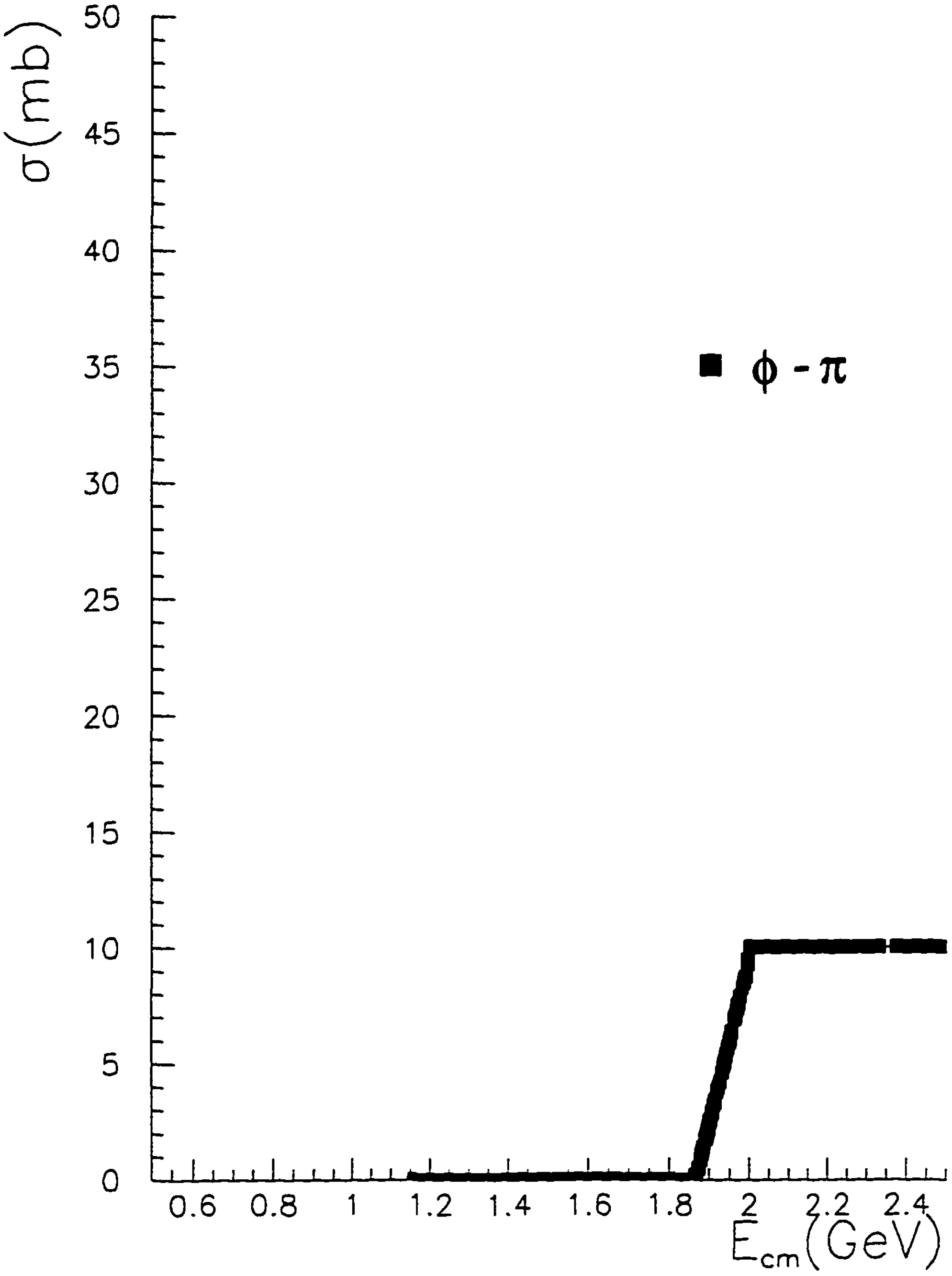

Figure A5.37: $\phi - \pi$ cross sections

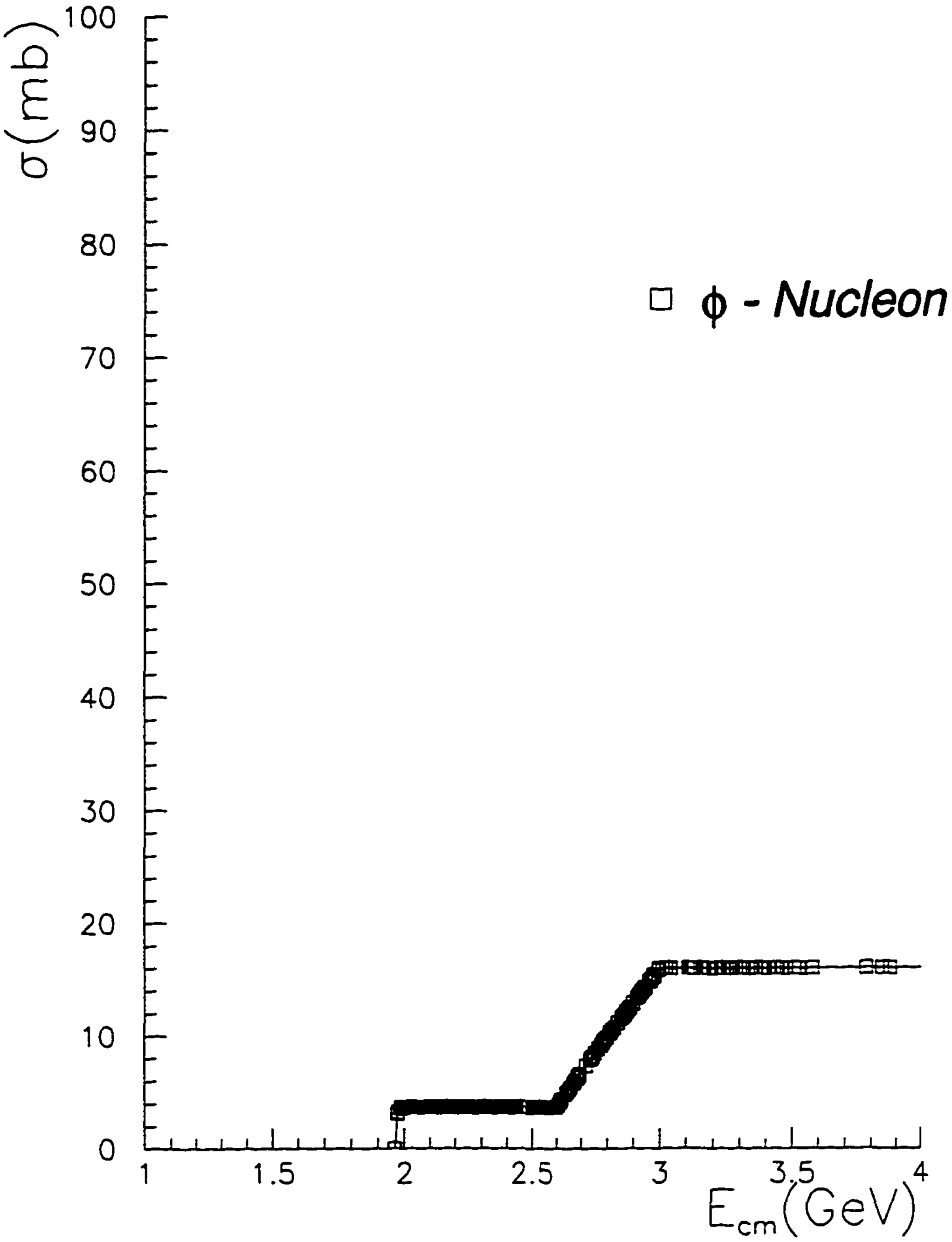

Figure A5.38: ϕ - Nucleon cross sections

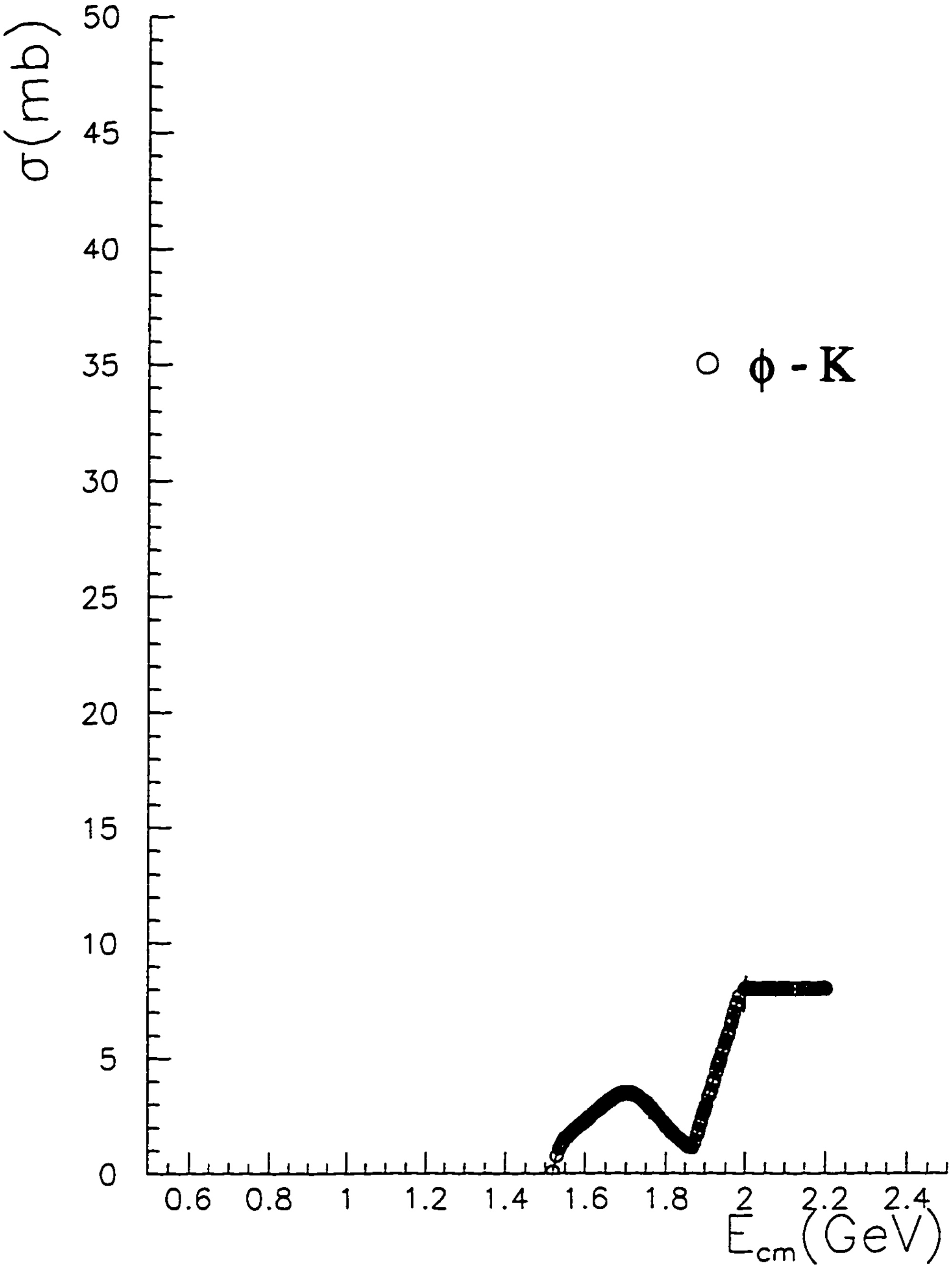

Figure A5.39: φ - Kaon cross sections

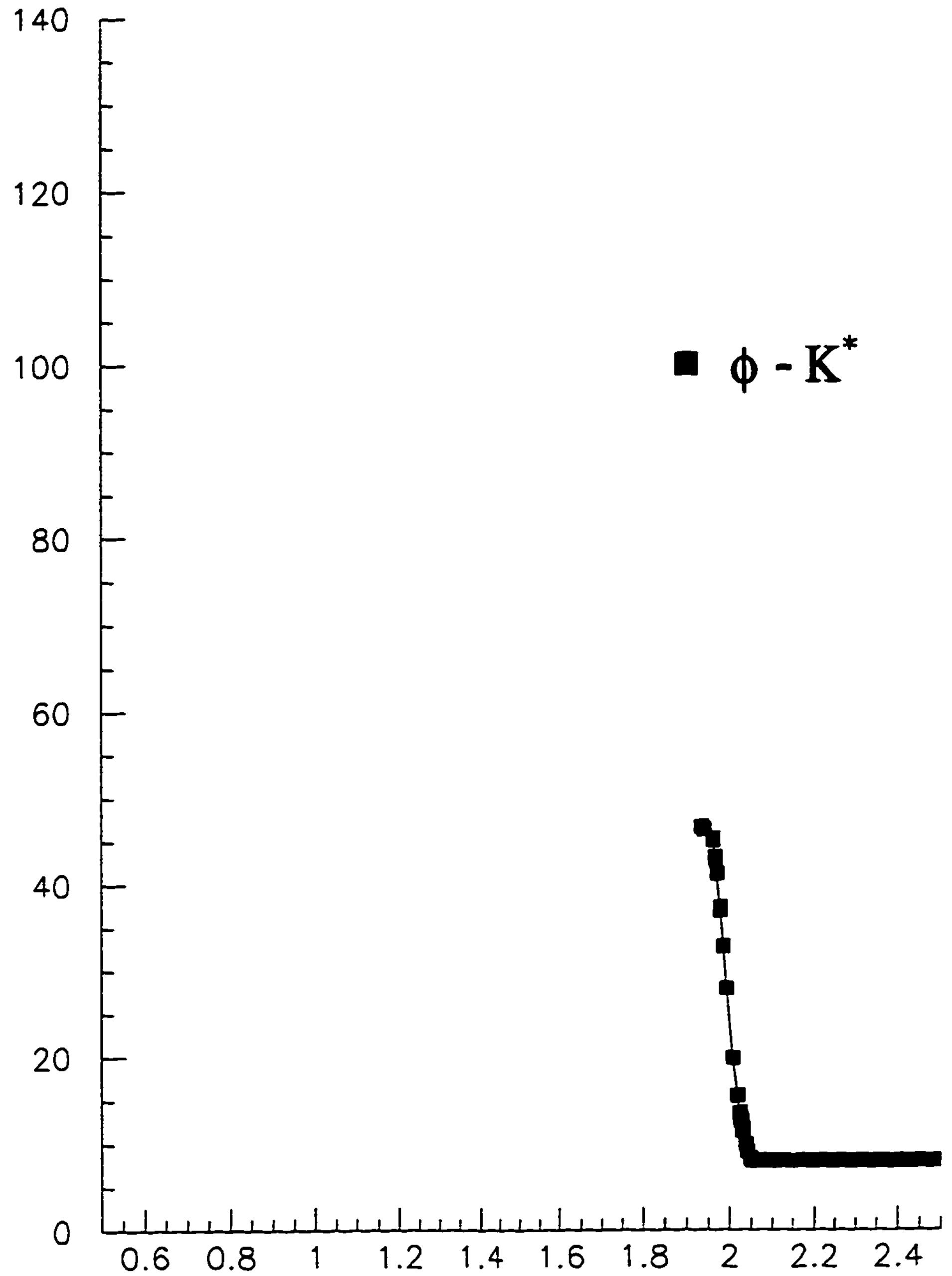

Figure A5.40: ϕ - K* cross sections

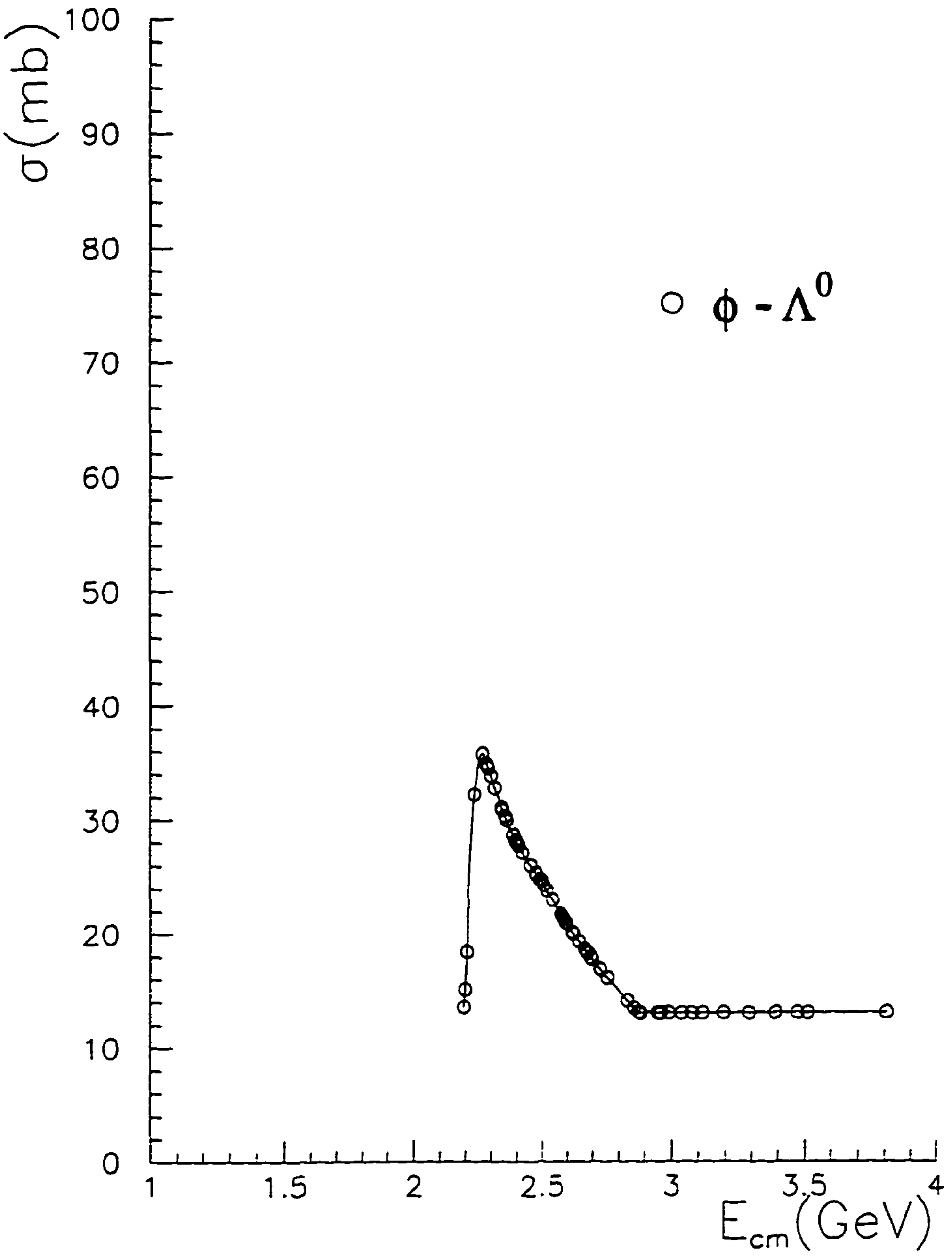

Figure A5.41: φ - Lambda cross sections

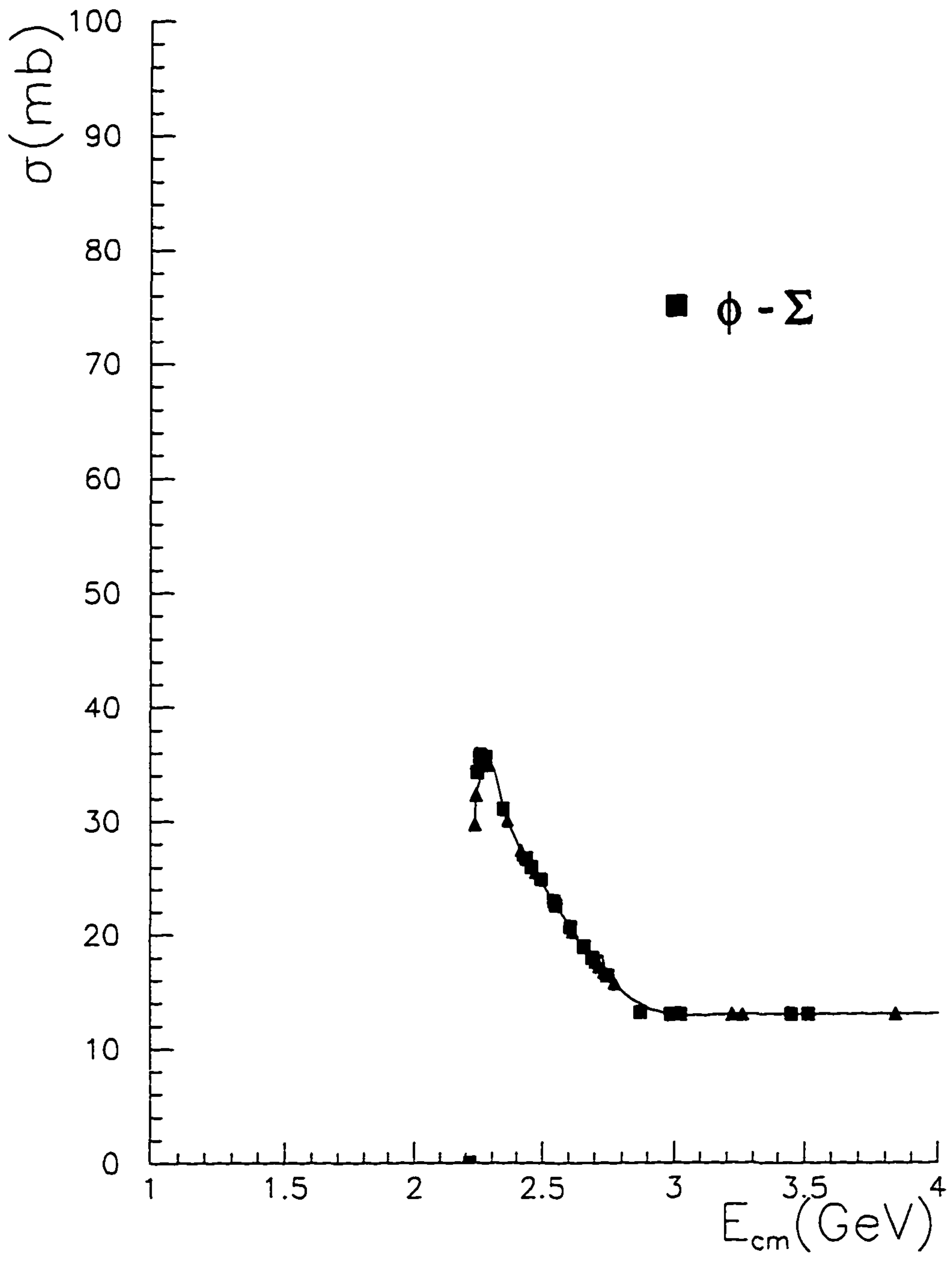

Figure A5.42: φ - Sigma cross sections

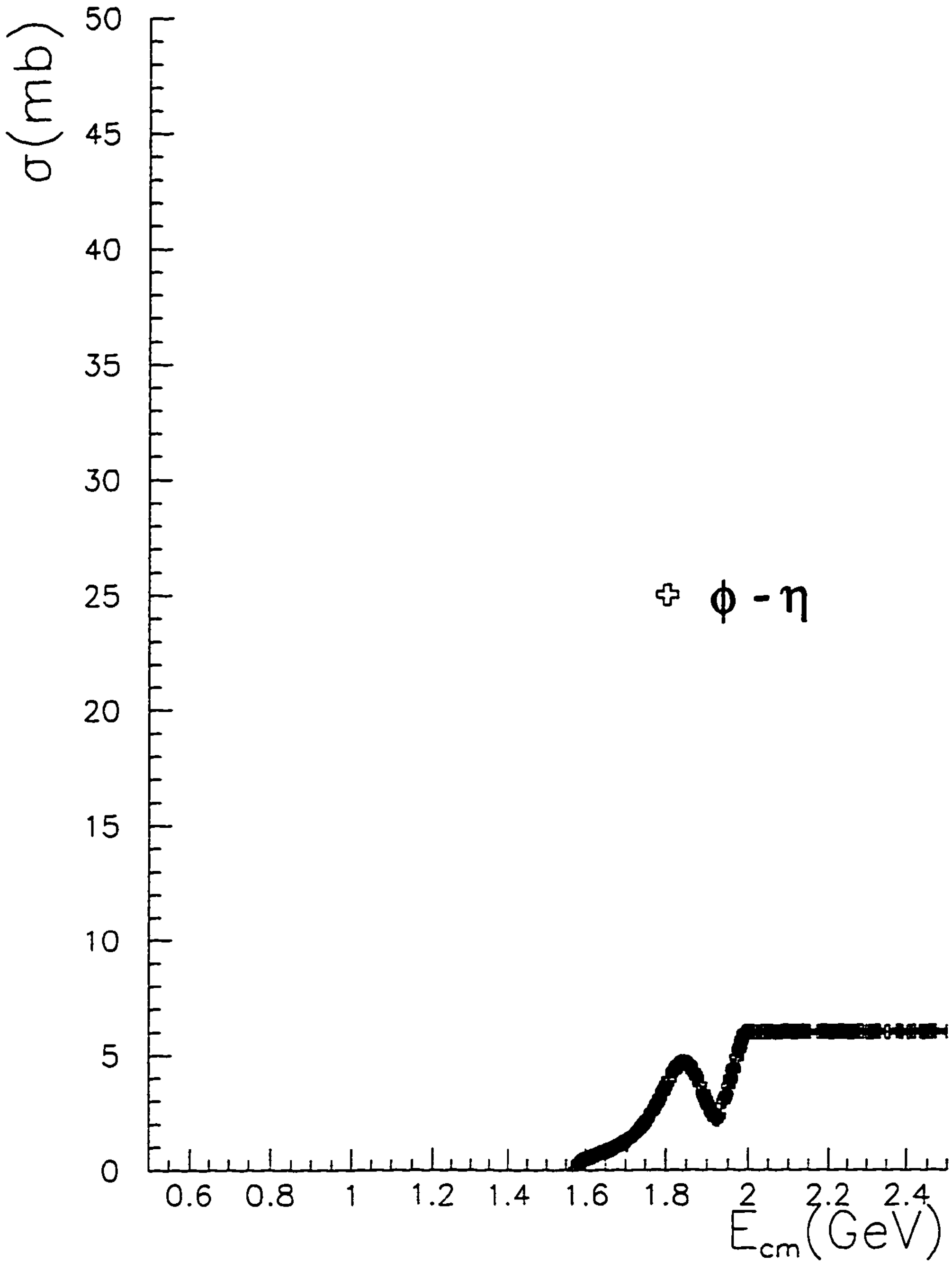

Figure A5.43: φ - eta cross sections

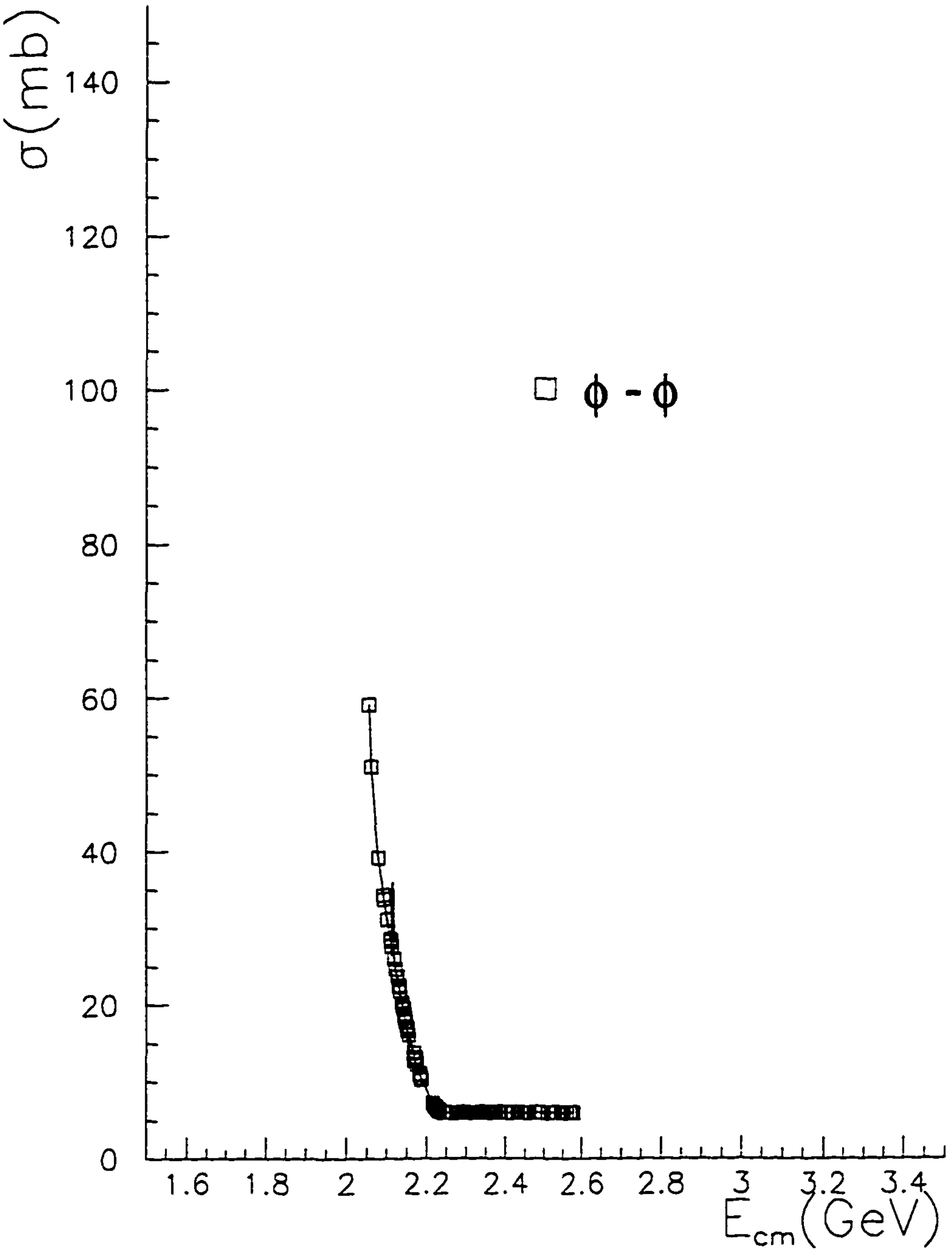

Figure A5.44: φ - φ cross sections

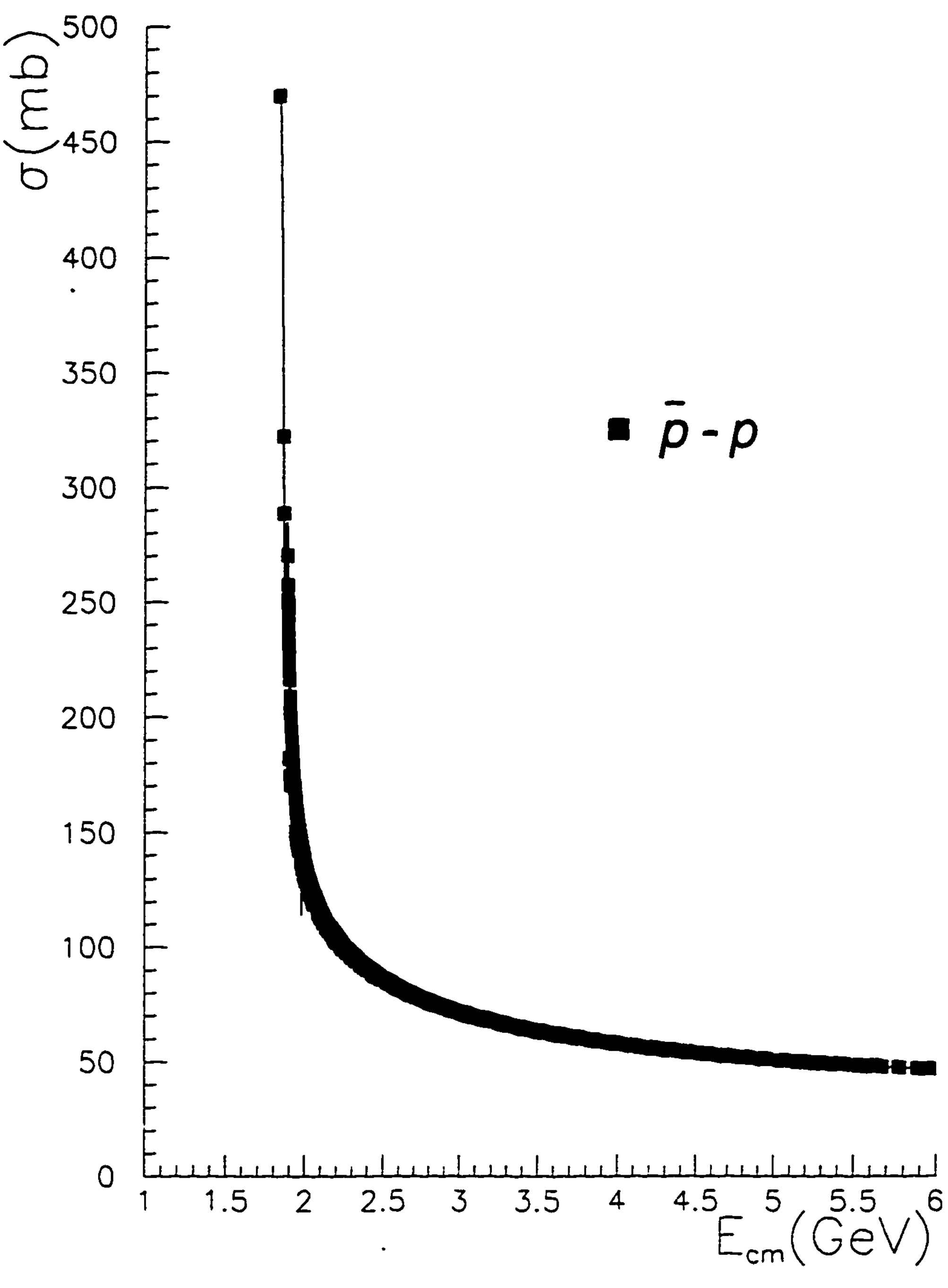

Figure A5.45: $\bar{p}$ - nucleon cross sections

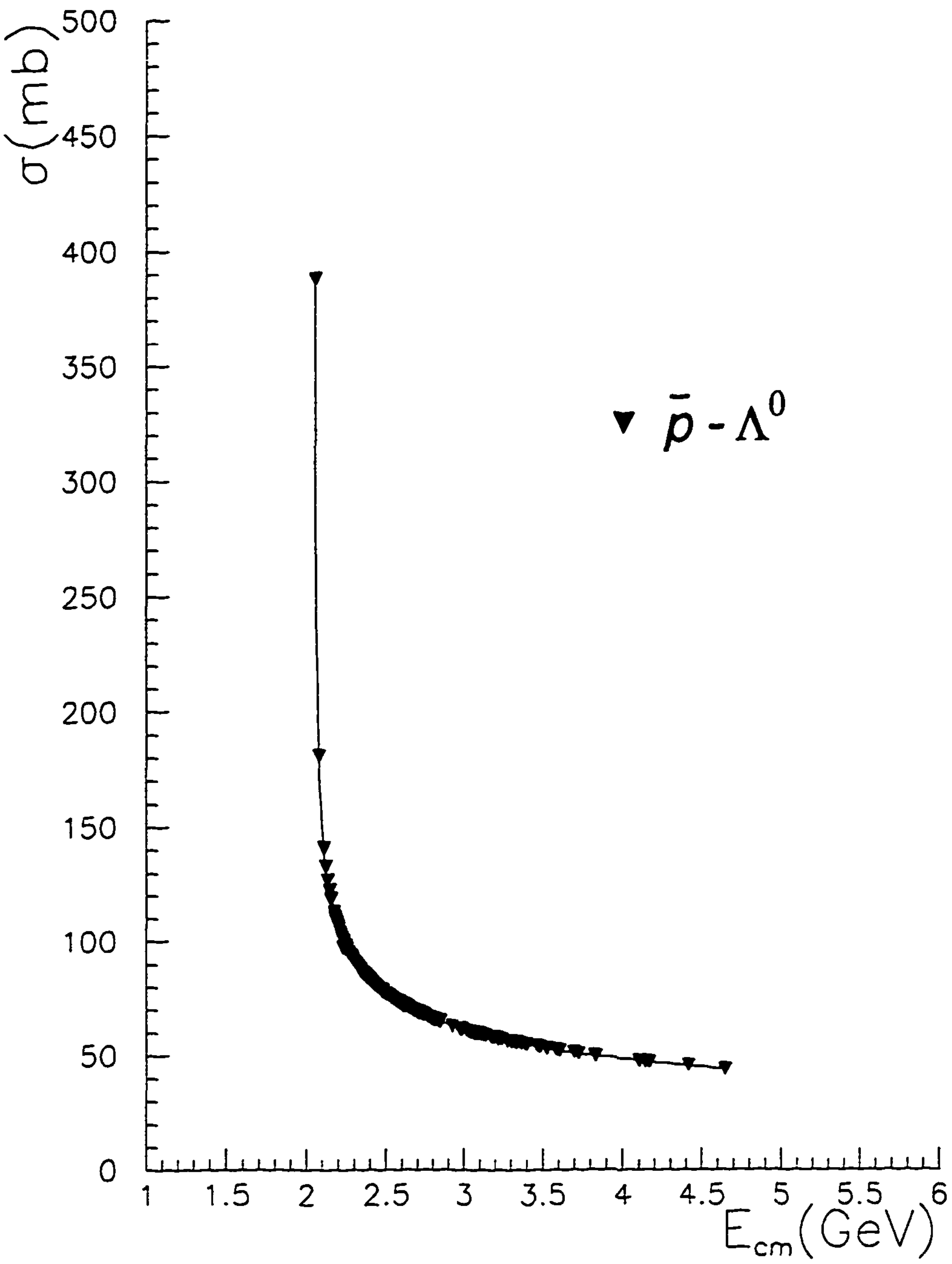

Figure A5.46: $\bar{p}$ - Lambda cross sections

Appendix 6

Calculation of π^-/p, π^-p/p and π^-p/p ratios

Lets assume that for a system of baryons at temperature T. a fraction f_1 of them are at the Δ(1232) state, f_2 in the N*(1500) state. f_3 in the N*(1700) state and f_0 in the ground state (protons and neutrons). In the N*(1700) state we also include Δ*(1700) states while the N*(1500) is dominated by N*'s (no Deltas). We calculate the π^-/p, π^-p/p and π^-p/p ratios. resulting from the decay of the above states. in terms of f_i's.

We start with the Δ(1232) state which decays to Nπ. The braching ratios are determined by Clebsch-Gordon coefficients [82]. If n is the initial number of protons and m the initial number of neutrons. then we get (figure A6.1):

$$\pi^- = f_1 \frac{n+3m}{6(n+m)} \tag{A6.1}$$

$$\pi^- p = f_1 \frac{2n+3m}{30(n+m)} \tag{A6.2}$$

$$\pi^- p = f_1 \frac{4n+m}{10(n+m)} \tag{A6.3}$$

$$p = f_1 \frac{2n+m}{3(n+m)} \tag{A6.4}$$

Next we consider the N*(1500) state. Since there are two charge states (N^{*+} and N^{*0}), a fraction n/n+m will be in the N^{*+} state and a fraction m/n+m in the N^{*0} state. From the particle data book we see that both charge states decay mainly to Nπ (50%) and Nππ (50%). The Nπ branching ratios are determined by Clebsch-Gordon coefficients. while the Nππ by data [90. 91] (figure A6.2):

$$\pi^- = f_2\left(\frac{3}{28}\frac{n}{n+m} + \frac{1}{3}\frac{m}{n+m} + \frac{11}{28}\frac{m}{n+m}\right) \tag{A6.5}$$

$$\pi^- p = f_2\left(\frac{3}{28}\frac{n}{n+m} + \frac{1}{3}\frac{m}{n+m} + \frac{5}{28}\frac{m}{n+m}\right) \tag{A6.6}$$

$$\pi^- p = f_2 \frac{3}{28}\frac{n}{n+m} \tag{A6.7}$$

$$p = f_2\left(\frac{n+2m}{6(n+m)} + \frac{9n+5m}{28(n+m)}\right) \tag{A6.8}$$

Finally, in the 1700 region, we estimate that an 80% of the nucleons are in the N*(1700) state, while the rest 20% are in the Δ* state. As in the 1500 region, a fraction n/n+m will be in the N^{*+} state and a fraction m/n+m in the N^{*0} state. Both charge states decay mainly to Nπ (50%) and Nππ (50%). The Nπ branching ratios are determined by Clebsch-Gordon coefficients. while the Nππ by data [90, 91] (figures A6.3, A6.4):

$$\pi^- = \frac{f_3}{1000(n+m)}(300n + 700m + \frac{80n + 120m}{3}) \tag{A6.9}$$

$$\pi^- p = \frac{f_3}{1000(n+m)}(230n + 340m + \frac{80n + 120m}{3}) \tag{A6.10}$$

$$\pi^- p = \frac{f_3}{1000(n+m)}(500n + 70m) \tag{A6.11}$$

$$p = \frac{f_3}{1000(n+m)}(522n + 358m + \frac{176n + 184m}{3}) \tag{A6.12}$$

Finally, the number of protons in the ground state are:

$$p = f_0 \frac{n}{n+m} \tag{A6.13}$$

By summing the protons from all the above sources ((A6.4), (A6.8), (A6.12) and (A6.13)) we get:

$$p = f_0 \frac{n}{n+m} + f_1 \frac{2n+m}{3(n+m)} + f_2(\frac{n+2m}{6(n+m)} + \frac{9n+5m}{28(n+m)}) + \frac{f_3}{1000(n+m)}(522n + 358m + \frac{176n+184m}{3}) \tag{A6.14}$$

$$\pi^- = f_1 \frac{n+3m}{6(n+m)} + f_2(\frac{3}{28}\frac{n}{n+m} + \frac{1}{3}\frac{m}{n+m} + \frac{11}{28}\frac{m}{n+m}) + \frac{f_3}{1000(n+m)}(300n + 700m + \frac{80n+120m}{3}) \tag{A6.15}$$

$$\pi^- p = f_1 \frac{2n+3m}{30(n+m)} + f_2(\frac{3}{28}\frac{n}{n+m} + \frac{1}{3}\frac{m}{n+m} + \frac{5}{28}\frac{m}{n+m}) + \frac{f_3}{1000(n+m)}(230n + 340m + \frac{80n+120m}{3}) \tag{A6.16}$$

$$\pi^- p = f_1 \frac{4n+m}{10(n+m)} + f_2 \frac{3}{28}\frac{n}{n+m} + \frac{f_3}{1000(n+m)}(500n + 70m) \tag{A6.17}$$

For the special case of $n = m$ (in Si $n = m = 14$) we get:

$$p = \frac{1}{2} \tag{A6.18}$$

$$\frac{\pi^-}{p} = \frac{2}{3}f_1 + \frac{10}{12}f_2 + \frac{16}{20}f_3 \tag{A6.19}$$

$$\frac{\pi^- p}{p} = \frac{1}{6}f_1 + \frac{13}{21}f_2 + 0.64f_3 \tag{A6.20}$$

$$\frac{\pi^- p}{p} = \frac{1}{2}f_1 + \frac{3}{28}f_2 + 0.57f_3 \tag{A6.21}$$

$$\Delta^{++} \longrightarrow \frac{4n+m}{10(n+m)} f_1 \qquad (p\pi^{+})$$

$$\Delta^{+} \begin{array}{ll} \nearrow & \dfrac{2}{3} \times \dfrac{3n+2m}{10(n+m)} f_1 \qquad (p\pi^{0}) \\ \searrow & \dfrac{1}{3} \times \dfrac{3n+2m}{10(n+m)} f_1 \qquad (n\pi^{+}) \end{array}$$

$$\Delta^{0} \begin{array}{ll} \nearrow & \dfrac{1}{3} \times \dfrac{2n+3m}{10(n+m)} f_1 \qquad (p\pi^{-}) \\ \searrow & \dfrac{2}{3} \times \dfrac{2n+3m}{10(n+m)} f_1 \qquad (n\pi^{0}) \end{array}$$

$$\Delta^{-} \longrightarrow \frac{n+4m}{10(n+m)} f_1 \qquad (n\pi^{-})$$

Figure A6.1: Decay of Delta(1232) state.

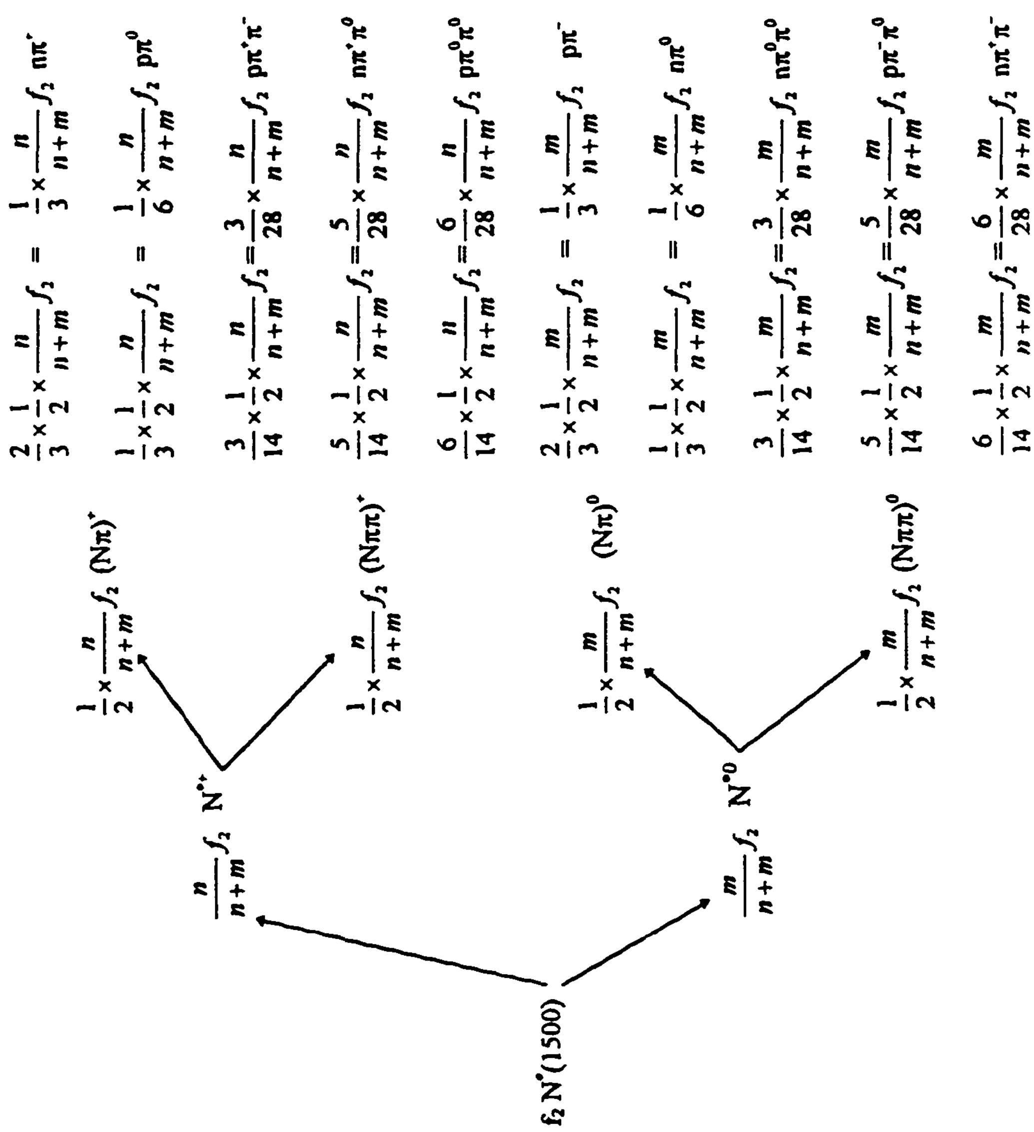

Figure A6.2: Decay of N*(1500) state

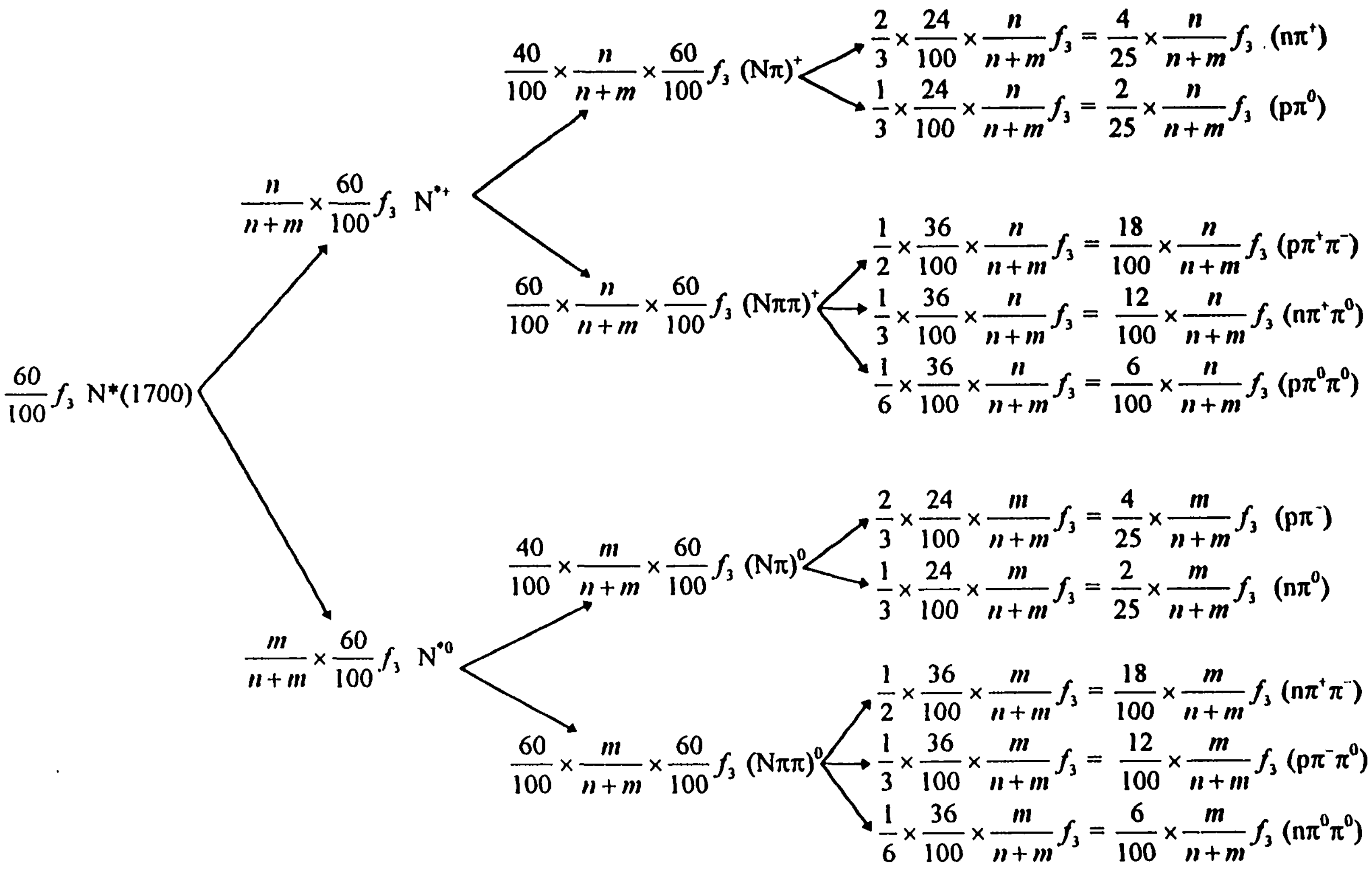

Figure A6.3: Decay of N*(1700) state.

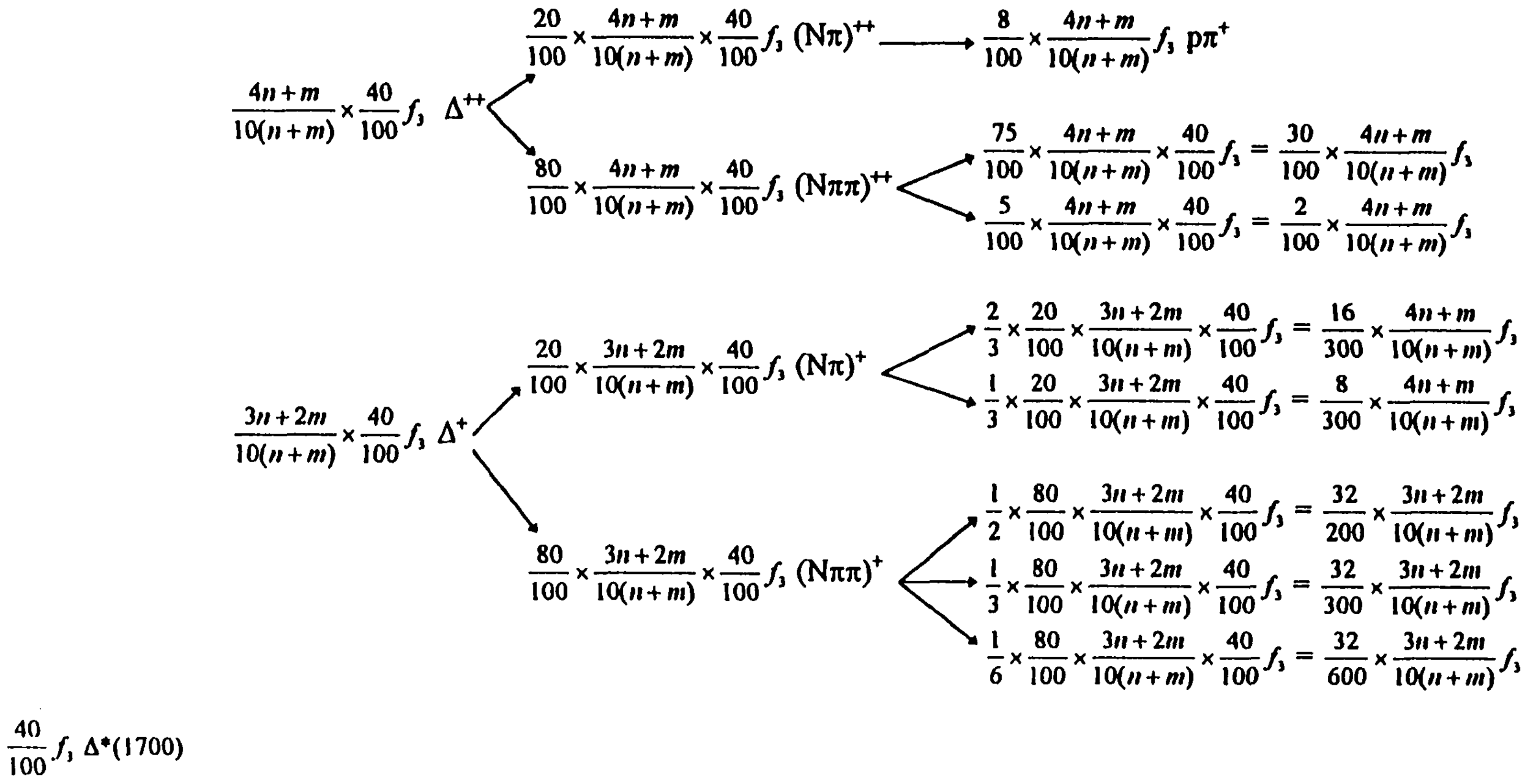

Figure A6.4: Decay of $\Delta^*(1700)$ state.

$$\frac{2n+3m}{10(n+m)}\times\frac{40}{100}f_3\ \Delta^0$$

$$\frac{n+4m}{10(n+m)}\times\frac{40}{100}f_3\ \Delta^-$$

$$\frac{20}{100}\times\frac{2n+3m}{10(n+m)}\times\frac{40}{100}f_3\ (\mathrm{N}\pi)^0$$

$$\frac{80}{100}\times\frac{2n+3m}{10(n+m)}\times\frac{40}{100}f_3\ (\mathrm{N}\pi\pi)^0$$

$$\frac{20}{100}\times\frac{n+4m}{10(n+m)}\times\frac{40}{100}f_3\ (\mathrm{N}\pi)^-$$

$$\frac{80}{100}\times\frac{2n+3m}{10(n+m)}\times\frac{40}{100}f_3$$

$$\frac{2}{3}\times\frac{8}{100}\times\frac{2n+3m}{10(n+m)}f_3=\frac{16}{300}\times\frac{2n+3m}{10(n+m)}f_3$$

$$\frac{1}{3}\times\frac{8}{100}\times\frac{2n+3m}{10(n+m)}f_3=\frac{8}{300}\times\frac{2n+3m}{10(n+m)}f_3$$

$$\frac{1}{2}\times\frac{32}{100}\times\frac{2n+3m}{10(n+m)}f_3=\frac{32}{200}\times\frac{2n+3m}{10(n+m)}f_3$$

$$\frac{1}{3}\times\frac{32}{100}\times\frac{2n+3m}{10(n+m)}f_3=\frac{32}{300}\times\frac{2n+3m}{10(n+m)}f_3$$

$$\frac{1}{6}\times\frac{32}{100}\times\frac{2n+3m}{10(n+m)}f_3=\frac{32}{600}\times\frac{2n+3m}{10(n+m)}f_3$$

$$\frac{20}{100}\times\frac{n+4m}{10(n+m)}\times\frac{40}{100}f_3\ \mathrm{n}\pi^-$$

$$\frac{75}{100}\times\frac{n+4m}{10(n+m)}\times\frac{40}{100}f_3\ \mathrm{n}\pi^-\pi^0$$

$$\frac{5}{100}\times\frac{n+4m}{10(n+m)}\times\frac{40}{100}f_3\ (\mathrm{p}\pi^-\pi^-)$$

Figure A6.4: Decay of $\Delta^*(1700)$ state (continued).

References

[1] J. E. Dodd, *The ideas of particle physics - An introduction for scientists*, Cambridge University Press, 1984.

[2] *Particle Physics: a Los Alamos primer*, edited by Necia Grand Cooper and Geoffrey B. West, Cambridge University Press, 1988.

[3] L. B. Okun, *Particle Physics. The Quest for the Substance of Substance*, Harwood Academic Publishers, 1984.

[4] Donald H. Perkins, *Introduction to High Energy Physics*, (3rd edn), Addison-Wesley Publishing Company, Inc., 1987.

[5] J. D. Jackson, *Classical Electrodynamics*, second edition, John Wiley and sons, 1975.

[6] T. Kinoshita, *Quantum Electrodynamics*, Advanced Series on Directions on High Energy Physics-Vol. 7, World Scientific, 1990.

[7] G. Arnison *et al.*, Phys. Lett. **B122**, 103 (1983), and Phys. Lett. **B126**, 398, (1983).

[8] P. Bagnaia *et al.*, Phys. Lett. **B129**, 130, (1983).

[9] M. Banner *et al.*, Phys. Lett. **B122**, 476, (1983).

[10] F. E. Close, *An Introduction to Quarks and Partons*, Academic Press, London, 1979.

[11] M. Kaku, *Quantum Field Theory: A Modern Introduction*, Oxford University Press, 1993

[12] V. Barnes *et al.*, Phys. Rev. Lett. **12**, 204 (1964).

[13] P. D. Collins, Alan D. Martin, *Hadron Interactions*, Bristol, 1984.

[14] Yu L. Dokshitzev, V. A. Khoze, A. H. Mueller and S. I. Troyan, *Basics of Perturbative QCD*, Editions Frontieres, 1991.

[15] A. Mueller, *Perurbative QCD*, Advanced Series on Directions on High Energy Physics-Vol. 5, World Scientific, 1989.

[16] G. Martinelli, *Standard Model, Hadron Phenomenology and Weak Decays*, Advanced Series on Directions on High Energy Physics-Vol. 8, World Scientific, 1991.

[17] R. C. Hwa, *Quark-Gluon Plasma*, Advanced Series on Directions on High Energy Physics-Vol. 6, World Scientific, 1990.

[18] Berndt Muller, *The Physics of Quark-Gluon Plasma*, Lecture Notes in Physics, Vol. **225**, Springer-Verlag, 1985.

[19] *A Brief Description of The Relativistic Heavy Ion Collider Facility (RHIC)*, Brookhaven National Laboratoty Report, BNL Report #: BNL-49177, 1993.

[20] B. K. Johnson, *The M.I.T. Bag Model*, Acta Polonica Vol. **B6**, 865, 1975.

[21] Cheuk-Yin Wong, *Introduction to High-Energy Heavy-ion Collisions*, World Scientific, 1994.

[22] B. Muller, *Physics Of Quark-Gluon Plasma*, in Proc. of the NATO Advaced Study Institute (ASI) on Particle Production in Highly Excited Matter, held July 12-24, 1992, edited by H. H. Gutbrod and J. Rafelski, Plenum Press, 1993.

[23] M. Jacob in *Relativistic Heavy ion Collisions*, Edited by Rudolf C. Hwa, Chong-shou Gao,Ming-Han Ye, Proceedings of the CCAST (World Laboratory Symposium held at Institute of High Energy Physics, Academia Sinica, Beijing, PRC, Gordon And Breach Science Publishers, June 1-13, 1994.

[24] *RHIC and Quark Matter. Proposal for a Relativistic Heavy Ion Collider at Brookhaven National Laboratory*, BNL Report # 51801, 1984.

[25] *Conceptual Design of the Relativistic Neavy Ion Collider RHIC*, BNL Report # 52195, 1989.

[26] Proc. of the 4th Int. Conf. on Magnet Technology, Sept. 19-21, 1972, BNL, MPS Note #17.

[27] A. Etkin, *et al.*, *Modular TPC's for Relativistic Heavy-Ion Experiments*, Nuclear Instruments and Methods in Physics Research, Vol. **A283**, 557-566, (1989).

[28] F. Sauli, *The time projection chamber for heavy-ion collisions: trends and perspectives*, Z. phys. C - Particles and fields **38**, 339-352, (1988).

[29] *The Time Projection Chamber*, AIP Conference Proceedings, Number 108, Edited by J. A. Macdonald, 1984.

[30] Jay N. Marx and David R. Nygren, *The Time Projection Chamber*, Physics Today, October 1978.

[31] Ronald J. Madaras and Piermaria J. Oddone, *Time-Projection Chambers*, Physics Today, August 1984.

[32] A. Etkin *et al.*, Nucl. Instr. and Methods in Phys. Research, **A323**, 224-227, (1992).

[33] T. Ferbel, *Experimental Techniques in High Energy Physics*, Addison-Wesley Publishing Company, Inc., 1987.

[34] Richard Fernow, *Introduction to Experimental Physics*, Cambridge University Press, 1986.

[35] S. E. Eiseman *et al.*, Phys. Lett. **B248**, 254, 1990.

[36] A.C.Saulys *et. al.*, MPS Data Acquisition System, Computer Physics Communications 57**,** 353-357, (1989).

[37] S. J. Lindenbaum *et al.*, Nucl. Phys. **A461**, 431c - 442c, 1987.

[38] P. Koch, B. Muller and J. Rafelski, *Physics Reports* **142**, 167, (1986); P. Koch, Z. Phys. C **38**, 269, (1988).

[39] J. Rafelski and R. Hagedorn, *Statistical Mechanics of Quarks and Hadrons*, ed. H. Satz, North Holland, Amsterdam, 1981.

[40] T. Matsui, B. Svetisky, and L. D. McLerran, Phys. Rev. **D34**, 783 (1986); K. Kajentie, M. Kataja, and P. V. Ruuskanen, Phys. Lett. **B179**, 153 (1986).

[41] S. Nagamiya, Nucl. Phys. **A544**, 5c-26c (1992).

[42] T. Abbott *et al.*, Phy. Rev. Lett. **64** (1990) 847.

[43] A. M. Rossi *et al.*, Nucl. Phys. **B84**, 269 (1975).

[44] W.Q. Chao, C.S. Gao and Y.L. Zhu, Nucl. Phys. **A514**, 734-748 (1990).

[45] R. S. Longacre *et al.*, Nucl. Phys. **A566**, 167c - 174c, (1994).

[46] S. E. Eiseman *et al.*, Phys. Lett. **B297**, 44-48, 1992.

[47] A. C. Saulys *et al.*, Proceedings of the XIII Particles and Nuclei International Conference (PANIC '93), June 27 - July 3, 1993, Perugia, Italy.

[48] T. Abbott *et al.*, Nucl. Instr. and Methods in Phys. Res. **A290**, 41-60 (1990).

[49] M.Gonin, *Meson production from the E802 and E866 Experiments at the AGS*, in Proc. of Heavy Ion Physics at the AGS HIPAGS '93, ed. G.S.F. Stephans, S.G. Steadman and W.L.Kehoe, (MITLNS, Cambridge, MA, 1993) p.184.

[50] T. Sung, *Strange Particle production*, in Proc. of Heavy Ion Physics at the AGS HIPAGS '93, ed. G.S.F. Stephans, S.G. Steadman and W.L.Kehoe, (MITLNS, Cambridge, MA, 1993) p.230.

[51] Y. Wang, *Production of ϕ Mesons in Central Si+Au Collisions at 14.6A GeV/c*, in Proc. of Heavy Ion Physics at the AGS HIPAGS '93, ed. G.S.F. Stephans, S.G. Steadman and W.L.Kehoe, (MITLNS, Cambridge, MA, 1993) p.239.

[52] T. Abbott *et al.*, Phys. Rev. **C50**, 50 (1994).

[53] R. Mattiello, H. Sorge, H.Stöcker, W. Greiner, Phys. Rev. Lett. **63**, 1459, (1989).

[54] H. Sorge, R. Mattiello, A. Jahns, H.Stöcker, W. Greiner, Phys. Lett. **B27**, 137-142, (1991).

[55] Y. Pang, T. J. Schlagel and S. H. Kahana, Phys. Rev. Lett. **68**, 2743-2746 (1992).

[56] S. Kahana *et al.*, *Physics at the AGS with a Relativistic Cascade*, in Proc. of Heavy Ion Physics at the AGS HIPAGS '93, ed. G.S.F. Stephans, S.G. Steadman and W.L.Kehoe, (MITLNS, Cambridge, MA, 1993) p.263.

[57] A. Shor and R. Longacre, Phys. Lett. **B218**, 100, (1989).

[58] R. Longacre, *HIJET with AGS Physics and N*'s*, in Proc. Heavy-Ion Physics at the AGS, (Massachusetts Institute of Technology, Jan. 1993), (eds.) G.S.F. Stephens, S.G. Steadman, and W.L. Kehoe, MITLNS-2158, 304, (1993).

[59] V. Blobel *et al.*, Nucl. Phys. **B69**, 454, (1974).

[60] E. Efstathiadis, Ronald S. Longacre, *Strangeness results from the RANDOM event generator for Si on Pb collisions at 14.5 GeV/c per nucleon*, in Proc. of The International Conference on Strangeness and Quark Matter, Sept. 1-5,1994, Crete, Hellas.

[61] K.S. Lee, M.J. Rhoades-Brown and U.Heinz, Phys. Rev. **C37**, 1452,1463, (1988).

[62] *Particle production in Highly Excited Matter*, Edited by H. H. Gutbrod and J. Rafelski, NATO ASI series, Plenum Press, New York, 1993.

[63] E. Efstathiadis, K. Zhao and Y. Zhu, *Strangeness enchancement in Heavy Ion Coliisions at the AGS*, in Proc. of The International Conference on Strangeness and Quark Matter, Sept. 1-5,1994, Crete, Hellas.

[64] A.C Saulys *et al.*, *Neutral Strange particle production at the AGS*, in Proc. of Heavy-Ion Physics at the AGS, (Massachusetts Institute of Technology, Jan. 1993), (eds.) G.S.F. Stephens, S.G. Steadman, and W.L. Kehoe, MITLNS-2158 (1993) 196.

[65] S. Ahmad *et al.*, Phys. Lett. **B325**, 322-326, (1994).

[66] H. Sorge, in Proc. of The International Conference on Strangeness and Quark Matter, Sept. 1-5,1994 Crete, Hellas.

[67] J. Simon-Gillo, Nucl. Phys. **A566**, 175c-182c (1994).

[68] J. Schukraft, Proc. of the International Workshop on Quark Gluon Plasma Signatures, October 1-4, 1990, Editions Frontieres.

[69] S. H. Oh, Proc. of the International Workshop on Quark Gluon Plasma Signatures, October 1-4, 1990, Editions Frontieres.

[70] J. Sollfrank, P. Koch, U. Heinz, Phys. Lett. **B252** (1990) 256.

[71] B. Cole, in Proc. of Heavy-Ion Physics at the AGS, (Massachusetts Institute of Technology, Jan. 1993), (eds.) G.S.F. Stephens, S.G. Steadman, and W.L. Kehoe, MITLNS-2158 (1993) 313.

[72] P. Siemens and J. Rasmussen, Phys. Rev. Lett. **42**, 880, (1979).

[73] G.E. Brown, J. Stachel, and G.M. welke, Phys. Lett. **253**, 19, (1991).

[74] S. Ahmad *et al.*, Phys. Lett. **B281**, 29 (1992).

[75] T.K. Hemmick, in Proc. of Heavy-Ion Physics at the AGS, (Massachusetts Institute of Technology, Jan. 1993), (eds.) G.S.F. Stephens, S.G. Steadman, and W.L. Kehoe, MITLNS-2158 (1993) 204.

[76] J. Harris *et al.*, Nucl. Phys. **A498** (1989) 133c.

[77] T. Akesson *et al.*, Z. Phys. **C46** (1990) 361.

[78] M. Gonin *et al.*, Phys Rev C **51**, 310, (1995).

[79] S. Gavin, Proc. of the Ninth International Conference om Ultra-Relativistic Nucleus-Nucleus Collisions, Gatlinburg, Tennessee, USA, November 11-15, 1991.

[80] T. Abbott *et al.*, Phys. Rev. **C50** 1027-1047 (1994).

[81] M. Gazdzicki, D. Rohrich, Z. Phys. **C65**, 215-223, (1995).

[82] Particle data book, Phys. Rev **D50** (1994).

[83] J. Dee, in Proc. of Heavy-Ion Physics at the AGS, (Massachusetts Institute of Technology, Jan. 1993), (eds.) G.S.F. Stephens, S.G. Steadman, and W.L. Kehoe, MITLNS-2158 (1993) 47.

[84] F. Videbæk, *Charged Particle Distributions in Heavy Ion Collisions at 14.6 GeV A/c*, in Proc. of Heavy-Ion Physics at the AGS, (Massachusetts Institute of Technology, Jan. 1993), (eds.) G.S.F. Stephens, S.G. Steadman, and W.L. Kehoe, MITLNS-2158 (1993) 89.

[85] C. Parsons, in Proc. of Heavy-Ion Physics at the AGS, (Massachusetts Institute of Technology, Jan. 1993), (eds.) G.S.F. Stephens, S.G. Steadman, and W.L. Kehoe, MITLNS-2158 (1993) 72.

[86] F. Videbæk, Phys. Rev. **C52** 2684-2693 (1995).

[87] S. Chapman *et al.*, Phys. Rev. Lett. 67 (1991) 1210.

[88] J. Stachel, Formation and Break-up of Hadronic Fireballs, in Proc. of the Workshop on Heavy Ion Physics at the AGS, March 5-7, 1990, Edited by Ole Hansen, p. 144.

[89] H. Sorge, Phys. Rev. **C49** R1253 (1994); UFTP 393-95, University of Frankfurt preprint.

[90] A. D. Brody *et al.*, Phys. Rev. **D4**, 2963 (1971).

[91] E. Flamino *et al.*, Compilation of cross sections IV π^+ induced reactions, CERN/HERA70-5 and Compilation of Cross-sections VI π^- induced reactions, CEN/HERA 70-7.